Flow and Heat Transfer Optimization in Ultra-Compact Heat Exchangers Enabled by Additive Manufacturing

Mohammed Almaghrabi

Lady Margaret Hall

University of Oxford

A thesis submitted for the degree of

Doctor of Philosophy

Hilary 2024

This thesis is dedicated to my wonderful parents, my beloved wife, my three precious angels (Sara, Sulaf, and Norah) and my supportive siblings

Your unwavering love and support have been a constant source of strength in my life.

I will forever cherish your boundless affection and care

ACKNOWLEDGMENTS

First and foremost, I praise Allah, the Almighty, for granting me this opportunity and the capability to proceed successfully with this journey.

I would like to express my sincere gratitude and appreciation to my supervisor, Prof. Budimir Rosic, for his continuous support, guidance, and patience throughout this study. My heartfelt thanks also go to Mitsubishi Heavy Industries for their invaluable support and assistance during this journey, especially to Dr. Koichi Tanimoto and Dr. Hiroyuki Nakaharai. I am equally grateful to my colleagues at the Oxford Thermofluids Institute for their insightful comments, enriching discussions, and unwavering support.

I extend my gratitude to all my colleagues who have supported me, particularly Wesley Ramm, Jaime Saw, Oguzn Murat, Simla, Hassan Ifty, Francisco Orieno, Mark Baker, and many others who have made this transformative journey possible. Your generous feedback, advice, and contributions have been invaluable. Your friendship has deeply enriched my life.

Lastly, my profound gratitude goes to my beloved family (my parents, my wife, and siblings), for their genuine encouragement, patience, and prayers. Without your incredible support, none of this would have been possible.

Abstract

This thesis investigates the optimization of flow and heat transfer in ultra-compact heat exchangers through the use of additive manufacturing (AM) techniques. The study begins with an analysis of Internal Longitudinal Fins Channels (ILFC) and Central Inclined Finned Channels (CIFC). While ILFC improves heat transfer, it increases pressure drop, thereby compromising performance. A parametric study on CIFC demonstrates a 115% performance improvement due to the introduction of swirl flow, optimizing thermal-hydraulic efficiency. Further exploration of swirl devices reveals substantial gains, with optimal configurations achieving a 166% improvement over smooth channels. The use of materials with higher thermal conductivity also provides a 9% performance boost. These findings were validated through numerical simulations and experimental setups developed at the Oxford Thermofluids Institute (OTI), which featured modular designs for testing various cooling techniques. Additionally, the thesis includes the design and testing of a heat exchanger comprising nine cells, using constant inlet fluid temperatures for more realistic temperature profiling across the cells. This approach contrasts with previous models assuming constant wall temperatures. A novel manifold design was developed and tested, ensuring superior flow uniformity across heat exchanger cells, confirming its effectiveness compared to conventional manifold designs.

Table of Contents

LIST OF FIGURES

LIST OF TABLES

LIST OF ACRONYMS

Symbol	Definition
A_c	Cross sectional area of the channel, [m^2]
C_p	Specific Heat at Constant Pressure, [J/kg .K]
D_h	Channel Hydraulic Diameter, [m]
H	Fin Height, [m]
HR	Height Ratio
L_{ch}	Channel Length, [mm]
N	Number of swirler's blades
Nu_{sw}	Average Nusselt Number for the swirler Case
Nu_s	Nusselt Number for the Fully Developed Smooth Case
Nu	Nusselt Number Using D_h as a Characteristic Length
P	Channel pressure, [N/m^2]
PF	Thermal-hydraulic performance factor
PP	Pumping Power
PR	Pitch Ratio
Q	Heat Input, [W]
Re_{D_h}	Reynolds Number Using D_h as a Characteristic Length
S_u	Source Term, [N/m^3]
T_i	Inlet Temperature, [K]
T_m	Mean fluid Temperature, [K]
T_w	Temperature at the Wall, [K]
V	Volumetric Flow rate
W_{ch}	Channel Width, [m]
W_{ch}	Channel Width, [m]
u^+	Dimensionless Velocity
u_t	Wall Friction Velocity ($=\sqrt{\tau_w / \rho}$), [m/s]
y	Normal Distance to the Wall, [m]
y^+	Dimensionless Wall Distance.
f_{sw}	Average friction factor for the swirler case
f_s	Friction Factor for the Fully Developed Smooth Case
u_i	Absolute Velocity in the i^{th}Direction, [m/s]

x_i	Coordinate in the i^{th} Direction
t	Fin Thickness, [mm]
c^+	an Empirical Constant (c^+ = 5.45)
e	Rib Height, [mm]
f	Friction factor -
h	Convection Heat Transfer Coefficient, [W/m^2.K]
k	Thermal Conductivity [W/m.K]
$keff$	Effective Thermal Conductivity, [W/m.K]
k_l	Laminar Thermal Conductivity, [W/m.K]
p	Fin Pitch, [mm]
q·	Wall Heat Flux, [W/m^2]
x	Axial Coordinate, [m]

Greek symbols

α	Angle of attack, [degree]
τ	Shear Stress, [N/m^2]
ΔP	Pressure Drop [N/m^2]
ΔT	Temperature Difference, [K]
μ_l	Laminar Dynamic Viscosity, [Pa.s]
p	Channel Perimeter, [m]
ε	Effectiveness
μ	Dynamic viscosity, [Pa.s]
ν	Kinematic Viscosity, [m^2/sec]
ρ	Density, [kg/m^5]
τ_w	Wall Shear Stress, [N/m^2]

Subscripts:

ch	Channel
D_h	Hydraulic Diameter
eff	Effective
f	Friction
i	Term Number, Tensor Index (1, 2, 3).
i	Inlet
PP	Pumping Power
r	Ribbed case
sw	Swirler case
s	Fully Developed Smooth Case

w	Wall
X	Component in x-Direction.
Y	Component in y-Direction.
Z	Component in z-Direction.

Superscripts:

-	Time Averaged Value
'	Fluctuating Component

Abbreviations:

2D	Two Dimension.
3D	Three Dimension.
CFD	Computational Fluid Dynamics
CIFC	Central Inclined Finned Channel
FVM	Finite Volume Method
NTU	Number of Transfer Units
IEEE	Institute of Electrical and Electronics Engineers
ILFC	Internal Longitudinal Fins Channel
SIMPLE	Semi-Implicit Method for Pressure-Linked Equations
SISE	Side Inlet Side Exit

CHAPTER 1 INTRODUCTION

1.1 Additive Manufacturing

In the realm of manufacturing engineering technology, the last few decades have witnessed a paradigm shift, primarily driven by the advent of Additive Manufacturing (AM), also known as 3-D printing technology. This revolutionary approach diverges fundamentally from traditional manufacturing methods. Unlike conventional processes, which predominantly involve material removal, AM constructs objects by sequentially adding material layers, closely following three-dimensional CAD models. This methodical alteration not only minimizes material waste but also significantly reduces energy consumption, thereby aligning with modern sustainable engineering practices. AM's versatility extends to various metals through processes like Selective Laser Sintering (SLS), Selective Laser Melting (SLM), Electron Beam Melting (EBM), and Direct Metal Laser Sintering (DMLS).

AM has been utilized in many areas, such as aerospace, automotive, electronics, biomedical, etc. [1]. Giant companies such as Siemens and General Electric are attracted by this invention and started making a big investment in additive manufacturing. To increase the capabilities of the Selective Laser Melting (SLM), which is one of the AM techniques, Siemens has inaugurated an AM facility in Sweden. In February 2017, Siemens accomplished a new breakthrough that no other companies worldwide have reached. The first full load test of an additively manufactured gas turbine blade was performed [2]. In addition, General Electric (GE) was able to save a significant amount of money by printing a nozzle for their leap jet engine as one part, where it usually made of twenty different parts via the conventional manufacturing processes.

In the past, designers regarded stochastic roughness as unavoidable phenomena, which can occur due to the manufacturing process, corrosion, erosion and so on. Thus, with AM, designers

can choose the shape and pattern of surface roughness, which will make the roughness regarded as an imperative design parameter.

1.2 Heat transfer enhancement techniques

Heat transfer enhancement techniques are classified as passive and active as shown in Figure 1.1. Examples of the single phase heat transfer technique were explained in [3]. Among several techniques, modifying the channel geometry by adding surface roughness, ribs, and fins to promote the swirl flow and secondary flow has the potential to promote the heat transfer and pressure drop. The target of this study is to use the passive technique to enhance the heat transfer while minimizing the pressure drop.

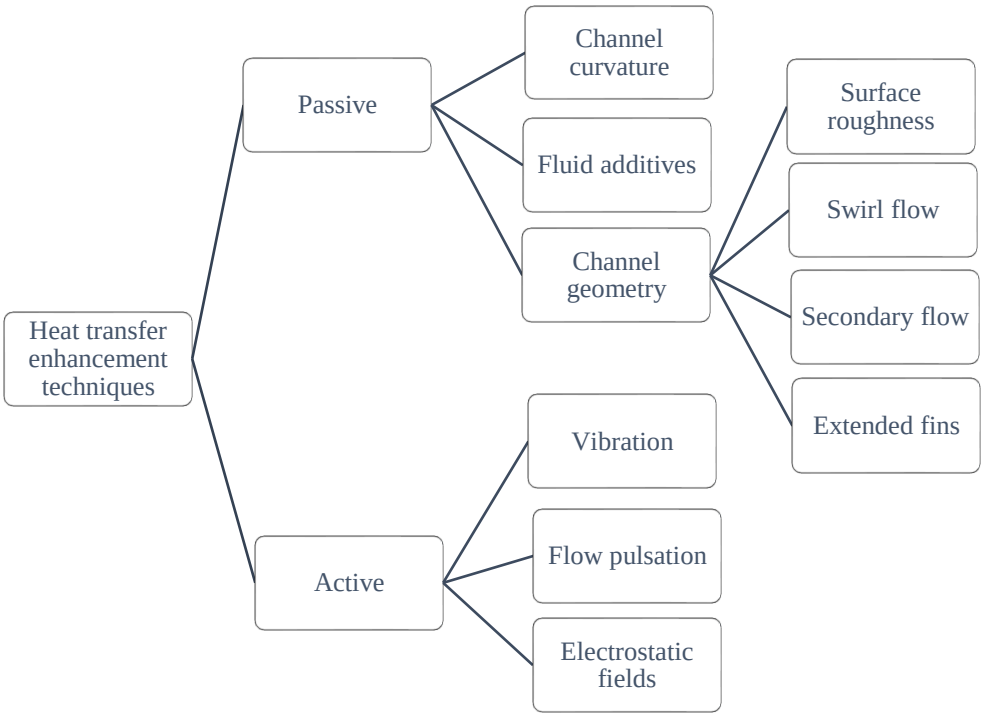

Figure 1-1: Heat transfer enhancement classification.

Surface roughness in a heat exchanger refers to irregularities or texture present on the internal surfaces of the heat exchanger tubes or channels through which the fluid flows. These irregularities can affect the heat transfer characteristics and overall performance of the heat exchanger in several ways [4–6]:

1. Heat Transfer Enhancement: In certain cases, controlled surface roughness can be intentionally introduced to enhance heat transfer. For example, surface texturing techniques such as dimples, ribs, or grooves can be used to increase the effective surface area and promote turbulence, thereby improving heat transfer performance.
2. Boundary Layer Disturbance: Surface roughness can disrupt the boundary layer formed near the heat transfer surface. This disruption can reduce the thickness of the boundary layer, leading to improved heat transfer rates between the fluid and the heat exchanger surface.
3. Enhanced Turbulence: Surface roughness can disrupt the flow of the fluid, leading to increased turbulence. Turbulence promotes better mixing, leading to improved heat transfer. However, excessive turbulence can also increase pressure drop within the heat exchanger.
4. Fouling: Surface roughness can also promote fouling by providing sites for the accumulation of deposits and contaminants. Fouling reduces heat transfer efficiency and increases energy consumption by insulating the heat transfer surface and reducing the heat transfer area.
5. Corrosion: Surface roughness can accelerate corrosion rates by providing crevices or pits where corrosion processes can initiate. Corrosion can degrade the heat exchanger's structural integrity and reduce its lifespan.
6. Pressure Drop: Surface roughness increases frictional resistance to fluid flow, resulting in higher pressure drop across the heat exchanger. This can affect the pumping power required to circulate the fluid through the system and may impact overall system efficiency.

In heat exchanger design and operation, engineers must carefully consider the effects of surface roughness on heat transfer, pressure drop, and fouling. Surface treatments, coatings, or material

selection may be employed to mitigate the negative impacts of surface roughness or to enhance heat transfer performance, depending on the specific requirements and operating conditions of the heat exchanger system.

Fins in a heat exchanger are extended surfaces that are attached to the heat transfer surface to enhance heat transfer between the fluid flowing inside the tubes or channels and the surrounding medium (usually air or another fluid). Fins significantly increase the surface area available for heat transfer without significantly increasing the volume or weight of the heat exchanger. Here are some key points about fins in heat exchangers [7–9]:

1. Purpose: Fins are primarily used to increase the heat transfer surface area and thereby improve the heat transfer rate. They are commonly employed in applications where high-efficiency heat transfer is required, such as in air-cooled heat exchangers, automotive radiators, air conditioning systems, and electronic cooling systems.
2. Types of Fins:

- Plate Fins: These are flat, rectangular fins attached perpendicular to the heat transfer surface.
- Louvered Fins: These fins have louvers or corrugations that increase the surface area for heat transfer.
- Pin Fins: These are cylindrical or pin-shaped fins attached to the surface.
- Wavy Fins: Fins with a wavy or sinusoidal profile, which increases the surface area compared to straight fins.
- Serrated Fins: Fins with serrations or notches along their length, which disrupt boundary layers and enhance heat transfer.
- Integral Fins: Fins that are an integral part of the heat exchanger surface, usually formed by extrusion or machining.

3. Heat Transfer Mechanism: Fins increase heat transfer primarily through convection. They provide additional pathways for heat to be transferred from the primary surface to the surrounding fluid (air or another fluid). Fins also help in spreading the heat more uniformly over the heat transfer surface, reducing temperature gradients and improving overall efficiency.
4. Design Considerations: The design of fins in a heat exchanger involves considerations such as fin geometry (height, thickness, spacing), material selection (conductivity, corrosion resistance), and the overall arrangement of fins to optimize heat transfer while minimizing pressure drop and cost.
5. Effectiveness: In the context of fins, effectiveness refers to the measure of a fin's ability to enhance heat transfer relative to the heat transfer that would occur without the fin. It depends on factors such as the thermal conductivity of the fin material, fin geometry, fluid properties, flow conditions, and operating parameters.

Swirl flow in a heat exchanger refers to the movement of the fluid within the exchanger that has a rotational or swirling component. This swirling motion can affect the heat transfer characteristics and effectiveness of the heat exchanger in several ways [10–13]:

1. Enhanced Heat Transfer: Swirl flow improves heat transfer by disrupting boundary layers and promoting better mixing within the fluid. This increased mixing reduces thermal resistance, leading to more efficient thermal exchange between the fluid and heat exchanger surfaces.
2. Heat Exchanger Design: The design of heat exchangers can be optimized to promote swirl flow, such as using internal baffles or twisted tube geometries. These designs can induce and control swirl in the fluid flow to maximize heat transfer.

3. Reduced Fouling: Swirling flow can also help in reducing fouling on heat exchanger surfaces by promoting a more uniform distribution of fluid and preventing the accumulation of deposits.

However, it's important to note that while swirl flow can enhance heat transfer, it may also increase pressure drop within the heat exchanger system. Therefore, the design and optimization of heat exchangers involving swirl flow require a careful balance between heat transfer enhancement and pressure drop considerations.

1.3 Compact Heat Exchangers

For the past few decades heat exchangers have been widely used in many applications including aerospace, power generation, petrochemical industry, air conditioning and refrigeration, electronics, transportation, food engineering and others [14]. Due to the rapid increase in energy demands, manufacturers are thriving to reduce energy consumption and increase the system efficiency by exploiting thermal management methodologies. Compactness of the heat exchanger is one of the methods to increase the energy system efficiency due to its advantage of reduced weight, good thermal performance, low energy requirement and cost [15].

The surface area to volume ratio is an important factor in heat exchanger design and performance. It essentially describes the ratio of the heat transfer surface area to the volume of fluid contained within the heat exchanger, more area leads to more efficient heat transfer. It impacts heat exchangers as follows:

1. Effectiveness: A higher surface area to volume ratio generally leads to enhance heat transfer. This is because a larger surface area allows for more effective exchange of heat between the fluid and the surroundings.

2. Compactness: Heat exchangers with a high surface area to volume ratio can be more compact in size compared to those with a lower ratio, while still achieving the desired heat transfer rates. This is particularly advantageous in applications where space is limited or where minimizing the size and weight of the heat exchanger is important.
3. Heat Transfer Rate: The surface area to volume ratio directly influences the rate at which heat can be transferred between the fluid and the heat exchanger surface. A higher ratio means that a larger portion of the fluid comes into contact with the heat transfer surface, leading to faster heat exchange.
4. Design Considerations: Engineers often aim to maximize the surface area to volume ratio in heat exchanger design while balancing other factors such as pressure drop, fluid flow characteristics, and manufacturing feasibility. This involves optimizing the geometry of the heat exchanger (such as tube length, diameter, and arrangement) to achieve the desired balance between heat transfer efficiency and practical considerations.
5. Materials Selection: The choice of materials for constructing the heat exchanger can impact the surface area-to-volume ratio. Materials with higher thermal conductivity allow for thicker walls without compromising heat transfer efficiency, ensuring structural integrity while maintaining effective thermal performance. Optimizing geometry is also critical to maximizing the surface area-to-volume ratio.

Overall, the surface area to volume ratio is a critical parameter in heat exchanger design, as it directly affects the heat transfer performance and efficiency of the system. Balancing this ratio with other design considerations is essential for optimizing the overall performance of the heat exchanger in various applications. The surface area to volume ratio of a gas to liquid compact heat exchanger is above 700 m^2/m^3 and for a liquid-to-liquid heat exchanger is above 400

m^2/m^3. A great example from nature of such a compact system is the human lungs which has an area density of about 17500 m^2/m^3 [16].

Since convection is the main heat transfer mode on the heat transfer process of the compact heat exchanger, one can augment heat transfer by modifying the surface area (A), heat transfer coefficient (h), or both (hA) from the basic energy balance for single phase conviction Eq. (1.1). In this study the enhancement technique of heat transfer is achieved by utilizing some of the passive techniques such as roughen surface, extended surface (i.e. fins), insert and swirl devices. The purpose of using this technique is to increase surface area for heat dissipation and disturb the boundary layer which gives the main resistance to the heat transfer or to give a great mixing to the bulk of the fluid. However, the presence of extended surfaces in the system poses more resistance to the flow, thus the pressure drop penalty must be considered in the design phase. Designing such systems involves a tradeoff between heat transfer and fluid dynamics behavior.

$$Q = hA(T_w - T_f) \tag{1.1}$$

1.4 Exploration of Manifold Design in Heat Exchangers

The manifold in a heat exchanger is more than just a conduit for fluid flow; it is a critical component that significantly influences the heat exchanger's efficiency and effectiveness. In the context of compact heat exchangers, where space and efficiency are of paramount importance, the design of the manifold becomes even more crucial. One of the significant challenges that has emerged in manifold design is the issue of flow maldistribution. This phenomenon occurs when the working fluid within the heat exchanger is not evenly distributed, leading to localized areas of high or low heat transfer. Such maldistribution can severely impair

the overall performance of the heat exchanger, resulting in inefficiencies and potentially shortening its operational lifespan.

The causes of flow maldistribution are multifaceted, stemming from various design and operational factors. These include the geometric configuration of the manifold, the flow dynamics within the manifold, the properties of the working fluid, and the operating conditions of the heat exchanger.

Recognizing the critical nature of this issue, this study aims to explore the manifold design of heat exchangers with a focus on mitigating the problem of flow maldistribution. The study aims to leverage the advanced capabilities of Additive Manufacturing to explore new manifold geometries that were previously unachievable. This innovative manufacturing method allows for the creation of complex designs that can significantly improve fluid distribution within the heat exchanger. Computational Fluid Dynamics (CFD) simulations will be used to optimize the design of the manifold.

By improving manifold design, the study has the potential to enhance the efficiency of heat exchangers, leading to more effective thermal management solutions in various industrial applications. This, in turn, could have far-reaching impact on energy conservation and sustainability. The successful optimization of manifold designs could revolutionize how we approach the design and operation of heat exchangers, potentially leading to more eco-friendly and cost-effective thermal management systems in a wide range of applications. This would not only signify a significant improvement in engineering design but also underscore the role of innovative manufacturing techniques like Additive Manufacturing in solving complex engineering challenges. The outcomes of this study are anticipated to provide valuable insights and set new benchmarks in the design of efficient, high-performance heat exchangers.

1.5 Goal and Objectives

The primary goal of this study is to investigate various methods for enhancing heat transfer in ultra-compact heat exchangers enabled by additive manufacturing (AM). The most promising concepts are developed, designed, and experimentally validated. The following objectives are established to achieve this goal:

1. To examine the heat transfer characteristics and flow dynamics of ultra-compact heat exchangers and explore the potential of AM capabilities to further enhance their overall performance.
2. To conduct a numerical investigation using computational fluid dynamics (CFD) and conjugate heat transfer (CHT) methods to evaluate different passive heat transfer enhancement techniques applied in ultra-compact heat exchangers.
3. To investigate the impact of swirl flows on the friction factor and heat transfer characteristics.
4. To understand the flow physics of the most promising concept and analyse its thermal-hydraulic performance.
5. To validate the numerical models with experimental testing to ensure accurate performance prediction.
6. To design and optimize a novel manifold architecture aimed at improving flow uniformity.

Through this study, the author intends to contribute significantly to the field of compact heat exchanger design, utilizing the unique capabilities of Additive Manufacturing to push the boundaries of current engineering solutions.

1.6 Plan for Patent/Publications

1.6.1 Patent Filing Plan

The innovative designs introduced in this study address critical challenges in heat exchanger performance. The first innovation is the swirl device, which significantly enhances heat transfer efficiency while minimizing pressure drop of the system. The second innovation is the new manifold design, which enhances flow uniformity, further contributing to improvements in heat transfer performance.

To protect the intellectual property, two separate patent applications will be filed under the jurisdiction of Saudi Arabia by Q2 2025. The patents will cover:

1. The innovative design of the swirl device for enhanced heat transfer and flow dynamics in ultra-compact heat exchangers.
2. The new geometrical configuration of the improved manifold.

1.6.2 Publication Plan

The findings of this study contribute to the field of heat transfer and compact heat exchanger design. A detailed publication plan has been developed to disseminate these results to both the scientific community and industry practitioners:

1. **Journal Submissions:**
    - A manuscript focusing on the thermal-hydraulic performance of the one-passage swirl device channel will be submitted to the *International Journal of Heat and Mass Transfer* by Q3/2025.
    - A second paper focusing on ultra-compact heat exchangers and heat transfer techniques for enhancing thermal-hydraulic performance enabled by additive

manufacturing (AM) will be submitted to *Applied Thermal Engineering* by Q3/2025.

2. **Conference Presentations:**
    - The results on heat transfer enhancement techniques and experimental findings will be presented at the 12th International Conference on Heat Transfer and Fluid Flow (HTFF 2025), which is scheduled for August 19–21, 2025, in Paris, France.

Through these publications, the study aims to make a meaningful contribution to academic research while fostering innovation in industrial applications.

CHAPTER 2 LITERATURE REVIEW

This chapter discusses several techniques that have been proposed to enhance the heat transfer and pressure drop on heat exchangers. The approaches are presented and discussed comprehensively. It also presents and summarizes the various additive manufacturing techniques used to fabricate heat exchangers with complex geometry. In addition, the chapter summarizes the previous related research and identifies the research gaps in this research area.

2.1 Heat Transfer Enhancement

Overall, heat transfer enhancement techniques play a vital role in optimizing thermal management systems across various industries. Heat transfer enhancement techniques for heat exchangers aim to improve thermal performance by increasing the rate of heat transfer. These techniques can be broadly categorized into passive and active methods. The passive techniques do not require external energy and rely on the geometry, materials, or flow behaviour to enhance heat transfer. Examples include surface modifications, such as extended surfaces (fins), rough surfaces, corrugated or wavy surfaces, inserts, twisted tape inserts, wire coils, mesh, vortex generators, baffles, helical flow paths. In turn, active methods require external energy input to manipulate flow or surface conditions, improving heat transfer. Examples include mechanical aids, vibrations, fluid flow manipulation (injection or suction), jet impingement, electrical and magnetic, surface heating or cooling, and ultrasonic and acoustic techniques. By leveraging innovative designs, advanced materials, and optimized fluid dynamics, engineers can achieve significant improvements in heat transfer efficiency, leading to more efficient and sustainable thermal systems.

2.1.1 Extended surfaces promote swirl flow

Swirl flow techniques are among the most effective passive heat transfer enhancement methods. They involve the generation of rotational or helical flow patterns within the heat

exchanger to disrupt the thermal boundary layer, enhance fluid mixing, and increase heat transfer coefficients [17–19]. These methods are widely studied and implemented due to their simplicity, effectiveness, and compatibility with various heat exchanger configurations.

Swirl flow creates secondary flows or vortices that [20]:

1. Disrupt the laminar sublayer, increasing turbulence even in low Reynolds number regimes.
2. Enhance mixing between the core and boundary layers of the fluid, improving heat transfer.
3. Increase the residence time of fluid in the heat exchanger, providing more opportunity for heat exchange.

There are many Techniques to generate swirl flow, such as twisted tape inserts, helical inserts, vortex generators, grooved and corrugated surfaces, and wire coil inserts. Table 2-1 summarizes the heat transfer and pressure drop of heat exchangers use swirl flow. They can increase the heat transfer coefficient by up to 50–300%, depending on the method and operating conditions. While swirl flow techniques enhance heat transfer, they also increase pressure drop. Many reviews on passive heat transfer techniques can be found in the literature such as the work of Liu and Sakr [21]. Extended surfaces and swirl flow devices are two effective enhancement techniques which are seen in a wide range of applications [22].

Swirl flow can be generated by the shape of the channel itself or by means of insertion of swirl generators such as twisted tapes, coiled wires, helical inserts, axial propellers, among others. Swirl flow can be continuous as a result of inserting twisted tape, coiled wires or similar continuous devices. On the other hand, decaying swirl flow can be generated as a consequence of placing discontinuous twisted tape inserts or axial propellers with smooth region gap in between them. This smooth gap allows the swirl flow to decay before it enter the successive device which re-intensify the swirling flow again. The augmentation of heat transfer associated with swirl flow is attributed to numerous effects: increased the path length of the flow,

increased the speed of the flow by introducing the tangential velocity component particularly near the channel wall and secondary flow generation which mixes the flow. The presence of such secondary flows leads to an increase to both friction losses and heat transfer rates [23]. Therefore, attention must be given to the pressure drop penalty associated with such an enhancement when designing a heat exchanger.

Table 2-1 Summary of different swirl flow techniques and their thermal performance factor (PF)

Ref.	Modifications	Re	PF	Nu/Nu_o	f/f_o	Fluid
[24]	Short length twisted tape	5000 10000 20000	0.98 0.95 0.91	1.3 1.24 1.16	2.31 2.23 2.1	Air
[25]	Alternate clockwise and counterclockwise	5000 10000 20000	1.35 1.26 1.18	2.52 2.18 1.8	6.62 5.26 3.58	water
[26]	Jagged twisted tape	5000 10000	1.17 1.09	2.22 1.93	6.86 5.61	water
[27]	Butterfly twisted tape	5000 10000	1.6 1.53	4.74 3.73	26.6 14.8	water
[28]	Twin Delta winged tape	5000 10000	1.24 1.12	2.54 2.1	8.78 6.64	Water
[29]	Delta winglet twisted tape	5000 10000 20000	1.22 1.18 1.15	2.24 2.08 1.94	6.3 5.65 4.83	Water
[30]	Twisted tape with winglet vortex generator	5000 10000 20000	1.56 1.48 1.38	3.16 2.95 2.83	8.47 9.33 9.85	Air
[31]	Twisted tapes with alternate axes and triangular wing	5000 10000 20000	1.42 1.25 1.13	2.87 2.34 1.96	8.4 6.7 5.6	Water
[32]	Perforated rib	5000 10000 20000	2.8 2.45 1.9	4.8 4.4 3.6	5.0 5.9 6.8	Air
[33]	Punched triangular vortex generator	5000 10000 20000	2.7 2.48 2.2	1.95 2.1 2.21	0.38 0.6 1.0	Air
[34]	Curved delta wing vortex generator	250 1500	2.14 2.39	4 15	6.5 245	Water

[35]	Multiple conical stripes	300	1.89	2.54	2.4	Water
		1500	2.49	7.63	28.74	
[36]	Inner twisted square duct and outer circular pipe	500	1.38	1.8	2.2	Air
		1000	1.41	1.9	2.4	
[37]	Counter-twisted oval tubes	500	1.35	1.5	1.35	Air
		1000	1.53	1.8	1.6	
[38]	Co-Twisting oval pipes	500	1.22	1.26	1.09	Air
		1000	1.33	1.4	1.15	

2.1.2 Artificial roughness

In order to further develop highly efficient heat exchanger, designers and researchers are turning to additive manufacture (AM) technologies due to the vast array of applications and present limitations of traditional production processes. AM has opened up a universe of possibilities for redesigning heat exchangers into cutting-edge designs, sizes, and forms. Optimized geometries with improved surfaces, regulated surface roughness, fully controlled and organized porous structures, and the removal of the necessity for brazing or welding are just a few of the remarkable benefits of AM-enabled heat exchangers. AM can control the main features affecting the heat transfer and pressure drop in heat exchangers, such as surface roughness, fin thickness, and fin heights. Therefore, the ability to design and produce incredibly small features becomes possible as AM accuracy advances. These incredibly thin characteristics allow for the reduction of tube wall thickness, the construction of new geometries, and enhanced complexity at smaller scales. The overall thermal resistance drops with decreasing wall thickness, increasing the heat exchanger's efficacy in the process. It is therefore possible to design and produce heat exchangers that are smaller and more compact. The AM method and material chosen will determine the lowest feature thickness that can be

achieved. It was reported that Direct Metal Laser Sintering (DMLS) [39], Polyjet [40], and Lithography-based Ceramic Manufacturing (LCM) [41] methods could produce a thickness as small as 150, 32-100, and 100 μm, respectively.

Tunning the design of the heat exchanger by adding surface features directly affects its ability to improve heat transfer. In general, heat transfer enhancement techniques can be classified into two categories. The first one is passive technique where no external power is required, and the second one is the active technique where an external power is required. In this study, the former technique is investigated to promote the heat transfer, by introducing swirl to the flow and increasing the effective heat transfer surface area. However, using this method to augment heat transfer is always accompanied with an increase in pressure drop which can increase the pumping power requirement and the total cost. Thus, many researchers have attempted placing different turbulator shapes (circular, triangular, square, etc.) on a smooth surface to examine its effect on the heat transfer and flow characteristics.

In 1981, the pioneer work by Tuckerman and Peace [42] shed the light on the concept of microchannel heat sink. Lee and Garimella [43] investigated numerically a three dimensional microchannel of a rectangular cross section at three different aspect ratios. A correlation for the local and the average Nusselt numbers along the axial distance were obtained for the thermally developed laminar flow. The correlations found to be in a good agreement with other experimental data. Chai et al. [44] studied numerically the characteristics of laminar flow and heat transfer in microchannel heat sink with offset ribs on sidewalls. The Reynolds number ranged from 190 to 838. The offset ribs increased the heat transfer and pressure drop as expected. However, the increase rate of heat transfer declined as Reynolds number increased while the friction factor increased. The highest performance factor found with the forward triangular offset ribs when Reynolds number is less than 350 while the rectangular offset ribs show the lowest performance factor. Ghani et al. [45] did a similar study to [44] where the

mini-channel they tested have secondary oblique channel and rectangular ribs on the sidewalls. The range of Reynold number for this work were from 100 to 500. The study tested the effect of four different configurations on the overall thermal-hydraulic performance. The best overall performance obtained by the microchannel with secondary oblique and rectangular ribs on the sides. This superiority attributed to the larger flow area introduced by the secondary oblique channels.

To augment the overall thermal performance in conventional channels, Dong and Ebadian [46] conducted a numerical study to examine the effect of four internal fins on heat transfer characteristics of thermally developing flow in elliptic ducts. A uniform wall temperature was applied axially and peripherally. The fully developed Nusselt number was four times higher than that for the smooth elliptic duct. Huq et al. [47] tested experimentally the heat transfer performance of an internally finned tube. The range of Reynolds number was from 2.6×10^4 to 7.9×10^4. The results showed an improvement of about 52% when compared to that of a smooth tube.

Many researchers have used repeated ribs as an artificial roughness [48–52]. Han [53,54] carried out an experiment on a square duct with ribs being placed on opposite sides of the walls. Reynolds number ranged from 7000 to 90,000 which was fully turbulent air flow. The study examined the impact of the rib height to hydraulic diameter and rib pitch to rib height on the heat transfer and friction characteristics. Consequently, the smooth wall adjacent to the ribbed wall was enhanced by 25%. Furthermore, the examined duct compared to a four-sided smooth duct, and the Stanton number of the ribbed duct was about 2.2 times the smooth one. However, this heat transfer enhancement is associated with an increase in the friction factor for up to 6 times that of the smooth duct. A correlation that accounted for the angle and pitch of the rib was developed in the same experiment [54]. Another experiment to investigate the effect of channel aspect ratio and rib angle of attack was done by Han three years later [55]. This time

the ribs were placed on top, and bottom walls of the channel and Reynolds number ranged from 10,000 to 60,000. The rib angles of attack and the channel aspect ratios were 90^o, 60^o, 45^o and 30^o, and 1, 2 and 4, respectively. At constant pumping power, an augmentation of about 30% on heat transfer occurred at the square channel with rib angle of attack 30^o and -45^o when compared to the rib angle of attack 90^o at the rectangular channel. At the end, a correlation that accounted for rib pitch, angle, height, channel aspect ratios and different Reynolds numbers was established.

Lau et al. [56] conducted an experimental study to the impact of nine different rib shapes (transverse and discrete ribs) on heat transfer and friction factor. As a result, when the angle of attack was 90^o the discrete ribs showed an increase of about 15% on the average Stanton number over the transverse ribs. However, when the ribs were angled, the transverse ribs showed about 20% increase over the discrete ribs.

The effect of two kinds of dimples (i.e., oval and circular) on heat sink fin was tested numerically and experimentally [57]. The range of Reynolds varied between 500 and 1650. Accordingly, an enhancement in the thermal performance without the penalty of pressure drop was achieved. Moreover, the oval dimple showed better thermal performance enhancement when compared to the circular dimple. In a comparable study, Patel and Borse [58] found a proportional relationship between Reynolds number and the thermal performance. Also, the study demonstrated that a higher Nusselt number was obtained with the staggered arrangement of the dimples when compared to the inline configuration.

2.1.3 Topological optimization

The rising necessity to maximize heat dissipation and performance has prompted new approaches to HX design [59]. Lattice structures, for example, have been shown to improve heat transmission and, as a result, HX efficiency [60]. A lattice structure is made up of solid

struts that are topologically arranged in a periodic configuration known as a cell, which is repeated one or more times [61]. The lattice structures provide extraordinary mechanical resistance, resulting in extremely efficient load support systems, as well as unique crossflow heat exchange possibilities. The heat from the heated fluid is dissipated locally through the reticular structure via conduction and convection as a result of a crossflow of cool fluid that propagates through the pores' channels. The combination of strong thermal conduction and convection with low flow resistance in the lattice structure's vacant spaces yields very efficient heat exchange [62–64]. Traditionally, lattice structures have been made using standard manufacturing procedures, which have numerous limitations in terms of designs [60]. In contrast, the introduction of contemporary AM methods has enlarged the conceivable geometries that may be made [65,66]. At the moment, research into the usage of hollow structure is underway. The combination of a lattice structure with a crystalline structure has the potential to considerably improve thermal efficiency. These novel hollow-walled HXs made by AM have significant promise for industrial growth, but the correlations between heat transmission, losses, and structural type must to be adequately investigated [67,68]. Nonetheless, several limitations of lattice structure and thin feature manufacturability by AM remain a barrier that scientific research is actively attempting to address. The constraints of minimum and maximum inclination, thickness, and accuracy may not necessarily ensure the realization of complicated and thin geometry in complex constructions.

2.1.4 Flow maldistribution

Flow maldistribution in heat exchangers is a critical issue that can significantly affect their performance and efficiency. It refers to the uneven distribution of fluid flow within the channels of a heat exchanger. It can arise due to various factors such as improper design of the manifold system, manufacturing tolerances, fouling, thermal expansion, and improper installation. Numerous experimental and CFD studies have been conducted to investigate flow

maldistribution in heat exchangers. These experimental studies often involve flow visualization techniques, pressure drop measurements, and temperature measurements to quantify the extent of maldistribution and its effects on heat transfer performance.

Lu and Wang [69] quantified the flow instability by introducing the velocity maldistribution factor (ω), presented by the following equation:

$$\omega = V_{std}/V_{avg} \tag{2.1}$$

Table 2-5 lists some studies on the thermo-hydraulic performance using different inlet/outlet modifications. Researchers discovered that the I-type configuration (a flow path that resembles an "I" shape) has the lowest velocity maldistribution factor and pressure drop values when compared to the C (or U) and Z-type configurations [70,71]. The reason for this is the Coanda effect. The effect implies that when fluid strikes the bottom surface at the inlet and spreads in the manifolds before and after passing through microchannels, it forms a hydrophilic layer, causing the liquid to slip in that region. This increases the velocity of fluid in areas far from I/O locations. This effect is more pronounced in C and Z-type configurations, resulting in flow instability, owing to improved flow stability and lower pressure drop.

Huang et al. [72] and Tingzhen et al. [73] examined the efficiency of microchannels with multiple inlets, dome-shaped ribs, cavities, and cavity-rib combinations. They discovered that ribs provide the highest overall performance. The multi-inlet system provides fresh fluid at regular intervals, and the ribs beneath them raise heat transfer area and flow disturbance, thereby improving the pressure drop. Ribs' spherical geometry guides impinging flow, reducing it. Gan et al. [74] recommended modifying the configuration to include side outlets, which improves overall performance by decreasing the pumping power more. In another work on improving bottom surface temperature uniformity, repeated decreases in multi-inlet diameter were found to be more effective than equal diameters [75]. Mohammadi et al. [76] studied

triangular shapes for attaining a small volume and residence time in manifolds. They demonstrated that adding vertical spacing to a right-angled triangular manifold and making it trapezoidal improves flow uniformity. Tang et al. [70] compared triangular, rectangular, and symmetric trapezoidal manifold shapes for enhanced performance. The study concluded that symmetric trapezoidal shapes have the best flow distribution. Despite this, the rectangular manifold had the best thermal performance at the same pumping power. Samal and Moharana [77] analyzed various hierarchical manifold designs. They evaluated the performance of branched, rectangular, triangular, and trapezoidal shapes. The branched manifold demonstrated better uniform flow than others due to the symmetric distribution of flow velocity in the downward direction. As a result, bottom surface temperature uniformity was achieved even in the case of a branched manifold. While branched manifolds outperformed rectangular manifolds in terms of thermal performance, their overall performance was lower.

Table 2-2 Studies on thermo-hydraulic performance using different inlet/outlet modifications.

Ref.	**Study type**	**Channel type**	**Modification type**	**Comments**
[70]	CFD	Rectangular	Z-, I-, and U-type	I-type had 28% less thermal resistance at the same pumping power.
[71]	CFD	trapezoidal	Z-, I-, and U-type	I-type had the less flow maldistribution by 24%.
[78]	CFD	Rectangular	Alternate ports recharging type	Compared to conventional rectangular microchannel, this design had 62% higher thermal performance.
[79]	CFD			Compared to microchannel heat exchanger, this design had 124% higher overall performance.
[80]	CFD			Max overall performance of 1.8 was estimated.
[81]	CFD			This design showed higher temperature uniformity and overall performance.
[82]	CFD			Max overall performance of 1.8 was estimated.
[72]	CFD	Rectangular with ribs and cavities	Multi inlets/two opposite outlets	14% overall performance improvement was achieved.

[73]	CFD	Rectangular with ribs		14% overall performance improvement was achieved using ribs.
[74]	CFD	Rectangular with ribs	Multi inlets/side outlet	26% overall performance improvement was achieved using side outlet.
[75]	CFD	Rectangular	Multi inlets with fixed/variable radius	Better temperature uniformity was achieved using smaller diameters
[83]	CFD and Exp.	Rectangular double-layer	Straight and Nested arrays	10.5% overall performance improvement was achieved using nested array.
[84,85]	CFD and Exp.		X-structured, No mixing	The single X-structured counter flow had the highest overall performance, with an 8.56% increase over the counter flow double-layered conventional rectangular microchannel.

2.2 Additive Manufacturing Methods

Additive Manufacturing enables significant innovations for the next generation of more efficient heat exchangers. To create cost-effective mass products, heat exchangers have employed conventional manufacturing techniques like milling, injection molding, alignment, brazing/welding or a combination of these methods. These processes are still in use today. Typically, small-scale heat exchangers, like microchannel heat pumps, are constructed using stamping or folding methods to enhance heat transfer and feature fins for increased efficiency [86,87]. These methods limit the types of geometry and the size and thickness of parts that can be produced, such as pipe walls. AM could mitigate these limitations. AM is the process of fusing materials into three-dimensional forms by bonding them, typically in a stepwise fashion. Typically, a 3D CAD model is generated and then fed into splicing software that splits the model into thin horizontal slices. These slices are the instructions for the 3D printer to create each individual layer one by one. AM is not limited to the use of traditional plastics, but can also create parts made of alloys, ceramics, composites, and even biological materials [88]. Manufacturers are beginning to take advantage of the new technology. According to a 2016 Wohlers report, AM will generate about $5.2 billion in 2015; about 0.04% of total output [89].

Because the parts are built by adding successive layers, complex internal designs can be built with a single monolithic structure. This, along with the fact that different types of materials can be used, facilitates the production of heat exchangers that use less material, are smaller in volume, and have a higher heat capacity and reliability. Figure 2.1 shows some examples of heat exchangers produced by AM methods. Because AM enables rapid and inexpensive prototyping, researchers can design, manufacture, and test new heat exchangers in a short time. Tsopanos et al. [90] made one of the earliest examples of researchers using a metal AM heat exchanger for fabrication and testing. Two microscale heat exchangers and three mesoscale heat exchangers were rapidly fabricated by selective laser melting (SLM) and the heat capacity was determined experimentally. This section presents the AM methods that are commonly used to fabricate heat exchangers, and their cost effectiveness.

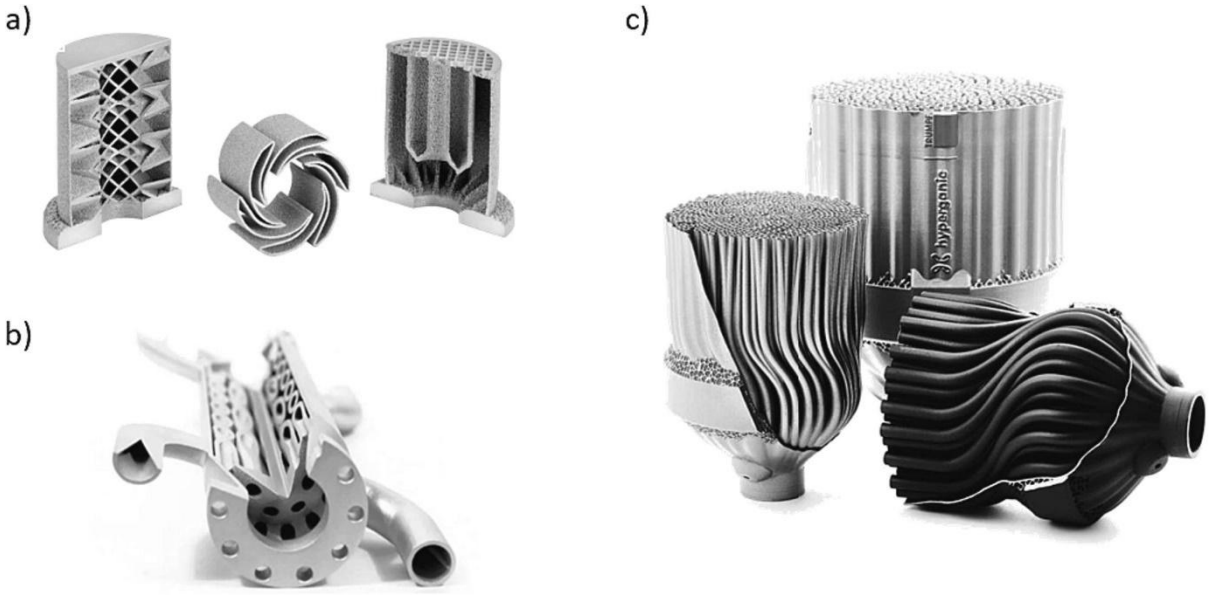

Figure 2-1 Heat exchangers fabricated via AM. a) 3D printed HXs [91], *b) monolithic HXs printed* [92], *c) new generation of heat transfer components* [93].

2.2.1 Laser Powder Bed Fusion for Metal Heat Exchangers

Laser Powder-Bed Fusion (LPBF) is the most widely used and adaptable AM method for fabricating metal heat exchangers. LPBF process is presented in Figure 2.2. As shown, metal

powder supply on one side and on the opposite side is the form stage (fabrication). The powder is moved from the reservoir using a powder scraper or roller to form an even layer on the build platform. Then, at that point, a laser is aimed at the powder to circuit or dissolve the powder to set it. The laser does this in the example of the cross segment of the part for that particular layer of the part being constructed. After lowering the build platform and spreading a new powder layer, the procedure is repeated until the entire part is constructed from the bottom to top. Direct Metal Laser Sintering (DMLS), also known as Selective Laser Sintering (SLS), and Selective Laser Melting (SLM) are collectively referred to as LPBF. It is one of the most seasoned metal This AM strategies available today; the principal business metal sintering machine was presented in 1995 [94]. Along these lines, the expense and accessibility of the technique is accessible for specialists to use to fabricate efficient heat exchangers. Table 2-3 highlights studies that include the utilization of LPBF to fabricate heat exchangers, heat sinks, or important parts (like tubing) and the significant discoveries of each.

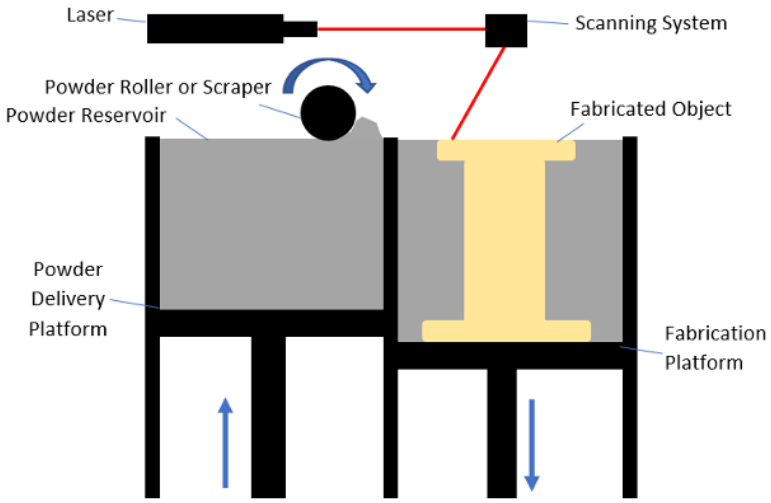

Figure 2-2 Basic approach of Laser Powder-Bed Fusion (LPBF)

Table 2-3 Some studies using L-PBF to produce HXs

AM method	Comment	Ref.
SLM	• HXs with micro and meso scale were produced.	[90]

	• Micro scale HXs showed consistent performance. • Meso scale HXs did not perform as good as available pin-fin HXs.	
	• Experimental studies for heat transfer and pressure drop for 4 HXs were conducted. • SLM produced HX using Aluminum 6061 as a potential material for several applications.	[95]
	• Aluminum 6061 was used to fabricate 5 HXs. • It was reported that extending the surface area alone does not necessarily enhance the overall heat transfer.	[86]
	• Aluminum 6061 and Stainless Steel 316L were used to produce 3 finned HXs. • The AM-enabled HXs had better performance than traditional designs. • Lower pressure drop was estimated.	[96]
	• AlSi10Mg and Ti6Al4V were used to fabricate cylindrical HXs with internal channels having various angles. • The performance mainly depended on the surface roughness and angle.	[97]
DMLS	• DMLS was proven as a suitable method to fabricate periodic cellular lattice HXs using AlSi10Mg alloy.	[98]
	• DMLS produced a roughened finned surface with 63% increase in the convective heat transfer.	[99]
	• The study proved that DMLS produced a manifold-microchannel geometry with a significant improvement in heat transfer.	[87]
	• Titanium alloy was used to fabricate air-water HX with manifold-microchannel feature. • 45-100% improvement in conductance and 15-50% enhancement in heat transfer coefficient at the same pressure drop were measured experimentally.	[100]
LPBF	• A multi-layered oscillating heat pipe was fabricated from Ti-6Al-4V and its performance was studied.	[101]

2.2.2 Metal Heat Exchangers via Cold Spray Additive Manufacturing

Cold Gas Dynamic Spray (CGDS), also known as Cold Spray, is the second most used method of producing heat transfer devices using metal AM methods. This process is possible by forming solid powder particles and adding material to the substrate. The acceleration of powder particles by a carrier gas flowing at supersonic speeds is responsible for their deposition [102]. Fin plate heat exchangers are a typical application area for CGDS. The efficiency of corrugated or striped fins has been proven to be limited in many experiments, while optimally positioned fin height and diameter ratio enhance the heat exchanger efficiency [103]. A general diagram of the process by which CGDS produces pin fin properties is shown in Figure 2.3. Using a

mask allows you to create geometry with a variable cross-section, such as pyramid strips. Table 2-4 lists all studies that used CGDS to fabricate heat exchangers, heat sinks or related components such as tubes, and the main results of each.

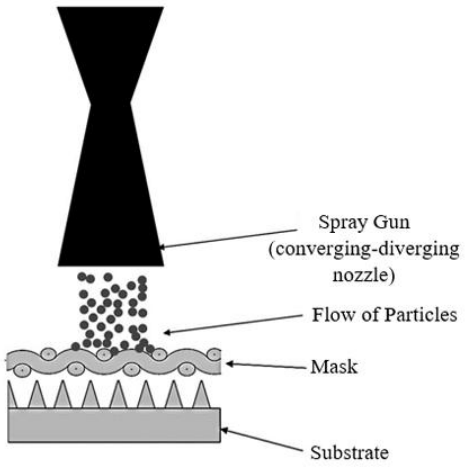

Figure 2-3 Schematic diagram shows the CGDS Process [102]

Table 2-4 Some studies using CGDS to produce HXs

AM method	Comment	Ref.
Wire-Arc Spraying	• Compact HXs were fabricated from alloy 625 deposited on the surface of nickel foam. • 20 PPI foam outperformed the 10 PPI foam in terms of heat transfer, but higher pressure drops due to its less pore size and more internal surface area.	[104]
CGDS	• The CGDS-produced pyramidal fin array outperformed standard straight cut fins at the same density and hydraulic diameter due to increased convective heat transfer coefficient from fluid mixing.	[102]
	• Studying the impact of fin height and density of pyramidal pin fins. • Raising fin height or density improves heat conductivity but leads to increased pressure loss.	[105]
	• Created two new geometric pin fin arrays: pyramidal and trapezoidal. • Two novel designs outperform typical rectangular fins for heat transmission, but result in higher pressure loss.	[106]
	• Various aluminum-alumina volume fractions were used to form pyramidal fin arrays. • Utilizing Aluminum-Aluminum feedstock powder instead of pure aluminum reduces the need for expensive polymer nozzles that soon wear out.	[107]

	• Materials used to create near-net-shaped pyramidal fin arrays were aluminum, nickel, and grade 34 stainless steel. • The aluminum powder surpassed all other types of material.	[106]
	• Used CGDS to build pyramidal pin fins. • Observations of double recirculation and flow bypass structures in fin wake zones.	[108]
	• Analyzed pressure losses and convective coefficients for square, round, and diamond base tapered pin fins. • Staggered layouts result in better convective coefficients and pressure losses.	[109]

2.2.3 AM Limitations and Design Constraints

Although AM has revolutionized the design and production of heat exchangers by enabling complex geometries and enhanced performance, it also has certain limitations and design constraints that must be considered:

a. Material Limitations

Restricted material options: Not all materials suitable for heat exchangers (e.g., certain alloys with high thermal conductivity) are compatible with AM processes [110] .

Anisotropy: AM components often exhibit anisotropic properties, where mechanical and thermal characteristics vary depending on the build direction.

Porosity and Microstructural Defects: AM processes can result in porosity or inclusions that affect structural integrity and thermal performance.

b. Surface Roughness

Higher surface roughness: AM often produces rough surfaces, which can increase pressure drop in fluid channels and reduce heat transfer efficiency unless post-processing is applied.

Post-processing needs: Additional finishing processes (e.g., polishing or machining) may be required, adding cost and complexity [111].

c. Geometric and Dimensional Constraints

Minimum feature size: While AM enables intricate geometries, there are limits to how small or thin features (e.g., microchannels or fins) can be printed accurately.

Overhangs and supports: Overhangs often require support structures during printing, which can be challenging to remove in internal channels or complex geometries.

Wall thickness: Very thin walls may be prone to warping, distortion, or damage during the printing or post-processing stages.

d. Thermal and Mechanical Performance

Thermal conductivity: The thermal conductivity of AM-produced materials can be lower than their conventionally manufactured counterparts due to internal defects or differences in microstructure.

Mechanical strength: AM parts may have reduced fatigue life or fracture toughness, which can be critical in high-pressure or high-temperature heat exchanger applications.

e. Size and Build Volume

Build volume limitations: The size of the heat exchanger is constrained by the build envelope of the AM machine. Large heat exchangers may need to be printed in multiple sections and assembled, introducing additional complexity and potential for leakage [112].

Scaling Challenges: While AM excels at small, intricate designs, scaling these to larger systems can result in diminishing returns in terms of cost and time.

f. Cost and Time

High Production Costs: AM is often more expensive than traditional manufacturing for large-scale production due to material costs and slower build times [113].

Time-Consuming: Printing intricate designs can take significant time, especially for high-resolution builds required for heat exchangers.

g. Design Constraints

Design for Additive Manufacturing (DfAM): Engineers must design with AM-specific constraints in mind, such as avoiding unsupported overhangs and ensuring adequate thermal and structural performance [114].

Complexity vs. Functionality Trade-Off: While AM allows for complex designs, overly intricate features may not always result in proportional performance gains.

Internal Feature Accessibility: Cleaning or inspecting internal channels post-production can be difficult, especially in compact and intricate heat exchangers.

8. Post-Processing Requirements

Support Removal: Removing supports in internal structures can be challenging or impossible without compromising the design.

Heat Treatment: Post-printing thermal treatments are often required to improve material properties, adding cost and complexity [113].

Surface Finishing: Additional polishing or coating may be necessary to reduce roughness and improve corrosion resistance [115].

2.2.4 Is AM a Cost-Effective Method?

It is worth considering whether AM can be priced similarly or comparably to conventional manufacturing. Compared to conventional production, AM has several benefits. Without tooling in the initial stages of the product development process, substantial expenses are taken out and part geometry can be modified without requiring additional time or money for new tooling [116]. Also, by using AM to make special parts orders, inventory can be reduced and

thus costs can be reduced. Raw materials for AM production are the only necessary inventory [117]. AM costs are estimated and compared with conventional manufacturing methods using various models. The first outstanding model is Hopkinson and Dickens [116]. Due to the start-up costs of traditional production methods such as injection molding, AM is much more cost-effective below a certain production volume. However, the situation is reversed if production volumes increase. Laureijs et al. [118] concluded that additive manufacturing of a GE engine bracket is less expensive than producing forged parts in many cases at high production volumes. Thomas and Gilbert [119] provided a comprehensive overview of AM cost benefits and explain several different cost models. Because heat exchangers are complex components, most studies provide only cost analyses of relatively simple components or assemblies. The cost effectiveness of AM compared to traditional manufacturing may be affected by the complexity of the part. Fera et al. [120] suggested a new model that uses the complexity of the part to be manufactured rather than the number of products to be manufactured as a determinant of AM use. Most of the presented models do not fully take into account the advantages offered by AM, and the models still need to be developed to better predict the economic competitiveness of AM. By considering both the production volume and the complexity of the details, it is possible to determine if AM methods are more cost-effective than conventional processes for manufacturing the heat exchanger. Therefore, it was concluded that AM can be more cost competitive than conventional manufacturing methods, but more precise models are still required to forecast realistic cost gains.

2.3 Summary

The literature review emphasizes that the passive technique is widely used to enhance the heat transfer and pressure drop associated with HXs. Swirl flow techniques represent a mature and highly effective approach to enhancing heat transfer in heat exchangers. Ongoing advancements in design optimization, material science, and computational modeling are

making these techniques even more efficient and practical, paving the way for their broader adoption across industries. The Emerging Trends in Swirl Flow Techniques include:

1. Integration with nanofluids to enhance thermal conductivity and heat transfer performance. Also, hybrid approaches with twisted tapes or helical inserts further amplify the benefits.
2. Additive manufacturing enables precise fabrication of intricate swirl-inducing geometries, such as complex grooved patterns or customized vortex generators.
3. Multi-Objective Optimization that uses machine learning and computational fluid dynamics (CFD) for optimizing swirl-inducing designs to achieve maximum heat transfer with minimal pressure drop.
4. Advanced materials to develop high-strength, corrosion-resistant materials to ensure the longevity of inserts in harsh operating conditions.

It was reported that the swirl Flow Heat Exchangers are used in many applications, such as radiators, intercoolers, exhaust gas recirculation (EGR) coolers, air conditioners and compact heat recovery systems, steam condensers, chemical reactors, and waste heat recovery units.

Efforts have been devoted to enhancing the thermal and hydraulic performance of heat exchangers in the turbulent regimes, swirl flow heat exchangers suffer from high pressure drop, scalability, customization, and reducing manufacturing and maintenance costs for widespread adoption. In addition, little attention has been paid to laminar flow which could be found in many applications. Although several techniques have been studied to enhance heat transfer, they increased the pressure drop. Therefore, this study focuses on the low Reynolds flow regime within different channel geometries. The present study will propose and study experimentally and numerically various passive techniques to improve the heat transfer in heat exchanger. The techniques will introduce swirl flow into the channel using swirl devices and

make use of two heat transfer mechanisms: extended surfaces area which will help in conducting the heat transfer and swirling the flow to impinge the flow in the four walls of the channels to enhance the flow mixing. Besides, the present study proposes and studies the performance of a novel manifold to enhance the flow uniformity, aiming to enhance the thermal and hydraulic performance of heat exchangers. As a result, this study seeks to contribute to this endeavor by addressing the current limitations and propelling the technology toward practical and optimized applications in thermal management systems. The outcomes of this study will have a direct impact on different applications that require precise control, low pressure drops, or unique operating conditions, such as electronics cooling, microreactors, and compact devices.

CHAPTER 3 METHODOLOGY

The current study uses a combination of numerical and experimental methods to examine the pressure drops and heat transfer characteristics in square channels with smooth and finned walls. To validate the predictions from the numerical simulations, the methodology involves conducting laboratory experiments. The numerical simulations are carried out using Ansys Fluent, while the experimental investigations are designed, manufactured, and commissioned at the Oxford Thermofluids Institute (OTI). A modular design of the experimental facility is implemented to allow for the interchangeability of parts of the working section and testing of various heat transfer cooling techniques. The purpose of the methodology chapter is to provide a detailed explanation of the setup, procedures, and post-processing used in both the numerical and experimental studies. A short summary of the existing parts and instrumentations utilized in this research will be provided. Additionally, this chapter discusses the advantages and limitations of each method and the measures taken to ensure the accuracy and reliability of the obtained results. In summary, this chapter establishes the groundwork for the subsequent analysis and discussion of the results.

3.1 COMPUTATIONAL WORK

The following sections which will be discussed are governing equations, computational domains, grid generation and independent study, code validation, and calculations.

3.1.1 Governing Equations

In general, HXs function at relatively low Mach numbers, and the temperature difference between the hot walls and the cooling fluid is not particularly high ($\Delta T \sim 10^{o}C$ - $30^{o}C$) such as in the electronic cooling applications, hence the following assumptions have been assumed.

- The flow is steady, three-dimensional, incompressible, and laminar.
- Constant thermo-physical properties.

- Neglect the viscous dissipation in the energy equation.
- Neglect the effect of natural convection and radiation.

Based on the above assumptions the governing equations take the following form:

3.1.1.1 Continuity Equation

The continuity (mass conversation) equation is developed by balancing the mass flow rate against a control volume in the fluid flow. The steady-state continuity equation is written in the tensor theory as [121,122],

$$\frac{\partial}{\partial x_i}(\rho u_i) = 0 \tag{3.1}$$

Where x_i is the coordinate in the i^{th} direction, u_i is the absolute velocity in the i^{th}direction, ρ is the fluid density, and i a tensor indicating 1, 2, 3.

3.1.1.2 Momentum Equation

The momentum equation is written as [121,122]:

$$\frac{\partial(\rho u_i u_j)}{\partial x_j} = \frac{\partial}{\partial x_j}\left[\mu_l\left(\frac{\partial u_i}{\partial x_j} + \frac{\partial u_j}{\partial x_i}\right)\right] - \frac{\partial p}{\partial x_i} + S_u \tag{3.2}$$

Where μ_l is the laminar dynamic viscosity, p is the pressure in Pa, and S_u is the source term. The term on the left side of the Eq. 3.2 is the net momentum efflux. The shear force or the diffusion term is presented by the first term on the right side; the second term is pressure gradient term which represents the pressure forces, and the last term represents the source term.

3.1.1.3 Energy Equation

The energy equation governs temperature distribution for the non-isothermal flow domain. This equation is derived from the application of the first law of thermodynamics to the elemental control volume and may be represented as [121,122]:

$$\frac{\partial(\rho C_p u_j T)}{\partial x_j} = \frac{\partial}{\partial x_j}\left(k\left(\frac{\partial T}{\partial x_j}\right)\right) + S_T \quad (3.3)$$

where S_T is the source term, k is the thermal conductivity, and C_p is the specific heat at constant

3.1.2 Grid Generation

Firstly, a smooth square channel is used as a base case to examine the effect of swirlers on the heat transfer and friction factor characteristics. In this study, where water has been used as the working fluid and Inconel 718 as the solid material, a single passage of the compact heat exchanger core is designed and used as the computational domain. Both smooth and swirler channel have a square cross-section with same hydraulic diameter D_h (5mm) and wall thickness t of (0.5mm), channel length, width and height of L_{ch} (202.5mm) x W_{ch} (5mm) x H_{ch} (5mm), respectively. Figure 3.1 illustrates the computational domain for the base smooth case used in this study.

The mesh is generated using Ansys Meshing and different mesh sizes are checked to find the optimum mesh size. For the smooth case, a refinement of the grid was achieved by varying the mesh size of the domain from 0.9 million to 3 million cells when Re = 300. Table 3.1 shows the average Nusselt number and friction factor at different mesh sizes for the smooth channel. The results obtained from mesh sizes of more than 2 million cells were the same, therefore the results from 2 million cells can be considered as grid independent results.

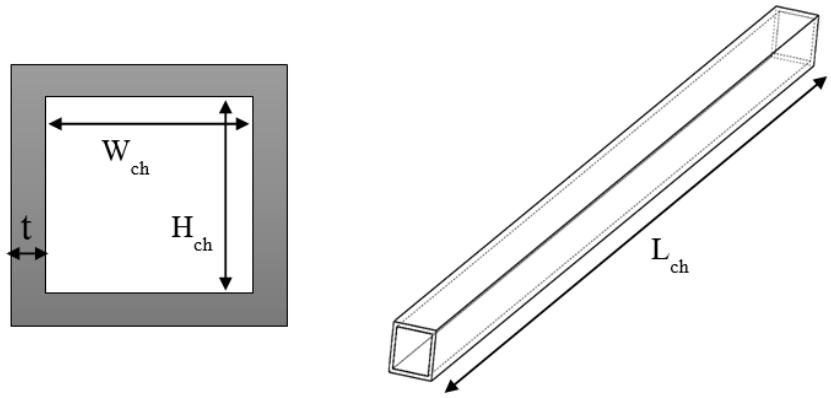

Figure 3-1 Smooth base case computational domain.

Table 3-1: Mesh independents test for smooth channel

Mesh Sizes	Average Nusselt Number	Friction Factor
910,332	4.82	0.177
1,2896,345	5.21	0.186
2,105,003	5.35	0.192
3,183,926	5.39	0.194

3.1.3 Calculations

In this section, all the expressions used in this study to evaluate the characteristics of heat transfer and fluid flow will be listed below.

The Reynold number is calculated based on hydraulic diameter and it is expressed as follows:

$$Re_{D_h} = \frac{\rho . v . D_h}{\mu} \quad (3.4)$$

Where μ and ρ are the fluid viscosity and density, respectively. The passage mean velocity is represented by v, and the hydraulic diameter by D_h which is calculated as follows:

$$D_h = \frac{4 . A_c}{P} \quad (3.5)$$

In order to account for the extra area of the heat transfer enhancement techniques (i.e. swirler) in the calculation of the HTC, Planes and polylines are inserted at 1mm intervals along the test section (201 planes and 201 polylines) to extract the local mass-weighted average of the fluid temperature at each plane and area-weighted average of wall heat flux and wall temperature at each polyline, as shown below.

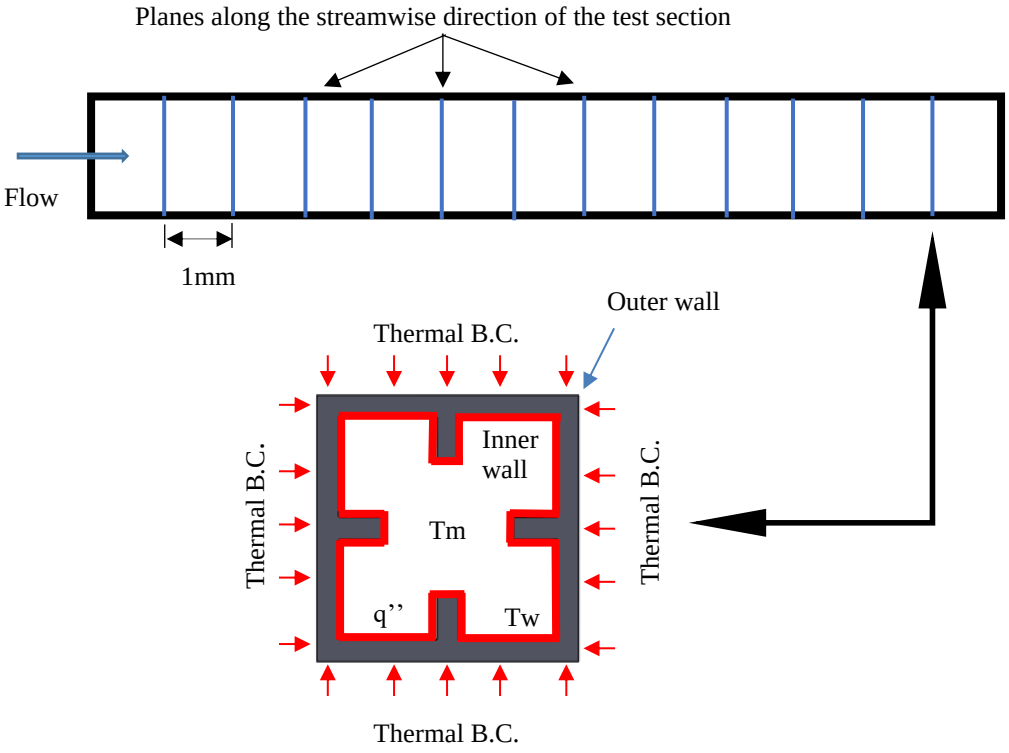

The local heat transfer coefficient h_x and local Nusselt number Nu_x based on the hydraulic diameter are then calculated as,

$$h_x = \frac{q_x''}{T_{w,x} - T_{m,x}} \tag{3.6}$$

$$Nu_x = \frac{h_x D_h}{k_f} \tag{3.7}$$

where q_x'' is the of local heat flux, $T_{w,x}$ is the local area-weighted average wall temperature over the selected wall surface, $T_{m,x}$ is the local mass-average fluid temperature and k_f is the fluid thermal conductivity.

while the average Nusselt number is calculated as follows,

$$\overline{Nu} = \frac{1}{L_{ch}} \int_0^{L_{ch}} Nu_x \, dx \tag{3.8}$$

where L_{ch} is the channel length.

To determine the pressure drop, it is convenient to deal with the friction factor which is given by

$$f = \frac{\frac{\Delta p}{L} D_h}{\frac{1}{2} \rho \, {u_m}^2} \tag{3.9}$$

Where L, u_m and Δp indicate the length of the channel, the mass-weighted average velocity and the pressure drop across the channel, respectively.

The Performance Factor (PF) is a key metric for evaluating the thermal-hydraulic performance of enhanced heat exchanger configurations compared to the baseline smooth channel. It considers both heat transfer enhancement and the associated pressure drop penalty, providing a comprehensive assessment of the swirlers' effectiveness. Using PF in this manner aligns with established methodologies in thermal-hydraulic performance evaluation [123] and allows for benchmarking against existing data [124], validating the approach and strengthening the credibility of the findings. To determine the optimum swirl configuration, PF is defined as the ratio of heat transfer enhancement to the increase in pumping power due to the passive enhancement techniques. The goal is to achieve a PF greater than one, indicating that the cooling technique enhances heat transfer while keeping pressure drop to a minimum when compared to the smooth channel. The derivation and evaluation of this factor are as follows:

$$Pumping\ Power\ (PP) = Voulematric\ Flow\ Rate\ (\dot{V})\ .\ Pressure\ Drop\ (\Delta P)$$

$$PP = (\frac{\pi d^2}{4}\ v)(2f\frac{L\rho v^2}{d})$$

$$PP = \frac{\pi}{2} d\ (\rho v)^3\ \left(\frac{1}{\rho^2}\right)\ fL$$

Solving for (ρv),

$$(\rho v) = (\frac{2\ \rho^2\ PP}{f\ (Ld)})^{\frac{1}{3}} \tag{3.10}$$

From Stanton number,

$$h = \rho\ v\ c_p\ St \tag{3.11}$$

For the same $c_p\ and\ \rho$, substituting (ρv) from Eq. 3.10 into Eq. 3.11 yields,

$$\frac{h_{sw}}{h_{s,fd}} = \frac{St_{sw}}{St_{s,fd}} \cdot \frac{(PP)_{sw}^{\frac{1}{3}}}{(PP)_{s,fd}^{\frac{1}{3}}} \cdot \frac{(Ld)_{s,fd}^{\frac{1}{3}}}{(Ld)_{sw}^{\frac{1}{3}}} \cdot \frac{(f)_{s,fd}^{\frac{1}{3}}}{(f)_{sw}^{\frac{1}{3}}}$$

For the same pumping power (i.e. $PP_{s,fd} = PP_{sw}$) and surface area ($(Ld)_{s,fd} = (Ld)_{sw}$)

$$\frac{h_{sw}}{h_{s,fd}} = \frac{St_{sw}}{St_{s,fd}} \cdot \frac{(f)_{s,fd}^{\frac{1}{3}}}{(f)_{sw}^{\frac{1}{3}}} = \frac{\frac{St_{sw}}{St_{s,fd}}}{(\frac{f_{sw}}{f_{s,fd}})^{\frac{1}{3}}} \tag{3.12}$$

This expression forms the basis for defining the Performance Factor (PF),

$$PF = \frac{\frac{St_{sw}}{St_{s,fd}}}{(\frac{f_{sw}}{f_{s,fd}})^{\frac{1}{3}}} = \frac{\frac{Nu_{sw}}{Nu_{s,fd}}}{(\frac{f_{sw}}{f_{s,fd}})^{\frac{1}{3}}} \tag{3.13}$$

In the second form of Equation (3.13), the Stanton number is replaced by the Nusselt number using the relation:

$$Nu = St \,.Re \,.Pr$$

This substitution is valid under the assumption of equal Reynolds number and Prandtl number across the surfaces being compared, which allows the Stanton number ratio to be directly expressed as a Nusselt number ratio.

3.2 EXPERIMENTAL WORK

3.2.1 Experimental Facility

A new low-speed test rig, shown in Figure 3.2, was constructed at the Oxford Thermofuids Institute at the University of Oxford. The aim of the rig was to provide CFD validation data for forced convection flows in one cell of an industrial ultra-compact heat exchanger. In order to match the Reynolds numbers used in the CFD simulations, the test rig was scaled up by a scaling factor of 8.88 which enable the use of air instead of water. The range of Reynolds numbers based on the hydraulic diameter was between 600 and 1500. The range was limited to the above Reynolds numbers due to the prescribed temperature constraints of the material and to satisfy the rise of the temperature across the heater mesh of up to 25K. It was not possible to get a temperature rise for Re numbers greater than 1500 with the current heater mesh power capabilities. On the other hand, for Re number below 600, the temperature rise exceeded the material melting prescribed temperature.

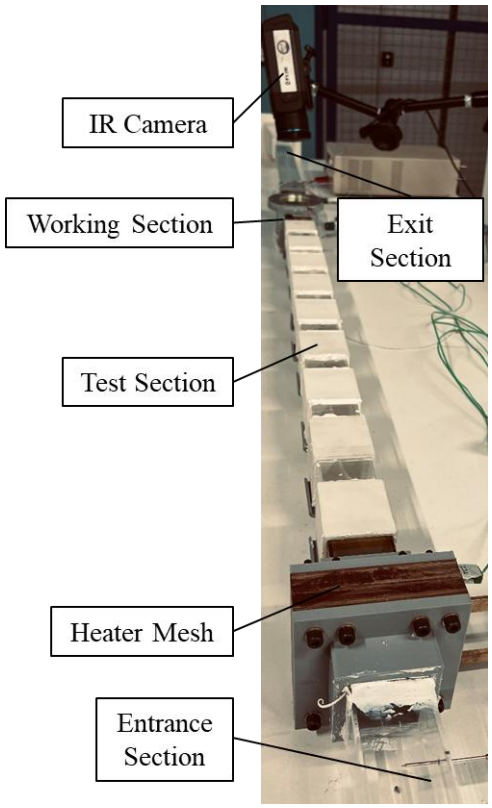

Figure 3-2: New low-speed test rig

The rig consists of a mass flow controller to provide the exact mass flow rate coming from the shop air. It is followed by a venturi meter to validate the mass flow rate entering the channel. After that comes a long entrance region so that the flow reaches the fully development condition before it enters the test section. By the end of the entrance region, a heater mesh is placed to introduce a temperature rise to the flow as it passes throw it. Then nine of the novel swirl devices placed in the channel to introduce swirl to the flow and impingement on the side walls. Before the exit section, a working section is placed with a Zn-Se window to allow the IR camera to measure the temperature difference on this section. The rig setup is shown in Figure 3-3.

3.2.1.1 Test section

The modular design of the test section is comprised of nine swirlers devises and a working section where the temperature measurements are taken via the IR camera. A novel geometry

can be designed in one device using SolidWorks, and then 3D printed into nine devices. These devices are then followed by a 3D printed working section which has two of the novel swirl devices and a window in between to take wall temperature measurements by IR camera.

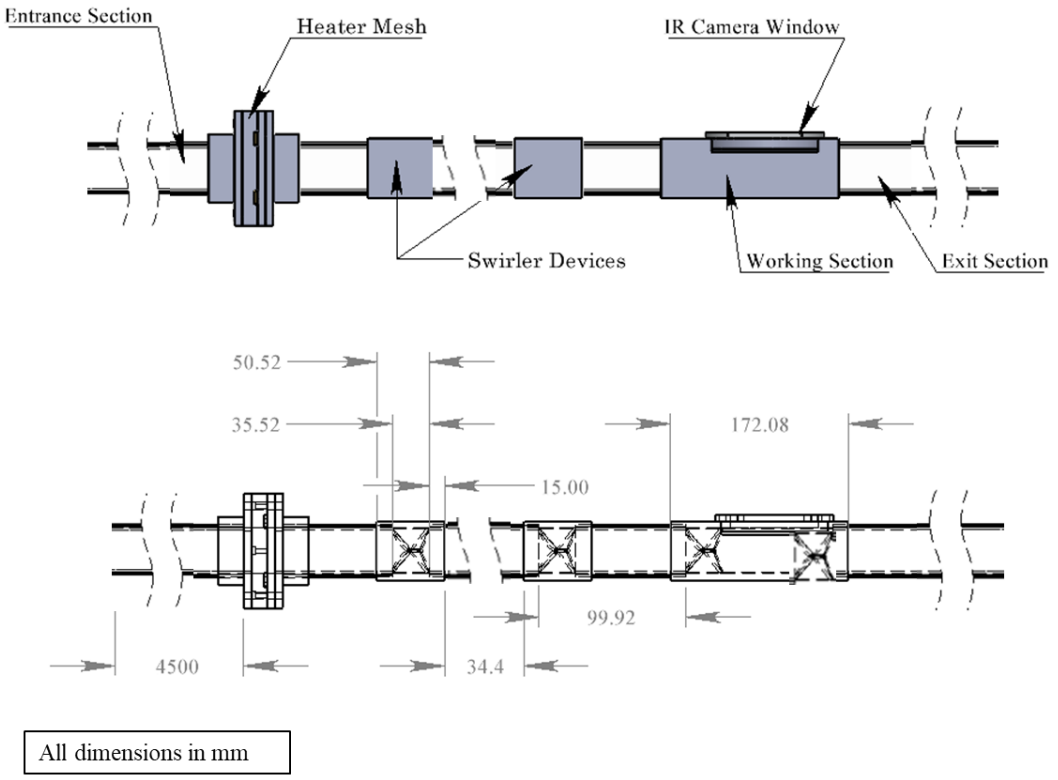

Figure 3-3: Low-speed test rig set-up for measuring pressure drop and heat transfer characteristic.

3.2.1.2 Swirler devices

The swirler devices were designed and printed by the author using the Selective Laser Sintering (SLS) technology, as shown in Figure 3-4. The selected material was Nylon PA/Nylon Glass Filled which is a type of thermoplastic material that consists of nylon reinforced with glass fibers. Nine devices were printed and used in the test section before the working section. Before taking any measurements, each swirl device was ascended by the ascending papers, as shown in Figure 3.4.

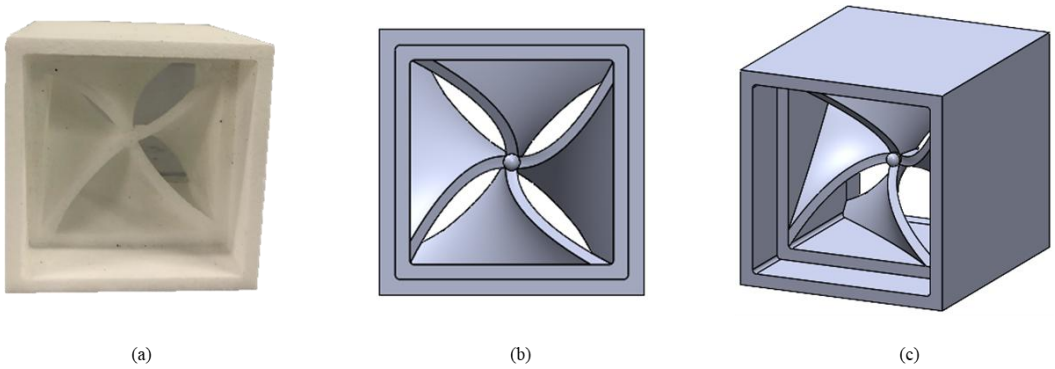

Figure 3-4: Swirler devices (a) 3D printed, (b and c) CAD model

3.2.1.3 Couplers

To connect the Perspex parts of the clear channel, six couplers were printed using the SLS technology. After connecting the different channel parts, silicon was used to ensure that air leakage is prevented while running the experiments and taking measurements.

3.2.1.4 Working section

An ultra-tough grey plastic material was used to 3D print the working section by Stereolithography (SLA) process. The walls made so thick to satisfy the 1-D semi-infinite assumption for the heat transfer coefficient measurements. The working section consists of two swirl devices cantered by the Zn-Se window to allow the IR camera for wall temperature measurements, as illustrated in Figure 3-5.

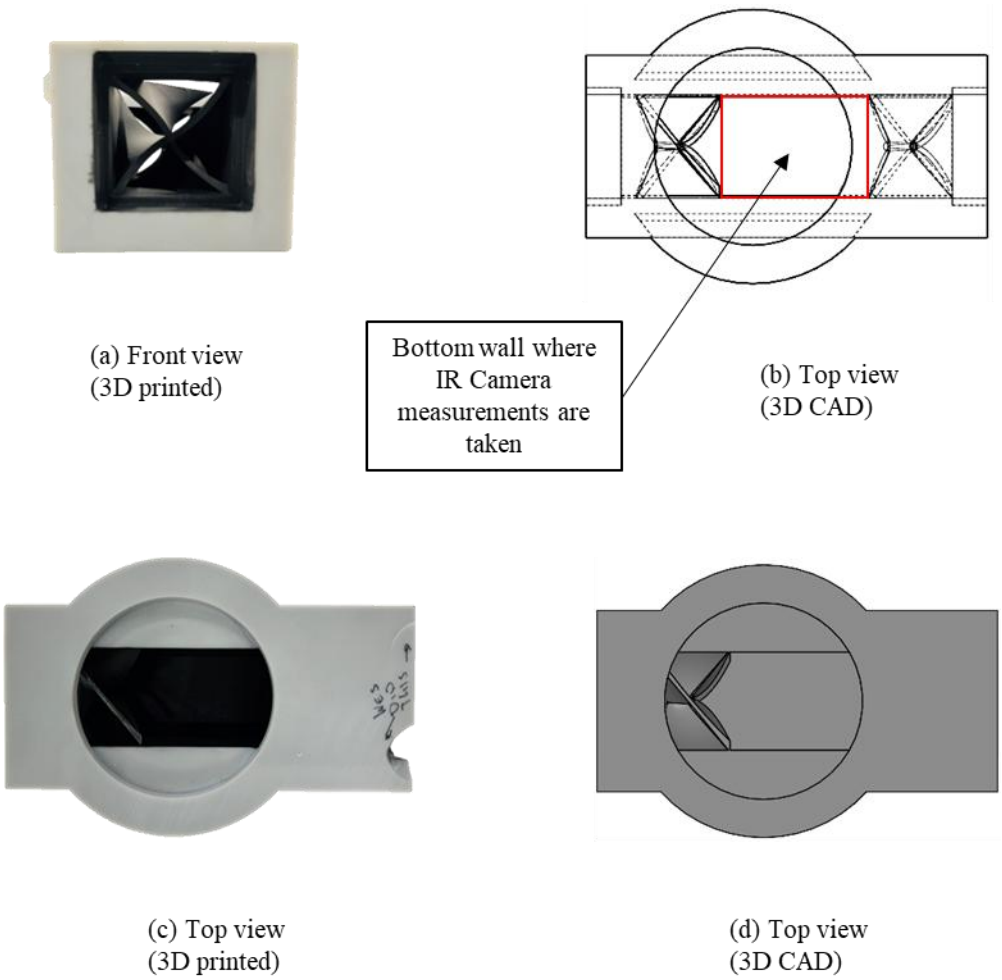

Figure 3-5: The arrangement of the working section (a, c, and d) 3D printed, (b) CAD model

3.2.1.5 Heater mesh

To conduct heat transfer studies, a fast response heater mesh was installed as a crucial component. The concept of this mesh design was initially introduced by Gillespie in 1996 [125] and is illustrated in Figure 3-6. The heater mesh was constructed with a woven steel wire mesh positioned in crossflow and connected to brass bus-bars for efficient electrical power dissipation, which provided a step change in the temperature of the incoming airflow.

To ensure the stability of the heater mesh, Tufnol plates were used for insulation and support of the mesh and upstream filters. This also guaranteed that no dust particles in the airflow

impacted the mesh, preserving its integrity and accuracy. The arrangement of the heater mesh can be shown in Figure 3-6(a).

In the design of the heater mesh, the diameter of the steel wires is the primary parameter to consider. This factor determines the electrical resistance of the mesh and thus, the electrical current that flows through the wires, ultimately dictating the temperature increase achieved. The rise in temperature through the mesh is dependent on the mass flow rate and the power dissipated via the mesh, as detailed in the following equation:

$$P = V\,I = \dot{m}\,c_p\,\Delta T \tag{3.14}$$

The power supply unit imposes a maximum voltage of 30 V to the system. This voltage limit results in a maximum temperature rise of 30K within the facility when the mass flow rate is 1kg/s and the specific heat capacity is 1005 $J.Kg^{-1}.K^{-1}$.

To ensure both compatibility and safety of the heater, a customized heater mesh carrier was designed. This crucial component was carefully manufactured in three distinct pieces, as illustrated in Figure 3-6. The resulting design allows for the secure fastening of the heater mesh by bolting the clamp flanges to the mesh carrier, with the heater mesh held securely between the two components. Once connected as a single unit to the upstream end of the test section, the heater can operate optimally with the utmost safety. Proper design of the heater mesh is crucial to avoid its failure due to manufacturing defects or dust accumulation.

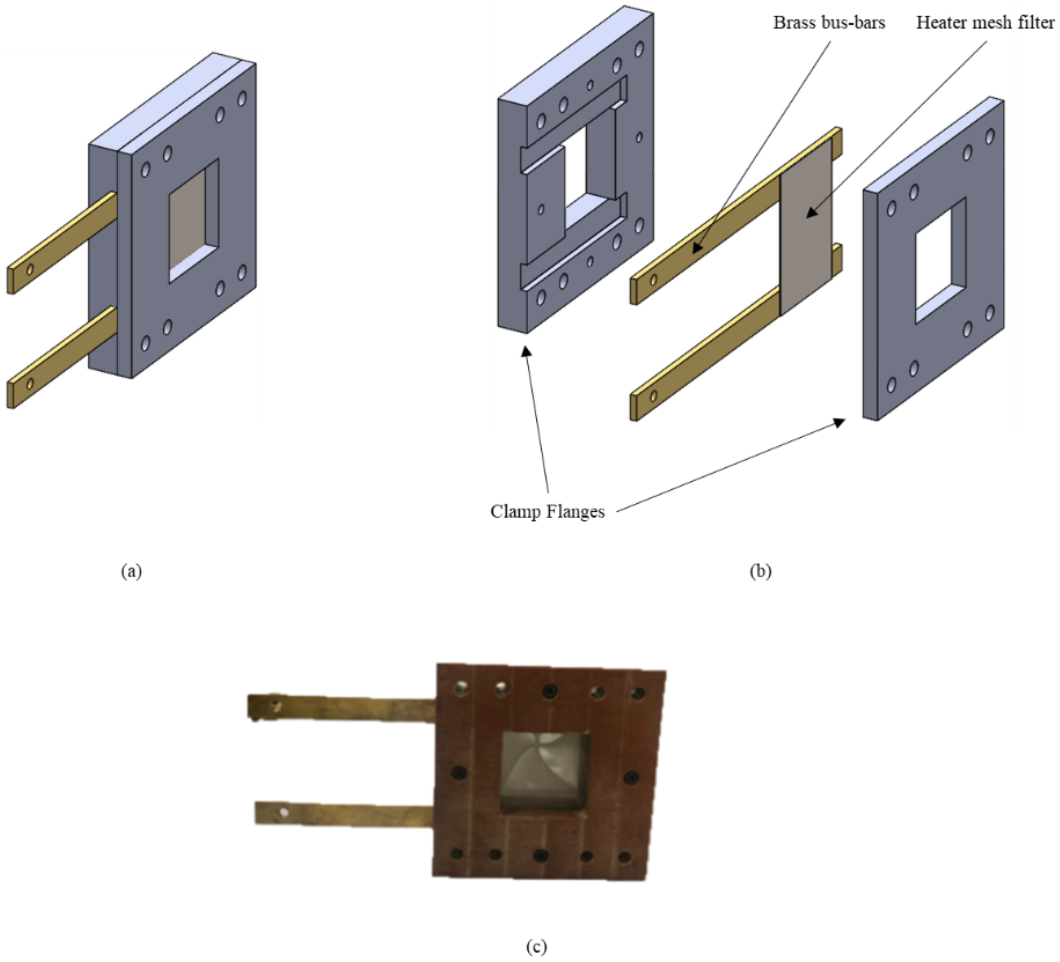

Figure 3-6 Heater mesh arrangement

3.2.1.6 Flow measurements.

3.2.1.6.1 Mass flow rate

Alicat MCR – 500 slm was used as a Mass Flow Controller (MFC) to control the volumetric flow coming from shop air with a single device (see Figure 3-7). This model can maintain accuracy and speed at flows from mass flow rate of 0.01 kg/s or Reynolds numbers of up to 10000. It is accurate and repeatable with up to ± 0.4 % of reading, ± 0.2 % of full scale. To validate the mass flow rate, an evaluation kit from Flusso, FLS110, which covers mass flow rate up to 500 slm was used upstream of the channel, as shown in Figure 3.7.

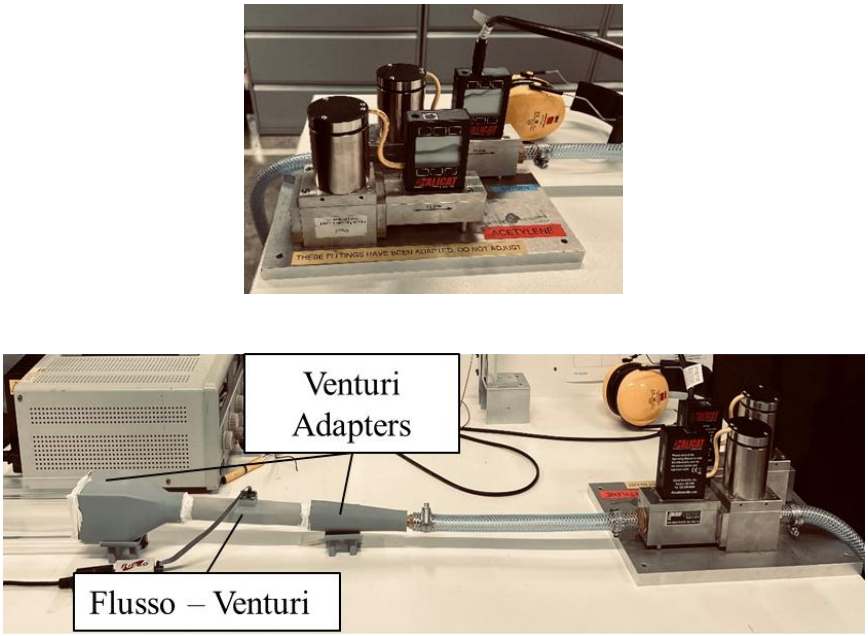

Figure 3-7 Pictures show Alicat flow meter and the evaluation kit from Flusso, FLS110

3.2.1.6.2 Hot-Wire Anemometer (HWA)

Velocity measurements were carried out utilizing a customized hot-wire anemometry (HWA) probe of the constant temperature anemometry (CTA) type, provided by DANTEC Dynamics. Figure 3.8 shows the HWA design with the roller. The probe was integrated with a metal component to facilitate easy movement of the probe without causing any damage, taking advantage of the probe cover. The HWA traverse holder was designed by the author to hold the HWA in place for traverse measurements. Four axial locations were selected within the entrance section to perform a velocity traverse to ensure the flow had fully developed before entering the test section. The measurements were taken at the following nondimensionalized streamwise locations of the entrance region $Z^* = \frac{z}{L_{entrance}}$, near the inlet (0.055), mid-section (0.491) and near the outlet of the entrance section (0.992).

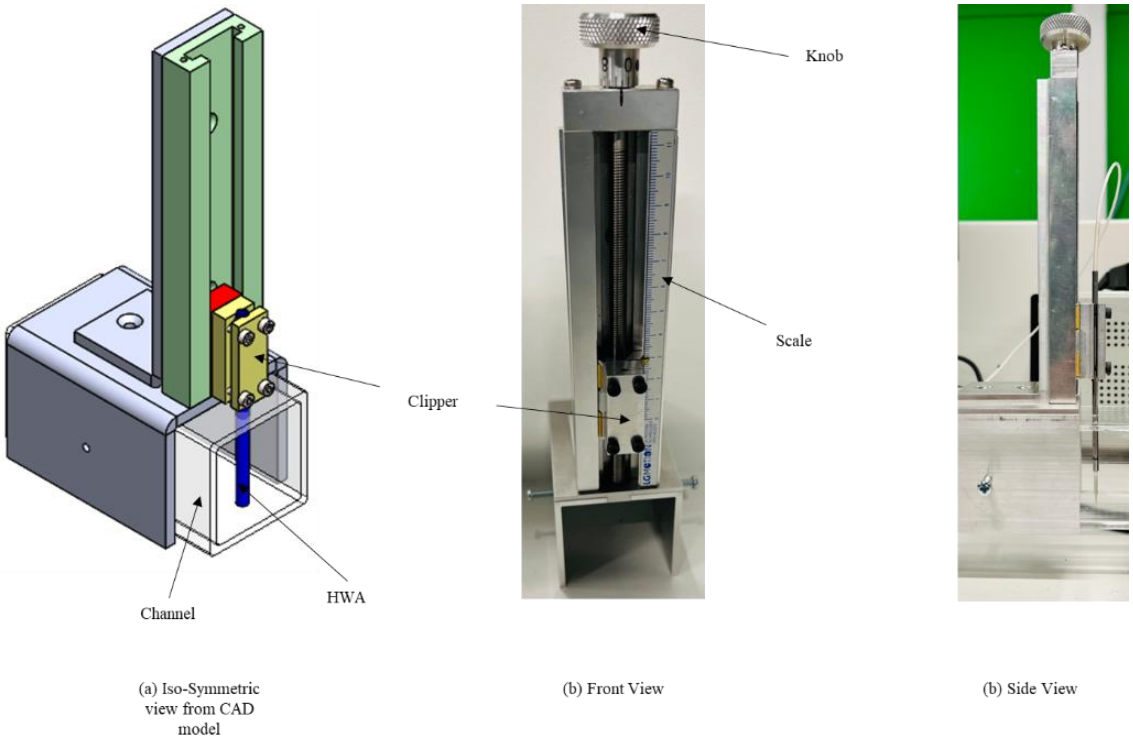

Figure 3-8 HWA design with the roller

In order to capture the data, the NI-9209 C series voltage input module [116] was utilized. Since HWA relies on indirect measurement, it is crucial to calibrate the probe in order to establish the correlation between voltage (V) readings and velocity magnitudes. To calibrate the probe, the DANTEC Dynamics Streamline Pro [117] shown in Figure 3-9 was employed. Two different nozzles, as depicted in Figure 3-9a, were utilized to set various velocities ranging from 0.02 to 5 m/s, and the corresponding voltages from the probe were recorded. A 4^{th} order polynomial fitting, as demonstrated in Figure 3.10, was then used to convert the voltages into velocities during the actual experiments [126]. In addition, the velocity profile at different streamwise direction is plotted in Figure 3-11 at two Reynolds numbers.

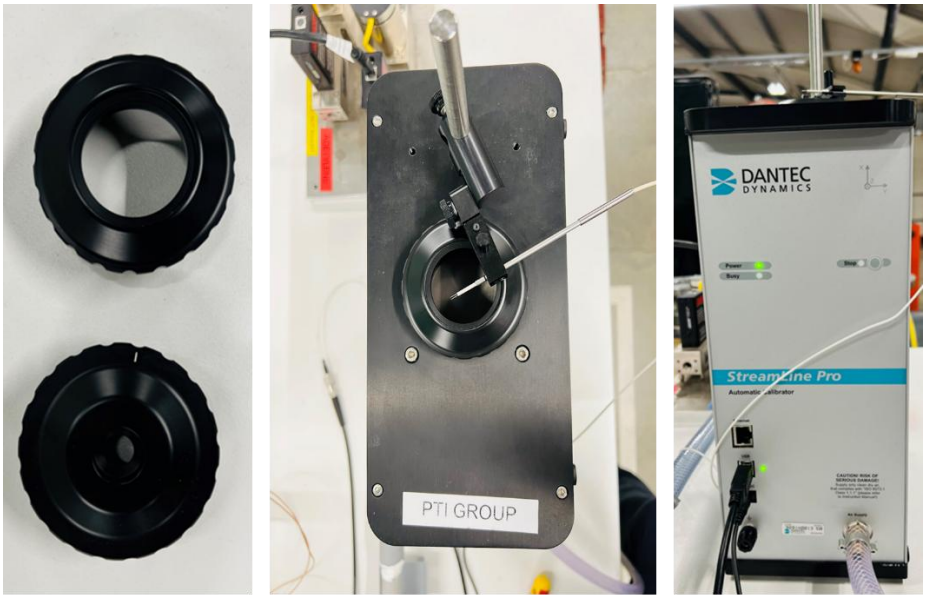

(a) (b) (c)

Figure 3-9 DANTEC Dynamics Streamline Pro

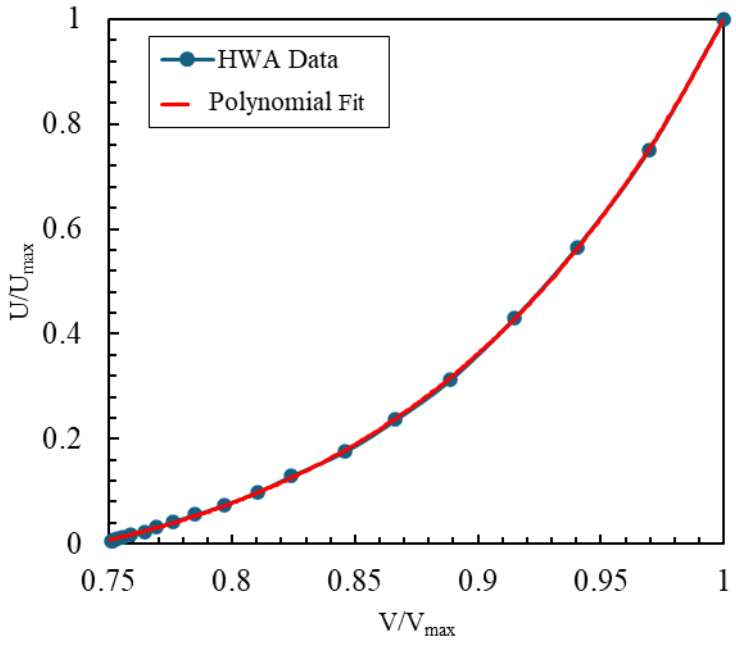

Figure 3-10 Velocity as a function of voltage during the actual experiment.

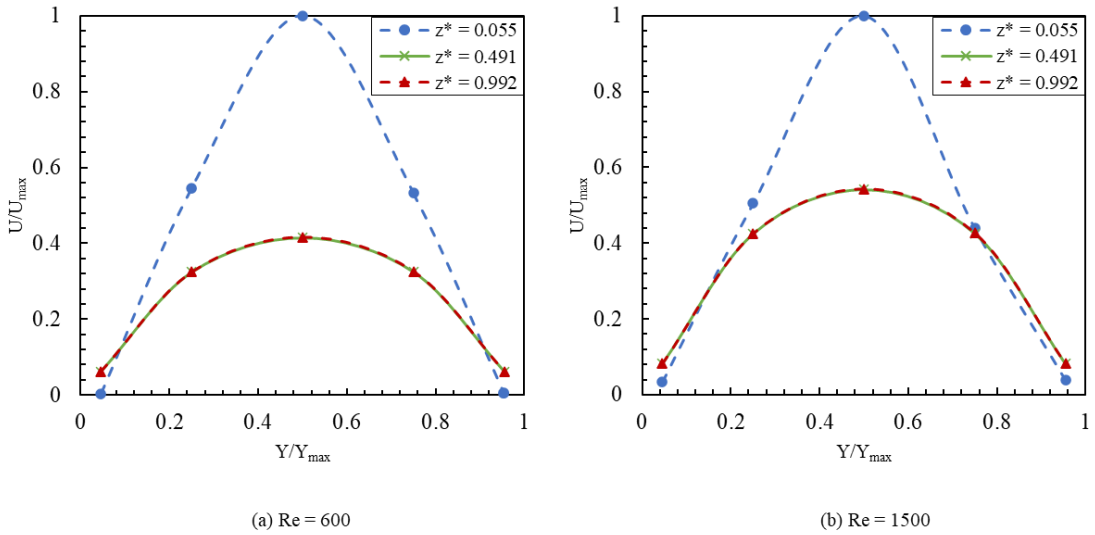

Figure 3-11 Velocity profiles at Re = 600 (a) and Re = 1500 (b)

3.2.1.6.3 Pressure drop

To measure pressure drop across the test section, four pressure tappings are placed in the inlet and outlet of the test sections as shown in Figure 3.12. Each four tabs connected to a manifold and the outlet of the manifold connected to a fully configurable industrial Differential Pressure Transmitter (DPT) as shown in Figure 3-13. The DPT model FCO332, used in this experiment, has the pressure range of ±50 Pa and an accuracy of less than 0.5% reading + 1 digit. The average value of the four pressure taps in each location is recorded as the inlet and outlet pressure. To develop the flow before it enters the test section, smooth entrance section of 4500 mm is added.

For the smooth case, the calculated friction factor from the experiment was compared against the Hagen-Poiseuille's equation, $f = \frac{57}{Re}$. The comparison can be seen in Figure 3-14 which shows a decent agreement between the values. Friction Factor Ratio, $FFR = \frac{f_{sw}}{f_s}$, was calculated based on the measured pressure drop data from both the swirler and smooth cases experimentally and then compared to CFD results. Figure 3-15 shows the fine agreement

between the CFD results and the experimental values at an error percentage of less than 6% at the highest Reynolds number.

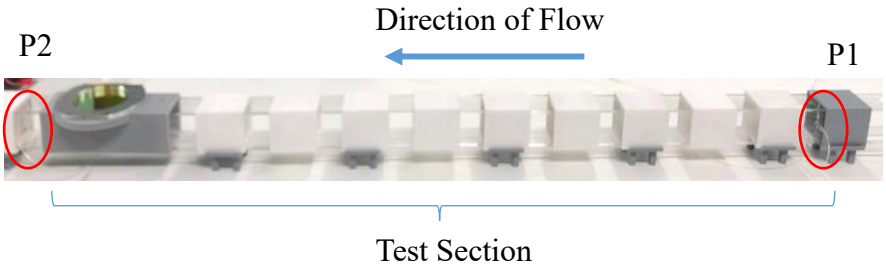

Figure 3-12 Test section showing the pressure taps

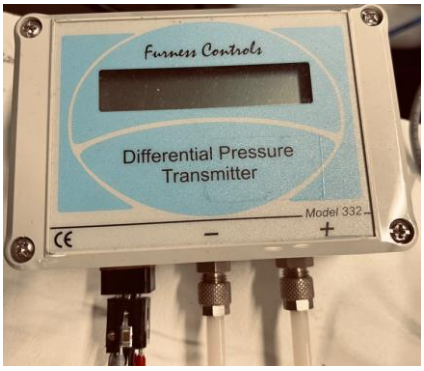

Figure 3-13 Differential Pressure Transmitter (DPT) used in this study

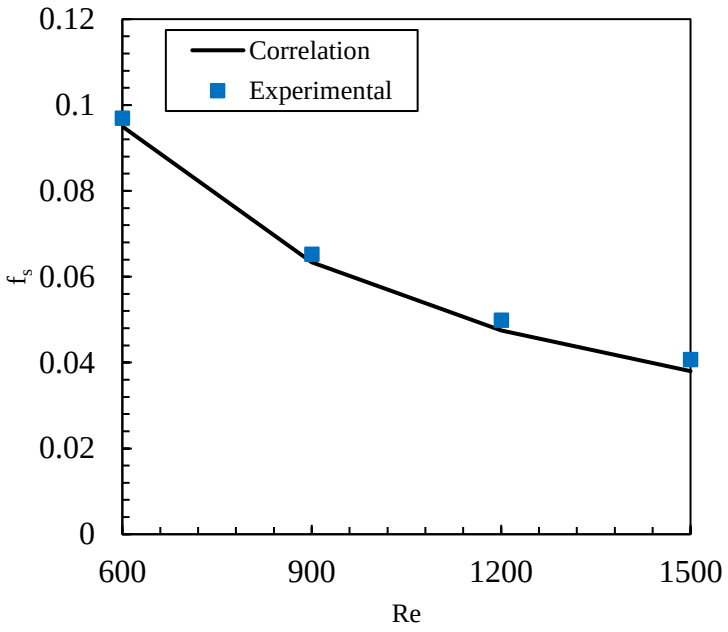

Figure 3-14 Friction factor from the experiment against Hagen-Poiseuille's equation

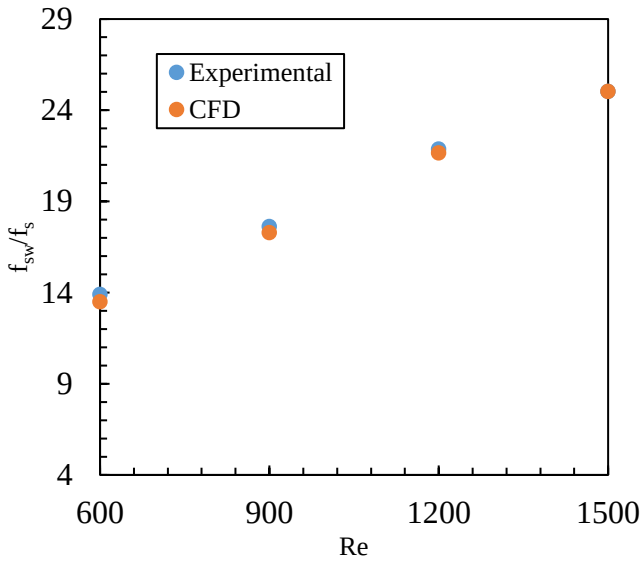

Figure 3-15 Comparison between the experimental and CFD Friction Factor Ratio

3.2.1.7 Heat transfer measurements

3.2.1.7.1 Bulk temperature

To measure the bulk temperature at different locations in the streamwise direction, five K-type class 1 with an accuracy of ±0.9°C thermocouples used which had a wire diameter of 0.2 mm. Temperature data from the thermocouples were recorded using a data acquisition system at a sample frequency of 10 Hz. Samples were taken over a period of 3 minutes giving 180 data points, averages were then computed using these 180 data points.

3.2.1.7.2 IR camera

In order to measure heat transfer coefficient, The IR camera is used to calculate the temperature difference which is induced by the heater mesh. The IR thermography is a technique of measuring surface temperature by measuring its radiation in the infra-red spectrum. This is based on Planck's Law (and Wien's Displacement Law). The IR camera works by detecting radiation intensity and assigning a greyscale value to each pixel that is related to the surface temperature. However, the camera has a limited spectral response within the IR range so the peak of the radiant power spectrum of the test body must lie within the camera's spectral range. In this study, a FLIR A655ac was used, which records over 7.5 μm to 14 μm. For a black-body in the range 280 K to 320 K, peak emission occurs at wavelengths in the range of 9 μm to 10.4 μm. To approximate a black-body, the working section must have an emissivity, $\varepsilon \approx 1$. It was coated with Matt Black Paint 400. Zn-Se was used for viewing windows as it has a high transmissivity, $\tau = 0.98$, over 8 μm to 11.5 μm. The location for the window is shown in Figure 3.16.

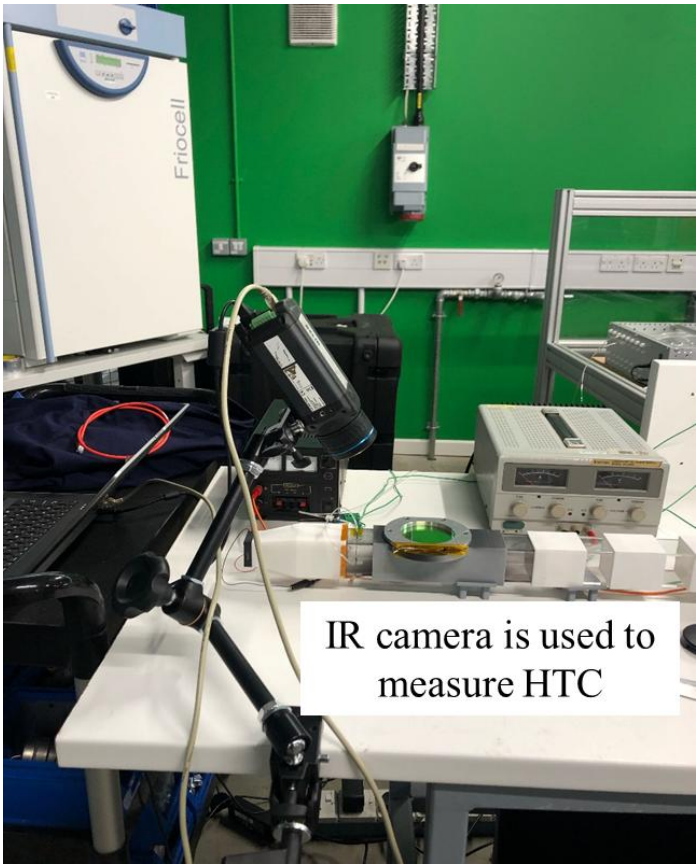

Figure 3-16: Zn-Se window location.

Infrared thermography uses a microbolometer that detects the incoming radiant power through a single area of the sensor. After calibration, the observed radiant power can be converted to temperature, which is then used to calculate the heat transfer coefficient. It provides a non-invasive method for full surface resolution of temperature. The FLIR X6900sc camera was used in this study. This camera has a resolution of 640 x 512, which allows for high-quality surface images. Cooling holes with a diameter of 0.6 mm are also detectable, but with high zoom and much lower resolution - the contour of the hole corresponds to about 3 x 3 pixels. An alternative model (the FLIR X8580) is capable of a much higher resolution (1280 x 1024 HD), but only allowed a maximum frame rate of 181Hz.

An ADC with a 16-bit architecture converts the inbound radiation from within the Focal Plane Array (FPA) to digitize it into Raw numerical value R(x, t) for range 0 to This raw numerical data is approximately linear with the incoming radiation. The equation for each pixel can be written as:

$$q_{cam}(x,t) = a\,.R(x,t) + b \tag{3.15}$$

where q_{cam} is the incident radiative heat flux on the pixel, and the constants a and b are the calibration factors to be determined by performing a black body calibration. Based on the factory value of a and b, the accuracy is about ±1 ^{o}C or ±1% over the range −20 to 350 ^{o}C [127].

Prior to conducting the trials, the camera was calibrated in situ. A black body calibrator was positioned in front of the camera, covering the entire field of view. The calibrator recorded the count values for the entire FPA as it stepped over surface temperatures ranging from 10 to 40 degrees Celsius. The mean count value was calculated by collecting 100 photographs at each given temperature and averaging them. The averaged data are then utilized to generate the quartic curve for each pixel, thereby calibrating the black body temperature to the raw count value for each pixel. Figure 3-17 shows the calibration curve for a single pixel. It was found that the difference in absolute temperature is within ±3 K. However, it is unknown how much of this is due to the surrounding radiance and how much is due to a drift in calibration from the camera's previous factory calibration. Kirollos and Povey [128] reported that the surrounding radiance can contribute up to 13-15% of the total incoming brightness, resulting in an absolute temperature differential of ±1 K, which contribute to uncertainty in Nusselt number by ±4.87% [129]

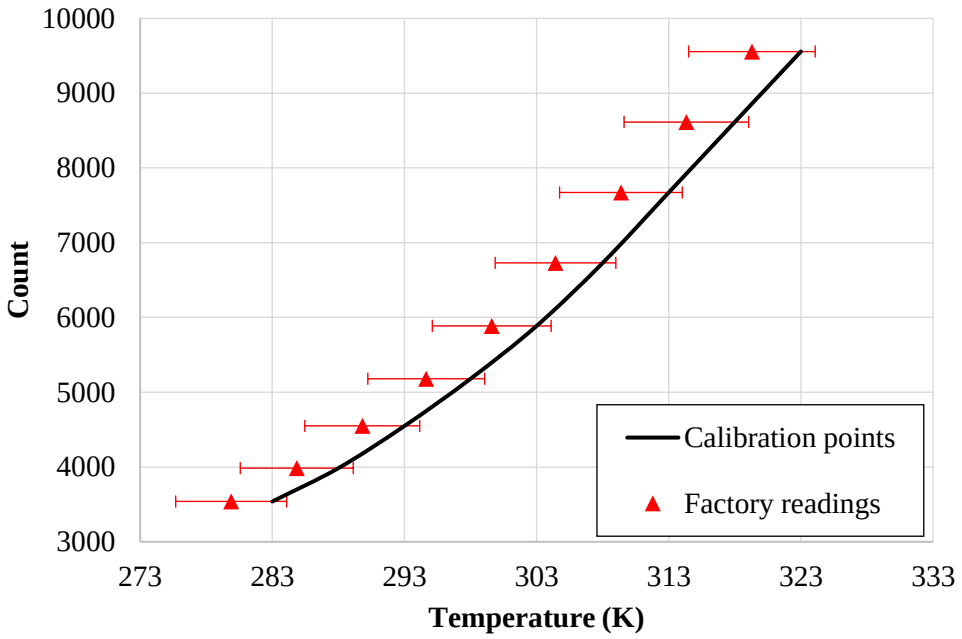

Figure 3-17 Black body calibration curve for a single pixel with factory calibration and quoted 3 K accuracy band (horizontal error bars)

3.2.1.7.3 HTC Determination Method for the Experimental Work

The Heat Transfer Coefficient (HTC) was calculated using a transient method that involves measuring the temperature history of the surface over time, denoted as T(t), using an Infrared (IR) camera. The IR camera captures the temperature distribution across the surface with high spatial and temporal resolution. From this temperature data, the heat flux q(t) is calculated, and the relationship between temperature and heat flux is then used to determine the HTC. This process is performed separately for each individual pixel of the IR camera, ensuring high spatial resolution in the HTC calculation.

The calculation methodology is based on the computational framework developed by Oldfield [130], which uses the Finite Impulse Response (FIR) function to post-process the temperature data. By assuming Linear-Time-Invariant (LTI) behavior for the thermal system, the impulse response of the system characterizes its output response. According to LTI theory, the output

response of the system to any arbitrary input is the convolution of the input with the system's impulse response.

In this approach, the IR camera captures the temperature distribution over time, providing a detailed temperature history T(t) for each pixel on the surface. From the measured temperature data, the heat flux q(t) is calculated using the transient heat conduction equations. An impulse response function is created by analyzing the system's step response, which is specific to the material properties and configuration observed by the IR camera. A rational transfer function is formulated using the MATLAB 'filter' function, where the numerator represents the system's output (heat flux) and the denominator represents the system's input (temperature). Using MATLAB's fftfilt function, the input temperature signal is convolved with the impulse response function. In the frequency domain, this involves computing the Fast Fourier Transform (FFT) of the input, performing point-by-point multiplication, and then using the Inverse FFT to obtain the convolution in the time domain. This convolution accounts for the system's response to the current input as well as to all previous inputs up to the current point.

This transient approach allows for the determination of the HTC as it accounts for the dynamic thermal response of the system.

3.2.1.7.4 Experimental Uncertainty Analysis

The uncertainties associated with direct measurements in this experiment are summarized in Table 3-2. The uncertainty in the indirect measurement value y arises from the uncertainties of the directly measured variables x_1 , x_2, x_3 , … , x_n. The propagation of these measurement errors is calculated using the error propagation formula, which is expressed as follows:

$$\frac{\delta y}{y} = \sqrt{[(\frac{\delta x_1}{x_1})^2 + (\frac{\delta x_2}{x_2})^2 + \cdots + (\frac{\delta x_n}{x_n})^2]} \quad (3.16)$$

The maximum uncertainty in the Nusselt Number (Nu) is calculated using Equation 3.16 as ±6.92%, and the maximum uncertainty in the Performance Factor (PF) is ±6.93%. The maximum uncertainty in the Friction Factor (f) is ±0.64%.

Table 3-2: Summary of Direct Measurement Uncertainty

Measurement Error	Instrument	Maximum Relative Error / %
HTC	IR Camera	±4.87
Bulk Temperature	K-type Thermocouples	±0.5
Flow Rate	MFC (Alicat MCR – 500 slm)	±0.4
Pressure Drop	DPT	±0.5

3.3 Model Validation

In order to check the validity of the computational fluid dynamic (CFD) solver code, two cases have been conducted: the first one to validate the smooth base case with an experimental data as outlined in [131] and the second one is to validate a mini-channel with ribs and secondary channels as outlined in Ref. [45].

The smooth case validation is done both numerically and experimentally in collaboration with an industrial partner. Even though the experiment was not done in the Oxford Thermofluid Institute, the author designed the experiment and was involved in all the experiment stages. The experiment has two setups, one for the pressure drop measurements and the other for the heat transfer measurements. The two setups and the results will be showing in the next subheadings.

3.3.1 Pressure drop measurement

To measure pressure drop across the channel, four pressure taps are placed in the inlet and the same for the outlet of the test section as shown in Figure 3.18. The average value of the four pressure taps in each location is recorded as the inlet and outlet pressure. The actual test piece

for the pressure measurement is shown in Figure 3.19. To develop the flow before it enters the test section, smooth entrance and exit sections of 500 mm are setup as shown in the pressure drop circuit in Figure 3.20. Friction factor was calculated from the measured pressure drop data and compared against the numerical results, which has the set up explained earlier, as well as the Hagen-Poiseuille's equation, $f = \frac{57}{Re}$, and the Colebrook's equation for laminar and turbulent flows, respectively. The relative roughness used to get the prediction in Fig. 3-21 is 0.01.

A good agreement between all the results is achieved as shown in Figure 3.21.

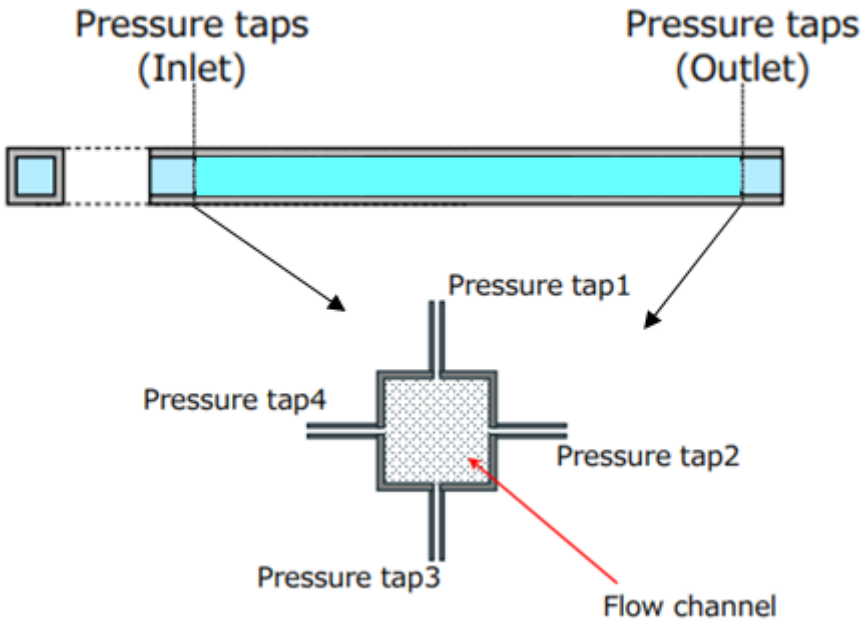

Figure 3-18:Test piece for pressure drop measurement (Top), and cross-section at pressure measurement point (Bottom)

Figure 3-19: Test piece for pressure loss measurement.

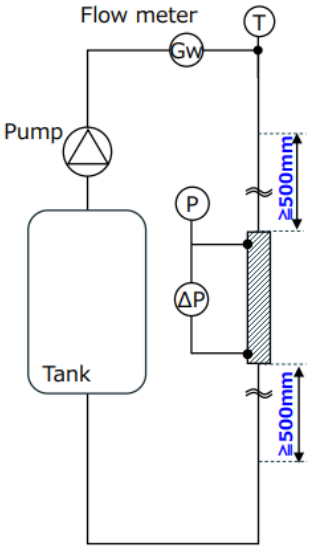

Figure 3-20: Pressure drop test setup.

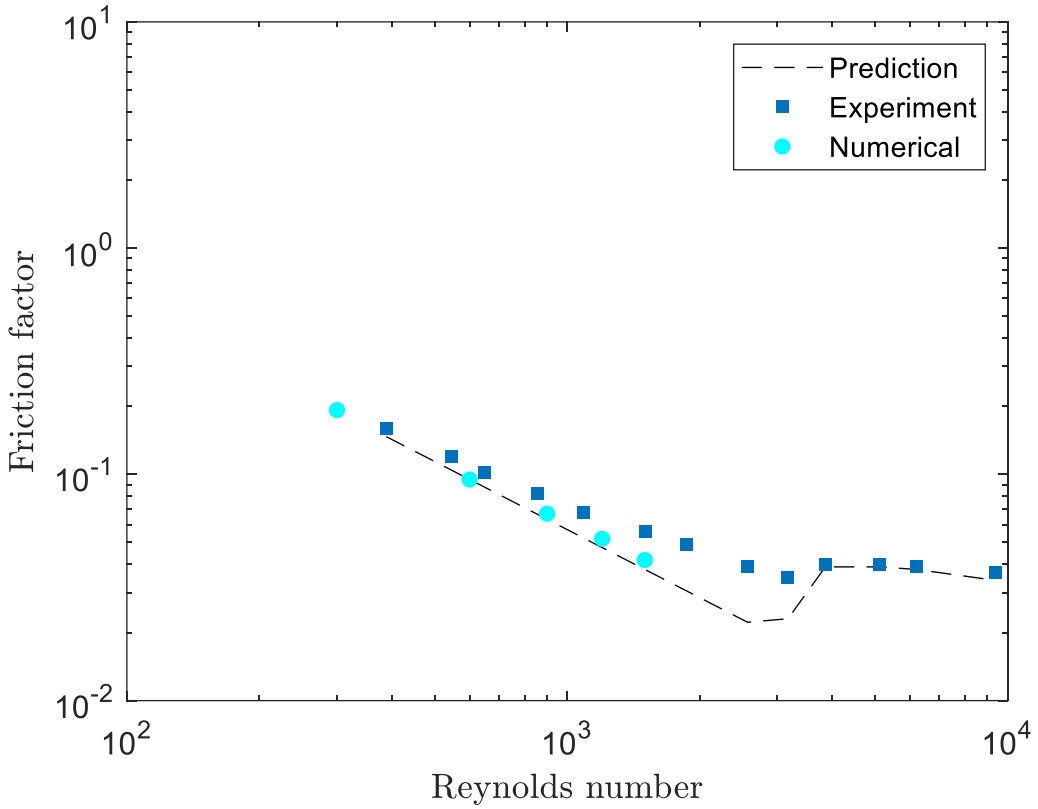

Figure 3-21: Friction factor of the smooth channel against Reynolds number comparing experimental and numerical with the Hagen-Poiseuille's equation, $f = \frac{57}{Re}$ and the Colebrook's equation for laminar and turbulent flows, respectively .

Another validation is performed by comparing the experimental and numerical results of the ribbed heat exchanger. The computational domain of this case is presented in Figure 3.22. Table 3.2 lists the deviations between the two approaches for Nusselt number, friction factor and performance factor. It can be concluded that the present mode is able to predict the fluid flow and temperature field accurately.

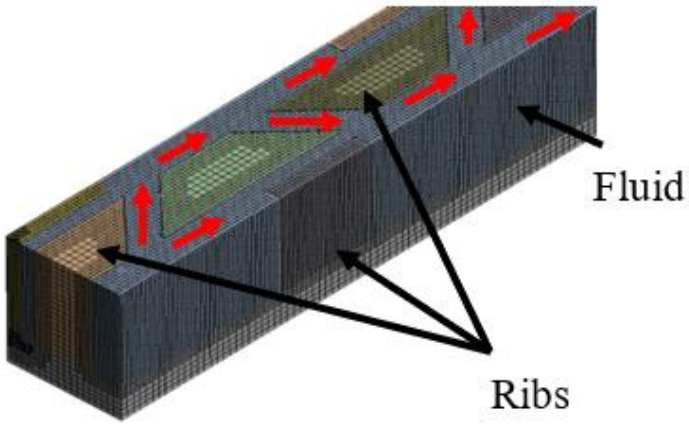

Figure 3-22 Mech and computational domain for the second validation case.

Table 3-3: Comparison between present numerical and validation results

Parameters	Present Results	Validation Results	% Deviation
$\frac{\overline{Nu_r}}{Nu_s}$	3.367	3.32	1.4 %
$\frac{\overline{f_r}}{f_s}$	5.475	5.5	0.45 %
PF	1.91	1.88	1.6 %

The experimental measurements are compared against the numerical results. A comparison of the Nusselt number ratio at different Reynolds numbers between the CFD and the experimental results are shown in Figure 3.23. The Reynolds number range varies from 600 to 1500. As expected, the heat transfer rate increases as the Reynolds number increase for both results. An percentage error of less than 5% between the numerical and the experimental results was observed.

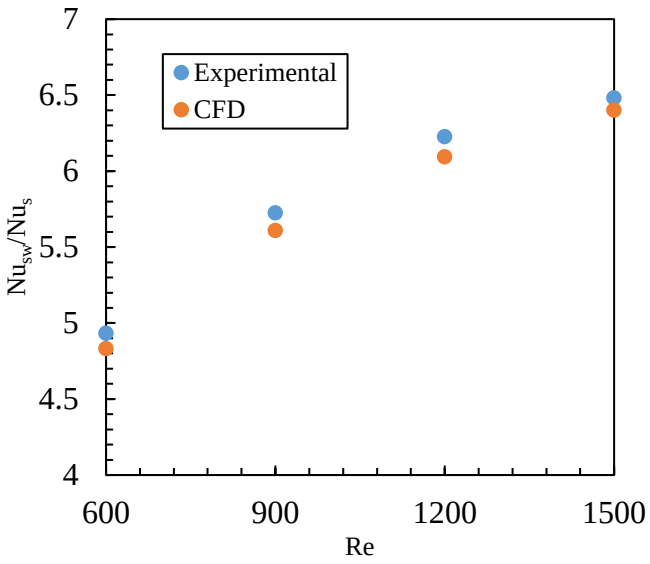

Figure 3-23 Nusselt number ratio as a function Reynolds number

Figure 3.24 shows the location where the IR camera capture the temperature field. Figure 3.25 illustrates the ability of the IR camera to capture the flow structure when using the swirl devices and compared against the CFD results of HTC. The swirl mechanism which allows the flow to impinge on the wall after it passes through the swirl device can be clearly seen in the Figure. It is found that the HTC calculated from the experiment and numerical data is deviated by 10%. In addition, the deviation in the performance factor is estimated to be less than 5%, as shown in Figure 3.26.

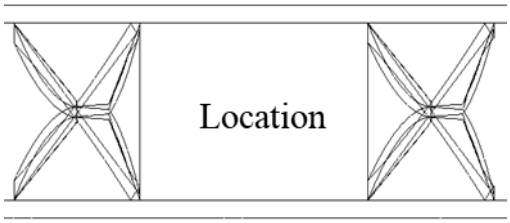

Figure 3-24 The location where the temperature field is captured.

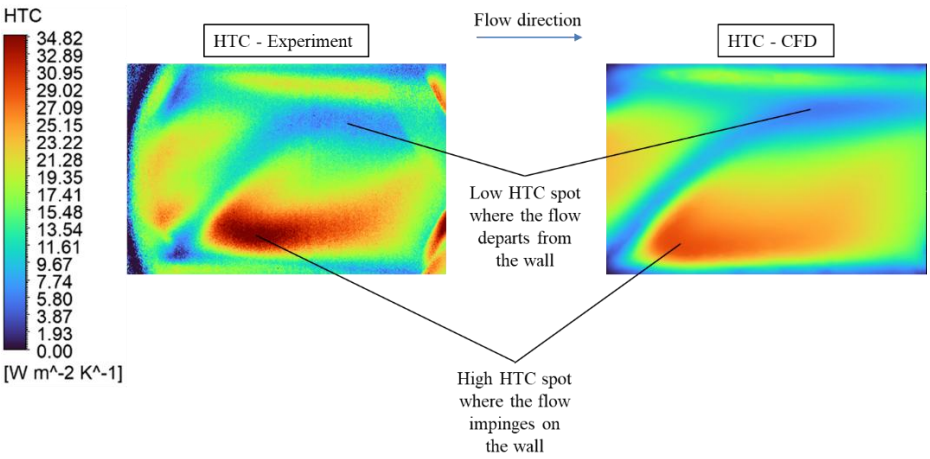

Figure 3-25 HTC contour from CFD (a) and from the Experiment (b).

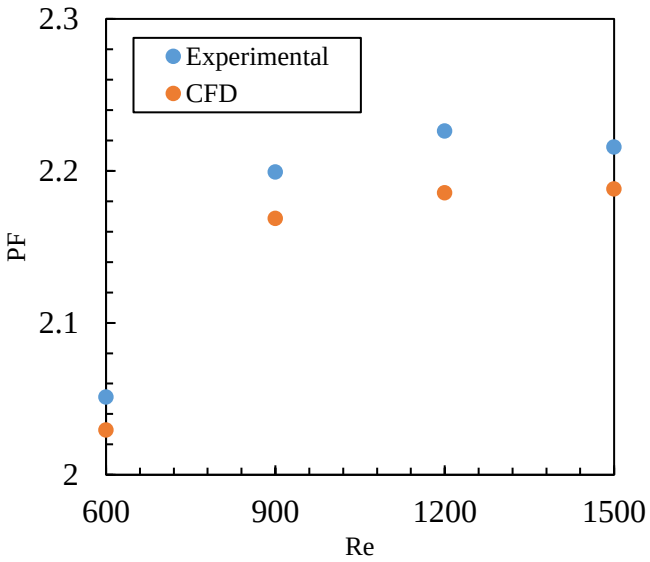

Figure 3-26 Performance factor as a function of Reynolds number

CHAPTER 4 FINNED AND RIBBED CHANNELS

This chapter studies the effect of ribbed and finned channels heat exchanger on heat transfer and fluid flow characteristics.

4.1 Computational Domain and Grid Generation

The Biot number for this study ranges from 0.03 to 0.16, indicating that the system operates in a regime where thermal gradients within the solid are present. Conduction within the solid and convection at the surface are both significant, meaning that the interaction between the two must be considered to some extent. water has been used as the working fluid and Inconel 718 as the solid material, a single passage of the compact heat exchanger core is designed as a conjugate heat transfer case.

Firstly, the Internal Longitudinal Fins Channel (ILFC) is tested to evaluate the effect of the extended surface on both heat transfer and friction factor characteristics. Figure 4-1 shows the computational domain which consists of a square cross-sectional channel with hydraulic diameter (D_h) equal to 0.005 m, wall thickness (t) equal to 0.0005 m, channel length (L_{ch}), width (W_{ch}) and height (H_{ch}) equal to 0.2025 m x 0.005 m x 0.005 m, respectively. Fin heights, h_f, were varied from 0.0005 m to 0.002 m.

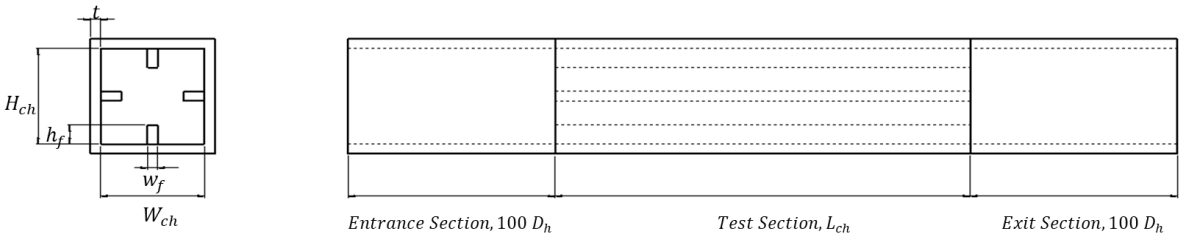

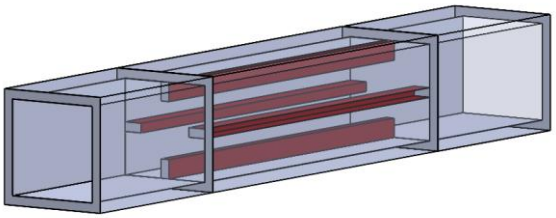

Figure 4-1 Computational domain of Internal Longitudinal Fins Channel (ILFC)

To enhance the heat transfer from four walls in the square channel, swirl flow needs to be introduced to impinge the flow on all the sides. To do this, Central Inclined Ribbed Channel (CIRC) was used to examine the effect of different geometric parameters on heat transfer and flow field. The square channel has the same dimensions as the ILFC. Inclined ribs were placed on the four walls of the channel as seen in Figure 4-2. Three rib inclination angles (α = 30°, 45°, 60°), five different values of the streamwise rib pitch ratio (RP), defines as ratio of the distance between two consecutive ribs over the hydraulic diameter, $PR = P/D_h$, and four different values of the rib height ratio (HR), defines as the height of the rib over the height hydraulic diameter, $HR = h_r/D_h$, were used to evaluate the effect of geometric parameters on heat transfer characteristics and flow field of the CIRC model.

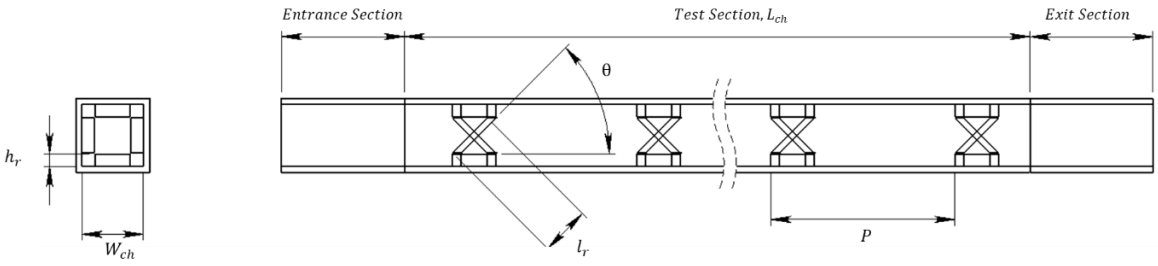

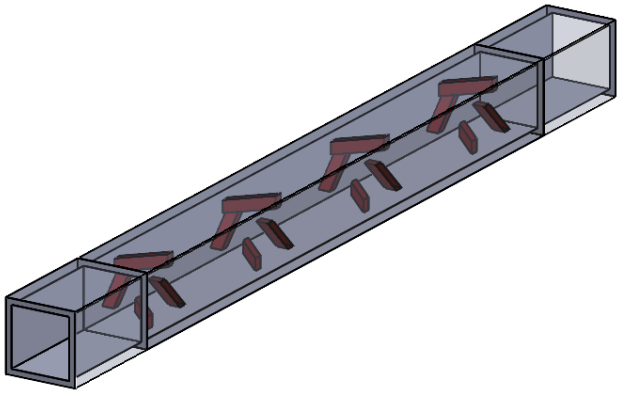

Figure 4-2 Computational domain of Central Inclined Ribbed Channel (CIRC)

4.2 Boundary Conditions

The boundary conditions were the same for all cases. Constant wall temperature applied on the sides, top and bottom walls, to simulate one passage of the heat exchanger core (cold cell) of which is in contact with four adjacent hot cells. To ensure that the flow is fully developed, and regardless of the Reynolds number, the entrance length was approximated as $L_{ent} = 100D_h$ [64]. This length was used in the first iteration to allow for the flow to develop. This approach provides confidence that the flow entering the test section in the second iteration is hydrodynamically fully developed.

All numerical simulations run through two stages in order to ensure that the flow is hydrodynamically fully developed at the inlet of the test section. In the first stage, a simulation of the adiabatic smooth channel with a constant mass-flow rate is conducted. The length of this section is varied according to the mass flow rate at the inlet. In stage two, velocity profile at the outlet of the channel from stage one was extracted and applied on the inlet of the test section while constant wall temperature is applied on the four walls of the channel as seen in Figure 4-3. In this case the thermal boundary layer is developing while the flow is hydrodynamically fully developed.

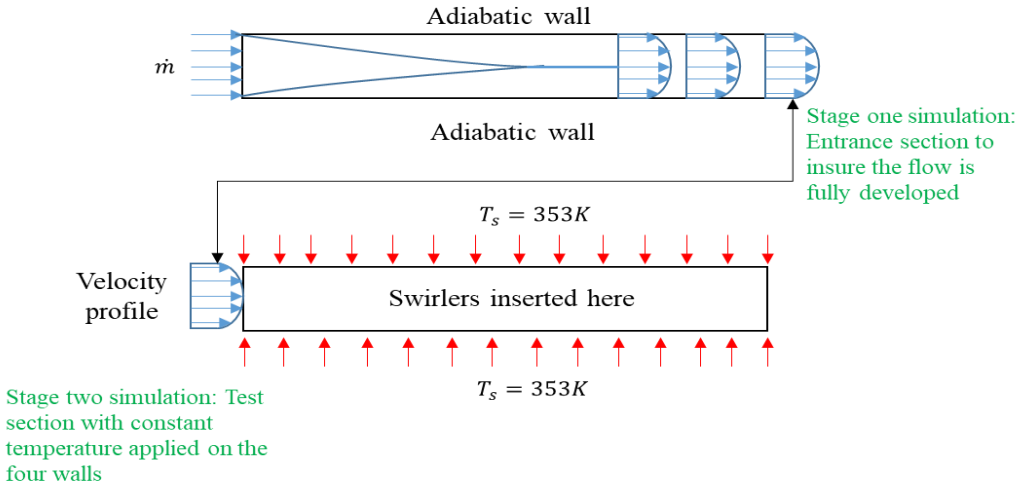

Figure 4-3 Illustration of the boundary conditions setup.

The specified boundary conditions on the test section were as follows:

1. Channel inlet at z = 0

$velocity\ profile$ from stage one

2. Channel outlet at z = 202.5mm

$P_f = P_{out} = 1\ atm$

For fluid $-K_s \left(\frac{\partial T_f}{\partial x}\right) = 0$

For solid $-K_s \left(\frac{\partial T_s}{\partial x}\right) = 0$

3. Walls from all sides

$T_s = 353\ K$

4. Inner walls of channel (fluid/solid surface)

$u = v = w = 0$

$$-K_s \left(\frac{\partial T_s}{\partial n}\right) = -K_f \left(\frac{\partial T_f}{\partial n}\right)$$

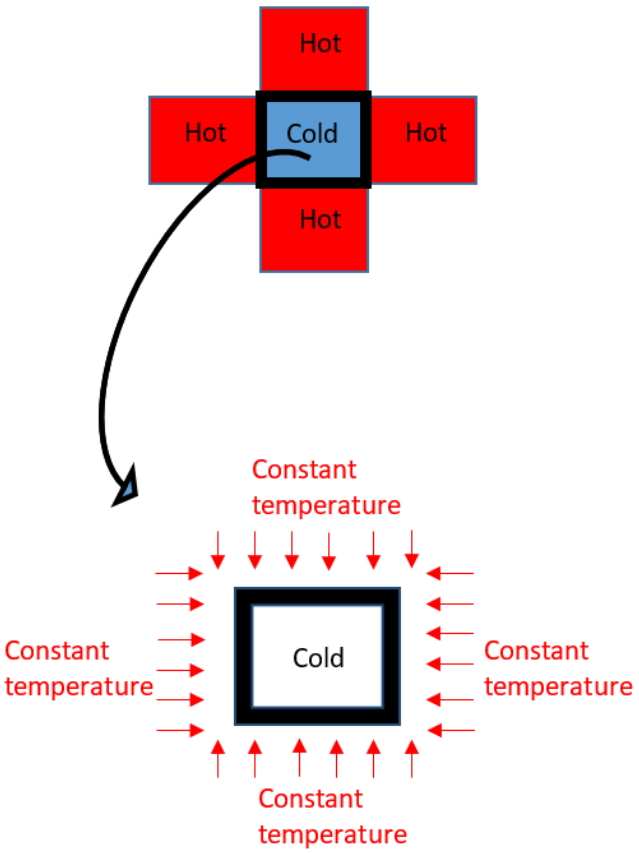

4.3 Mesh generation

For each case studied in this work, mesh was generated using Ansys Meshing to find the optimum mesh size. Refinement of the grid was achieved by varying the near-wall inflation layers. For example, it was changed from 10 to 25 layers for one of the models of the ILFC. This resulted in generating a mesh grid from 7 million to 10 million cells. Table 4.1 shows the average Nusselt number at different mesh sizes for the ILFC at Re = 600. The obtained results from mesh sizes of more than 7 million were about the same, therefore the results from 12 million cells can be considered as grid independent results.

Table 4-1 Average Nu and friction factor at different mesh sizes (ILFC, Re =600)

Mesh Sizes	Average Nusselt Number	Friction Factor
7,181,972	12.85	0.261
8,381,908	11.27	0.250
9,105,003	10.82	0.249
10,183,926	10.55	0.247

4.4 Results and Discussion

4.4.1 Internal longitudinal Fin Channel

4.4.1.1 Flow field

Figure 4.4 shows the velocity pattern for each case at the mid-channel when Re = 1200. In the smooth channel, the maximum velocity is found to be in the centre of the channel as expected. It is observed that as the height of the fin increases, the maximum velocity region is shifting progressively to four separate regions at the side quadrants of the square channel. This shift of the flow is caused by the presence of the fins in the channel which improved the flow in the stagnation areas (i.e. corners). The thinning of velocity boundary layer in the case of the finned channel when compared to the smooth channel is obvious.

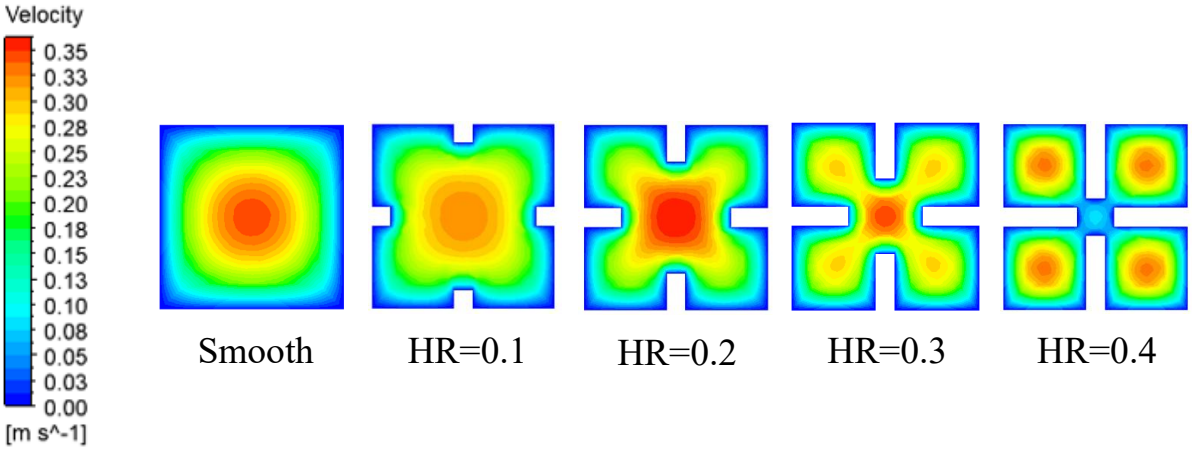

Figure 4-4: Velocity contours at mid-channel for different fin height ratios at Re = 1200.

Figure 4.5 (a) illustrates the location where the velocity distributions of different fin heights are taken in Figure 4.5 (b). In the smooth channel, the highest velocity can be seen at the centre of the channel. As the fin heigh increases, part of the central high velocity shifts to the side quadrants. This shift continues till at fin HR = 0.8, where the highest velocity completely shifts toward the side quadrants.

Figure 4.6 represents the variation of the averaged friction factor ratio, f_{fin}/f_s , where f_{fin} represents the averaged friction factor of the finned channel and f_s represents the averaged friction factor of the smooth channel, with different fin height ratios at different Reynolds numbers. There is a direct proportional relationship between the fin height ratios and the friction factor. As the fin height ratios increases, the friction factor ratio increases. It also notes that, the increase in Reynolds numbers slightly increases the friction factor ratios and this can safely conclude that Reynold number has minimal effect on the average friction factor ratios. The friction factor ratios of the finned channel rise to 5 times that of a smooth channel.

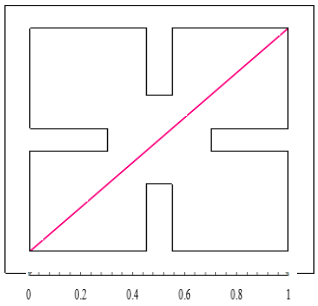

(a)

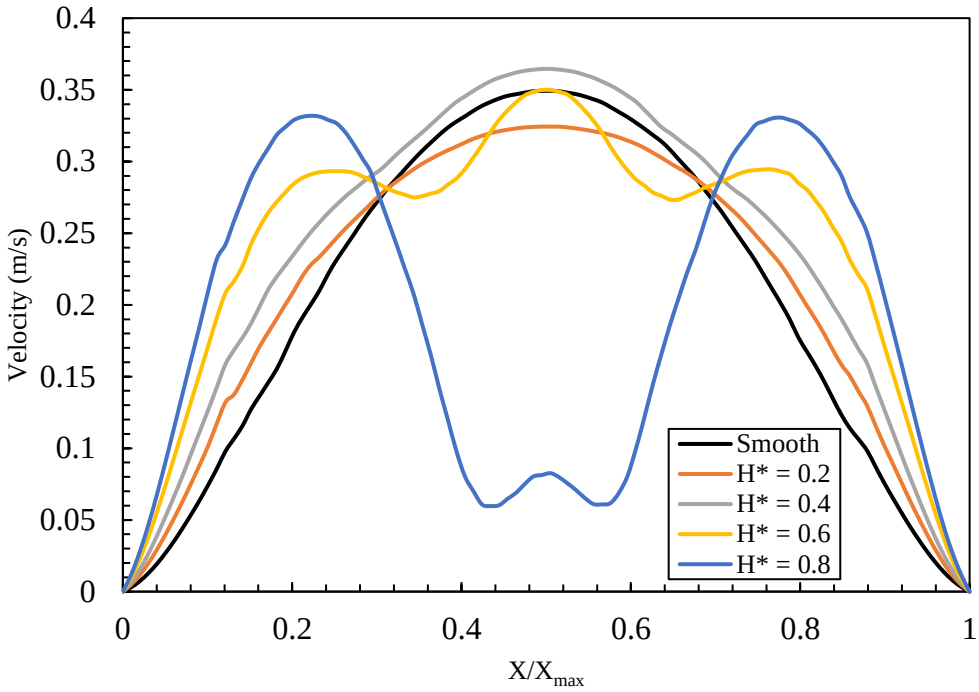

(b)

Figure 4-5: Velocity distribution along the diagonal line within the cross-sectional view shown in (a)

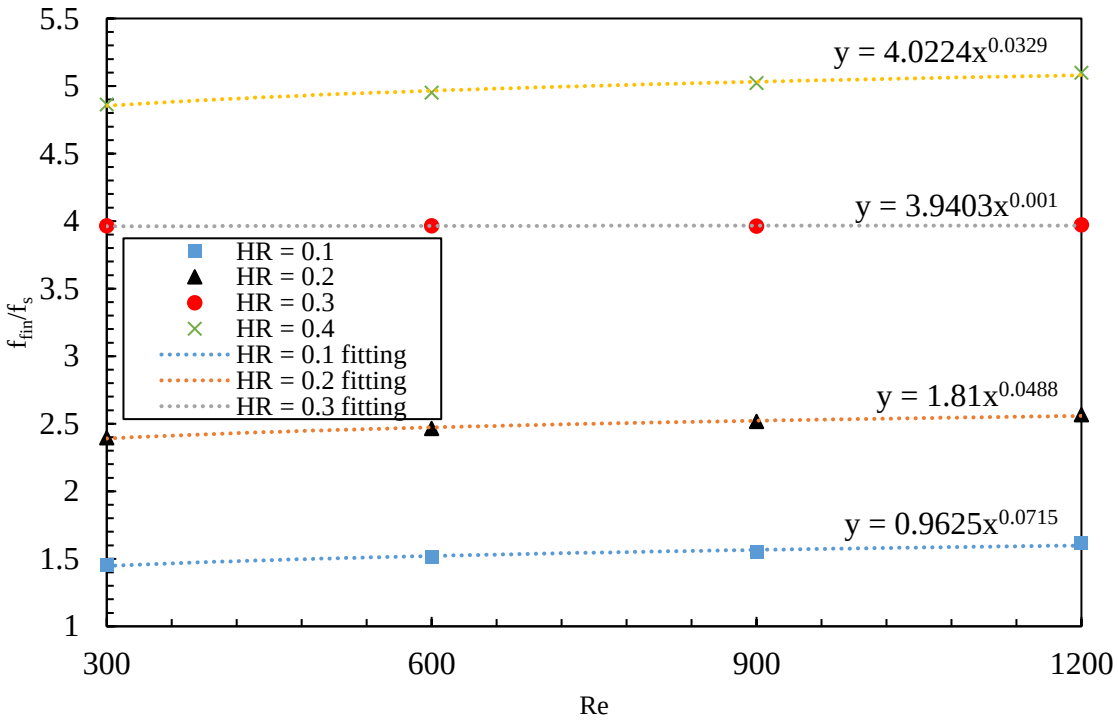

Figure 4-6: Averaged friction factor ratios variation against Reynold numbers at different fin heights ratio.

4.4.1.2 Heat transfer

Figure 4.7 shows the temperature contours at the outlet of the channel for different fin height ratios. It can be clearly seen that the higher the fin height gets, the more flow mixing is happening in the channel.

The best heat transfer augmentation is found at the case where HR=0.4 and that is due to the improvement of the flow found at the corner when compared with the other cases. It also illustrated that; the thermal boundary layer is becoming thinner as the fin height increases. Hence, the heat transfer enhanced when compared to the smooth channel. For a better visualisation to connect the relationship between the flow field and the heat transfer, a velocity and temperature contours at the outlet are shown back-to-back for all the cases and presented in Figure 4.8.

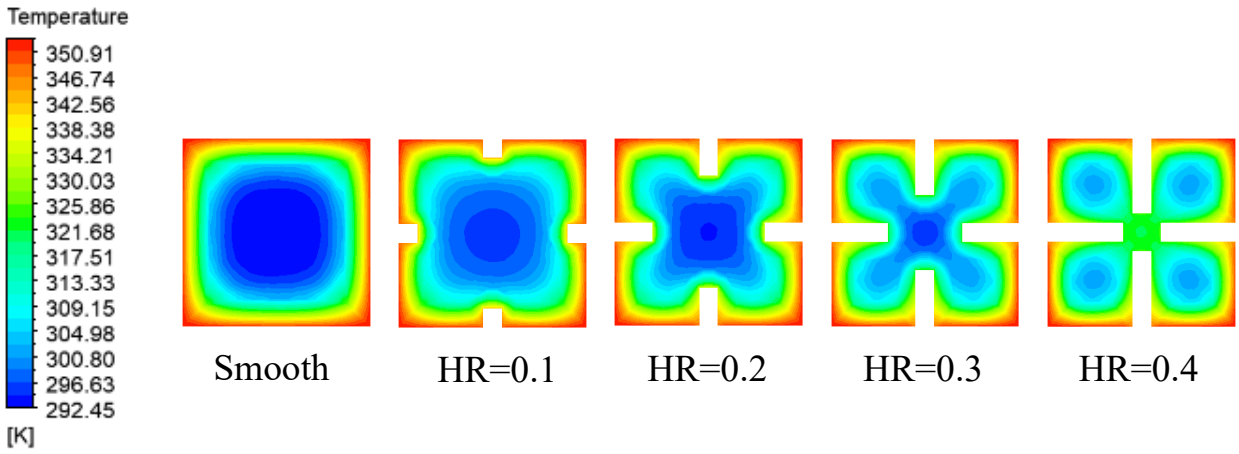

Figure 4-7: Temperature contours (outlet) for different fin height ratios at Re = 1200.

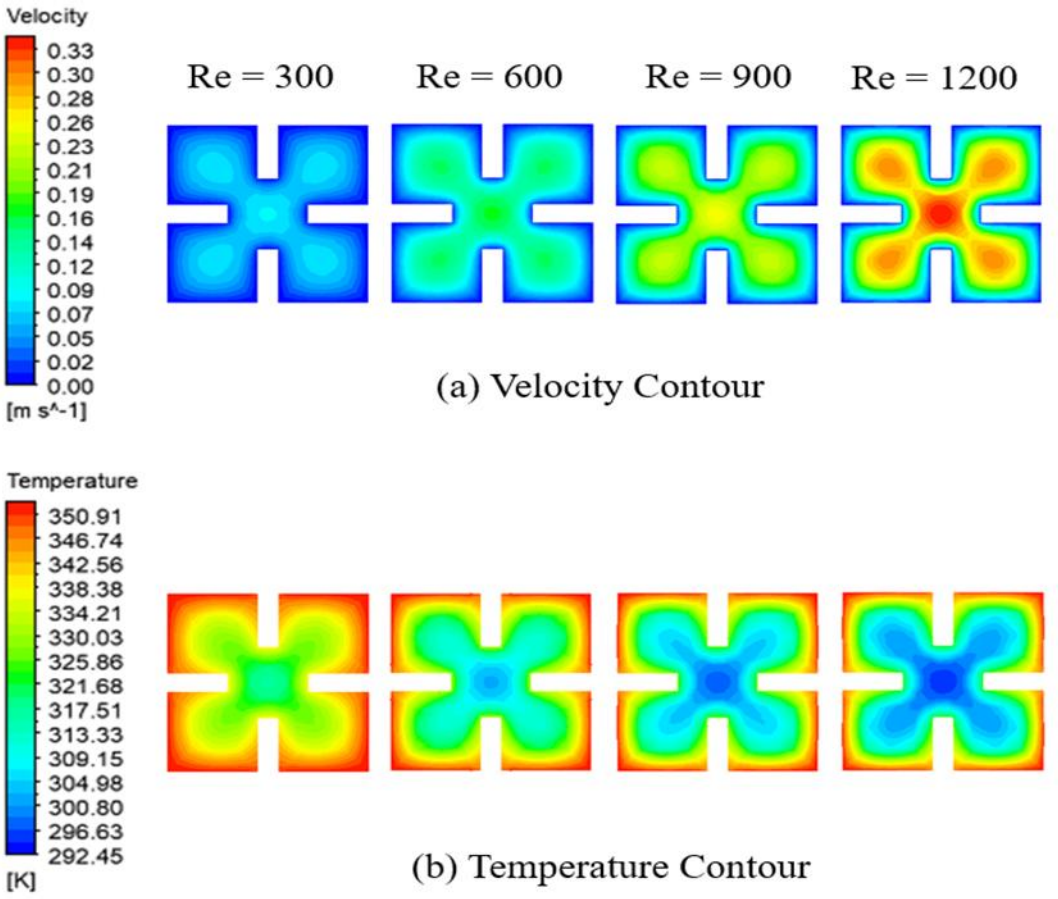

Figure 4-8 Velocity contours at the outlet (a), Temperature contours at the Outlet (b), for the HR = 0.3 at different Reynolds numbers.

Figure 4.9 demonstrates the averaged Nusselt number ratio, Nu_{fin}/Nu_s , where Nu_{fin} represents the averaged Nusselt number for the finned channel and Nu_sff represents the averaged Nusselt number for the smooth channel, for different fin heights cases at different Reynolds numbers.

An interesting finding worth mentioning in this figure is that the averaged Nusselt number slightly increases with Reynolds number for low fin heights (HR = 0.1 and 0.2) and it is likely due to the dominance of convection in these cases. At lower fin heights, the flow remains relatively unimpeded, and the increase in Reynolds number enhances the mixing of fluid layers,

reducing the thermal boundary layer thickness and promoting higher heat transfer rates. This results in a moderate increase in the Nusselt number as the Reynolds number rises.

For higher fin heights (HR = 0.3 and 0.4), the opposite trend occurs because the extended surface height introduces significant flow resistance and alters the flow regime. At larger Reynolds numbers, the increased velocity intensifies the frictional losses and causes flow separation or recirculation near the fin surfaces. These effects hinder effective heat transfer by reducing the direct interaction of the fluid with the fin surface. As a result, the average Nusselt number decreases with increasing Reynolds number in these cases. This behavior highlights the trade-off between enhanced heat transfer surface area and the adverse effects of flow disruption at higher fin heights. Even though this trend was noticed, the highest averaged Nusselt number was found at the case which had the highest fin height, HR = 0.4. The heat transfer enhancement was about 55% when compared against the smooth case.

When considering the pressure drop penalty associated with the heat transfer enhancement, the performance factor drops below one for all the cases. This means that the ILFC is only beneficial when considering augmenting the heat transfer rate. Figure 4.10 illustrates the overall performance factor for all the cases of the ILFC.

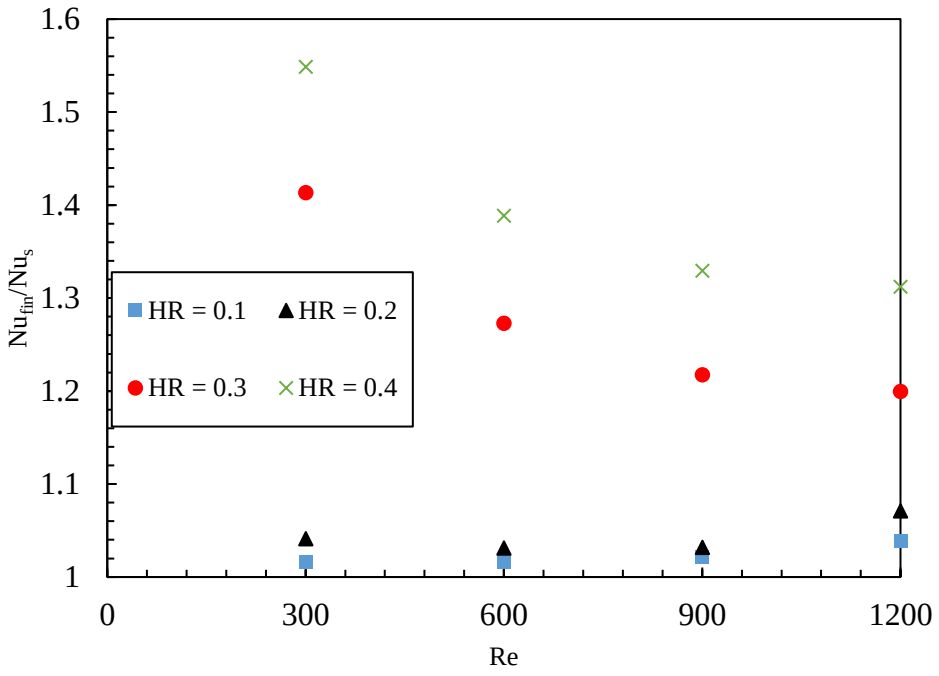

Figure 4-9: Average Nusselt number against Reynold numbers at different fin heights ratios

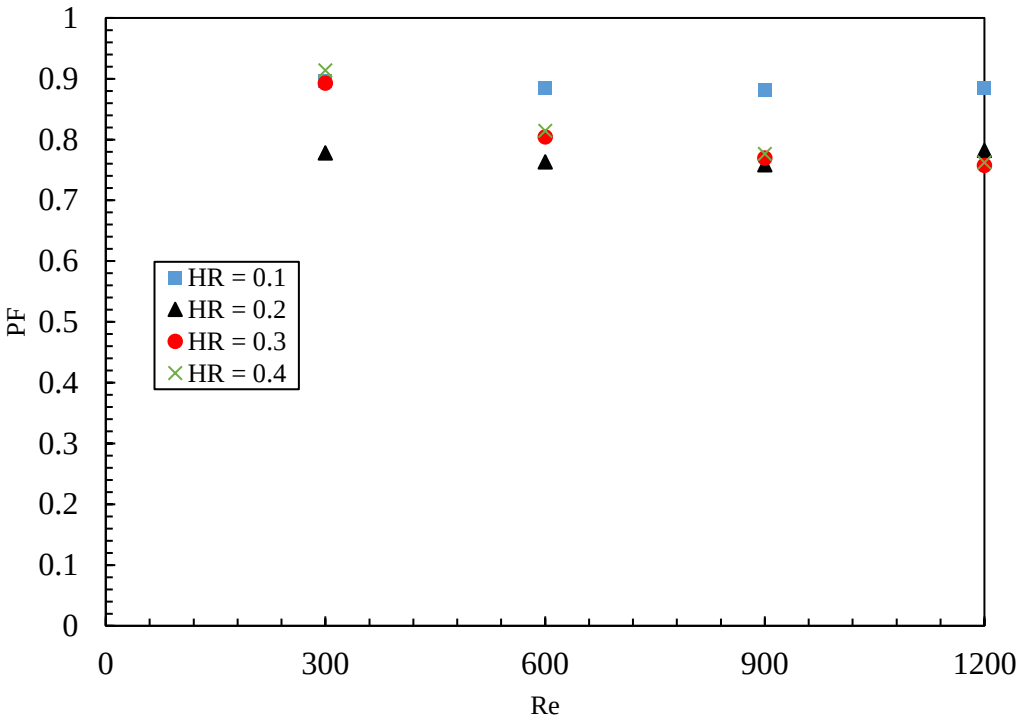

Figure 4-10: Performance factor against Reynolds numbers at different fin heights ratios.

4.4.2 Central Inclined Finned Channel

A single passage of the heat exchanger core for the Central Inclined Finned Channel (CIFC) is simulated to investigate its effects on the flow field and the heat transfer characteristics.

4.4.2.1 Flow field

The flow field of the CIFC is investigated in this section. The five locations shown in Figure 4-11 are selected to visualize the flow field. As shown in Figure 4-12, the velocity profile changes when flow goes throughout the channel at Re = 1200. It is found that the swirl flow is promoted, and thinner boundary layers are observed. As evidence of the swirl flow strength, Figure 4-13 shows the swirl strength Iso-surface at 41 s^{-1}. It is found that vertical structure is generated around the inclined fins where the heat transfer enhances, and pressure drop would increase. Figure 4-14 plots the average friction factor at different Reynolds numbers. It steadily decreases as the inlet velocity increases. It reduces from 0.4 to 0.2 when Re changes from 300 to 1500. This highlights the great impact of Re on the friction factor and pressure drop across the channel.

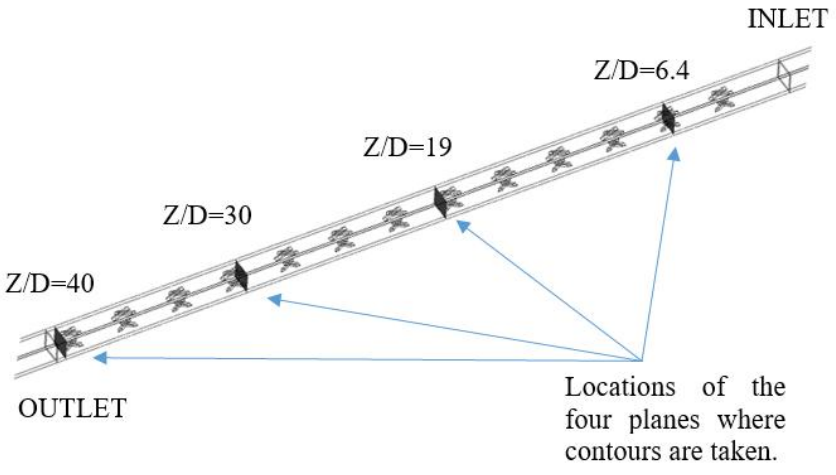

Figure 4-11 Locations of the planes where contours are taken

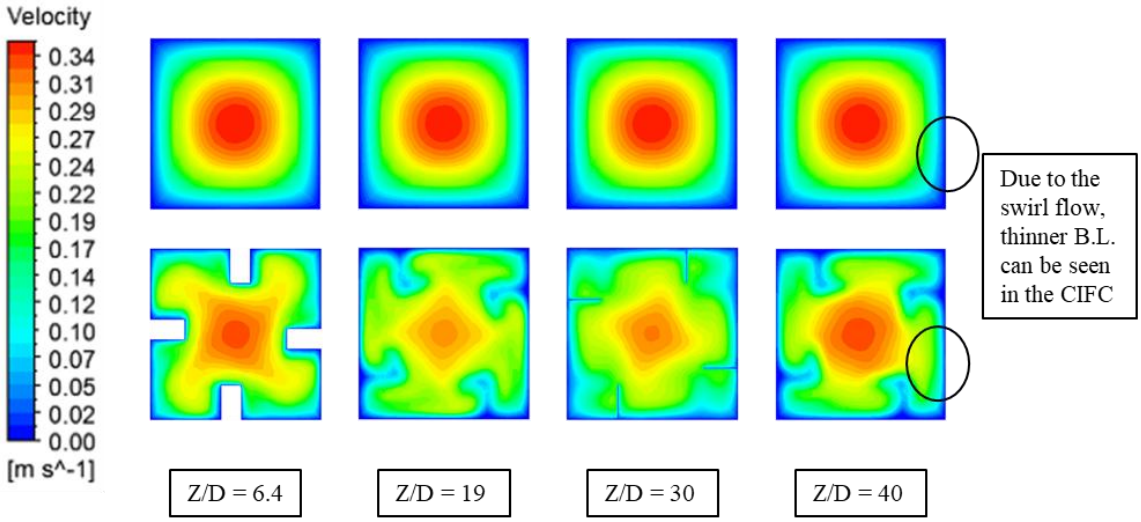

Figure 4-12: Velocity contour at four different locations along the streamwise direction at Re = 1200.

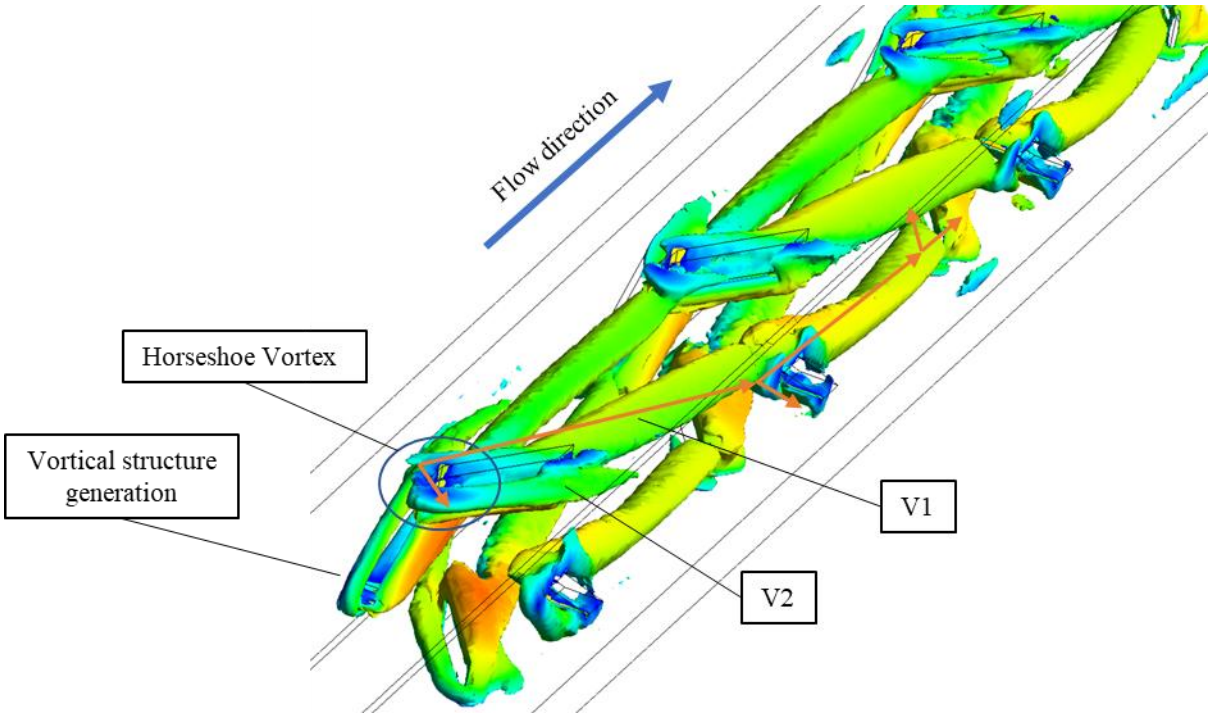

Figure 4-13: Swirl strength Iso-surface at 41 s^{-1} coloured with velocity for the CIFC ($\alpha = 30^{o}$, PR = 3, HR = 0.2, Re = 1200)

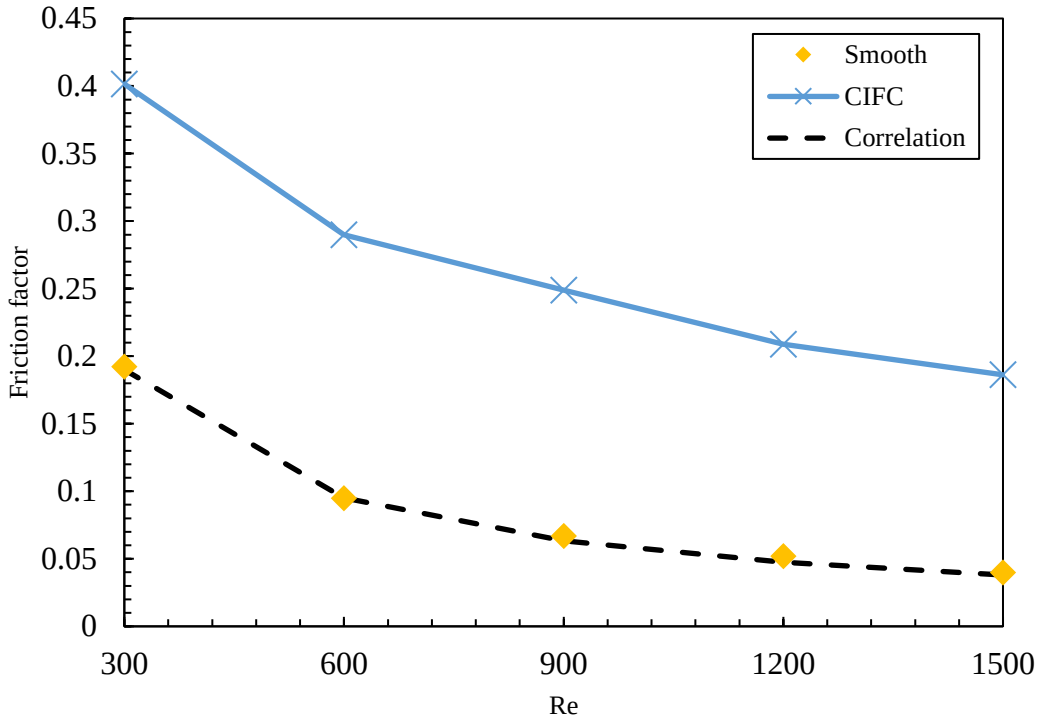

Figure 4-14: Friction factor at different Reynolds numbers for the Smooth and CIFC.

4.4.2.2 Heat transfer

The temperature contour at different streamwise locations at Re = 1200 is shown in Figure 4-15. As the flow progresses through the channel the flow mixes very well and the heat transfer rate increases when compared to the smooth case. The decrease in the temperature gradient of the fluid is evidence of this finding. Figure 4-16 shows the Nusselt number as a function of Re for the CIFC and the smooth channel. It can be seen that the Nusselt number gradually increases as the Re increases. It goes from 8.7 at Re = 300 to 29 at Re = 1500. It is calculated that the average Nu for the CIFC is about 3 times higher than the smooth channel at Re = 1500.

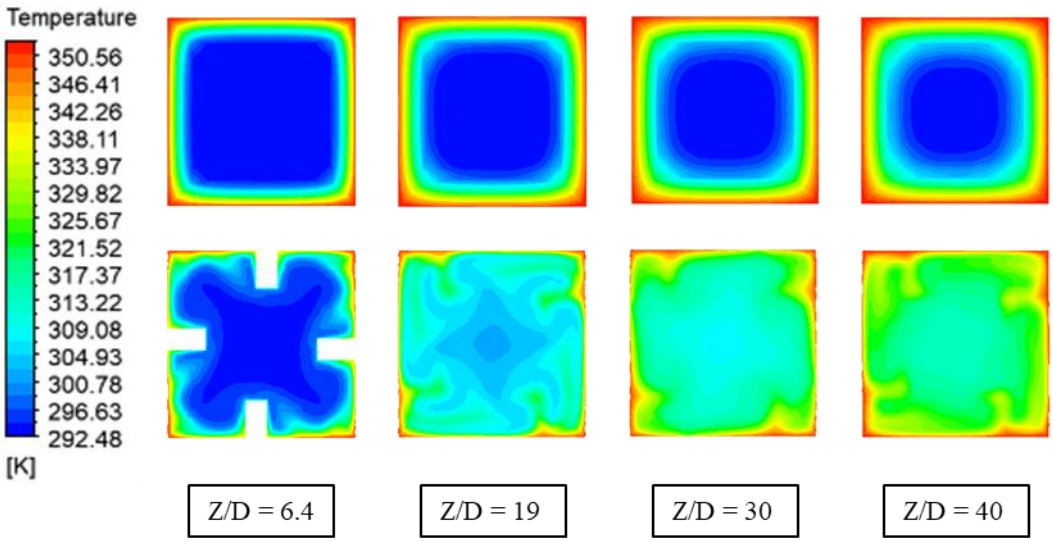

Figure 4-15:Temperature contour at four different locations along the streamwise direction at Re = 1200

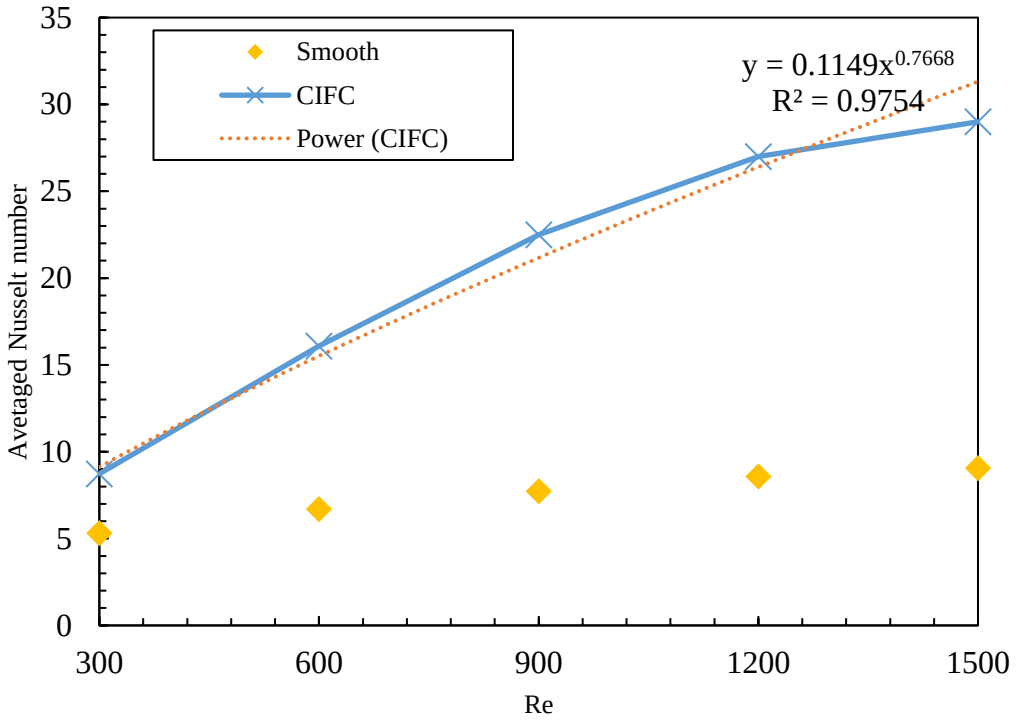

Figure 4-16: Averaged Nusselt numbers at different Reynolds numbers for the Smooth and CIFC.

4.4.2.3 Parametric Study

The design of the CIFC is being explored by changing one of the design parameters while keeping all other parameters constant. The impact of these adjustments on the heat transfer and flow within the channel will be examined in the subsequent sections.

4.4.2.3.1 Effect of angle of attack (α)

The variation in heat transfer rates, friction factors, and overall performance factors with different inclination angles, for a streamwise pitch ratio of 3, height ratio of 0.2, and five different Reynolds numbers ranging from 300 to 1500 are shown in the figures below.

Figure 4-17 presents the variation of Nusselt number ratio with different angles of attack at different Reynolds number. There is a direct proportional relationship between the Nusselt number ratio and the Reynolds number. As the Reynolds number increases, the Nusselt number increases for all the different angles of attack. The figure reveals that the bigger the angle of attack, the higher the averaged Nusselt number becomes and that's because of the stronger swirl generated and higher heat transfer coefficient, as shown in Figure 4-18 and 4-19. The highest heat transfer augmentation occurs at the largest angle of attack $\alpha = 60^{o}$ at Re = 1200 and the amount of augmentation is about 5.0 times higher than that of smooth case. The same trend can be seen on the friction factor in Figure 4-20 and that's because of the high-pressure losses and wall shear stresses observed as the angle of attack increases. The inclusion of pressure contours, as shown in Figure 4-21, is critical for understanding the flow characteristics within the heat exchanger and assessing the impact of design changes. The pressure contours provide valuable insights into the interaction of swirling flows with the channel geometry, highlighting regions of flow separation, recirculation, and acceleration caused by the inclined fins. Furthermore, visualizing pressure distributions allows for the identification of pressure drop gradients, which are directly linked to the pumping power requirements.

As plotted in Figure 4-21 and 4-22, the swirl strength increases and the flow impingements of the wall is stronger. When considering the pressure drop penalty associated with the heat transfer enhancement, the performance factor of 2.15 is the highest value obtained at $\alpha = 45^{o}$ at Re = 1500 which means an enhancement of 115% on the overall system performance was achieved when compared to the smooth case as shown in Figure 4-23.

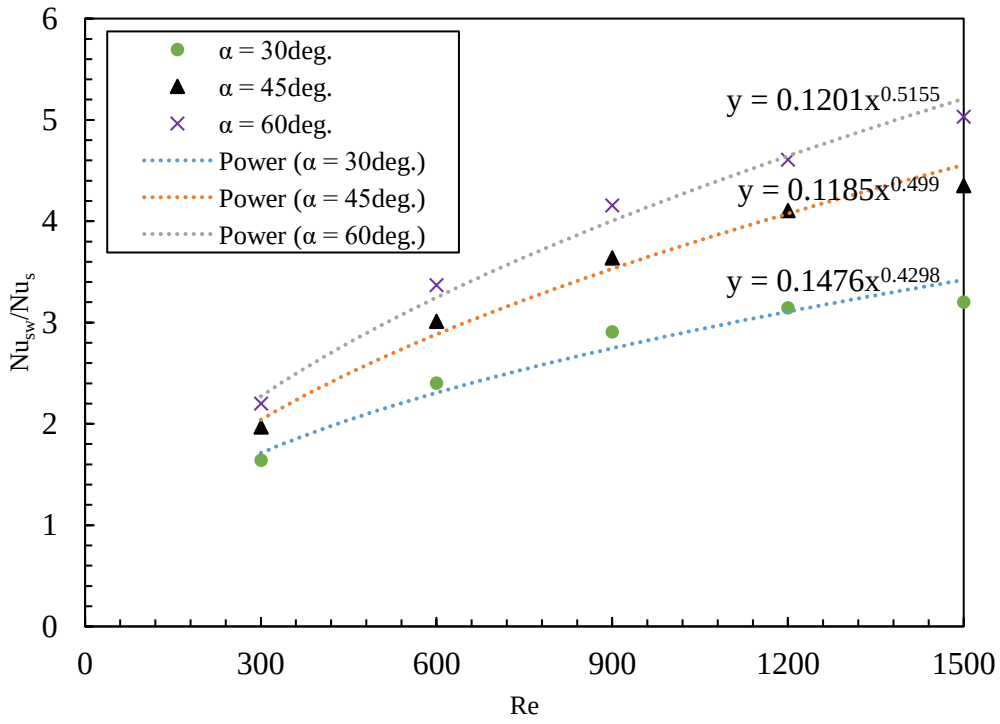

Figure 4-17: Averaged Nusselt number against Reynolds numbers at different fin inclination angles.

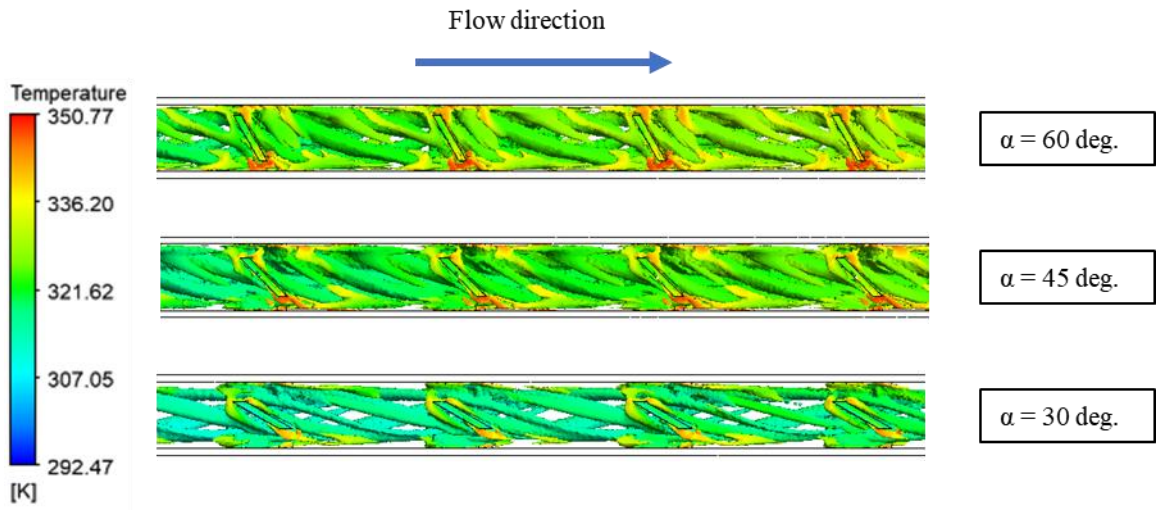

Figure 4-18: Swirl strength Iso-surface at 41 s^{-1} coloured with temperature for different inclination angles, Re = 1200.

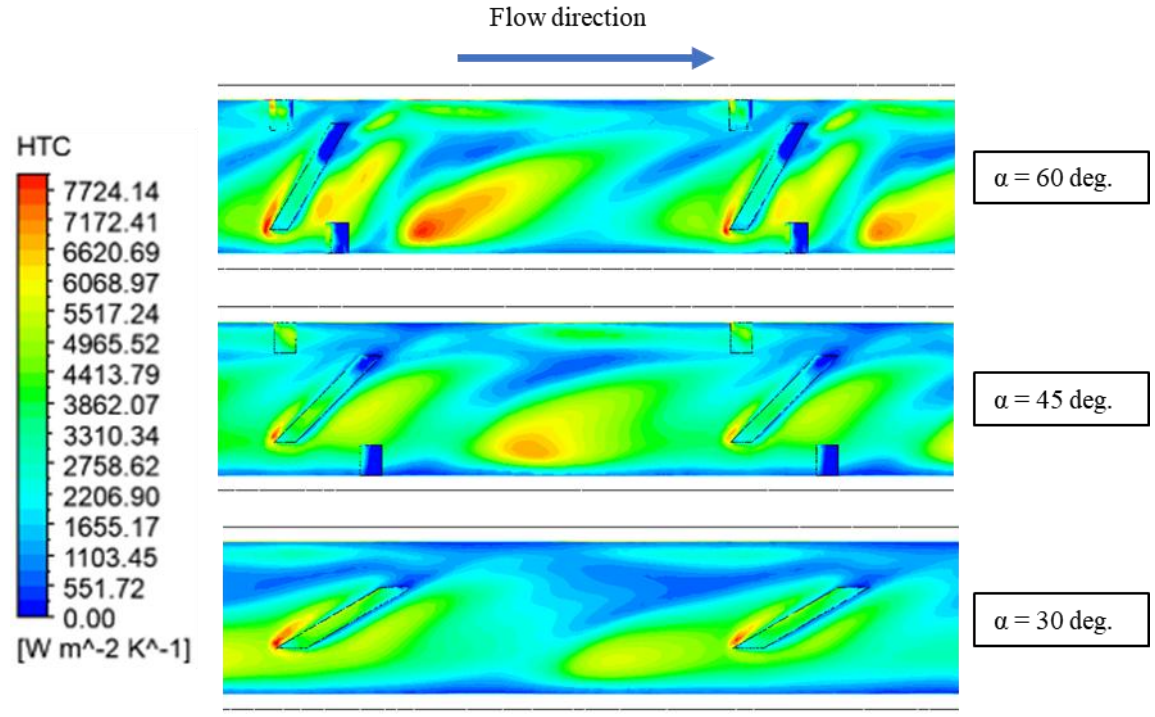

Figure 4-19: Heat transfer coefficient distribution along one of the walls at the midstream position for various inclination angles at Re=1200.

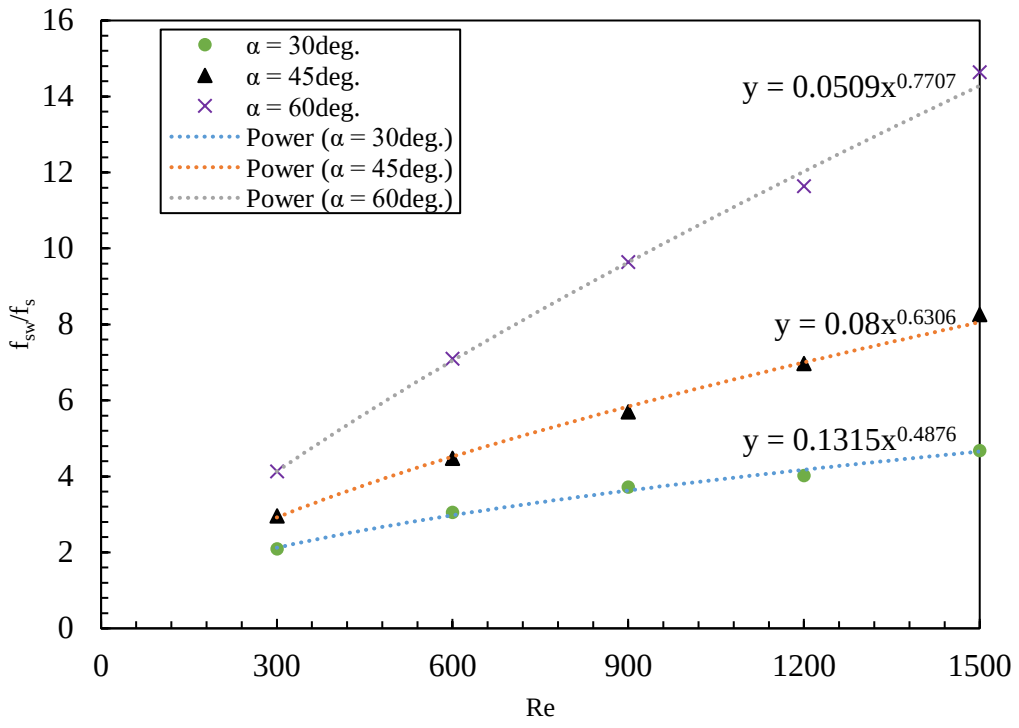

Figure 4-20: Averaged friction factor ratios against Reynold numbers at different fin inclination angles.

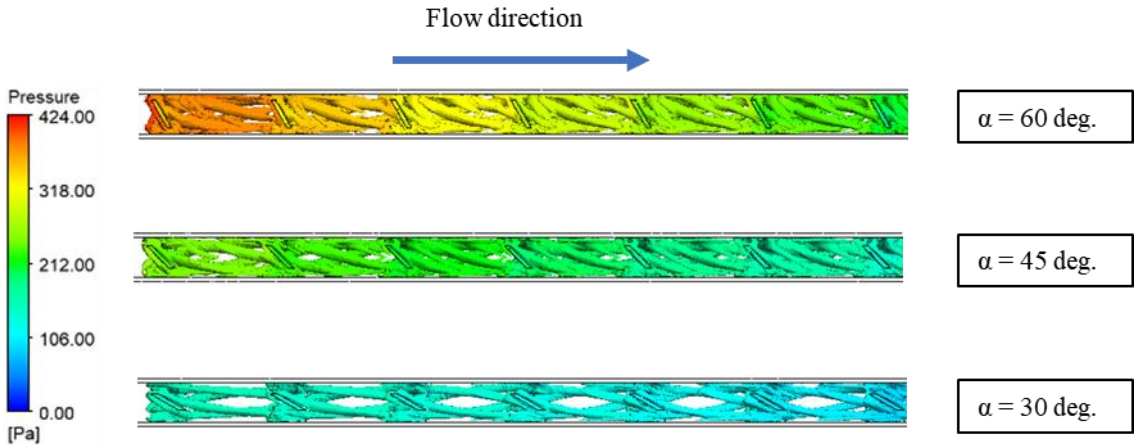

Figure 4-21: Swirl strength Iso-surface at 41 s^{-1} coloured with pressure for different inclination angles, Re = 1200.

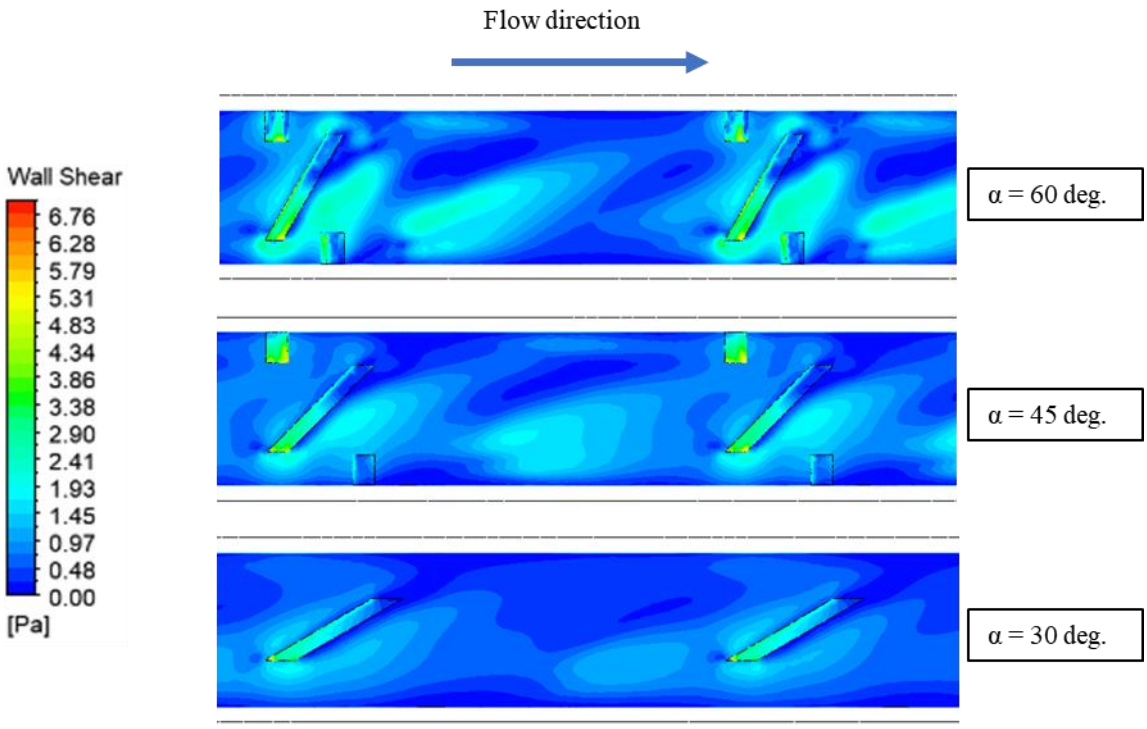

Figure 4-22:Wall Shear stress distribution along one of the walls at the midstream position for various inclination angles at Re=1200..

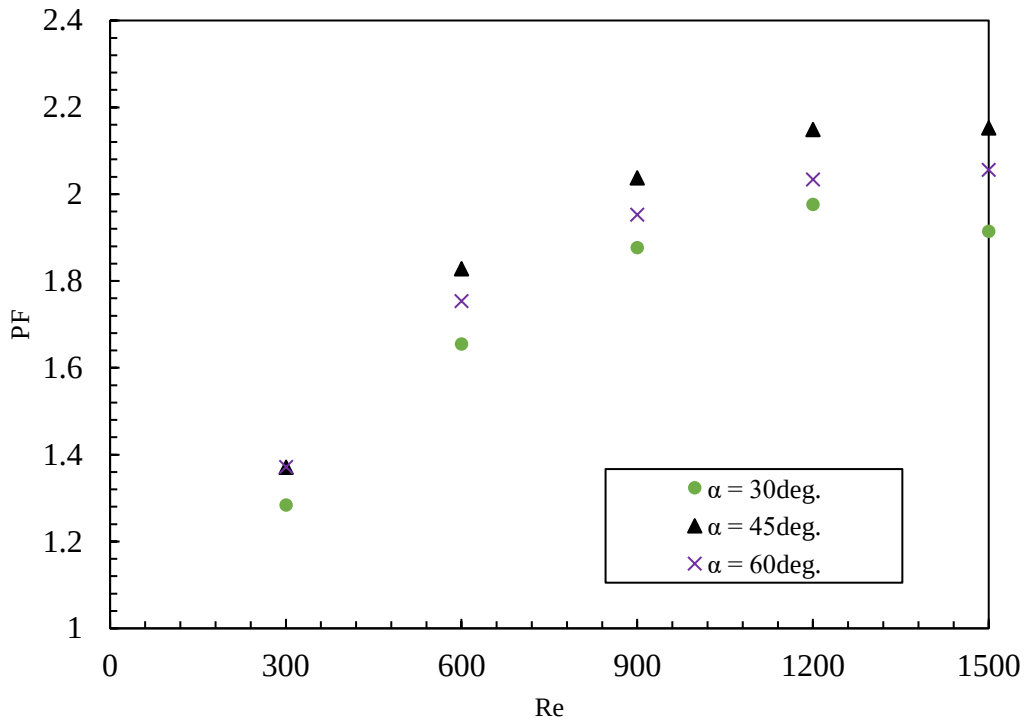

Figure 4-23: Performance factor ratios against Reynold numbers at different fin inclination angles.

4.4.2.3.2 Effect of streamwise pitch ratio (PR)

The variation in heat transfer rates, friction factors, and overall performance factors with different pitch ratios, for an angle of attack of 45°, height ratio of 0.2, and five different Reynolds numbers ranging from 300 to 1500 are shown in the figures below.

The pitch ratio is defined as the ratio of the distance between two consecutive fins over the hydraulic diameter, $PR = \frac{P}{D_h}$ where P represents the distance between two fins. Figure 4-24 demonstrates the variation of Nusselt number ratios with different pitch ratios at different Reynolds numbers. There is a direct proportional relationship between the Nusselt number and the Reynolds number. As the Reynolds number increases, the Nusselt number increases for all the different pitch ratios. The figure reveals that the smaller the pitch ratio, the higher the averaged Nusselt number becomes and that's because of the stronger swirl caused by placing more fins as can be seen in Figure 4-25. The effect of the PR clearly can be seen as the vortex

structure of the smallest PR is continuous whereas it decays in the case where PR = 6 indicating a less swirl effect when compared to the case where PR = 1.5. This directly affects the HTC as shown in Figure 4-26. The highest heat transfer augmentation occurs at the smallest pitch ratio (PR=1.5) at Re = 1200 and the amount of augmentation is 4.3 times higher than that of smooth case. The same trend is observed on the friction factor in Figure 4-27 and that's because of the high pressure losses resulted as the pitch ratio decreases, as shown in Figure 4-28 and 4-29. When considering the pressure drop penalty associated with the heat transfer enhancement, the performance factor of 2.1 is the highest value obtained at PR = 3 and 3 at Re = 1500 which means an enhancement of 110% on the overall system performance was achieved when compared to the smooth case as shown in Figure 4-30.

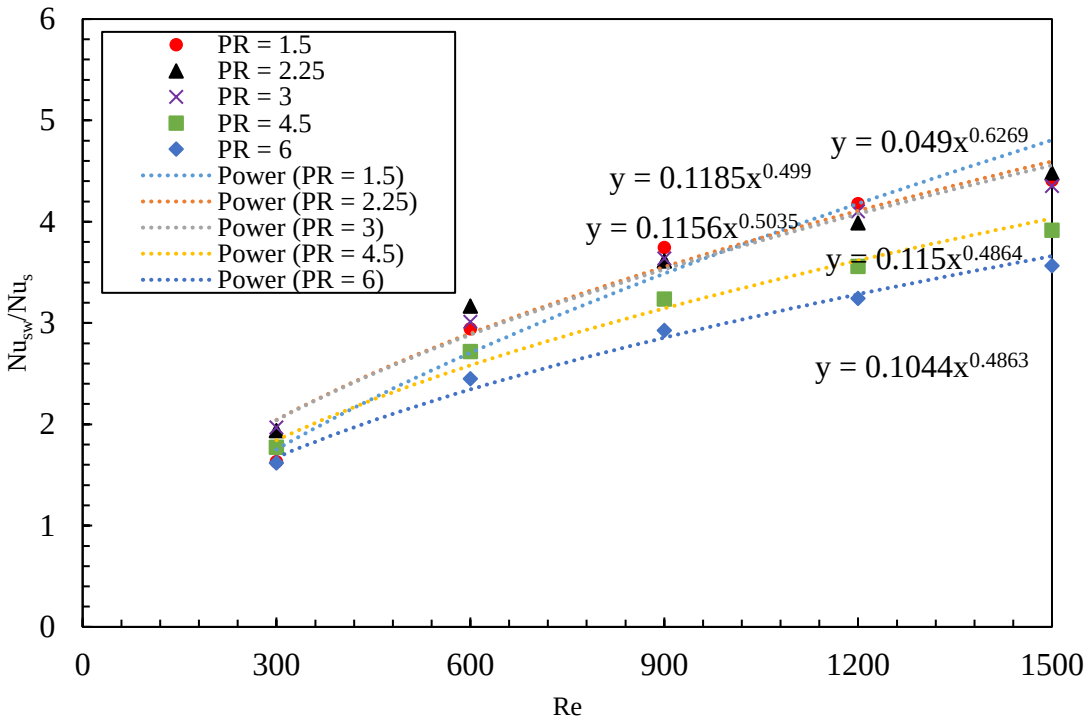

Figure 4-24: Nusselt number ratios against Reynold numbers at different fin pitch ratios.

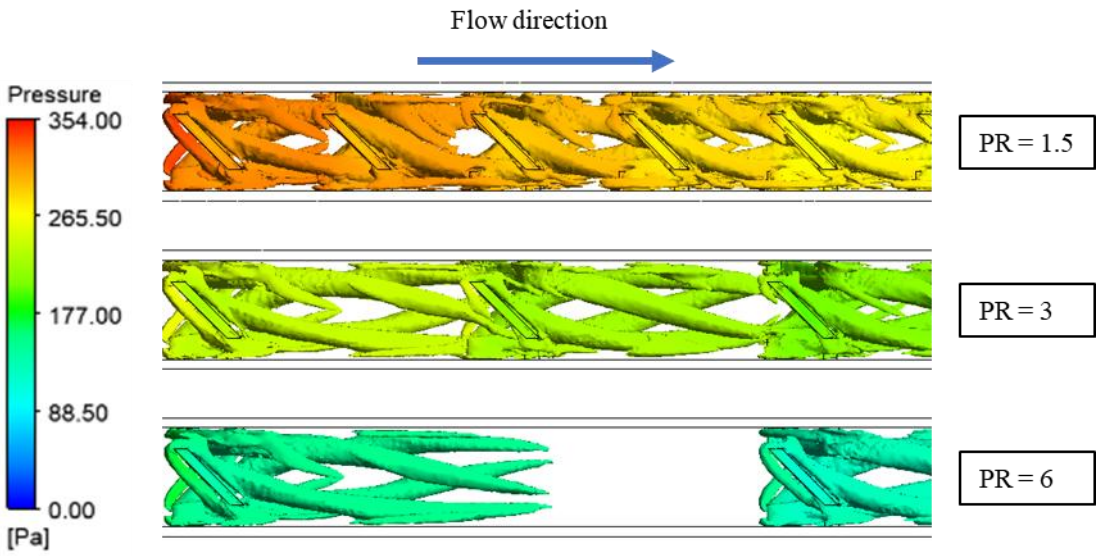

Figure 4-25: Swirl strength Iso-surface at 41 s^{-1} coloured with pressure for different pitch ratios, Re = 1200.

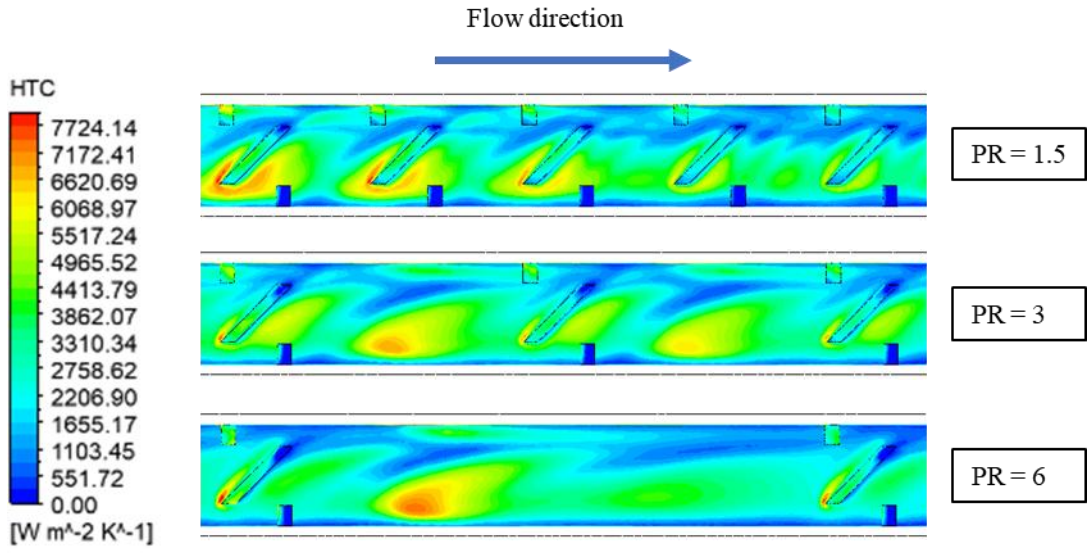

Figure 4-26: Heat Transfer Coefficient distribution along one of the walls at the midstream position for various inclination angles at Re=1200.

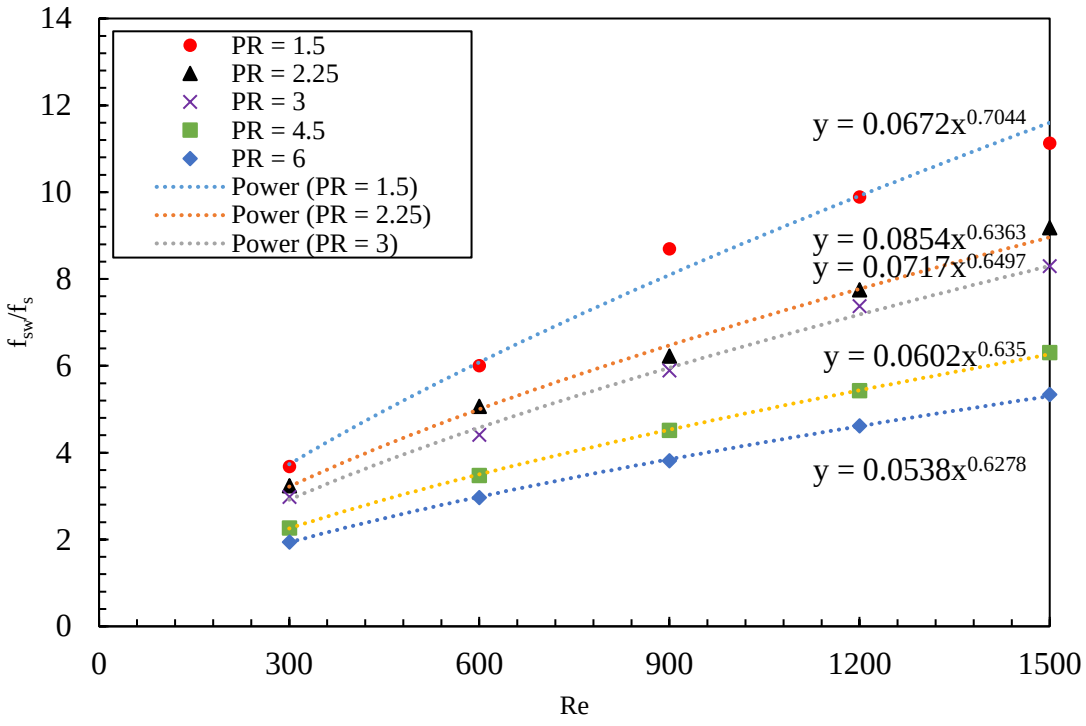

Figure 4-27: Friction factor ratios against Reynold numbers at different fin pitch ratios.

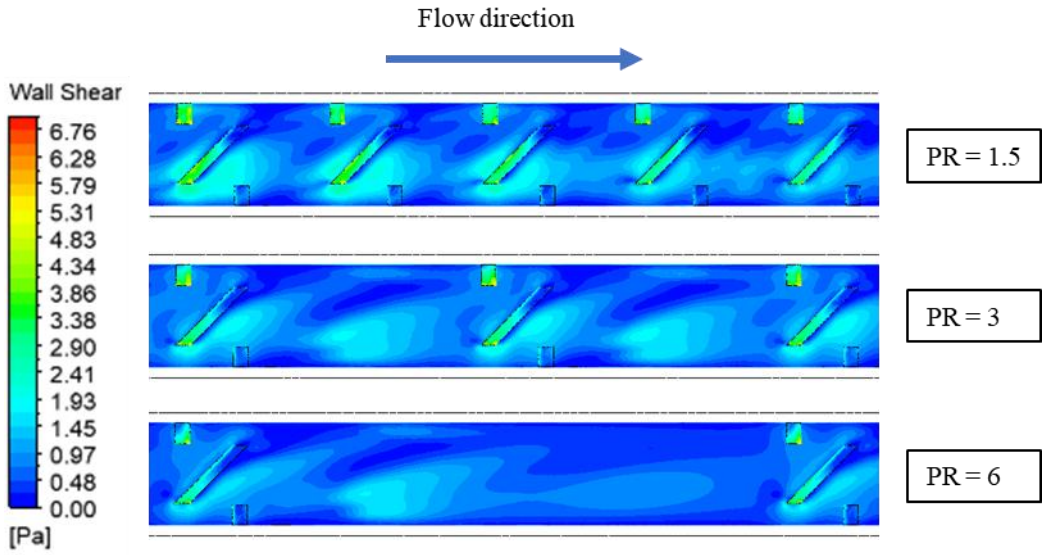

Figure 4-28: Wall Shear stress distribution along one of the walls at the midstream position for various PR at Re=1200.

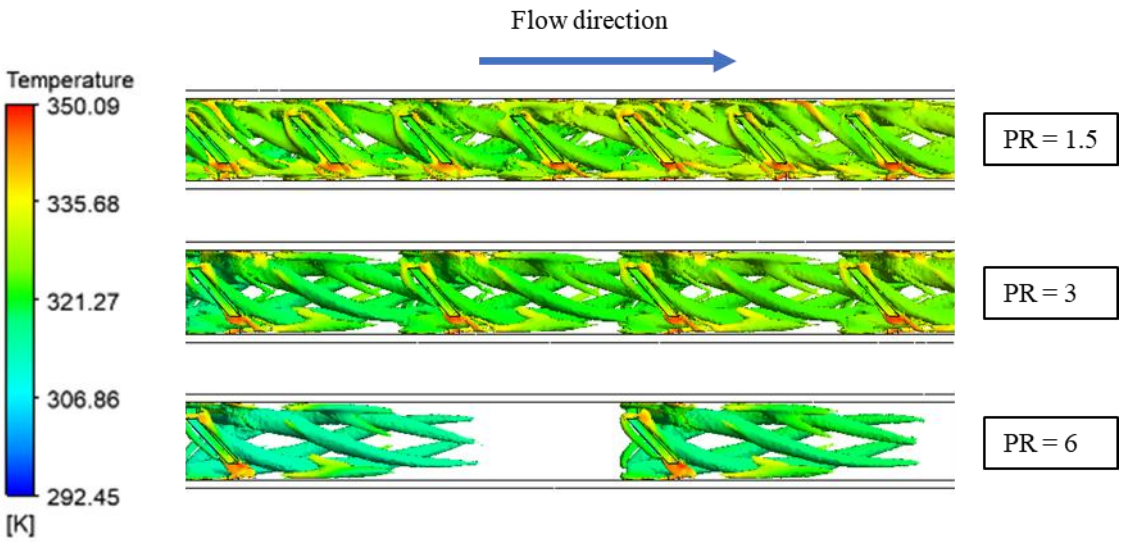

Figure 4-29: Swirl strength Iso-surface at 41 s^{-1} coloured with temperature for different pitch ratios, Re = 1200.

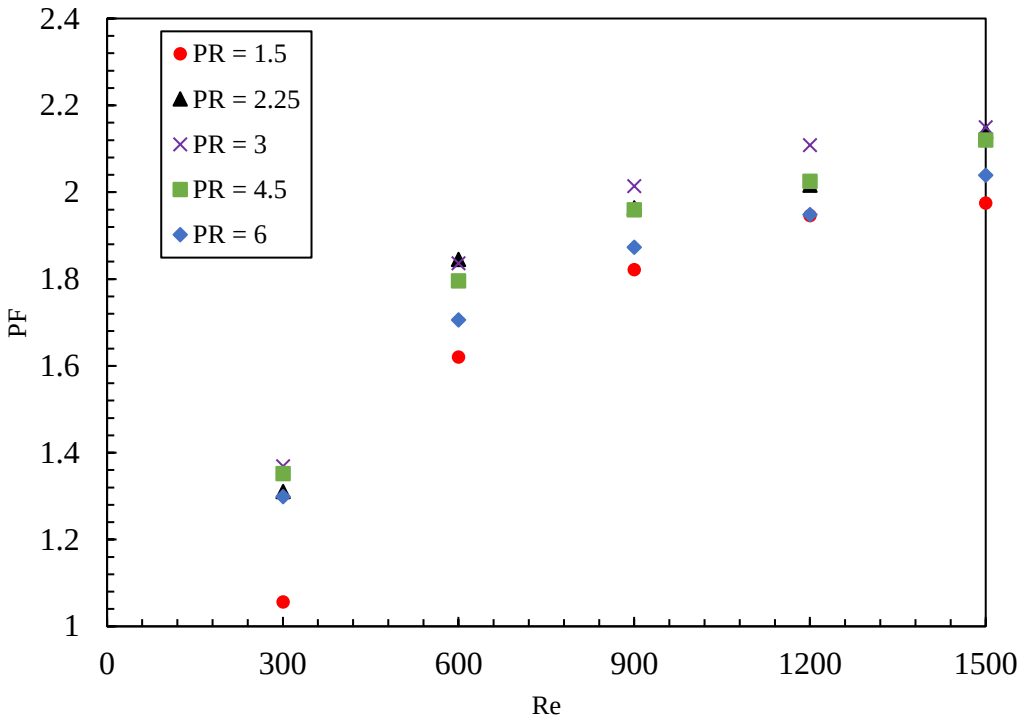

Figure 4-30: Performance factor against Reynold numbers at different fin pitch ratios.

4.4.2.3.3 Effect of fin height ratio (HR)

The variation in heat transfer rates, friction factors, and overall performance factors with different height ratios, for a streamwise pitch ratio of 3, angle of attack of 45º, and five different Reynolds numbers ranging from 300 to 1500 are shown in the figures below.

The Height Ratio (HR) is defined as the ratio of the height of the fin over the hydraulic diameter, $HR = \frac{h}{D_h}$ where h represents the actual height of the fin.

Figure 4-31 presents the variation of Nusselt number ratios with different height ratios at different Reynolds numbers. As the Reynolds number increases, the Nusselt number increases for all cases. The figure reveals that the higher HR, the higher the averaged Nusselt number becomes and that's because of the stronger swirl caused by the heigh of the fins, as shown in Figure 4-32. The vortical structure barely formed and quickly decays between the two fins in the case with the smallest height ratio (HR = 0.1). However, it is strongly formed in the case of the highest HR which impinges in the walls strongly and enhances the rate of heat transfer. As a result, the HTC increases as plotted in Figure 4-33 The highest heat transfer augmentation occurs at the higher HR (HR=0.4) at Re = 1500 and the amount of augmentation is 5.26 times higher than that of smooth case. The same trend is observed on the friction factor in Figure 4-34 and that's because of the high pressure losses found as the HR increases, as presented in Figure 4-35 and Figure 4-36. When considering the pressure drop penalty associated with the heat transfer enhancement, the performance factor of 2.15 is the highest value obtained at HR = 0.2 at Re = 1500 which means an enhancement of 115% on the overall system performance was achieved when compared to the smooth case as shown in Figure 4-27.

The results presented in this chapter are considered to be among the better ones when compared to the literature data for swirl flow, such as those mentioned in Table 2-1, though they may not be the best overall.

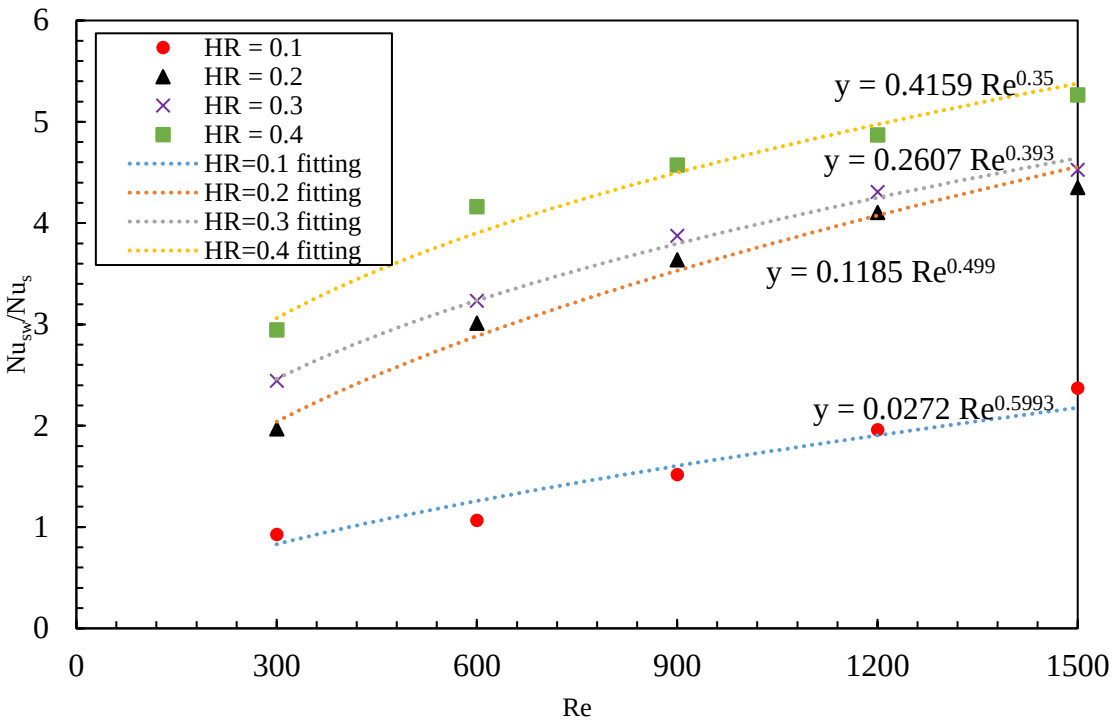

Figure 4-31: Nusselt number ratios against Reynold numbers at different fin height ratios.

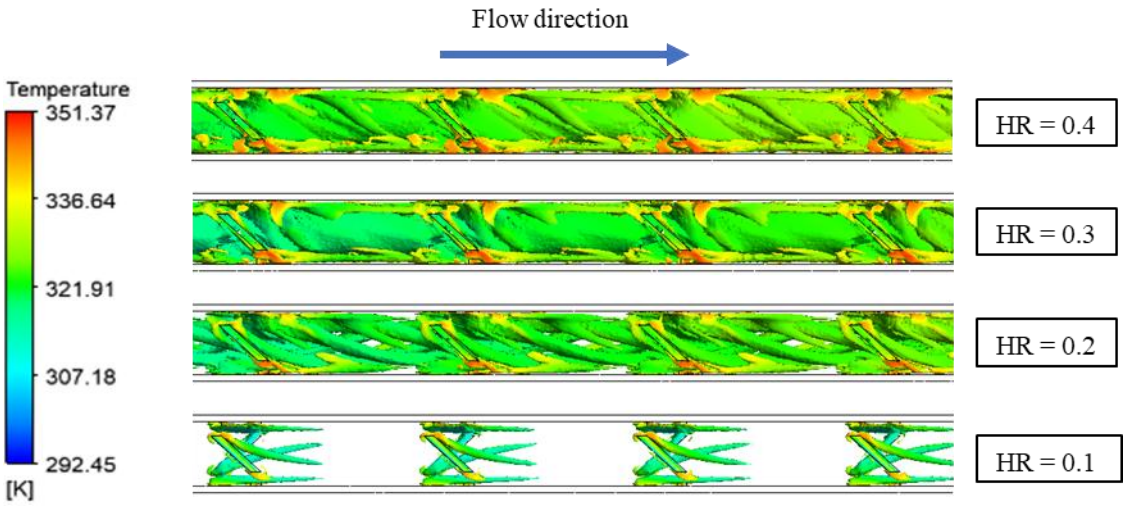

Figure 4-32: Swirl strength Iso-surface at 41 s^{-1} coloured with temperature for different height ratios, Re = 1200.

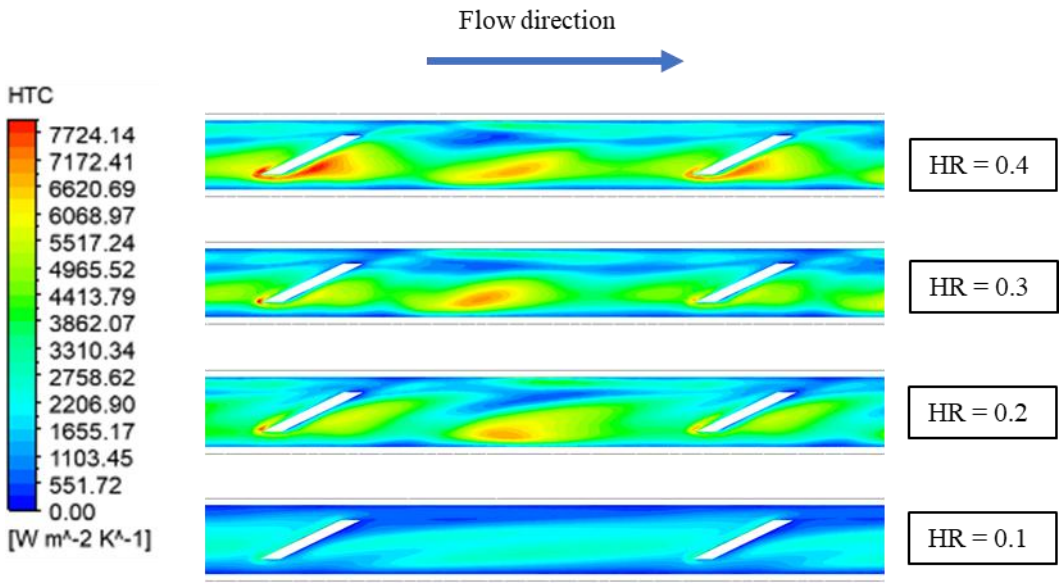

Figure 4-33: Heat Transfer Coefficient distribution along one of the walls at the midstream position for various HR at Re=1200.

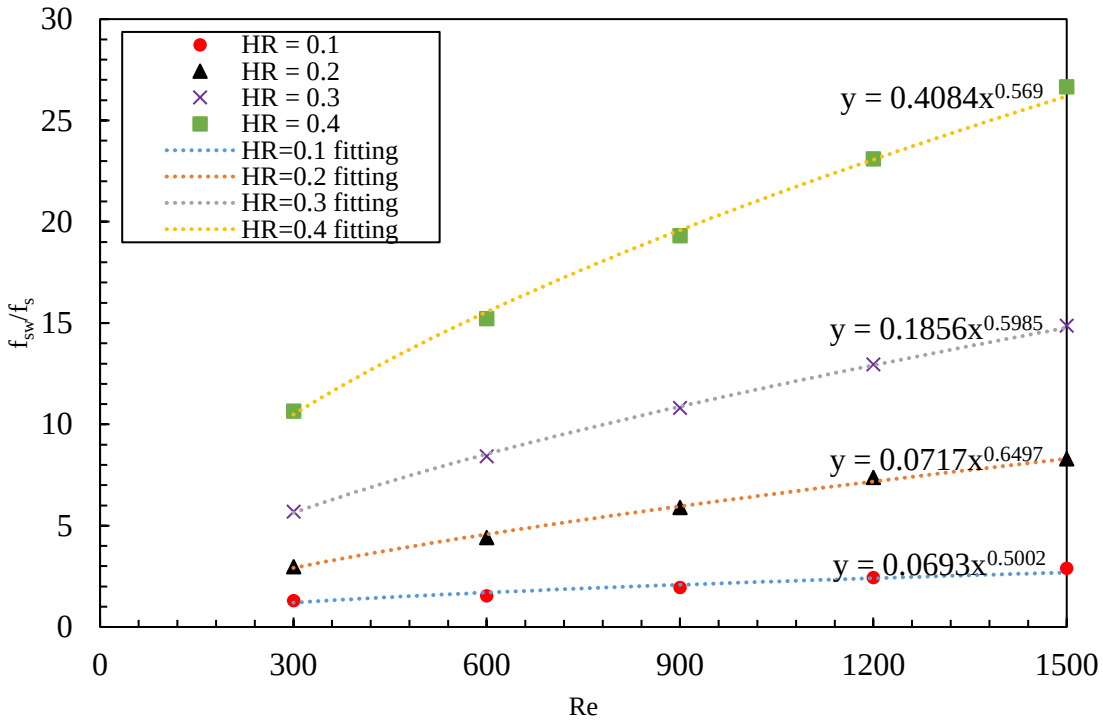

Figure 4-34: Friction factor ratios against Reynold numbers at different fin height ratios.

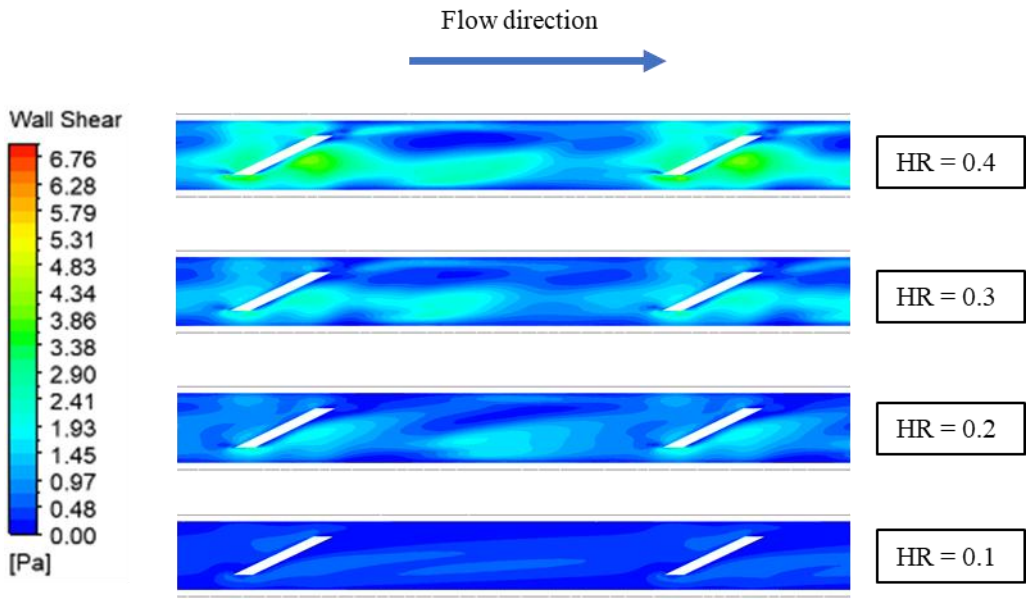

Figure 4-35: Wall Shear stress distribution along one of the walls at the midstream position for various HR at Re=1200.

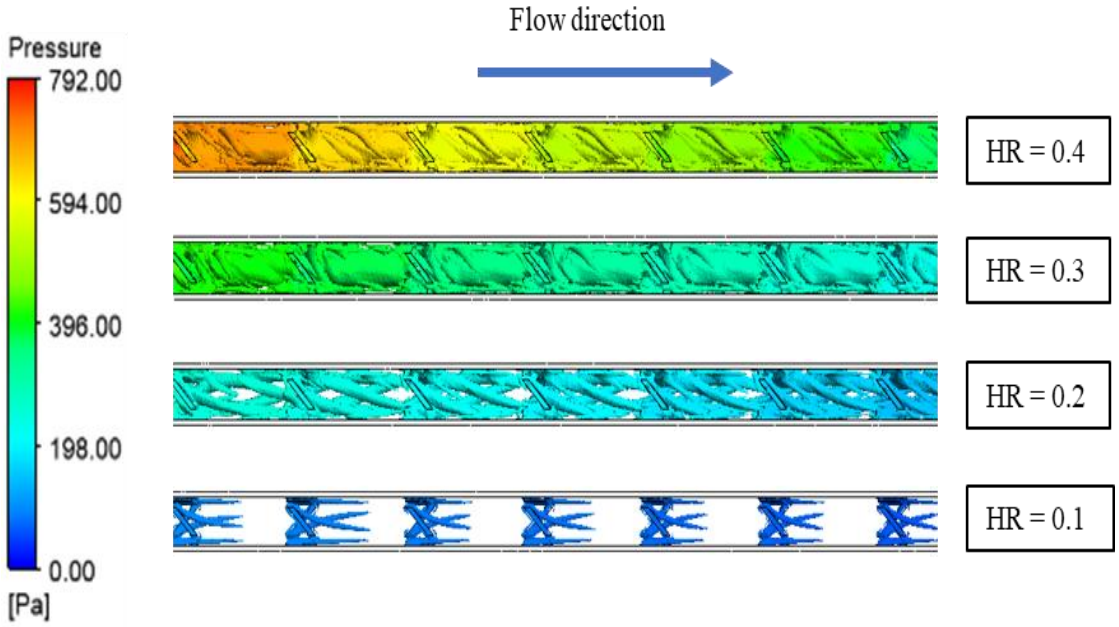

Figure 4-36: Swirl strength Iso-surface at 41 s^{-1} coloured with pressure for different height ratios, Re = 1200.

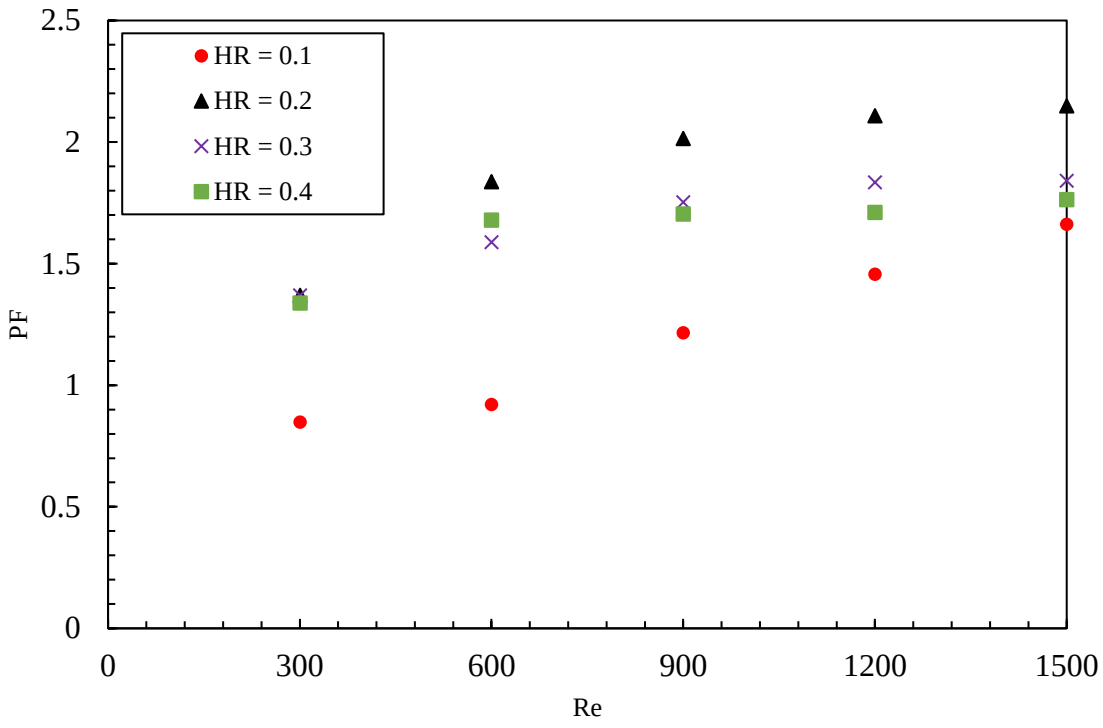

Figure 4-37: Performance factors against Reynold numbers at different fin height ratios

CHAPTER 5 INFLUENCE OF SWIRLER DESIGN ON HEAT TRANSFER AND FRICTION FACTOR CHARACTERISTICS

5.1 Introduction

In this chapter, a novel design that promotes swirl flow is proposed and studied. The following sections discuss the computational domains, grid generation and independent study, code validation, boundary conditions, and results and discussions.

5.2 Computational Domain and Grid Generation

The single-passage computational domain of the channel with swirl devices is shown in Figure 5.1. The fluid is and the solid material are water and Inconel 718. The dimensions of the channel are kept the same as the base smooth case. However, swirl devices (swirlers) are added to the channel to introduce swirl to the flow and augment the heat transfer while keeping the pressure drop as minimum as possible as shown in Figure 5.2. In order to 3-D print this device, the smallest dimension should be at least 0.4 mm. The values of the operational and geometrical parameters are represented in Table 5.1. A refinement of the grid was achieved by varying the mesh size of the domain from 8 million to 14 million cells for Re = 600, as illustrated in Figure 5.3. Table 5.2 shows the average Nusselt number and friction factor at different mesh sizes for the swirler channel. The obtained results from mesh sizes of more than 13 million were the same, therefore the results from 13 million cells can be considered as grid independent results. As shown in Figure 5.3, finer mesh near the wall region is implemented to capture the large velocity and temperature gradients and the y^+ value kept less than 1.

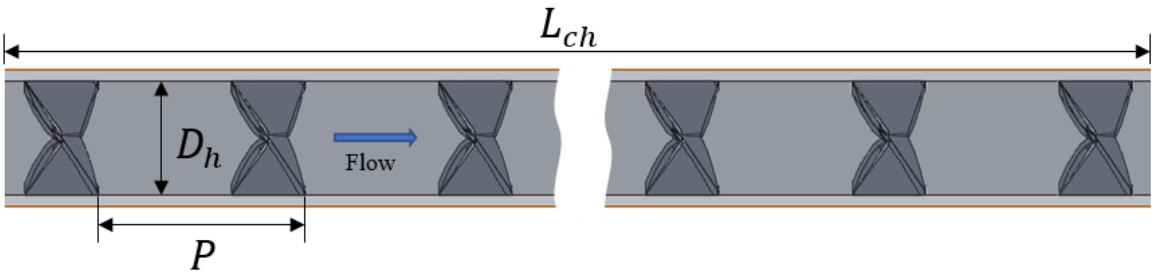

Figure 5-1 Swirler channel computational domain

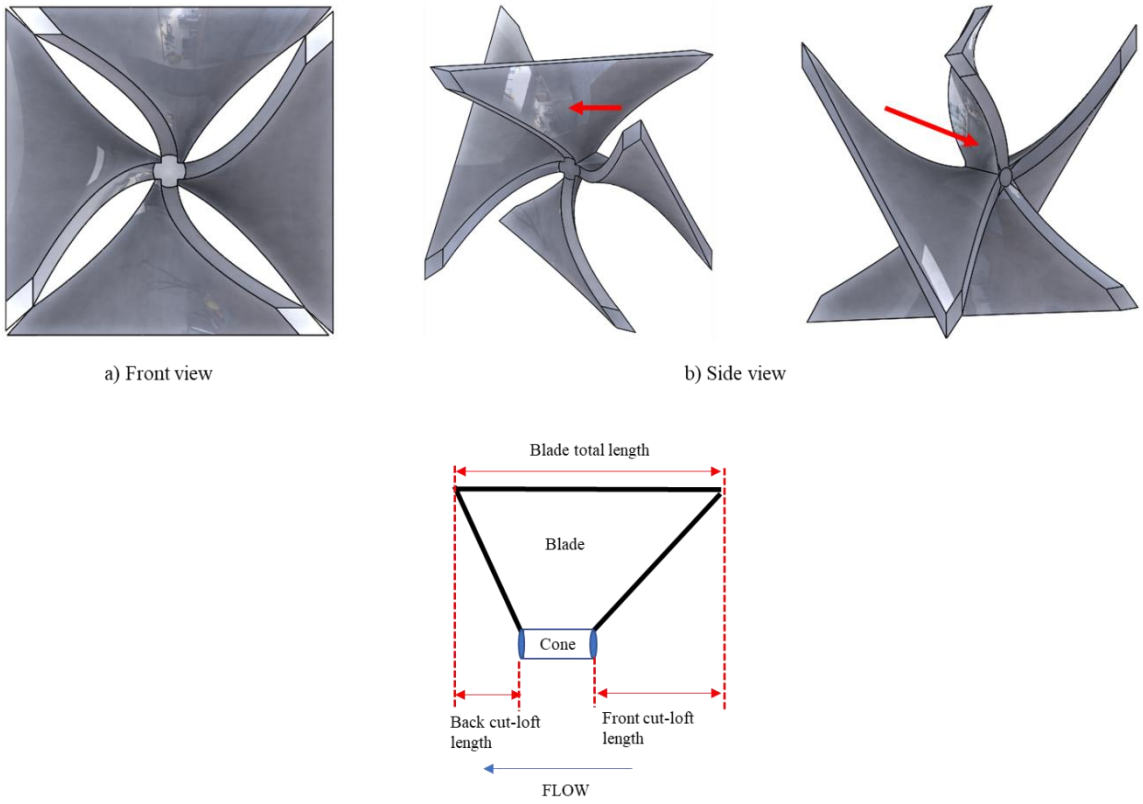

Figure 5-2 Swirler design: a) front view, b) side view, c) cut-loft illustration

Table 5-1: Values of operational and geometrical parameters

Parameter		**Value**
Mass-flow Rate		0.001-0.006 Kg/s
Constant wall temperature on external walls		353K
Reynolds number		300-1500
Swirler and channel dimensions	Swirler thickness, a	0.4 mm
	Channel width, W_{ch}	5 mm
	Channel height, H_{ch}	5 mm
	Length, L_{ch}	202.5 mm
	Pitch ratio, PR	1.5-4.5
	Swirler length	4 mm
	Loft angle, θ	45-90 deg.
	Back cut-loft length	1 mm
	Front cut-loft length	2 mm
	Cone length	1 mm
	Number of blades, N	3-5

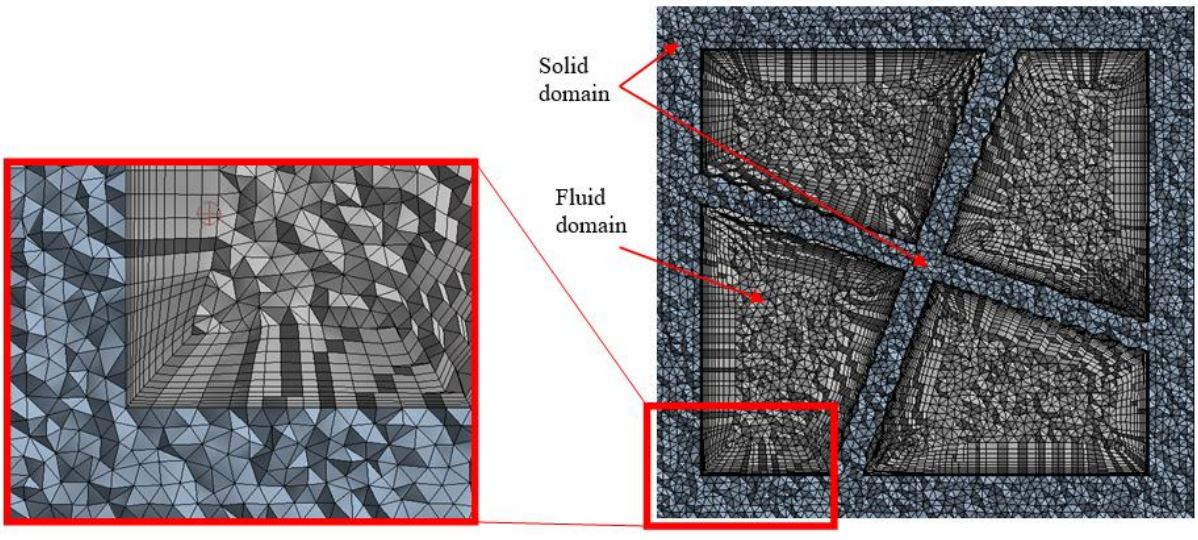

Figure 5-3 Mesh structure for the swirlers channel.

Table 5-2: Mesh independents test for swirlers channel

Mesh Sizes	Average Nusselt Number	Friction Factor
9 million	37.12	1.19
13 million	38.41	1.28
15 million	39.81	1.32
16 million	40.21	1.33

5.3 Boundary Conditions

The boundary conditions were the same for all cases. Constant wall temperature applied on the sides, top and bottom walls, to simulate one passage of the heat exchanger core (cold cell) of which is in contact with four adjacent hot cells. All numerical simulations run through two stages in order to ensure that the flow is hydrodynamically fully developed at the inlet of the test section. In the first stage, a simulation of the adiabatic smooth channel with a constant mass-flow rate is conducted. The length of this section is varied according to the mass flow rate at the inlet. In stage two, velocity profile at the outlet of the channel from stage one was extracted and applied on the inlet of the test section while constant wall temperature is applied on the four walls of the channel as seen in Figure 5.4. In this case the thermal boundary layer is developing while the flow is hydrodynamically fully developed.

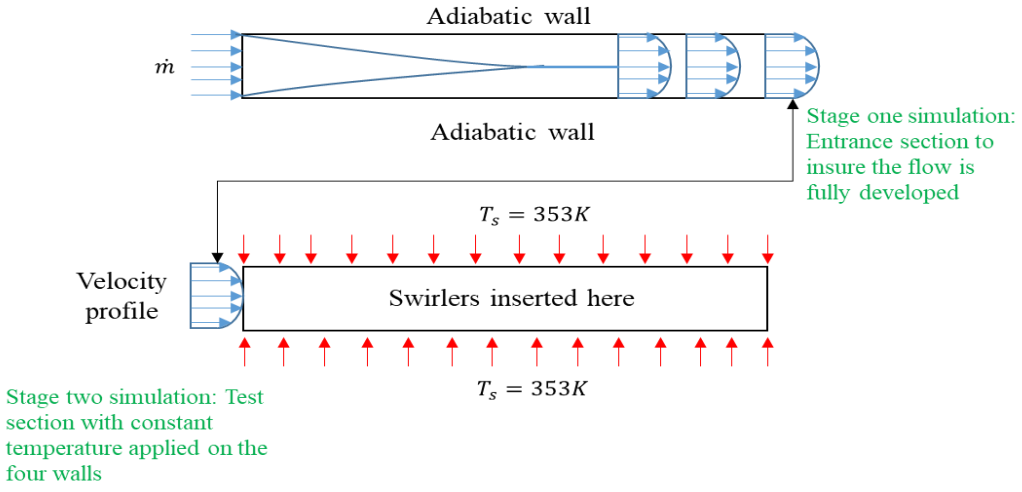

Figure 5-4: Simulation stages

The specified boundary conditions on the test section were as follows:

1. Channel inlet at z = 0

$velocity\ profile$ from stage one

2. Channel outlet at z = 202.5mm

$P_f = P_{out} = 1\ atm$

For fluid $-K_s\left(\frac{\partial T_f}{\partial x}\right) = 0$

For solid $-K_s\left(\frac{\partial T_s}{\partial x}\right) = 0$

3. Walls from all sides

$T_s = 353\ K$

4. Inner walls of channel (fluid/solid surface)

$u = v = w = 0$

$$-K_s\left(\frac{\partial T_s}{\partial n}\right) = -K_f\left(\frac{\partial T_f}{\partial n}\right)$$

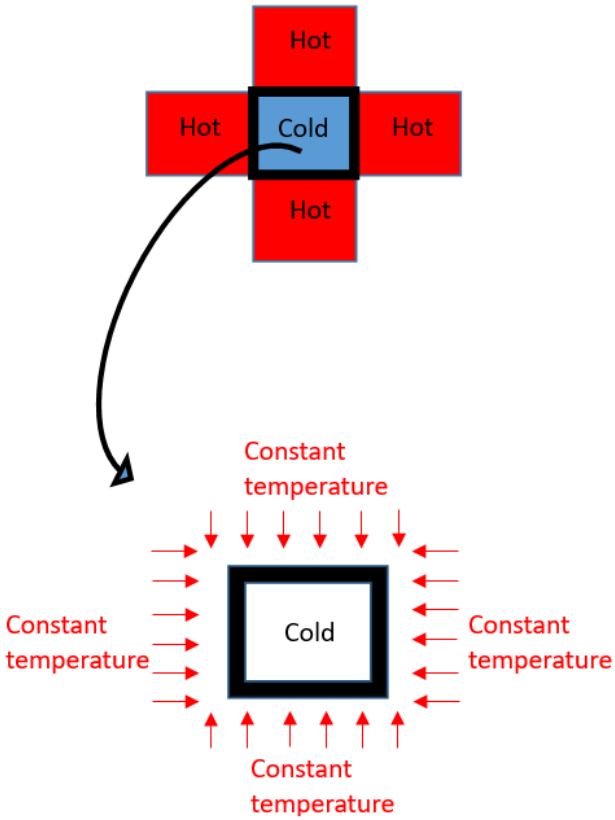

5.4 Results and Discussions

A single passage of the heat exchanger core for both the smooth and the swirl channel is tested. The flow field and the heat transfer characteristics of the smooth square channel as well as the swirler channel are investigated. To design the core heat exchanger with the arrangement explained earlier in this chapter, a channel with a square cross-section has been chosen due to its optimal shape for being heated from all sides. Yet, the stagnation areas which form in the four corners of the square cross-section of the smooth channel are associated with low convection heat transfer. One of the techniques to breaks these stagnation areas is by introducing swirl flow to the channel to enhance the mixing between the high temperature region near the wall and the low temperature region in the central part of the channel.

Since the smooth base case has been validated with the experimental and numerical codes, the following section will discuss the effect of the novel swirl devices, which has the following

parameters, N = 4, PR = 3 and θ = 90 degree, on the flow field and heat transfer of the system and its influence on both the flow field and the heat transfer characteristics when compared to the smooth case. The range of Reynolds numbers investigated in this study is from 300 to 1500.

5.4.1 Flow field

The design of the swirlers has been utilized to introduce swirl to the flow and increase the flow path as well as the surface heat transfer area along the channel as shown in Figure 5.1 and 5.2. The friction factor at different Reynolds numbers for both the smooth and the swirlers channel is shown in Figure 5.5. The numerical result of the smooth channel is in a close agreement with the correlation found in [23]. The friction factor results of the swirlers channel shows a similar trend to the smooth channel but at higher pressure drop and this is attributed to the presence of the swirlers.

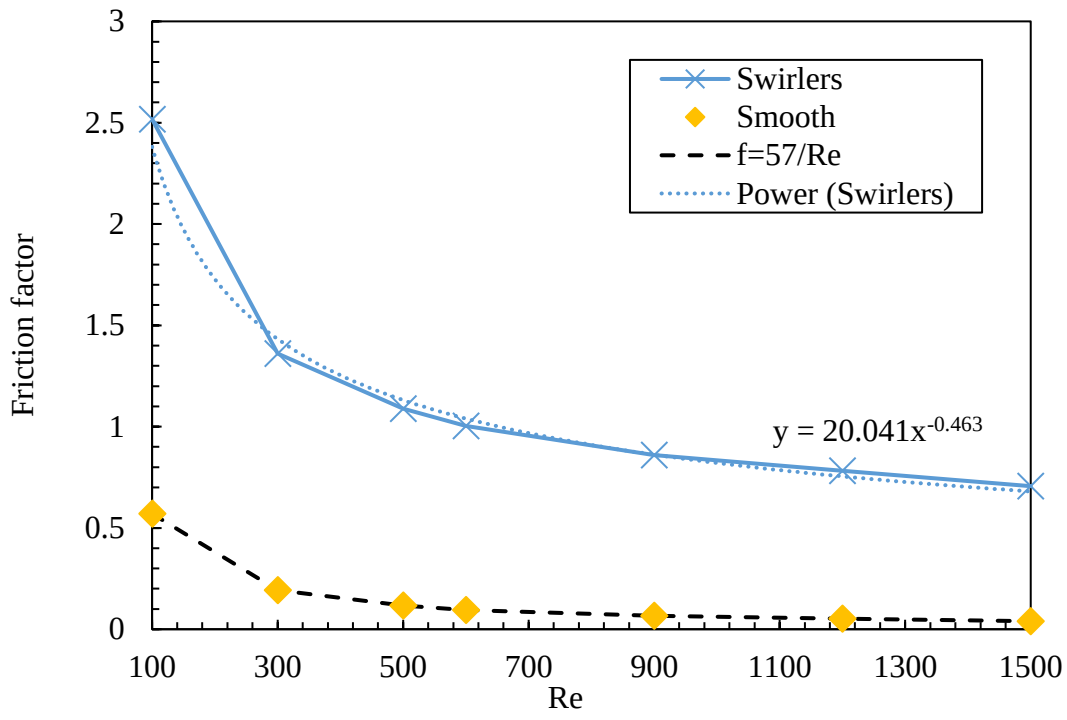

Figure 5-5: Friction factor at different Reynolds numbers for both the smooth and the swirlers channels.

An evaluation of the hydrodynamic entrance length for the swirl cases has been carried out and compared against the smooth for the laminar regime, $\frac{Z}{D} = 0.05Re$ [23], where $\frac{Z}{D}$ represents the non-dimensional streamwise location. Velocity profiles at different streamwise locations is plotted along the y-direction at Re = 300, 600, 900, 1200 and 1500 is shown on Figure 5.6, Figure 5.7, Figure 5.8, Figure 5.9 and Figure 5.10, respectively. A green dashed line is plotted to mark the thickness of the velocity boundary layer as Reynolds number increases from Re=300 to Re=1500. The velocity profile in these figures highlights the significant impact of the swirler design on the flow near the corners of the square channel compared to the smooth case (Z/D = 0). In the smooth channel, the velocity near the corners is minimal, indicating stagnant or slow-moving flow, which is typical due to the lack of turbulence in these regions. In contrast, the presence of swirlers (Z/D > 0) increases the velocity near the corners, as the swirling motion promotes enhanced mixing and momentum transfer across the channel cross-section. At higher Z/D values (e.g., Z/D = 20 and Z/D = 38), the effect of the swirler becomes more pronounced, with improved velocity distribution extending into the corners. This redistribution of the velocity field reduces stagnant zones, improves flow uniformity, and ensures better utilization of the entire cross-sectional area of the channel.

Furthermore, it can be noticed that as the inertial forces dominates, the thickness of the boundary layer decreases and gets flatter. Moreover, as the velocity increases the development length slightly increases. Therefore, the development length of the flow in the case of swirlers channel can be deduced from the figures as $5 \leq \frac{Z}{D} \leq 11$. By using the swirlers, the flow attains the full development at a shorter length when compared to the smooth channel which reaches the fully developed region when $15 \leq \frac{Z}{D} \leq 75$ at $300 \leq Re \leq 1500$. It is expected to see this great difference in the flow development length between the smooth and the swirlers channel and this can be attributed to the presence of the secondary flow which reduced the entrance length [23].

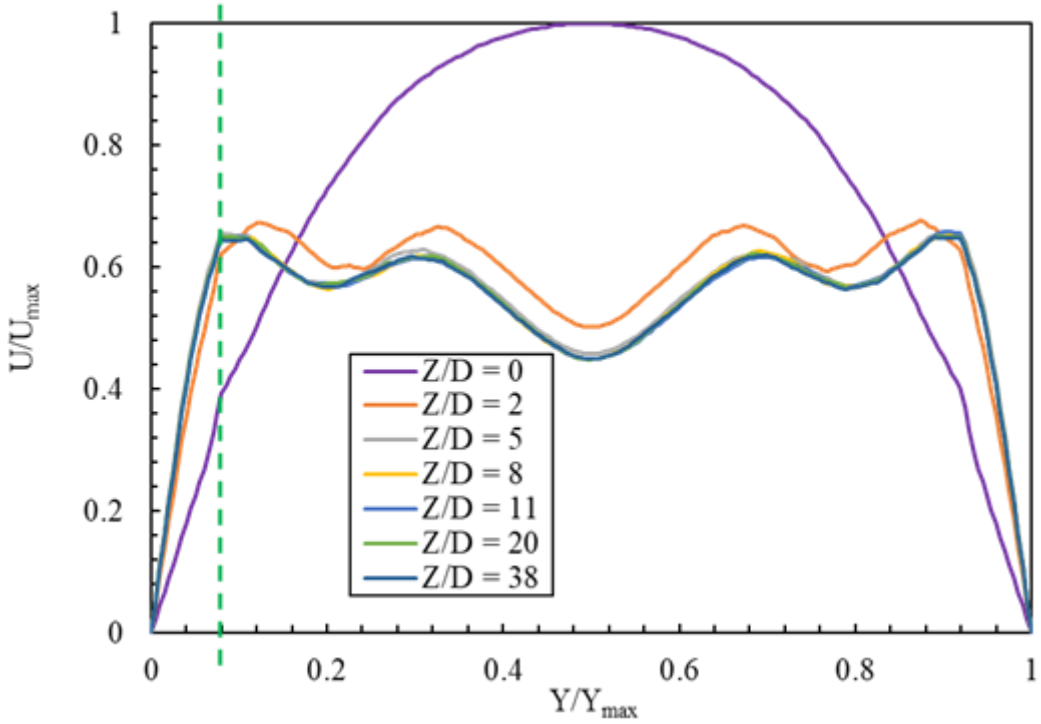

Figure 5-6 Velocity profile along the streamwise direction at Re=300.

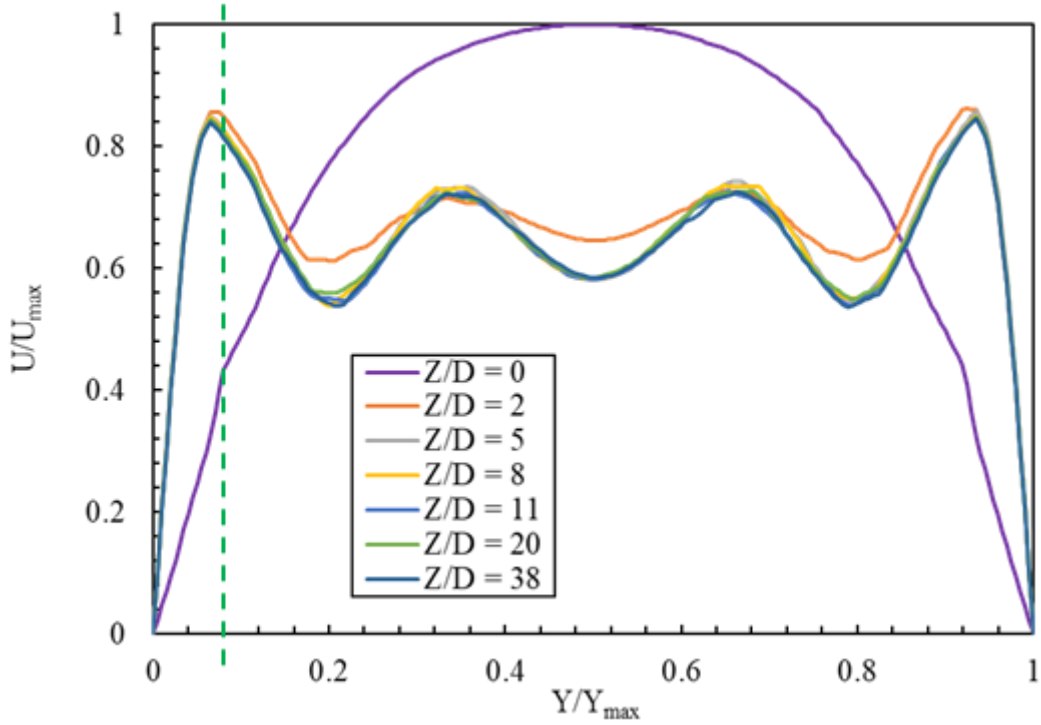

Figure 5-7 Velocity profile along the streamwise direction at Re=600.

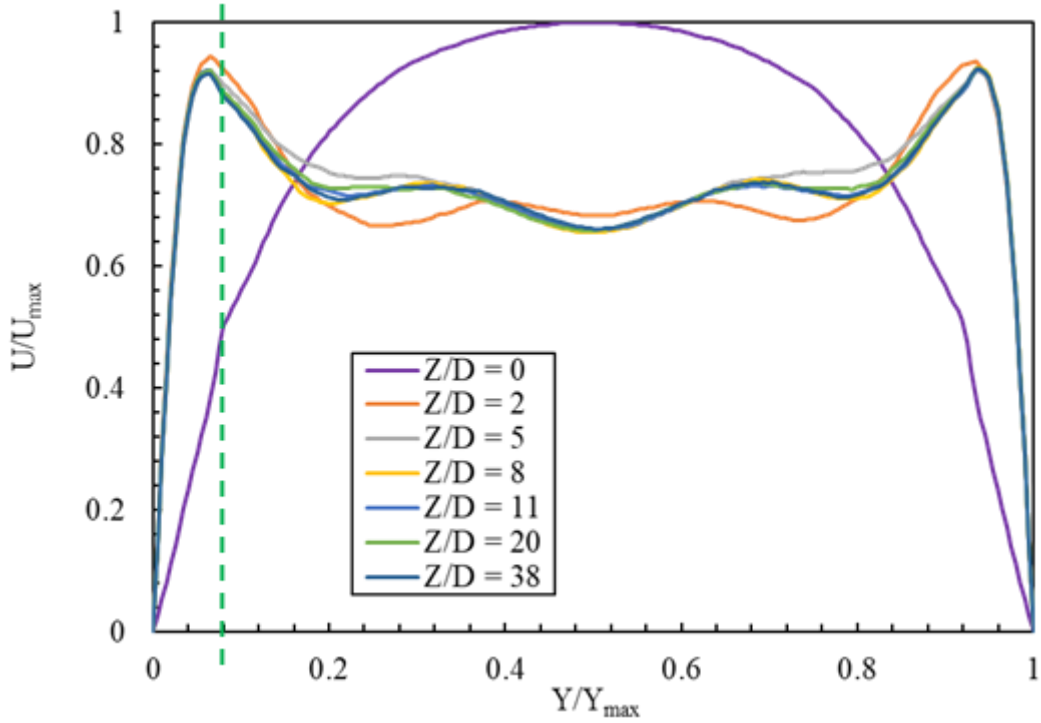

Figure 5-8 Velocity profile along the streamwise direction at Re=900.

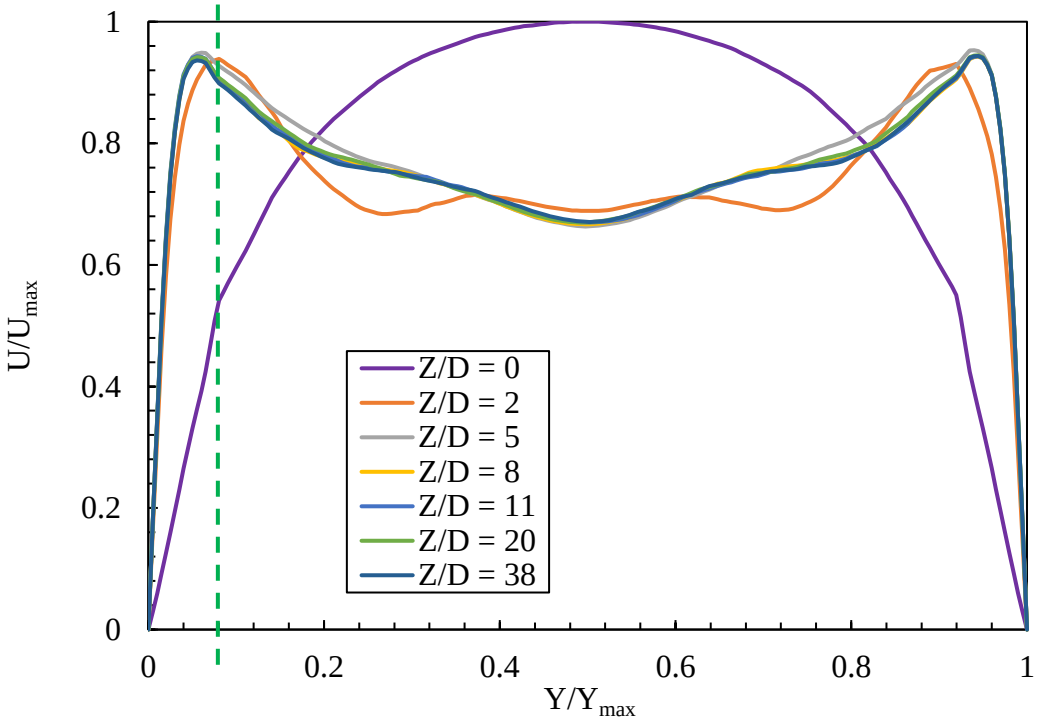

Figure 5-9: Velocity profile along the streamwise direction at Re=1200.

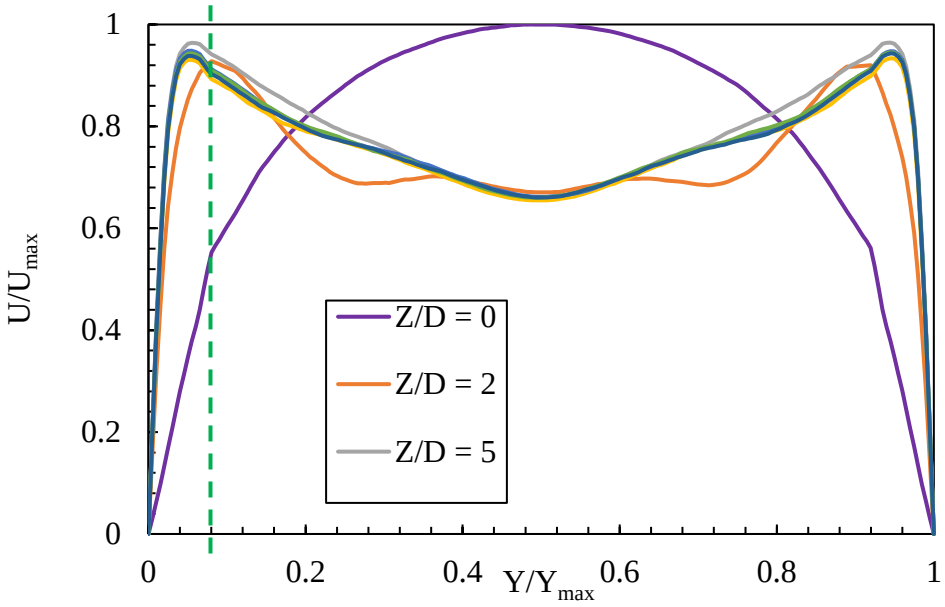

Figure 5-10: Velocity profile along the streamwise direction at Re=1200.

The local friction factor is calculated by dividing the flow domain into discrete planes along the streamwise direction, using the inlet plane as a reference. At each streamwise location, the average velocity is computed over the cross-sectional area of the plane. The pressure drop is calculated as the difference in pressure between the inlet plane and the downstream plane at the current location. The local friction factor variation with several different Reynolds number is shown in Figure 5.11. This plot gives further evidence for the attainment of the fully developed flow condition for the case of the swirlers channel. The repeated pattern of the local friction factor after $\frac{Z}{D} = 11$ is constant for the range of Re = 300 to 1500.

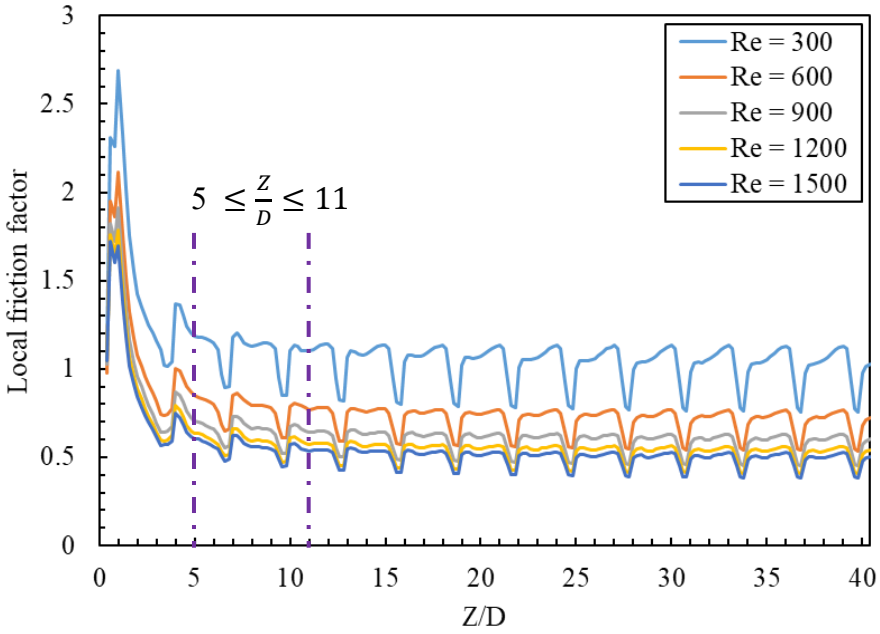

Figure 5-11: Local friction factor along the streamwise direction at different Reynolds numbers.

A similar trend is found in the local averaged velocity along the streamwise direction in Figure 5.12. The highest velocity found to be in the middle of the swirlers and this can be seen at all the different Reynolds numbers. The difference between the highest and the lowest velocities raises as the Reynolds number increase from 300 to 1500. The local wall shear stress along the channel is also show in Figure 5.13. The high velocity gradient in the middle of the swirlers gives the rise to the wall shear stress every time it passes through the swirlers. The conclusion which was drawn for the local velocity can be applied in the local wall shear stress as well since they are linked to each other.

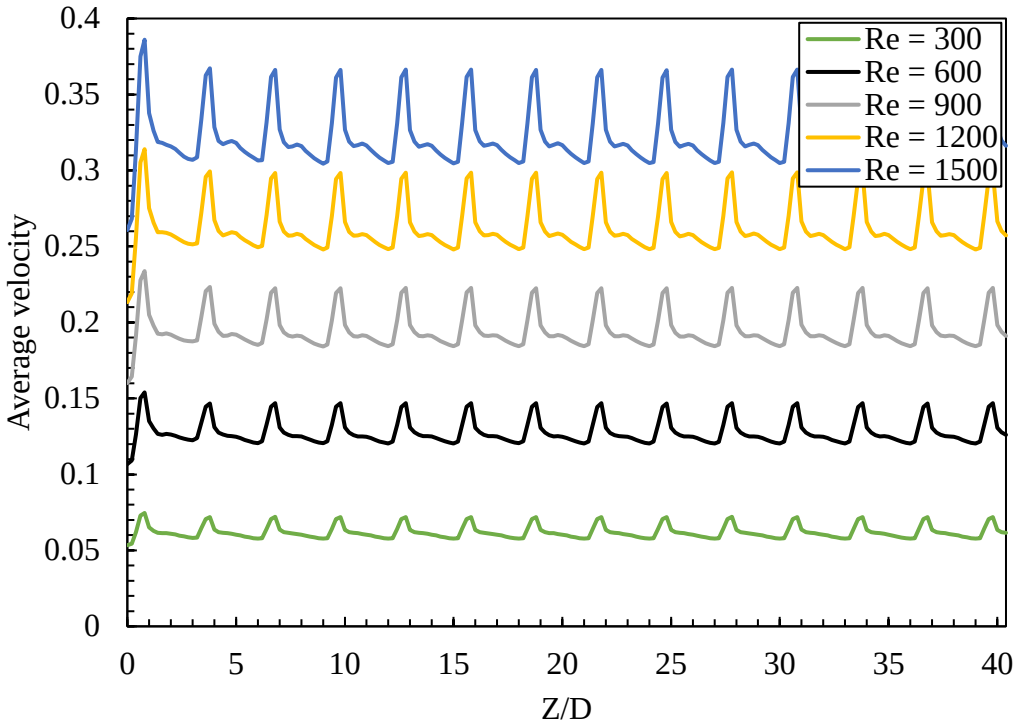

Figure 5-12: Local friction factor along the streamwise direction at different Reynolds numbers.

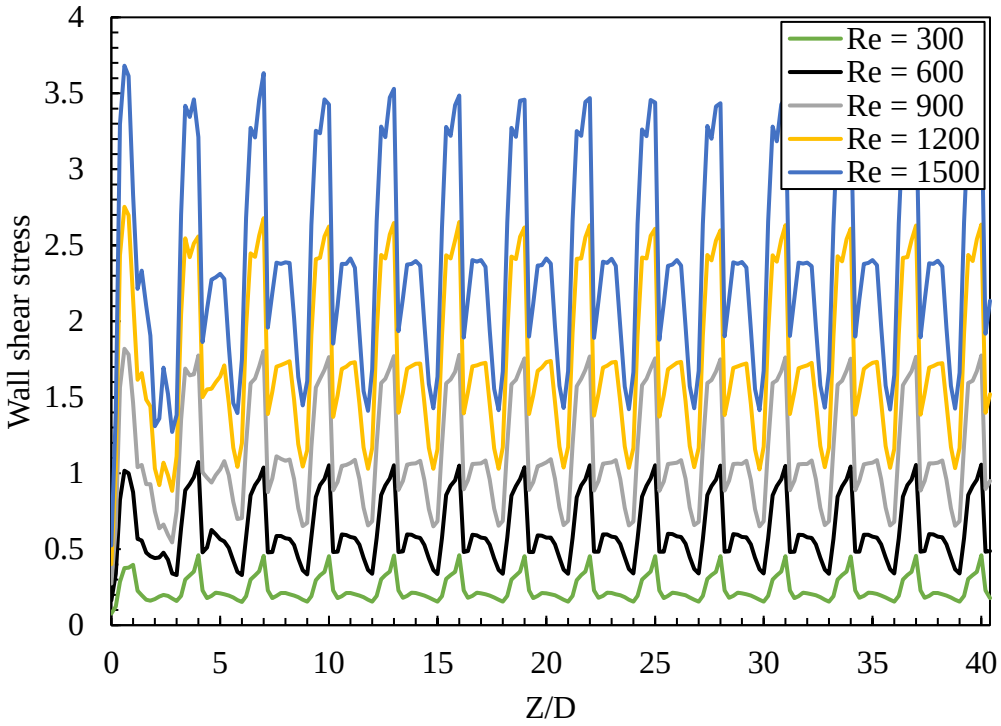

Figure 5-13: Local wall shear stress along the streamwise direction at different Reynolds numbers.

To investigate the influence of the swirl flow introduced by the swirler devices, a close look at the last two swirlers downstream of the channel before the outlet as shown in Figure 5.14 has

been conducted. The next three figures 5.15, 5.16 and 5.17 will illustrate the variation of local friction factor, velocity and wall shear stress, respectively, downstream of the channel from Z/D = 34 to the outlet of the test section.

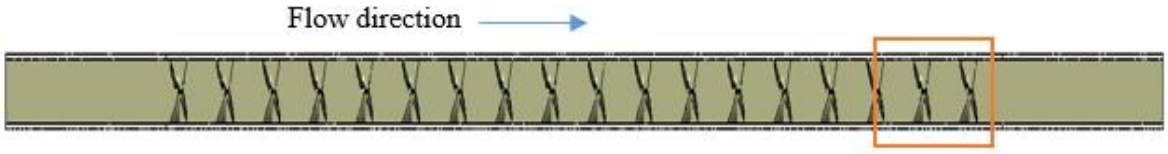

Figure 5-14 Location where the close look analysis took place from Z/D=34 to the outlet of the test section

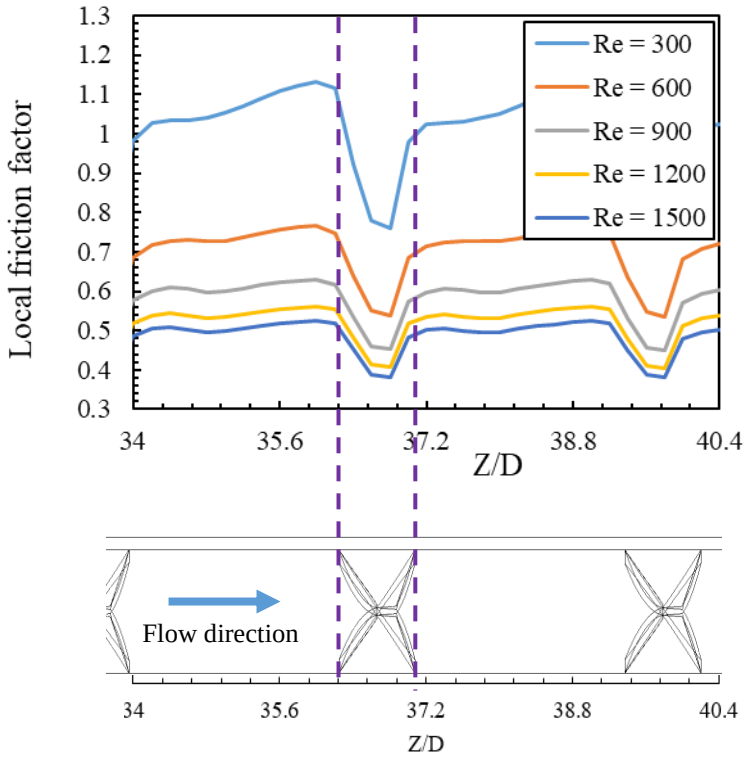

Figure 5-15: Local friction factor variation from Z/D=34 to the outlet of the test section

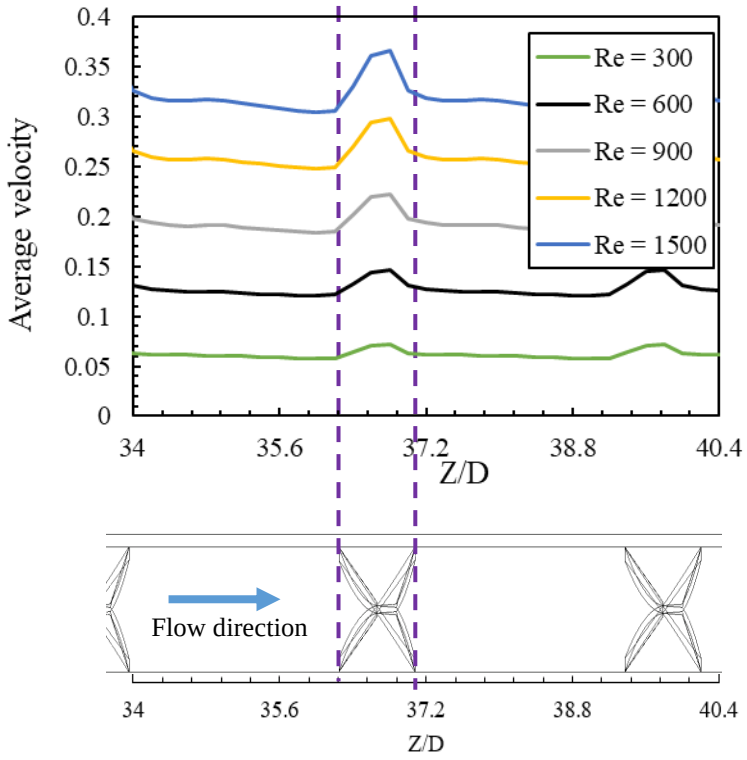

Figure 5-16: Local averaged velocity variation from Z/D=34 to the outlet of the test section

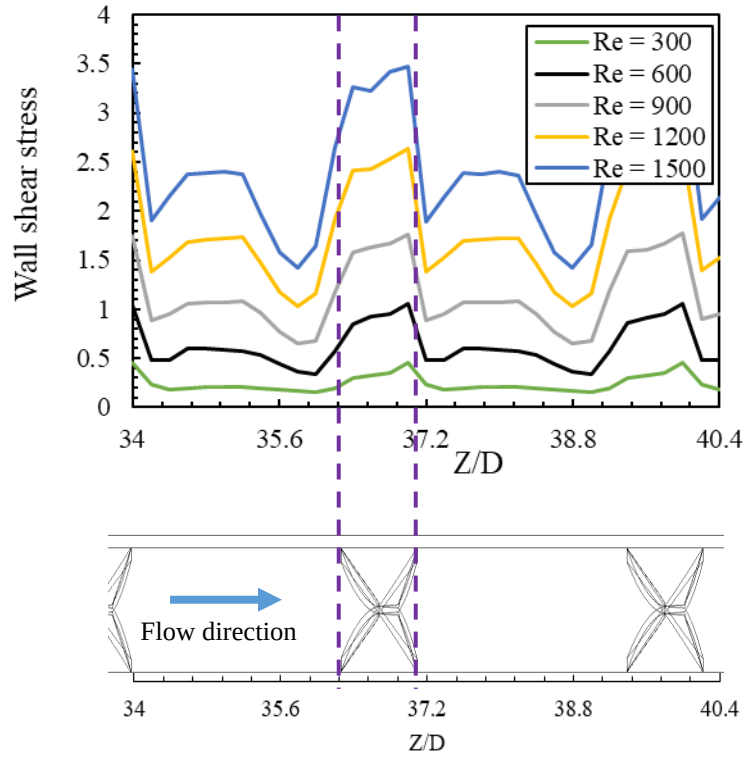

Figure 5-17: Local wall shear stress variation from Z/D=34 to the outlet of the test section.

The local friction factor represented in Figure 5.15 reveals that as the velocity increases inside the swirlers, the friction factor drops to its smallest value. Since the velocity of the flow starts to decline as the flow leaves the swirler as shown in Figure 5.16, the local friction factor starts to rise up gradually before it drops again when the flow reaches the subsequent swirler. This is also noticeable in the local wall shear stress plot in Figure 5.17 where similar trend is observed inside the swirler. The velocity gradient is at its highest value inside the swirler.

To examine the development of the hydrodynamic boundary layer for both cases, velocity and contours have been taken at four different cross-sectional planes along the streamwise direction. The four different locations are Z/D = 2, 19, 30 and 40 as shown in Figure 5.18.

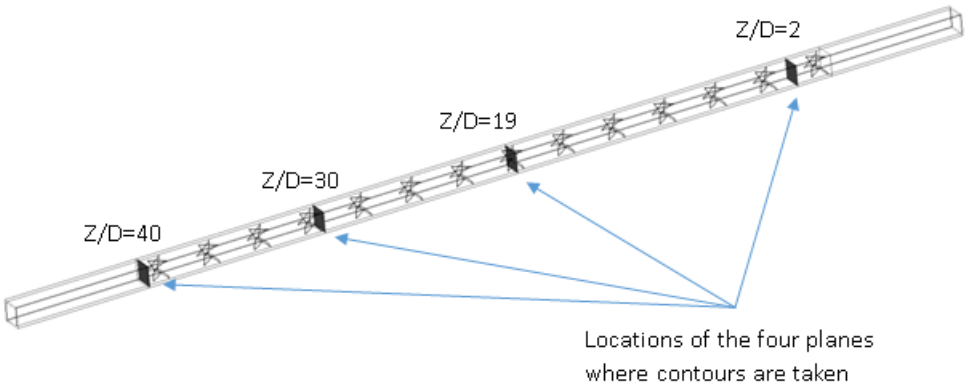

Figure 5-18 Locations of the four planes from the inlet on the streamwise direction.

Figure 5.19 demonstrates the velocity contours at different locations on the streamwise direction. At the inlet of the test section, the fully developed velocity profile is coming from the smooth entrance section. The velocity boundary layer interrupts when it passes through the first swirler, and it becomes again fully developed at Z/D = 5 to 11 depending on the value of Reynolds number.

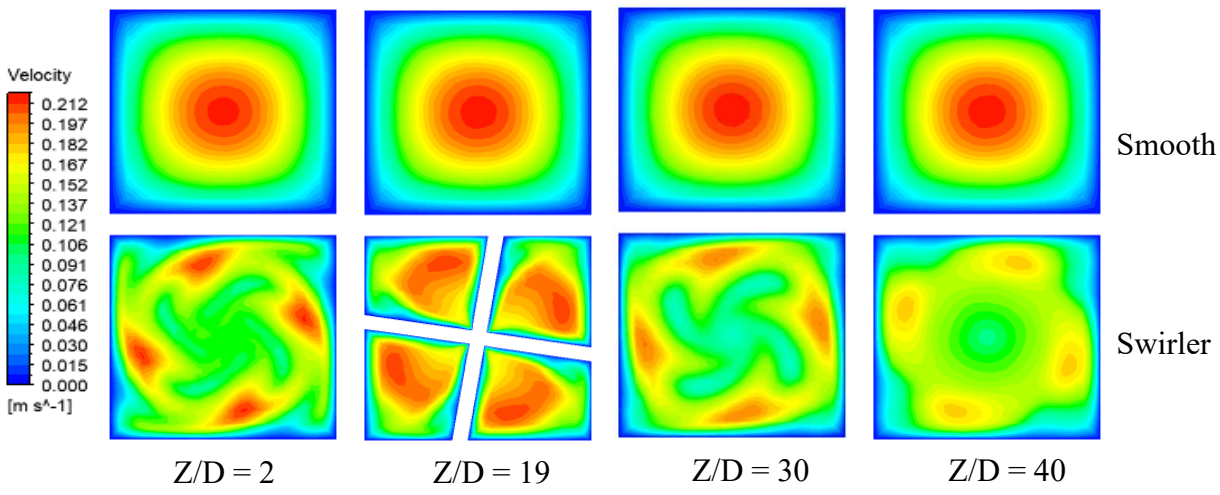

Figure 5-19: Velocity contours at different locations on the streamwise direction of the smooth and the swirler channel (Re=600, theta=65deg., PR=2.25, N=4)

It can be clearly seen that, the thick boundary layer in the smooth case causes the high velocity in the central region. On the other hand, the use of swirlers introduces a decaying swirl to the flow which disperse the flow towards the corner stagnation regions. Therefore, it washes away the growth of the boundary layer and mixes the near wall flow with the central region flow. Figure 5.20 represents the velocity contours and vectors between two consecutive swirlers at Z/D = 27.5, 28.5, 29.2 and 30. The swirlers intensifies the decaying swirl and washes away the boundary layer. As the flow leaves the swirler, vortices are formed in the four corners regions. The growth of these vortices gradually increases and signify the flow mixing between the flow particles near the wall and the central region. As a result of the presence of the vortex, the swirl flow departs from the wall to form a secondary flow.

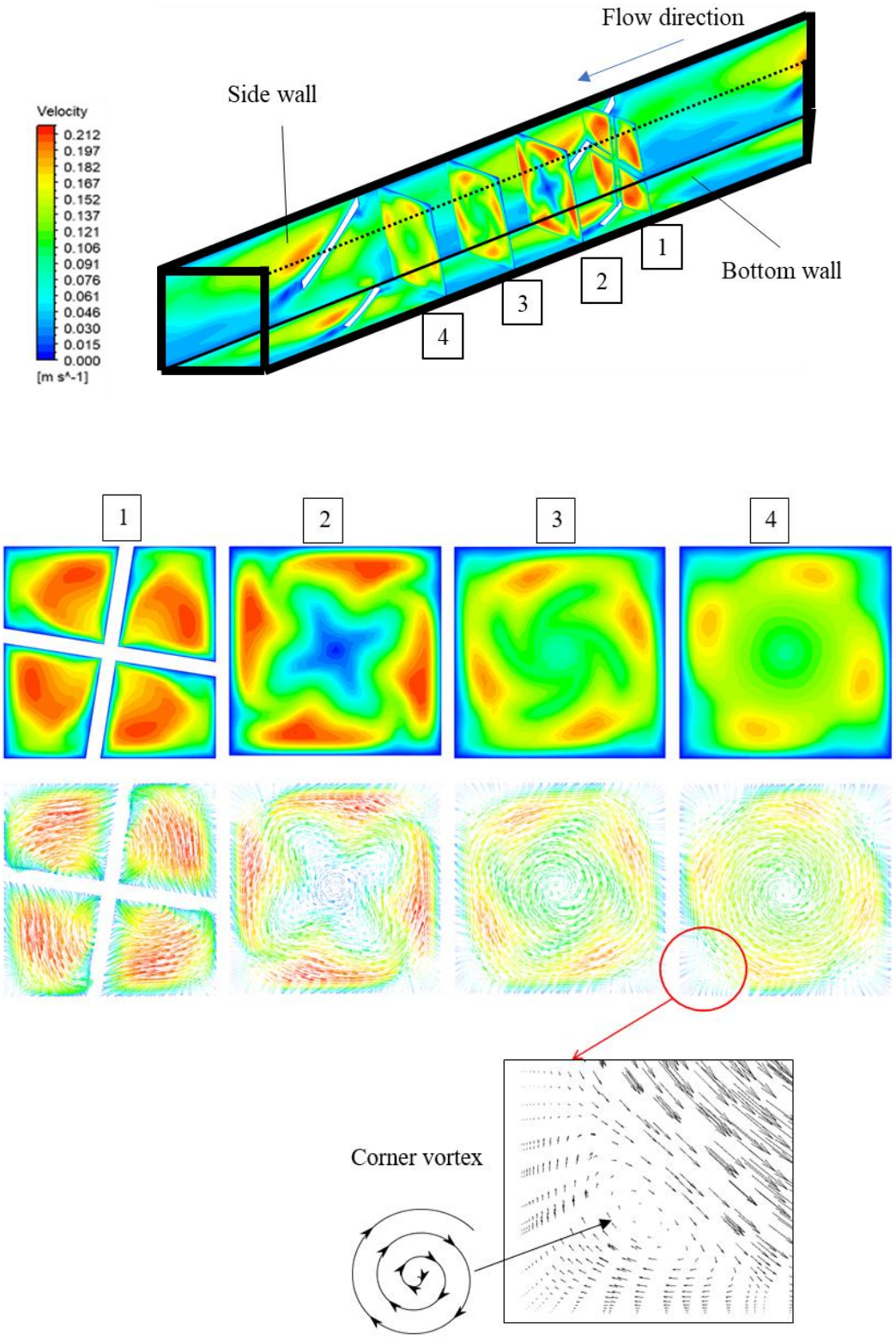

Figure 5-20 Velocity contours between two consecutive swirlers. The location is in the mid-channel when the flow is fully developed.

5.4.2 Heat transfer

The Nusselt number at different Reynolds numbers for both the smooth and the swirlers channel is shown in Figure 5.21. The numerical results of the smooth channel is in a close agreement with the correlation found in [23]. The heat transfer rate increases as the Reynolds increases. The increase in Nusselt number is much higher in the case of the swirler channel due to the influence of the swirler devices.

The impact of placing swirlers along the channel on the local Nusselt number at Reynolds number = 1500 is plotted in Figure 5.22. The highest local heat transfer coefficient can be found near the inlet of the test section due to the strong swirl caused by the first swirler which will decay as the thermal boundary layer develops. The local heat transfer coefficient reaches the fully developed pattern at the streamwise location of seven times the hydraulic diameter (Z/D = 7). Moreover, Figure 5.23 demonstrates the local Nusselt number at different Reynolds numbers for the swirlers channel only. To investigate the influence of the swirl flow introduced by the swirler devices, a close look at the last two swirlers downstream of the channel before the outlet as shown in Figure 5.24 has been conducted. Figure 5.24 illustrates the variation of local Nusselt number, downstream of the channel from Z/D = 34 to the outlet of the test section.

It can be observed that the Nusselt number value increases gradually from Z/D = 34.2 to its highest value in the smooth region at Z/D = 35.2 before it drops to its lowest value at Z/D = 35.8. The Nusselt value increases again from Z/D = 35.8 to its peak value at Z/D = 36.6 and then declines back till it leaves the swirler. To investigate this further, a closer look at the flow streamlines from Z/D = 34 to Z/D = 37, which covers a complete smooth region and one full swirler length, is conducted as seen in Figure 5.25. The vortices in the four corners of the channel starts to form as the flow leave the swirler. This can be seen clearly at Z/D = 34 and 34.2. These vortices grow gradually from the exit of the swirler to Z/D = 35.2. This distant associated with gradual increase the heat transfer as depicted in Figure 5.24. This increase can

be attributed to the growth of theses vortices as well as the increase in its strength which enhances the mixing of the flow molecules near the wall with the molecules in the central region. The strength of these vortices weaken as the flow goes from Z/D = 35.2 to 35.8 where the lowest Nusselt number is encountered. This drop of the heat transfer is attributed to two reasons: the first is that the vortices are decaying and weakening and the second reason is that the boundary layer starts to grow as the swirl decays. From Z/D = 35.8, the secondary flow returns back to its original strength before it enters the swirler where the peak value of Nusselt number is found in the middle of the device. As the swirl decays after it leaves the swirler, the value of the local heat transfer coefficient will drop again. Both the structure and the strength of these secondary flows are changing as moving along the smooth region till it almost disappear in the swirler.

Every time the flow passes through the swirler, it produces a strong decaying swirl which enhances the heat transfer. This enhancement is attributed to the effect of the swirl flow in disturbing the thermal boundary layer generated on the wall especially near the stagnation regions. Therefore, the enhancement of heat transfer was about 5.5 times that of the smooth case at Re = 1200. However, this enhancement is associated with a higher pressure drop penalty when compared to the smooth case. The increase of the friction factor is about 15 times that of the smooth case. The overall performance factor (PF), which evaluates the enhancement of heat transfer of the system while considering the pressure drop penalty associated with placing such devices at the same pumping power, is used. The overall performance factor of the swirlers channel increases by about 2.25 from that of the smooth channel.

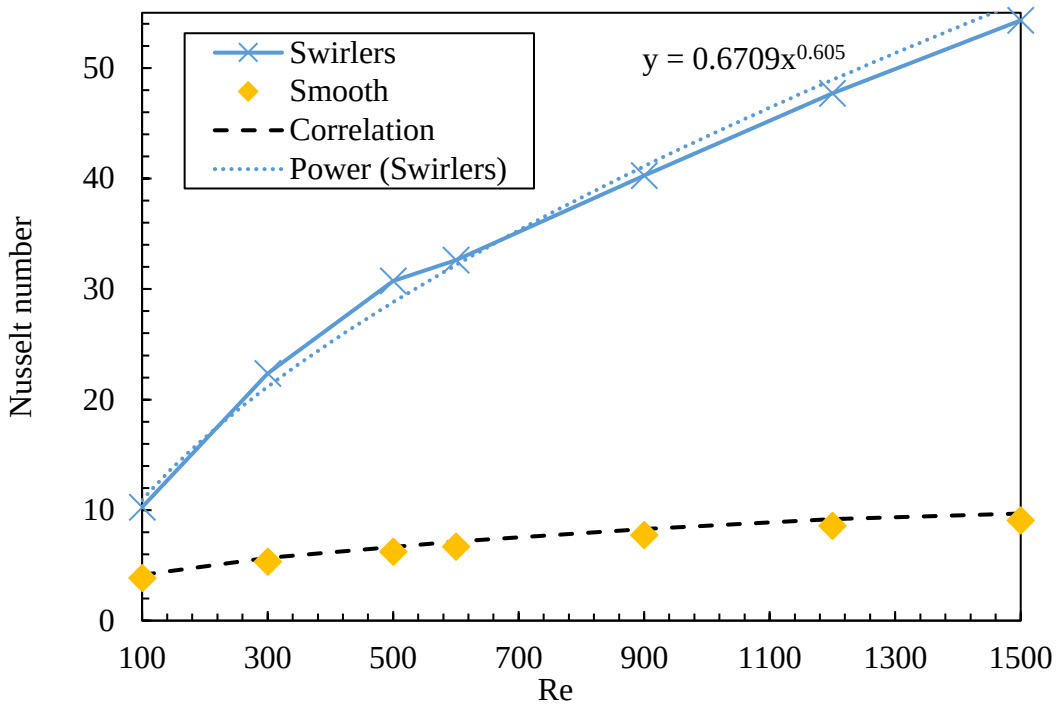

Figure 5-21 Nusselt number at different Reynolds numbers for both the smooth and the swirlers channels.

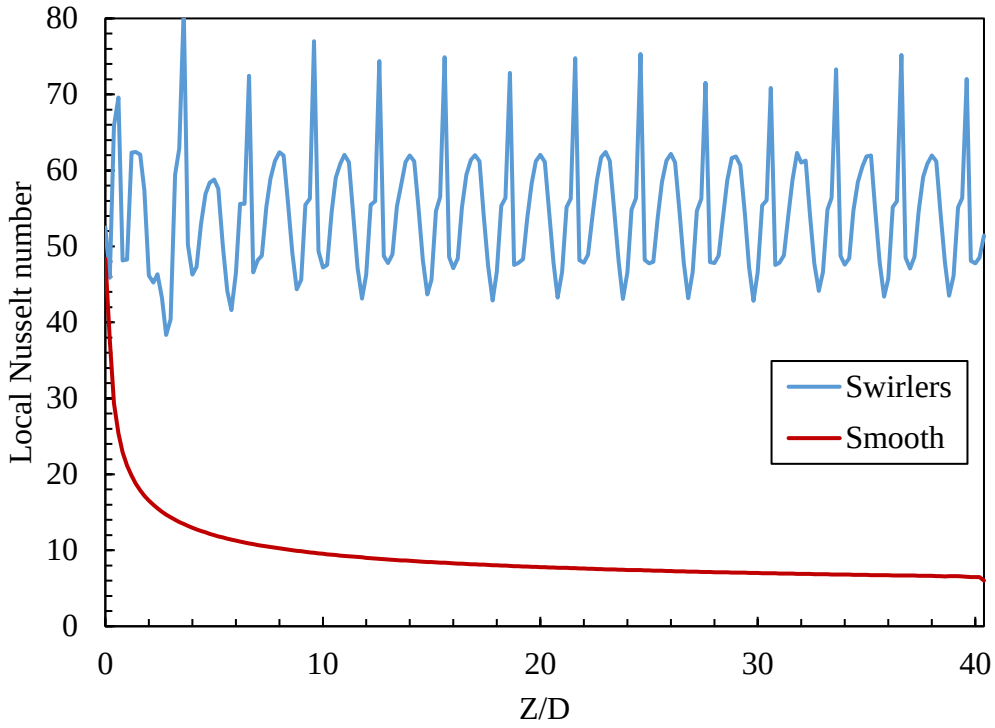

Figure 5-22 Local heat transfer coefficient distribution along the streamwise direction at Re = 1500.

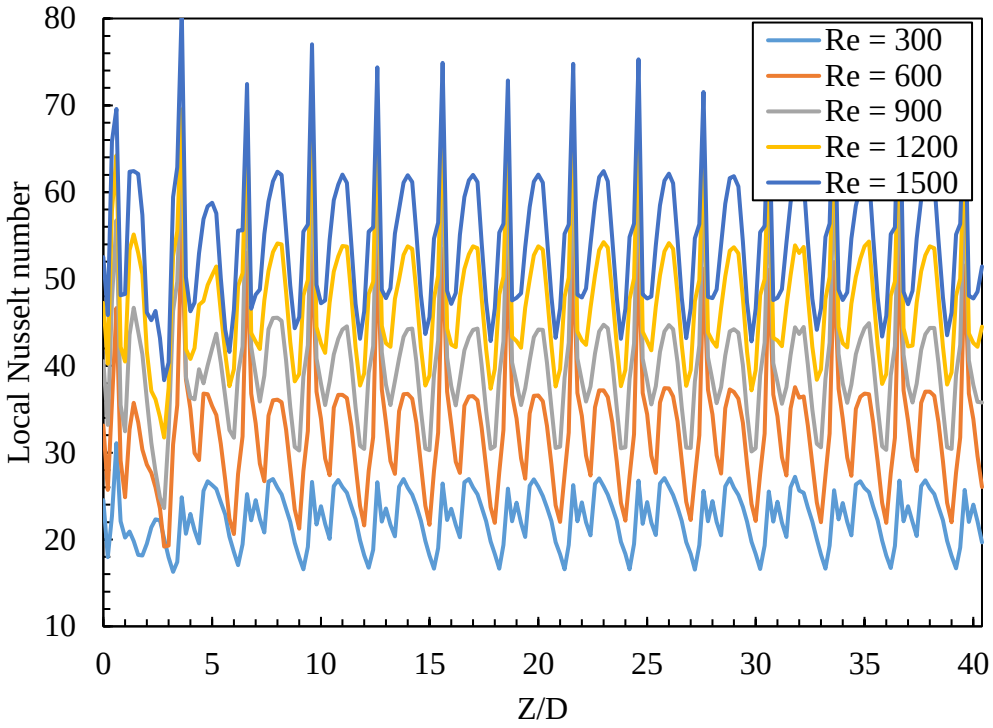

Figure 5-23 Local Nusselt number along the streamwise direction at different Reynolds numbers.

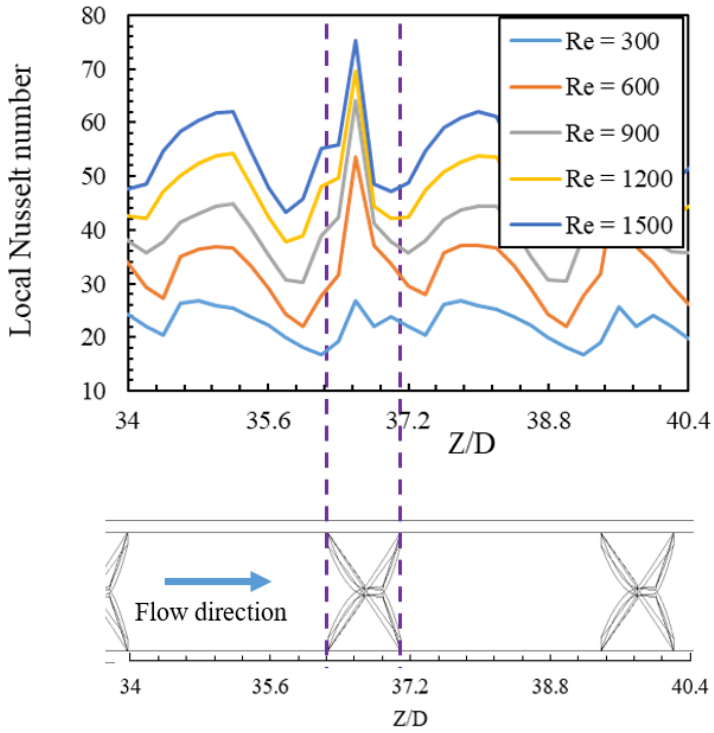

Figure 5-24 Local Nusselt number variation from Z/D=34 to the outlet of the test section

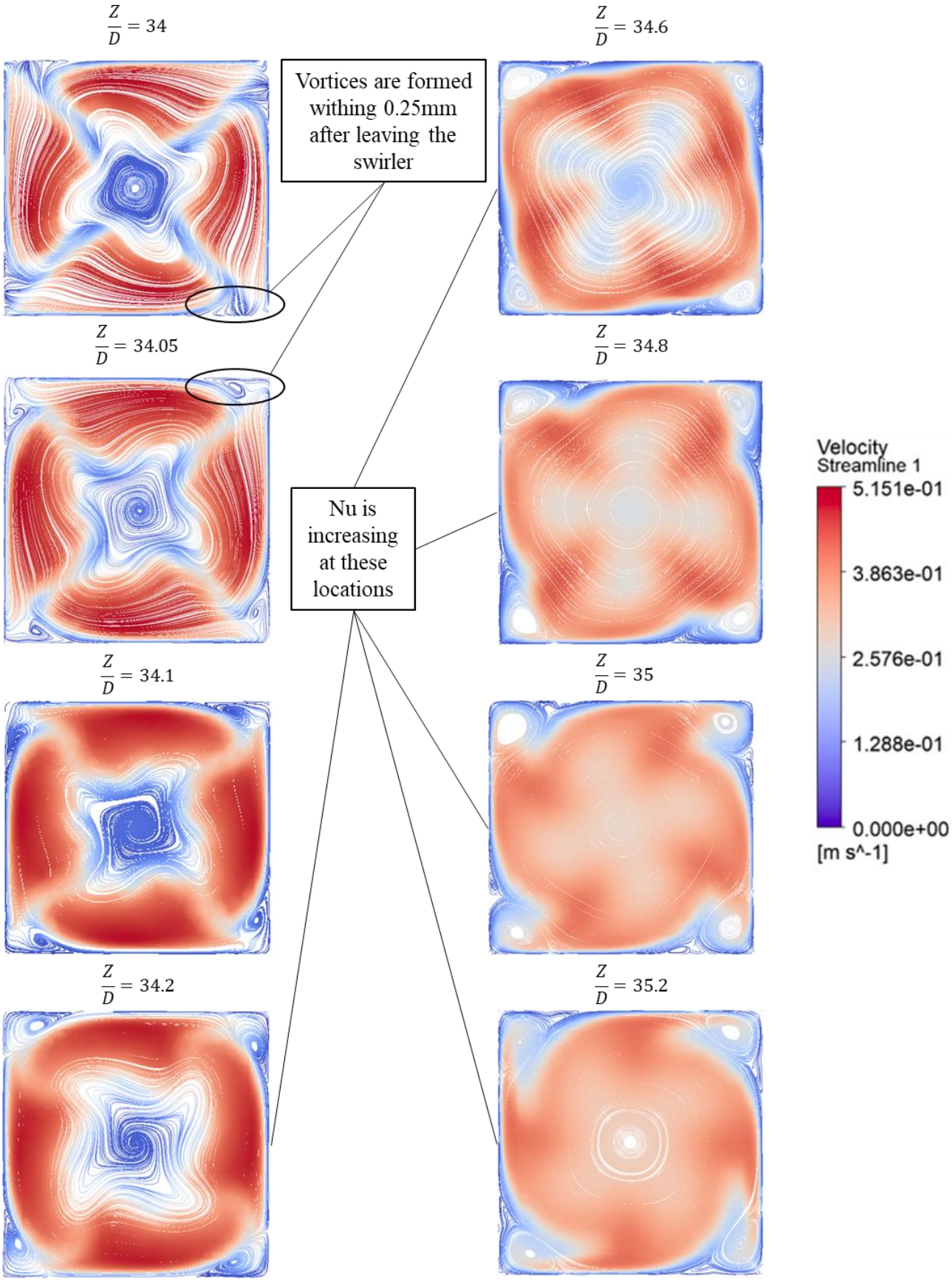
$\frac{Z}{D} = 34$
$\frac{Z}{D} = 34.6$
Vortices are formed withing 0.25mm after leaving the swirler
$\frac{Z}{D} = 34.05$
$\frac{Z}{D} = 34.8$
Nu is increasing at these locations
$\frac{Z}{D} = 34.1$
$\frac{Z}{D} = 35$
$\frac{Z}{D} = 34.2$
$\frac{Z}{D} = 35.2$
Velocity
Streamline 1
5.151e-01
3.863e-01
2.576e-01
1.288e-01
0.000e+00
[m s^-1]

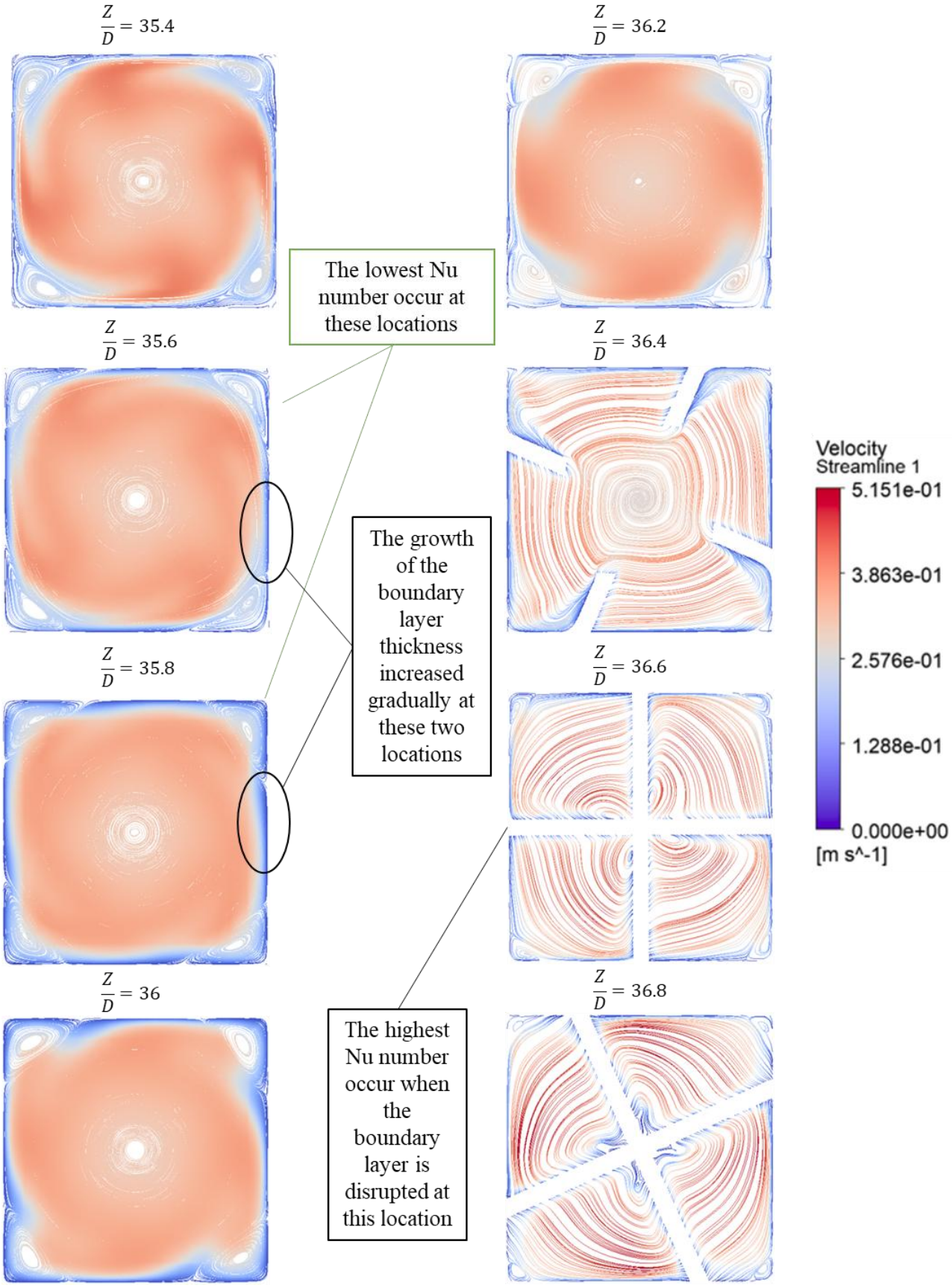

Figure 5-25 Flow streamlines at different planes along the streamwise direction from Z/D = 34 to Z/D = 37.

5.4.3 Parametric study

To parametrise the initial swirl channel design, one of the design parameters varies while all other parameters kept fixed. In the following sub-headings, the effect of these parameters on the heat transfer as well as flow field will be discussed.

5.4.3.1 Effect of loft angle (θ)

The loft angle is defined as the angle between the two rectangular sketches which form the lofted blade as shown in Figure 5.26. This loft angle varied from 45 degree to 90 degree to check the influence it has on the Nusselt number, friction factor and the overall performance factor. The following parameters kept constant (PR=3 and N=4).

Figure 5-27 represents the effect of loft angle on the heat transfer at different Reynolds numbers. The heat transfer increases gradually as Reynolds number increases for all the different angles. It can be noticed that the Nusselt number increases as the angle increases and that's attributed to the increase in the surface area and the strength of the flow impingement on the walls associated with the increase in the angle. The heat transfer enhancement with θ = 90 degree is about 5.5 time higher than that of the smooth case at Re = 1200.

Furthermore, the loft angle impact on the friction factor at different Reynolds numbers has the same trend as the Nusselt number. The friction factor rises as the Reynold number increases for the angles. A direct proportional relationship is found between the loft angle and the friction factor, the larger the loft angle, the higher friction factor values become. The friction factor rises from 8.9-fold to 15-fold from θ = 45 to 90, respectively at Re = 1200 as shown in Figure 5.28. This increase in friction factor is due to the increase in the swirler surface area which increases the flow destruction.

Figure 5.29 illustrates the overall thermal-hydraulic performance factor (PF) at the same pumping power for different loft angles at several Reynolds numbers. By varying the loft angle from 45 degree To 90 degree At Re = 1200, a 17% increase in the overall performance factor

was achieved. This difference increases as Reynolds number decreases. Since the case with θ = 90 degree achieved the highest performance factors among other angles, it will be used for further studies.

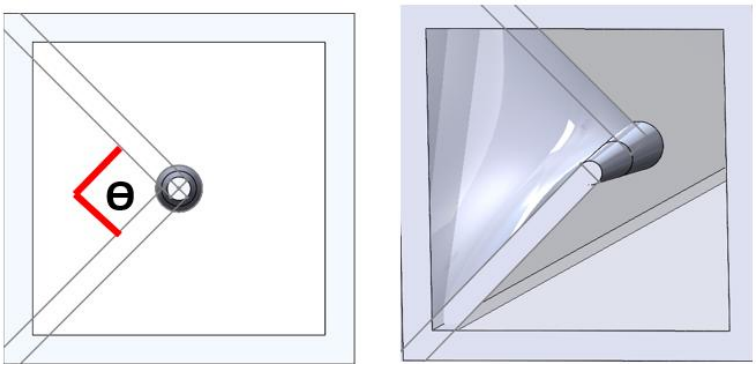

Figure 5-26 The loft angle definition: before the loft created (left) and after the loft creation (Right).

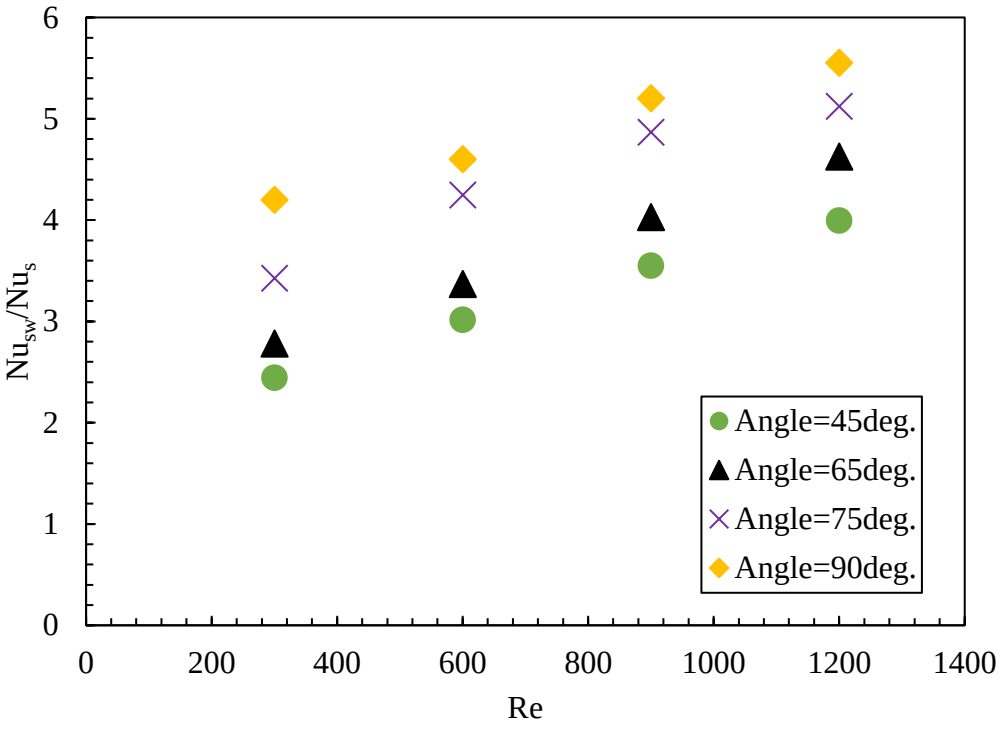

Figure 5-27 Averaged Nusselt number ratio variation against the loft angle at different Reynold numbers.

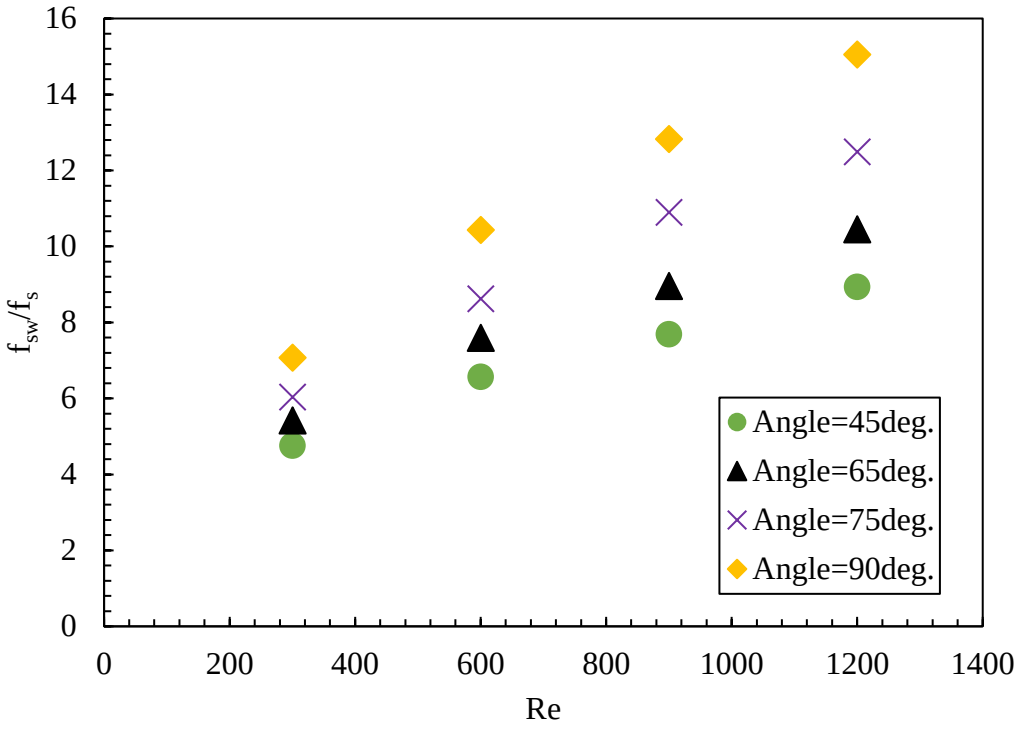

Figure 5-28 Averaged friction factor ratio variation against the loft angle at different Reynold numbers.

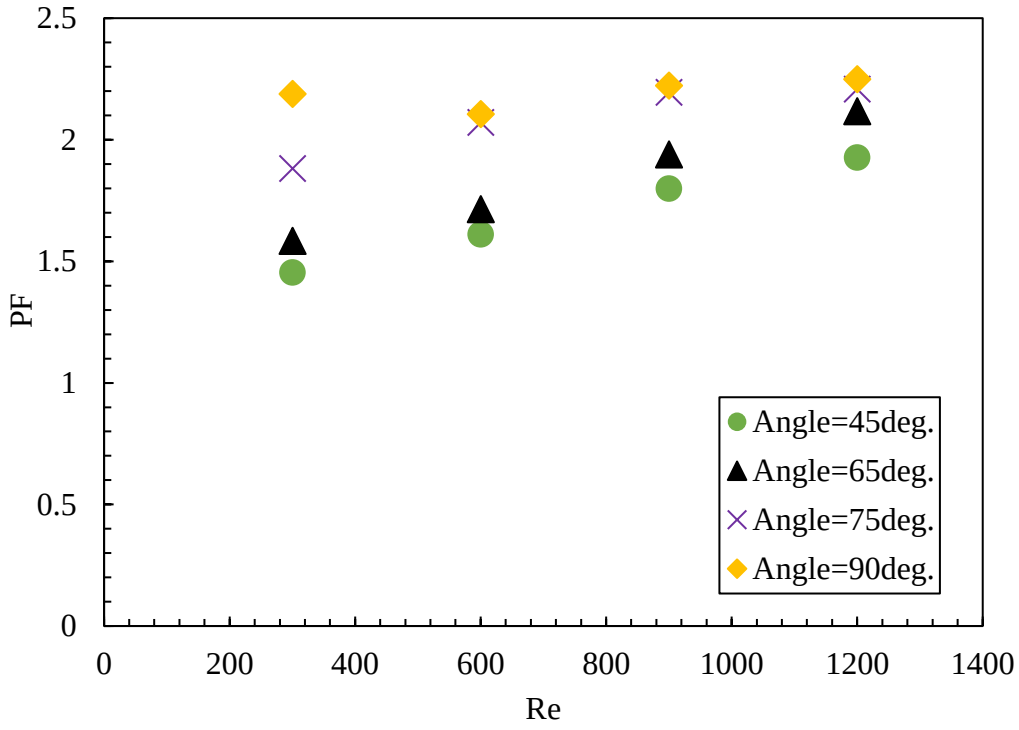

Figure 5-29 Performance factor variation against the loft angle at different Reynold numbers.

5.4.3.2 Influence of streamwise pitch ratio (PR)

The pitch ratio is defined as the ratio of the distance between two consecutive swirlers over the hydraulic diameter, $PR = \frac{P}{D_h}$, as shown in Figure 5.30. The range of the tested pitch ratios (PR) is 1.5 (27 swirlers), 2.25 (18 swirlers), 3 (14 swirlers) and 4.5 (9 swirlers).

Figure 5.31 presents the variation of Nusselt number with different pitch ratios at different Reynolds numbers. There is a direct proportional relationship between the Nusselt number and the Reynolds number. As the Reynolds number increases, the Nusselt number increases for all the different pitch ratios. The figure reveals that the smaller the pitch ratio, the higher the averaged Nusselt number becomes and that's due to the stronger swirl caused by placing more swirlers with the small pitch ratio. The highest heat transfer augmentation occurs at the smallest pitch ratio (PR=1.5) at Re = 1200 and the amount of augmentation is 6.86 times higher than that of smooth case. The same trend is observed on the friction factor in Figure 5.32 and that's because of the high pressure losses found as the pitch ratio decreases. When considering the pressure drop penalty associated with the heat transfer enhancement, the performance factor of 2.48 is the highest value obtained at PR = 2.25 at Re = 1200 which means an enhancement of 148% on the overall system performance was achieved when compared to the smooth case as shown in Figure 5.33.

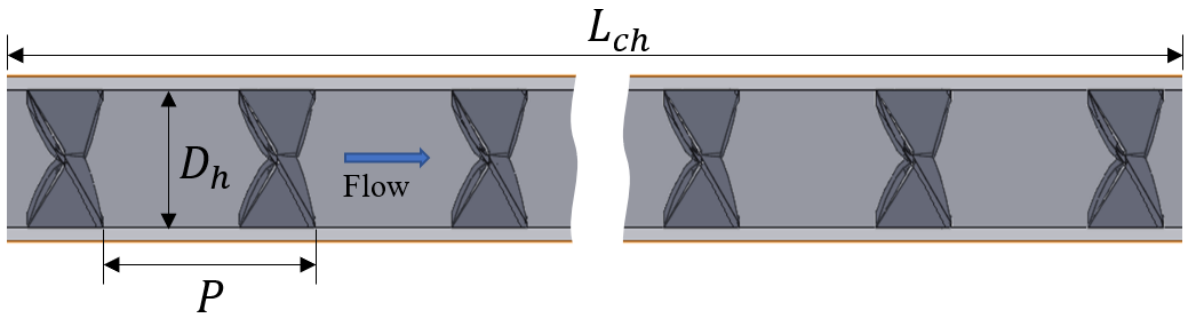

Figure 5-30 Pitch definition

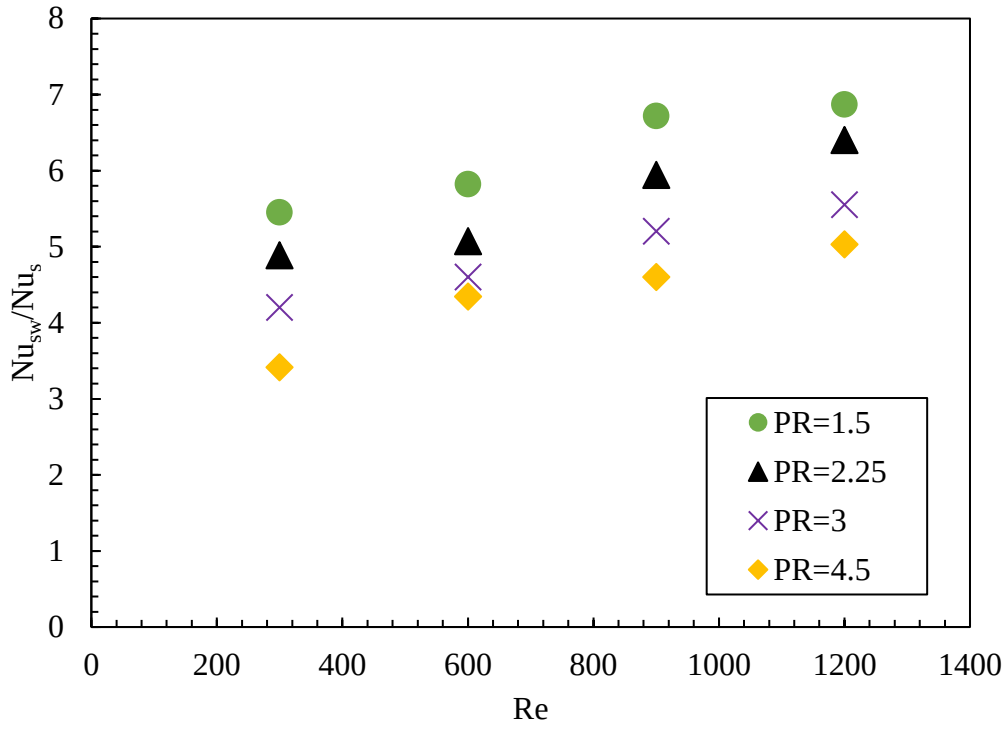

Figure 5-31 Averaged Nusselt number ratio variation against the pitch ratio (PR) at different Reynold numbers.

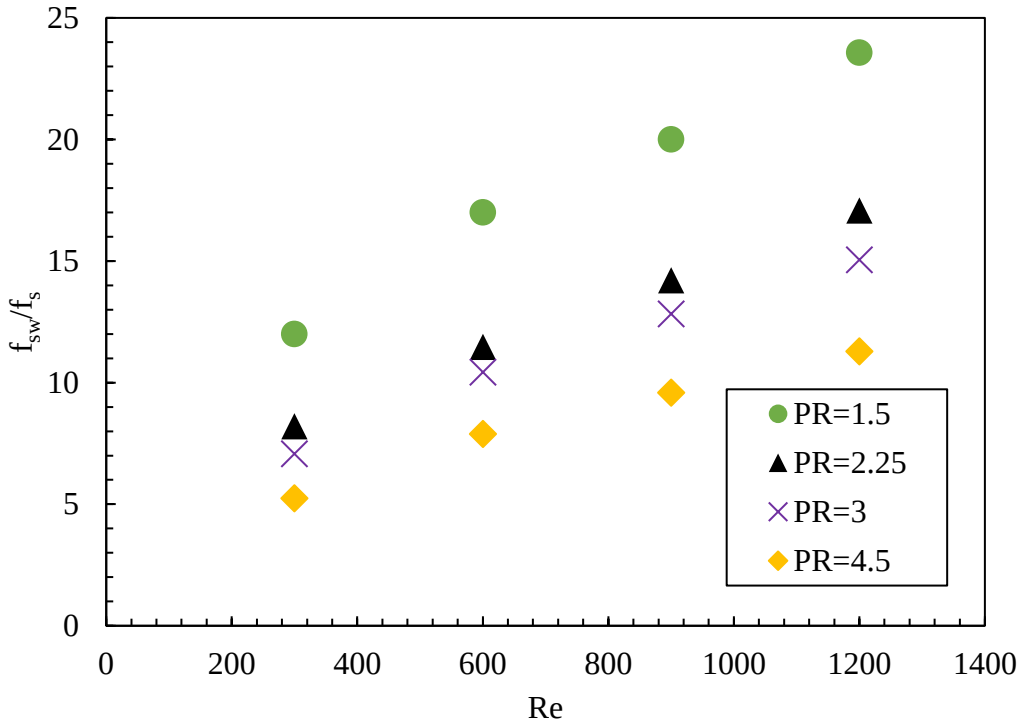

Figure 5-32 Averaged friction factor ratio variation against the pitch ratio (PR) at different Reynold numbers.

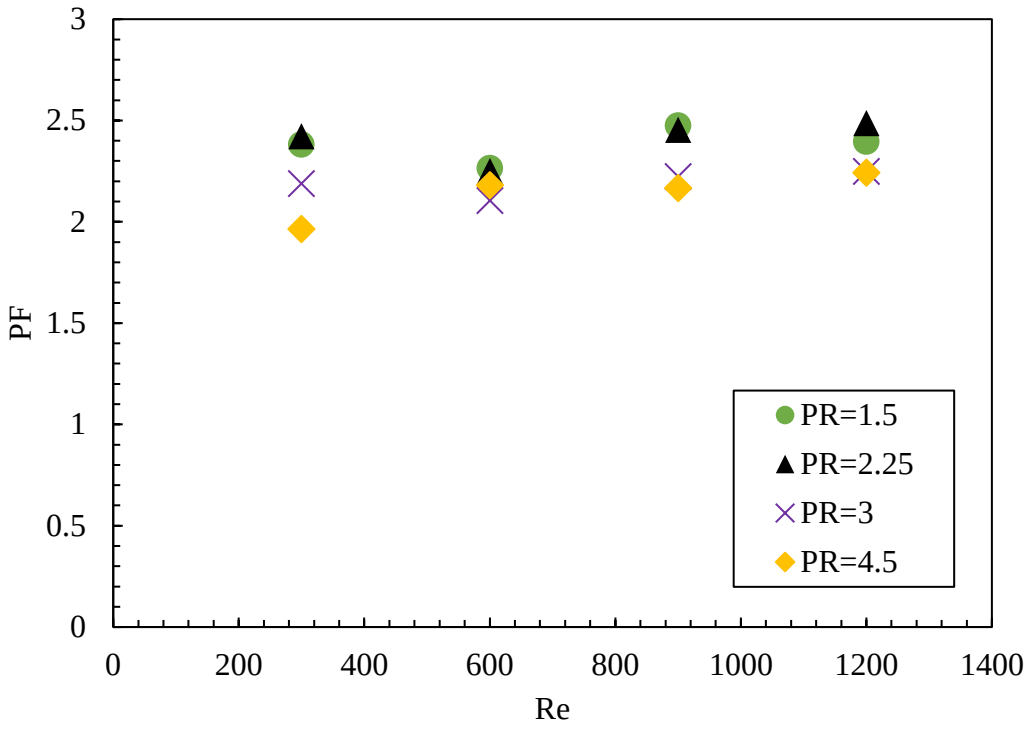

Figure 5-33 Performance factor variation against the pitch ratio (PR) at different Reynold numbers.

5.4.3.3 Effect of number of blades (N)

The swirler's number of blades varied from 3 to 5, to check its influence on the heat transfer, friction factor, and overall performance factor.

Figure 5.34 demonsterats the effect of the number of blades on Nusselt number at different Reynolds numbers. As the Reynolds number increases the Nusselt numbers increaes for all the different number of blades. A direct proportional relationship between the average Nusselt number and the number of blades is observed. With the increase of the number of blades, Nusselt number number increases accordingly and that's attributed to the stronger swirl imparted to the stream as the number of blades increases.

The effect of number of blades on friction factor has the same trend as the Nusselt numner. This is due to the higher dissipation of the dynamic pressure of the fluid as the number of blades increases as shown in Figure 5.35.

Considering the effect of number of blades on both heat transfer and friction factor at the same pumping power requirement at different Reynolds number, it is clear that from Figure 5.36, the swirler with 4 blades shows the best performance factor for all the range of Reynolds number.

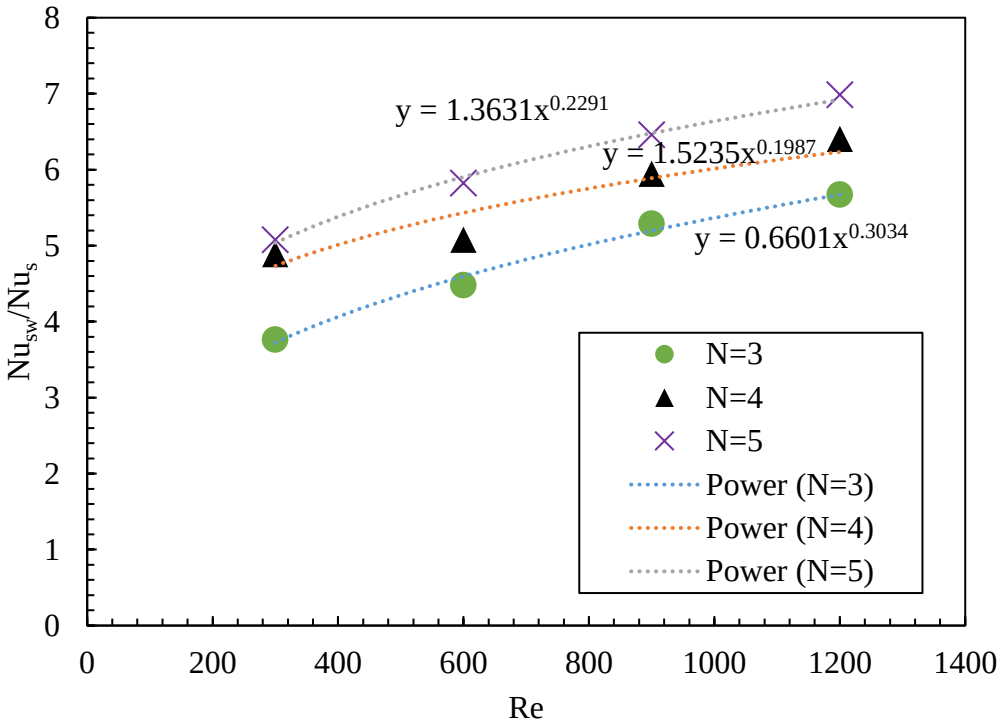

Figure 5-34 Averaged Nusselt number ratio variation against the number of blades at different Reynold numbers.

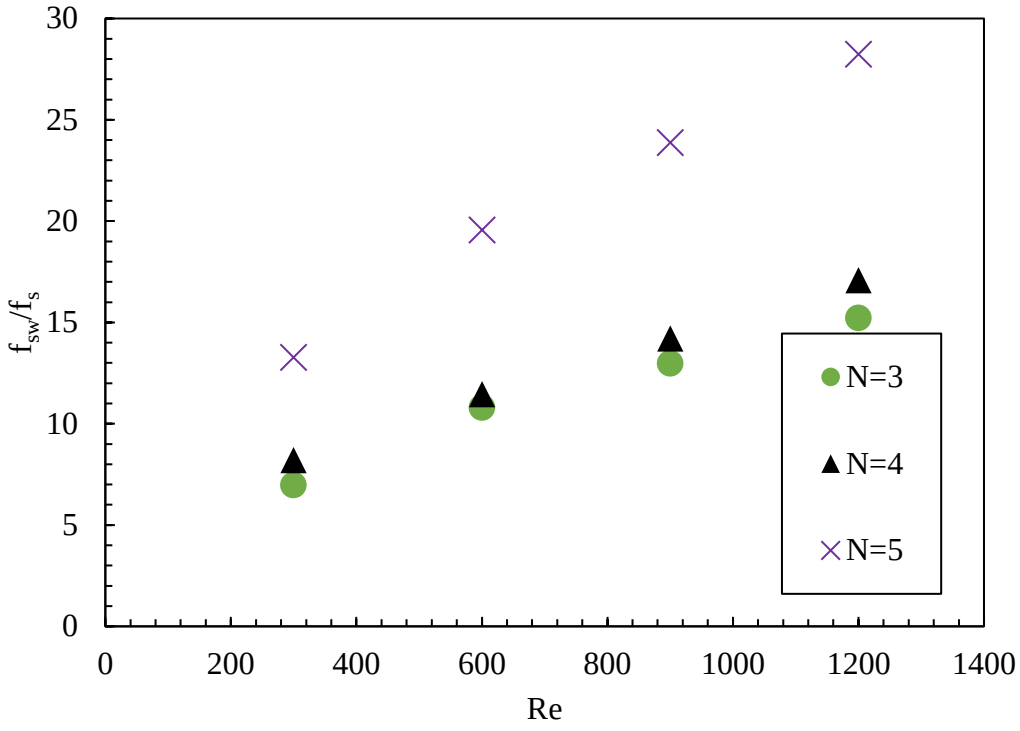

Figure 5-35 Averaged friction factor ratio variation against the number of blades at different Reynold numbers.

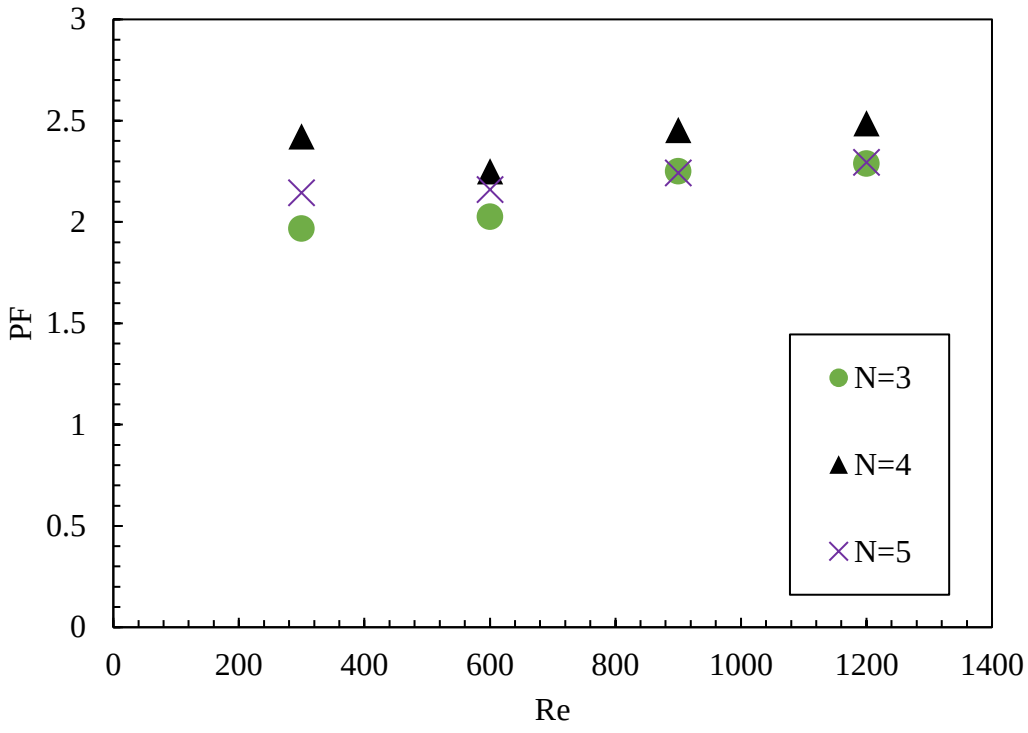

Figure 5-36 Performance factor variation against the number of blades at different Reynold numbers.

5.4.3.4 Effect of small structures downstream of the swirler

In order to enhance the flow mixing between the near wall fluid and the central region, small triangular structures are placed downstream of the swirler on the best swirlers channel case from the previous parametric study as shown in Figure 5.37. Its effect on the heat transfer and friction factor are investigated by comparing the case with and without structures back to back. The triangular structure has a base length of $L_{base}/D = 0.274$, first leg of $L_{first\ leg}/D = 0.08$ and second leg of $L_{second\ leg}/D = 0.228$.

The velocity and the wall shear stress contours of the two cases with and without structures are showing in Figure 5.38. The highest velocity and shear stress is spotted out in the vicinity where the flow impinges on the wall right after the flow exits the swirler. The presence of the small structure boosts the swirl and therefore strengthen the impingement on the walls and mixing of the fluid particles. Due to this strong impingement, the case with small structure experiences higher shear stress when compared to the case without structures.

Following what have been noticed so far, the heat transfer coefficient (HTC) contour in Figure 5.39 shows the high value of heat transfer coefficient at the areas where the flow impinges on the walls. The existence of the small structures forces the flow to move toward the central region where the flow particles near the wall mixes with the flow particles in the central region. This enhancement of mixing influences the overall heat transfer of the case with small structures.

Figure 5.40 displays the circulation generated behind the swirler's blade for the two cases. It can be noticed that, in the case with the small structures the circulation is stronger in a way that it is connected with the flow near the wall (the hot spot). This mechanism enhances the heat transfer by mixing the flow in the low temperature region with the high temperature region. On

the other hand, in the case without small structure the circulation is smaller and weaker which allows the flow to accelerate and escape without augmenting the flow mixing.

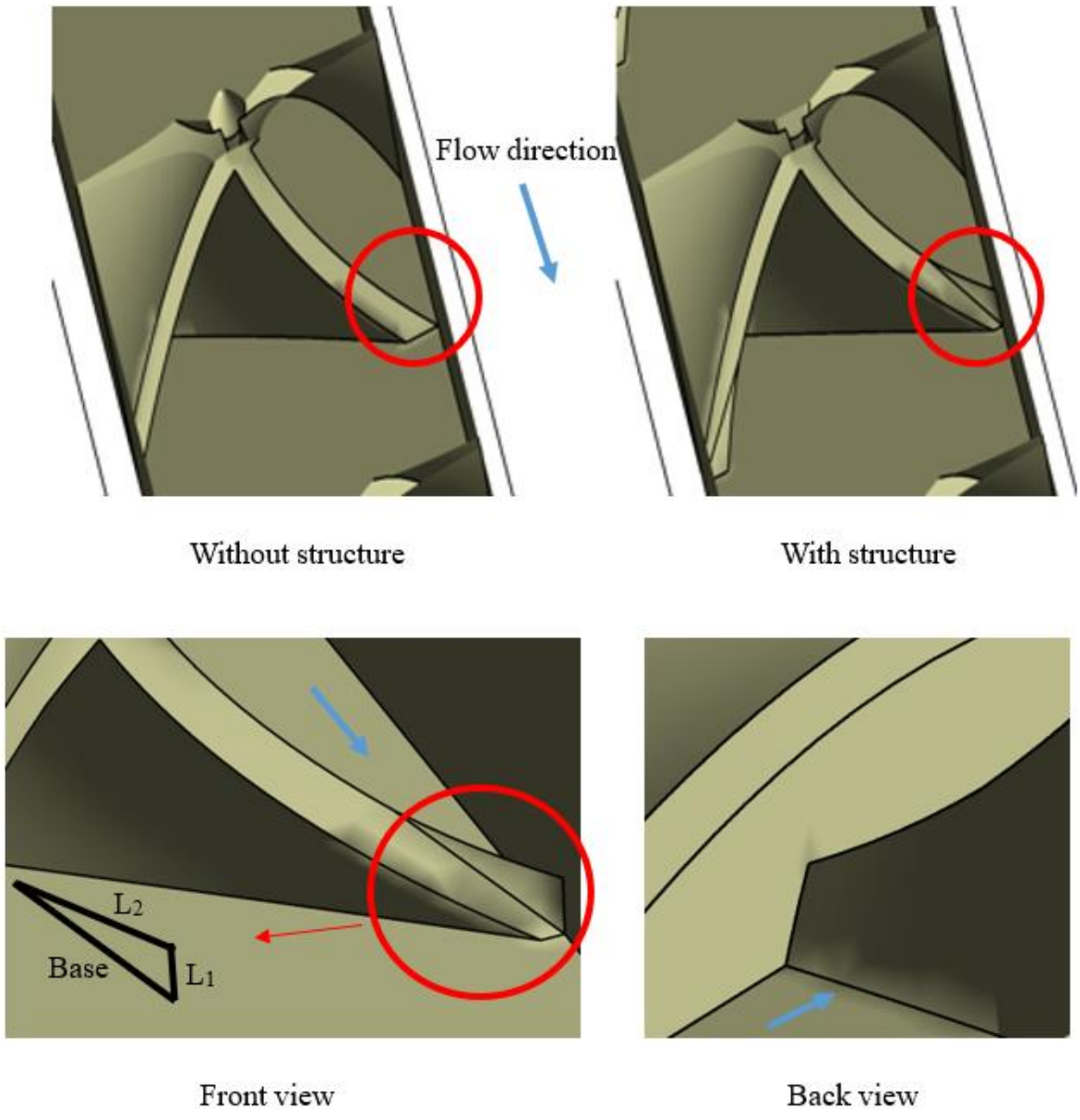

Figure 5-37 Swirlers with (Left) and without (Right) added triangular structure.

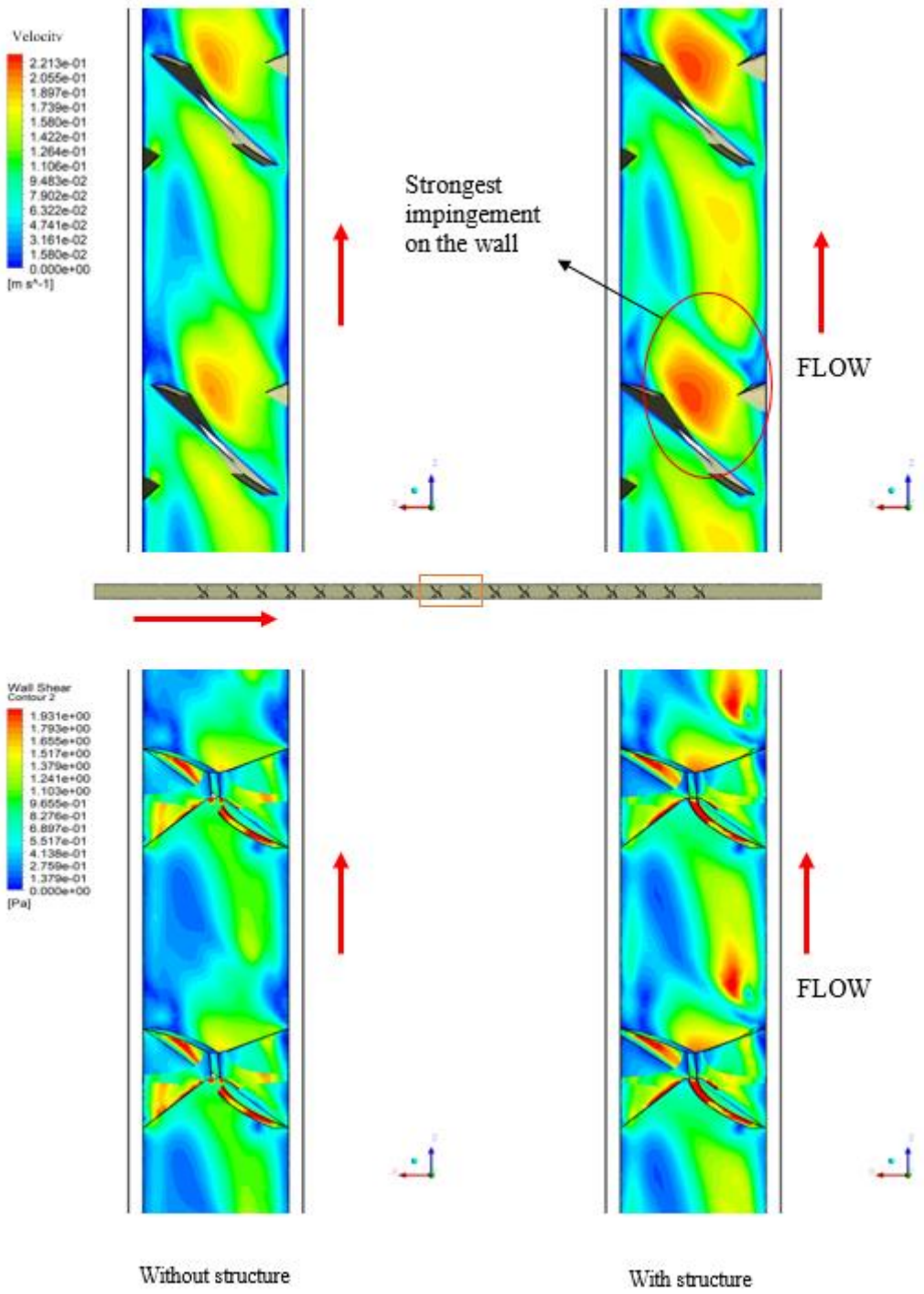

Figure 5-38 Velocity contour and the wall shear stress near the wall in the mid-channel (Re=600).

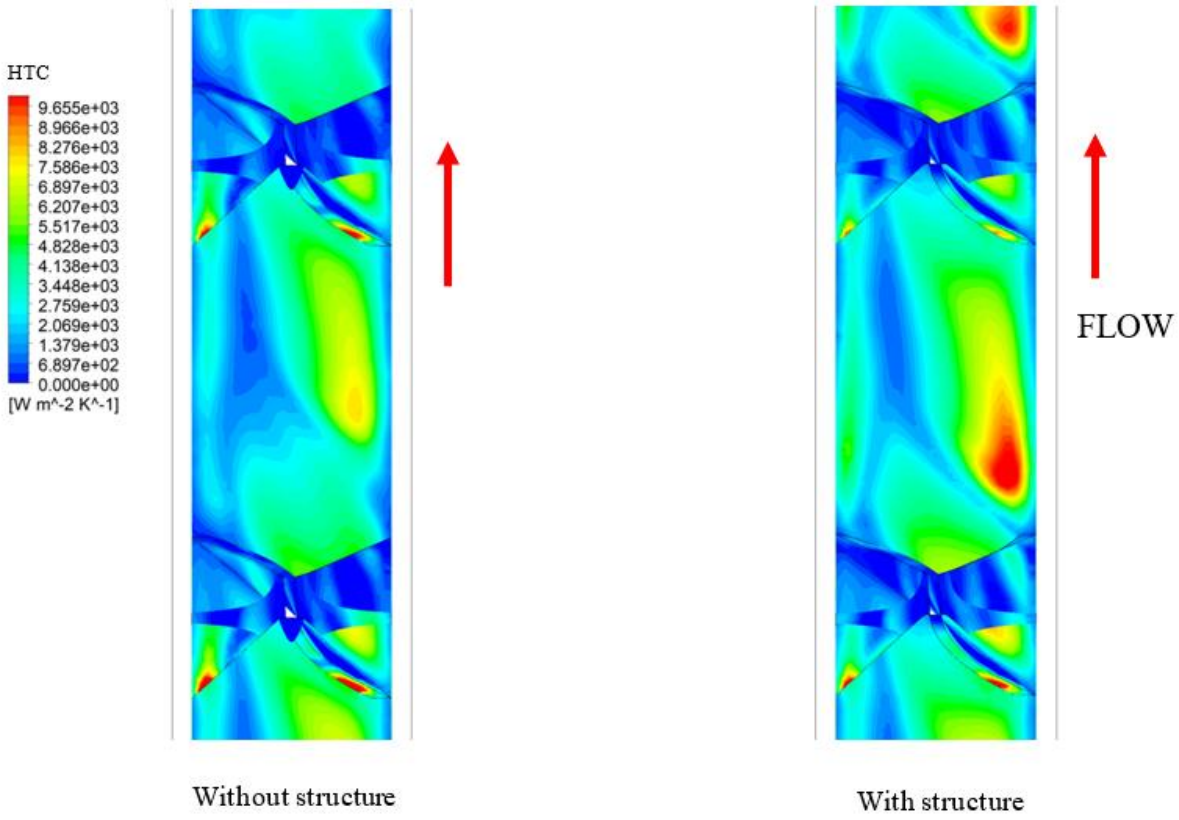

Figure 5-39 Heat transfer coefficient contour at the mid-channel (Re=600).

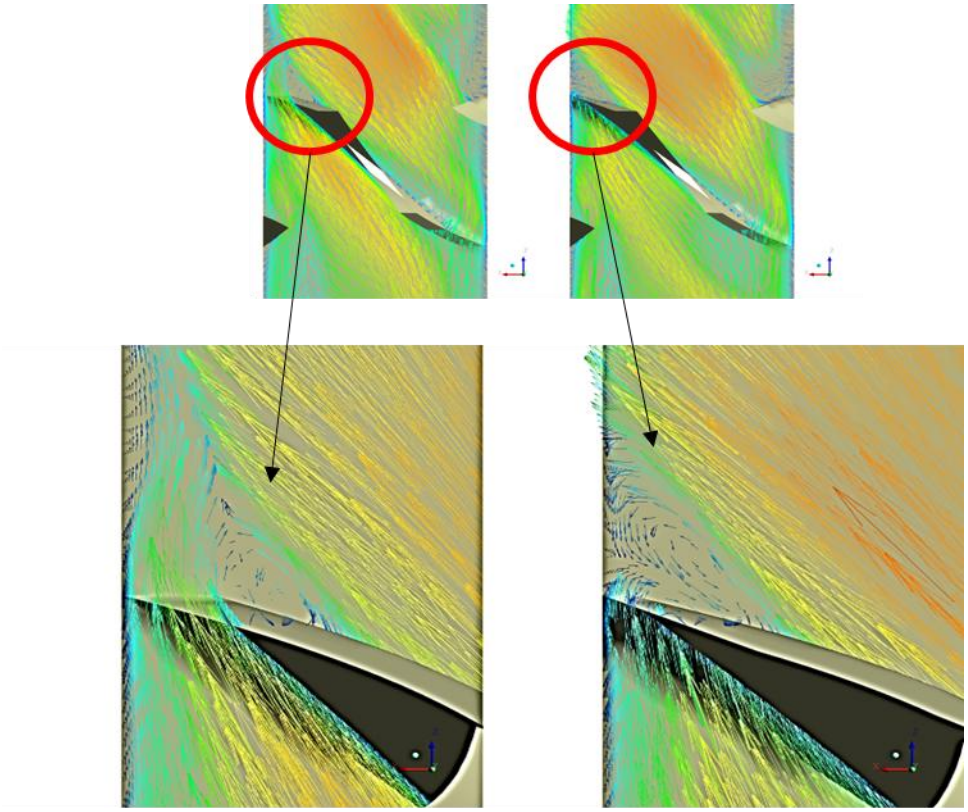

Figure 5-40 Recirculation zone behind the blade downstream of the swirler for the case with structures (Right) and for the case without structures (Left) at Re=600.

In addition, an iso surface of the temperature at T = 334 K is illustrated in Figure 5.41. This figure is confirming what have been found so far that the small structure does play a big role in enhancing the heat transfer rate. The case with small structures reached the same temperature value of T = 334K at Z/D = 34 that was reached by the other case at the outlet. This indicates more flow mixing is happening with the small structures case and higher bulk temperature value is obtained by the outlet of the test section.

The velocity iso-surface at u = 0.17 m/s is shown in Figure 5.42 shows the higher velocity associated with the small structure case which led to higher impingement on the walls and therefore more heat transfer.

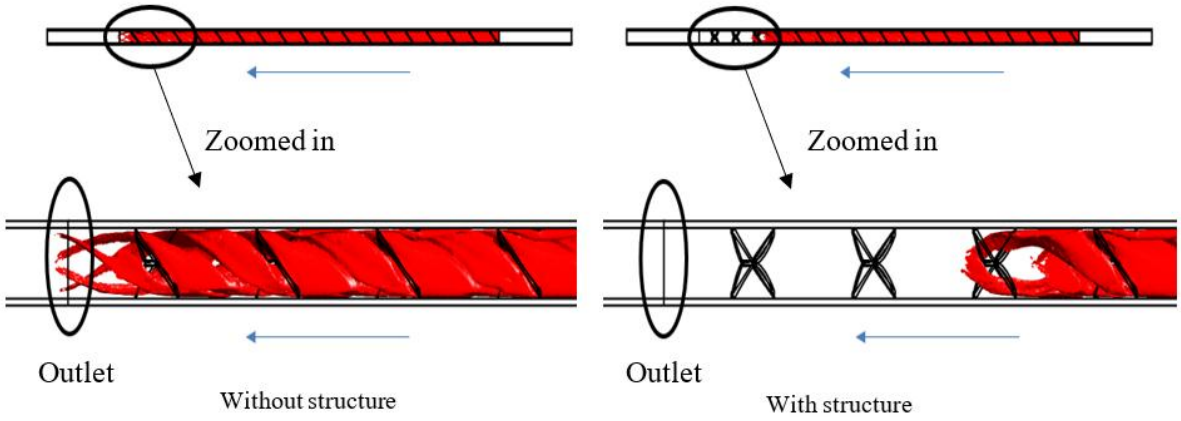

Figure 5-41 Temperature iso-surface at T = 334K for the case with structures (Right) and for the case without structures (Left) at Re=600.

Figure 5.43 are further evidence of the influence of adding the triangular structures. It shows the velocity contour, velocity vector and temperature contour form Z/D = 7.6 to 9.6. The mixing of the flow in the case with small structures enhances the mixing of the temperature as the flow progress throughout the channel.

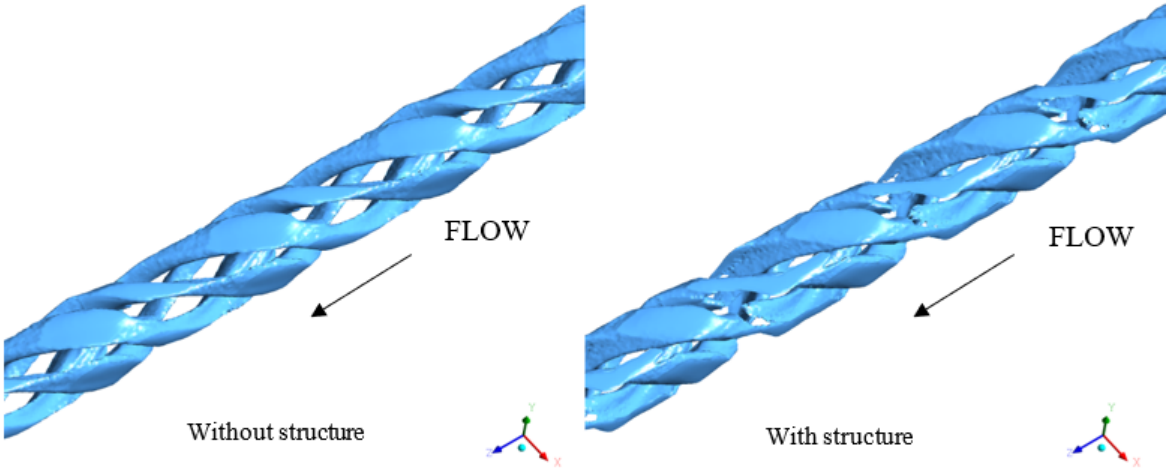

Figure 5-42 Velocity iso-surface at u=0.17m/s the case with structures (Right) and for the case without structures (Left).

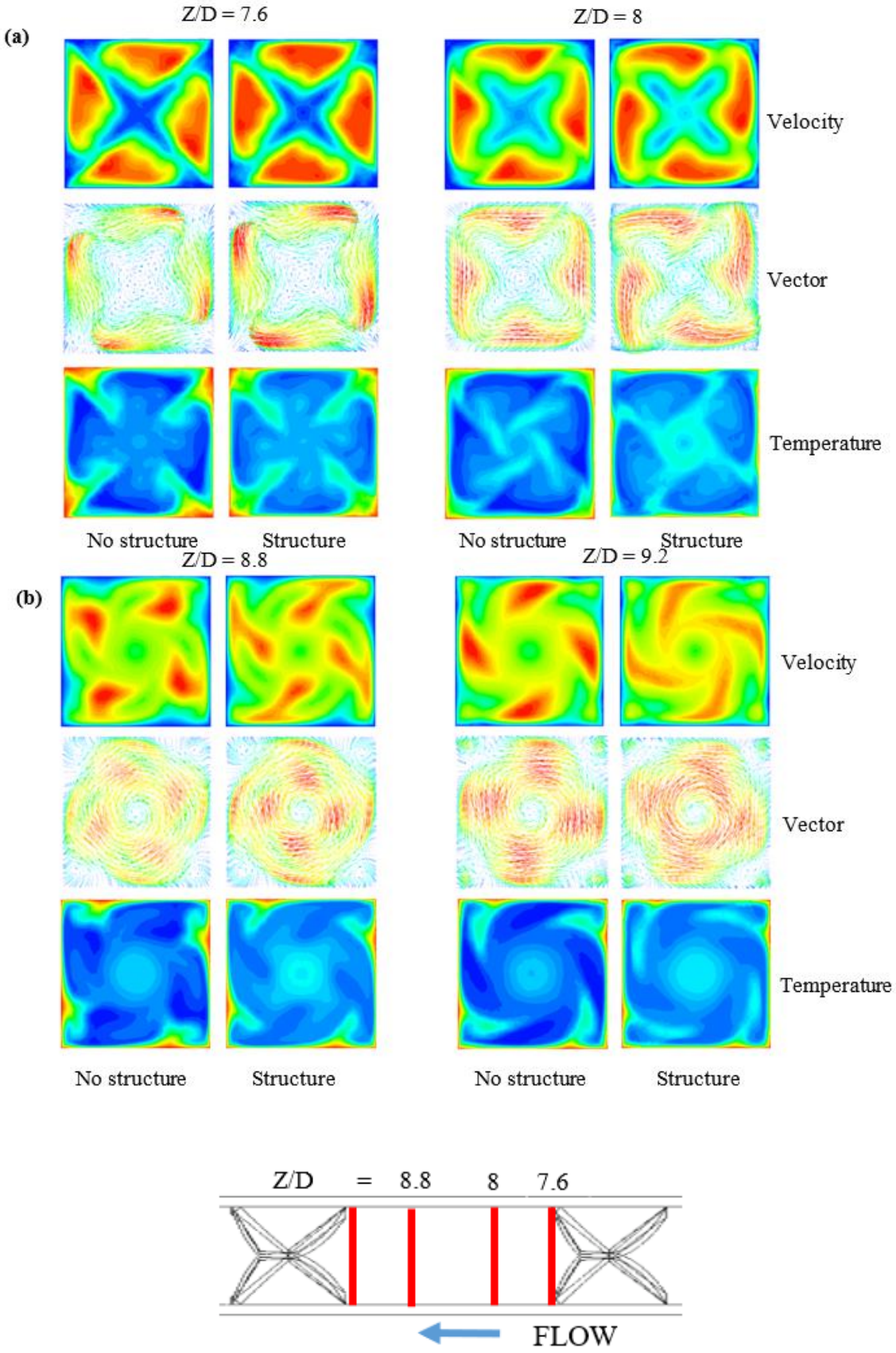

Figure 5-43 Velocity contour, velocity vector, and temperature contour on four planes between two consecutive swirlers, (a)contours, (b)locations where the contours are taken.

5.4.3.5 Effect of Reynolds number

The effect of Reynolds number is tested on the optimized case with small triangular structures (PR = 2.25, θ = 90, N = 4). Four different Reynolds numbers are tested, 300, 600, 900 and 1200.

Figure 5.44 demonstrates the effect of varying Reynolds number on the heat transfer. As Reynolds number increases the enhancement of heat transfer increases accordingly. A rise of about 30% is achieved from Re = 300 to Re = 1200. Pressure losses are higher as Reynolds number becomes larger and an increase of about 240% was noticed from Re = 300 to Re = 1200 as shown in Figure 5.45. Considering the heat transfer enhancement as well as the high pressure drop at the same pumping power, the performance factor did not change much from Re = 300 to Re = 1200. The highest value occurs at Re = 600 with around 13% difference from that of Re = 300 as shown in Figure 5.46.

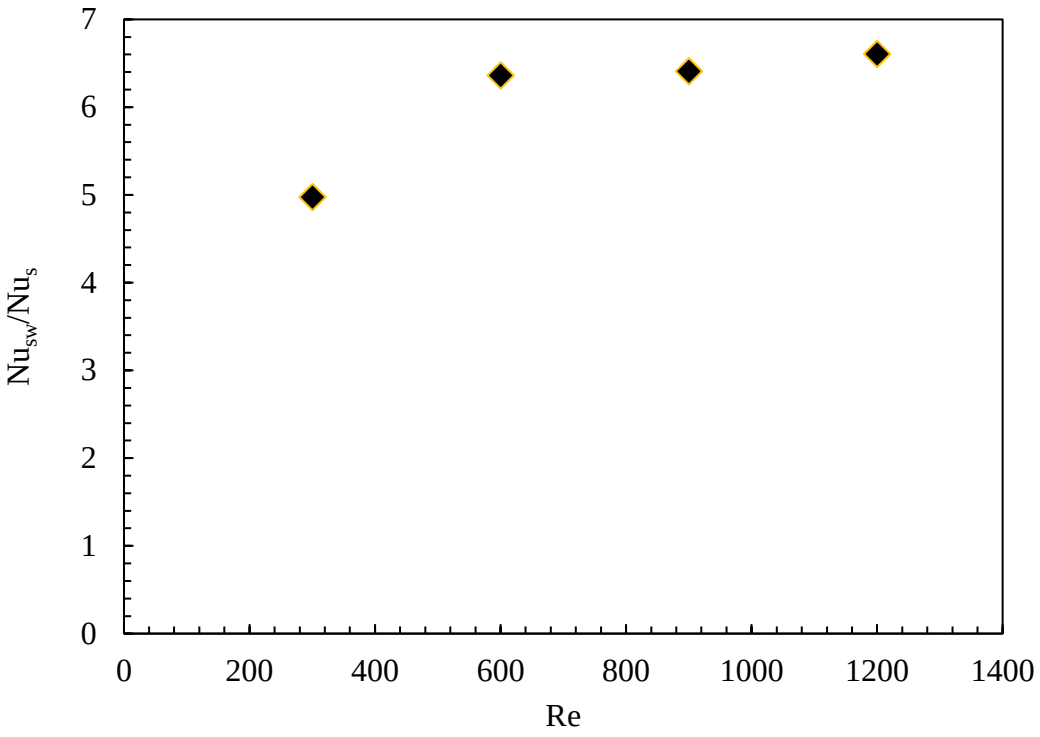

Figure 5-44 Averaged Nusselt number ratio against Reynolds number.

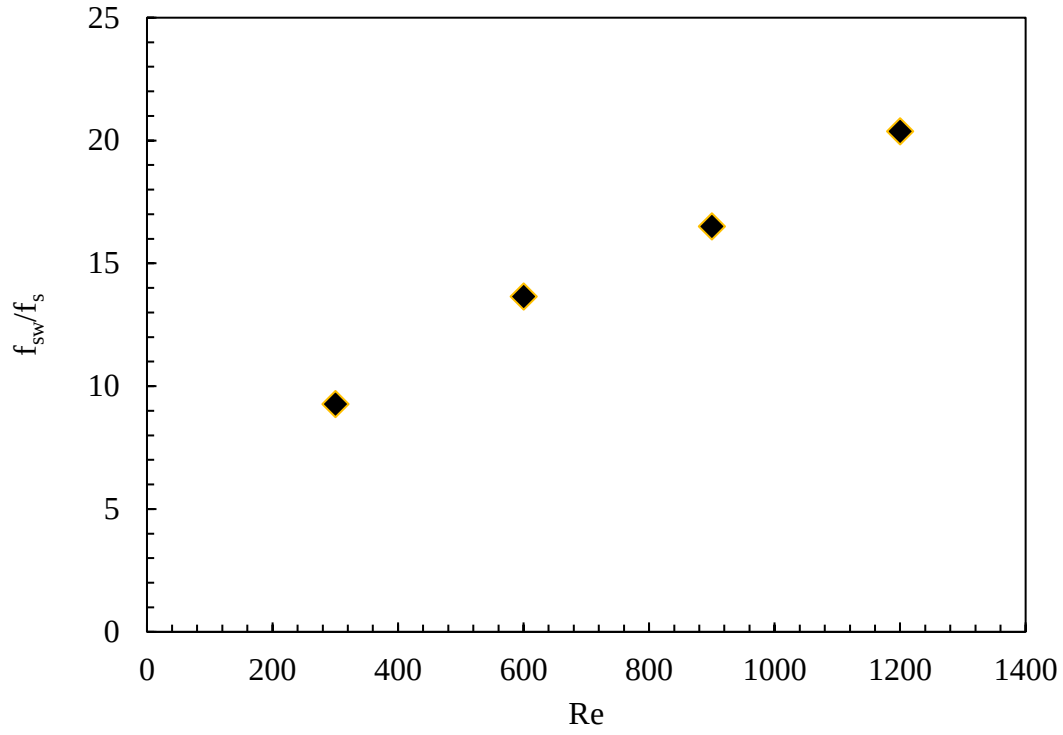

Figure 5-45 Averaged friction factor ratio against Reynolds number.

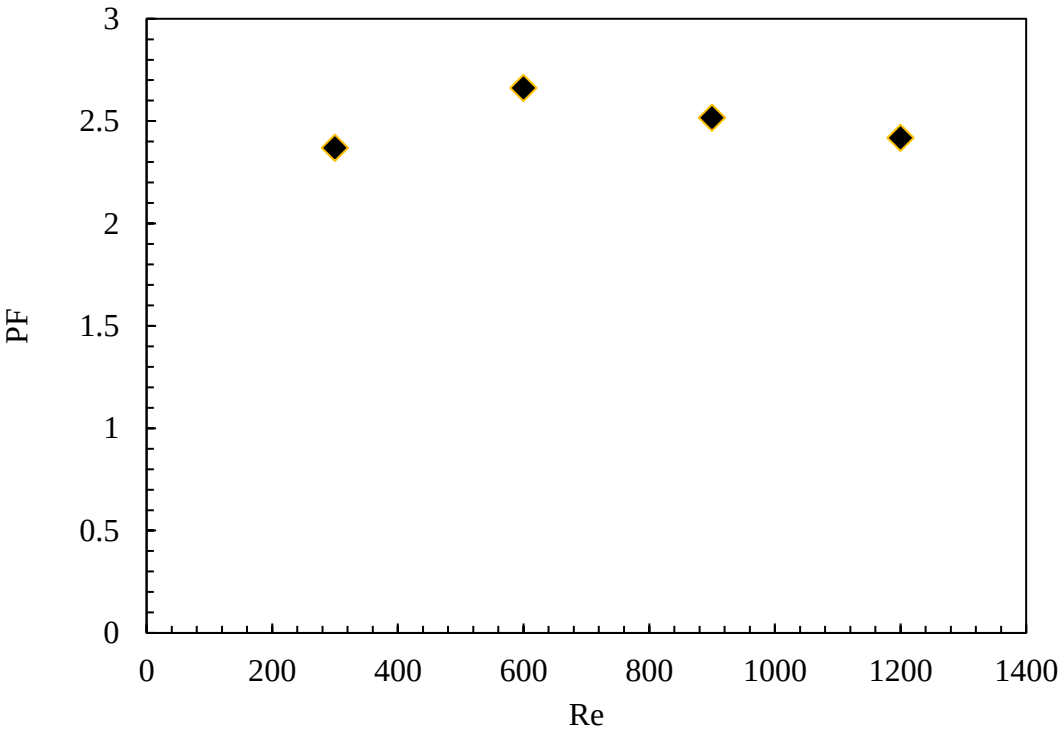

Figure 5-46: Performance factor against Reynolds number.

5.4.3.6 Effect of material

The solid material used with the cases so far is Inconel718 which can handle the high temperatures as well as corrosive environments [132]. However, this material has a very low thermal conductivity (K = 10.35) and that effects the amount of heat which conducts through the base to the swirlers. Figure 5.47 shows the temperature contours at four different locations for three different materials, Inconel718, Aluminium and Copper. Due to the low thermal conductivity of Inconel718, the heat is not being transferred to the central region and that means the full heat transfer surface area is not being taking advantage of.

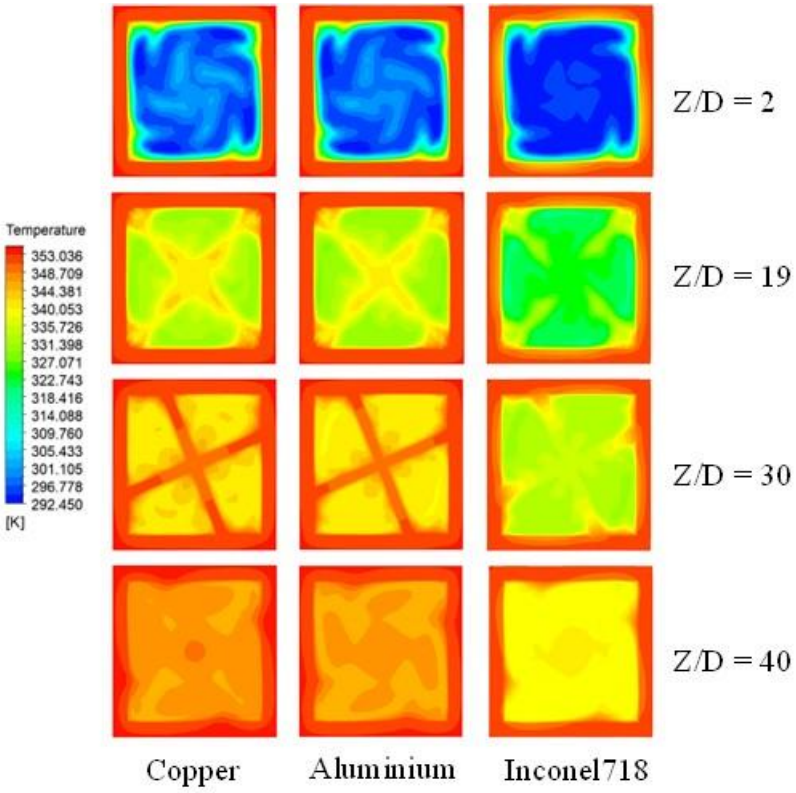

Figure 5-47 Temperature contours at four different locations for different materials

The optimum case with small structures is used to test the influence of different material on the overall performance factor of the system. It can be seen from Figure 4.48 that the heat conduction improved with the Aluminium and Copper as their thermal conductivity are much higher than Inconel718. Using materials with high thermal conductivity such as Aluminium and Copper improve the overall thermal performance by about 9% from that of low thermal conductivity material. Therefore, the performance factor associated with the Aluminium and Copper are 2.8 and 2.9, respectively as shown in Table 5-3.

Table 5-3 Performance factor comparison between different materials.

Material	PF	% Difference
Inconel 718	2.66	____
Aluminium	2.8	5.3%
Copper	2.9	9.0%

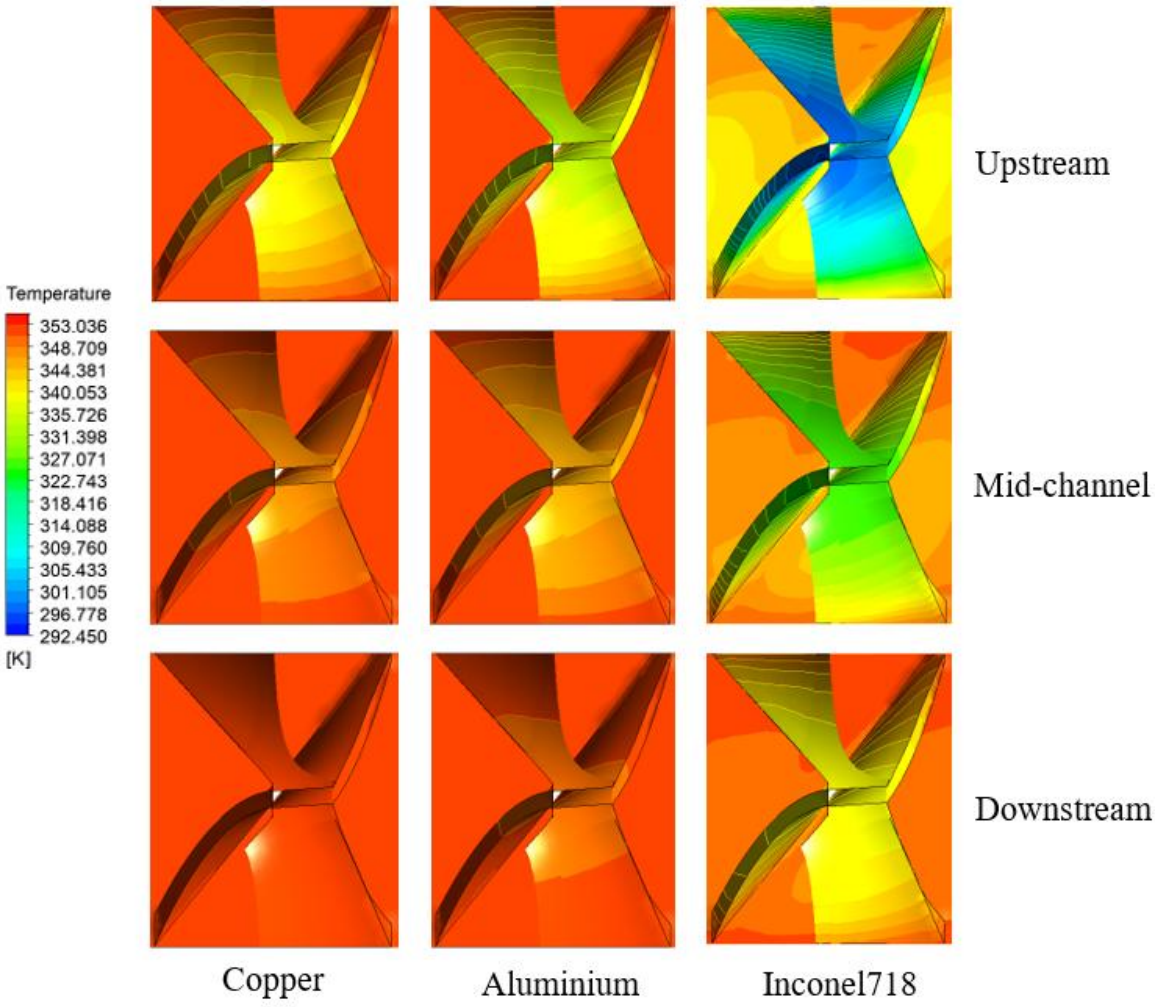

Figure 5-48 Temperature contours of swirlers in the upstream, middle and downstream of the channels.

5.5 Summary

In this chapter, a single passage of the heat exchanger core and the concept of the additive manufacturing are introduced. The numerical setup and code validation for both smooth and swirler channels are performed. To assess which swirler configuration is best, three design parameters are varied. These three parameters are the loft angle (θ), pitch ratio (PR) and blades number (N). The Nusselt number and friction factor of each case are obtained. A figure of merit named as thermal-hydraulic performance factor is used, which is defined as the ratio of heat transfer enhancement to the increase in pumping power due to the presence of the swirlers. The chapter starts with a comparison between the smooth base case and the swirler channel (θ = 90 degree, PR = 3, N = 4). Both heat transfer and friction factor are increased when the swirlers are added to the channel. This led to an overall increase of the performance factor by about 125% from that of the smooth channel. The highest thermal-hydraulic performance factor out of all the swirler cases found at the case with the following parameters (θ = 90 degree, PR = 2.25, N = 4). An increase of about 148% is achieved when compared against the smooth channel. To enhance the mixing of the flow, small triangular structures are added down stream of the swirler. Placing such structures augmented the overall performance factor by about 15% when compared to that of the optimised case. The value of the performance factor is 2.66 which means that about 166% enhancement when compared to the smooth channel. It is crucial to note that using more thermally conductive materials such as Copper improves the performance factor by about 9% when compared to low thermal conductive material such as Inconel718.

The predicted data from the CFD study for Nu and PF is summarized and correlated in Figures 5-49 and 5-50. The parameters of the correlations are listed in Table 5-4. These equations can be used to estimate the Nu and PF at different PR, N, and angles for the novel design presented in this chapter.

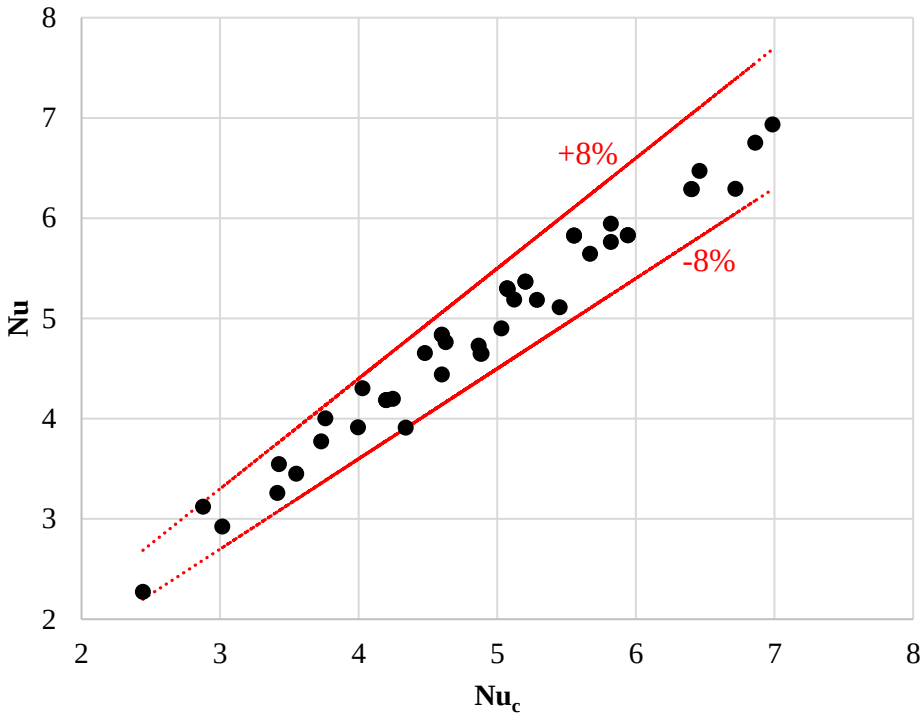

Figure 5-49 Relationship between predicted Nu from CFD and correlation

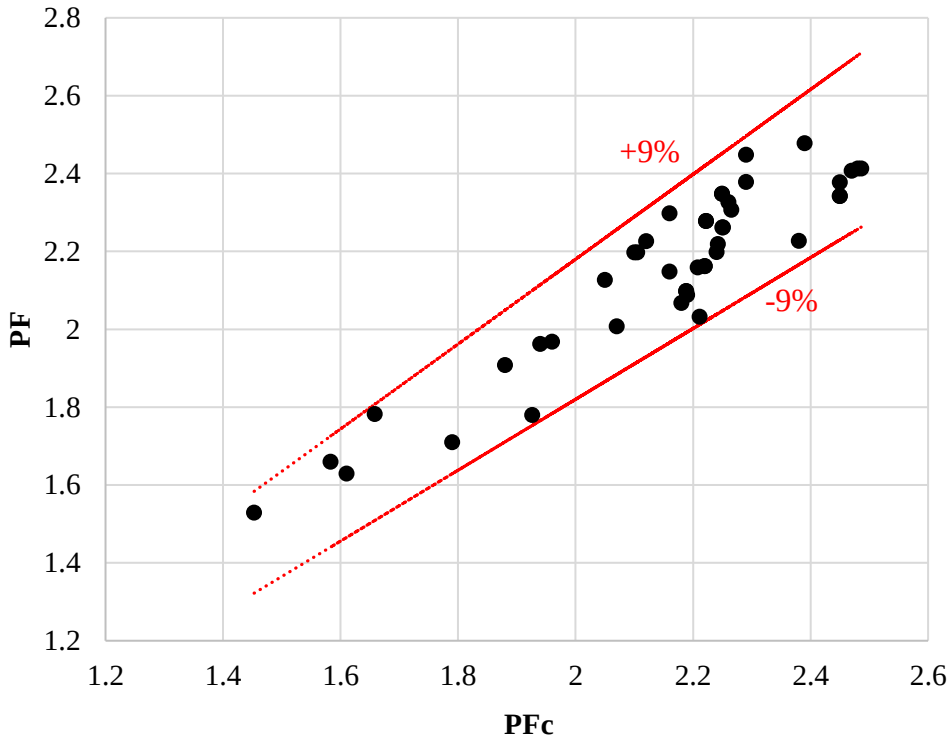

Figure 5-50 Relationship between predicted Nu from CFD and correlation

Table 5-4 Coefficients of the correlation equations for Nu and PF

Correlation	$a + b \times \left(\frac{\alpha\pi}{180}\right) + c \times PR + d \times N + e \times Re^{0.6}$					
	a	b	c	d	e	R^2
Nu	-1.632	2.437	-0.617	0.644	0.0413	0.92
PF	0.885	0.723	-0.0863	0.0356	0.0063	0.91

CHAPTER 6 HEAT EXCHANGER CORE ANALYSIS

6.1 Introduction

In the preceding chapters, the analysis assumed constant thermal boundary conditions on the walls. However, in this chapter, this is not valid because constant fluid temperatures were applied at the inlet sections of each cell within the heat exchanger core. This approach produces a temperature profile along the walls, differing from the previously assumed constant temperature conditions.

The entire heat exchanger, which consists of nine cells, was simulated to capture the detailed thermal and flow interactions across multiple cells of the heat exchanger. This choice was suitable for modeling the development of temperature profile along the flow path of the full heat exchanger stacks, which could not be achieved with one cell. The use of multiple cells allows for a more realistic representation of thermal gradients, ensuring that the design conclusions are robust and applicable to practical operating conditions.

Additionally, the nine-cell configuration enabled a comprehensive exploration of different swirl device arrangements, such as staggered and parallel configurations. This was essential to determine which combination would yield the highest effectiveness in enhancing heat transfer while maintaining acceptable pressure drops. Although this approach increased computational complexity, it provided critical insights into the optimal configuration strategies, supporting a more effective and practical heat exchanger design.

6.2 Computational domain

In the preceding chapters, the analysis of the heat transfer rate within the system was predicated on the assumption of constant thermal boundary conditions on the walls. In the present chapter, constant fluid temperatures to the inlet sections of each cell within the heat exchanger core

were applied. This approach yields a temperature profile along the walls, diverging from the previously assumed constant temperature boundary conditions.

Figure 6.1 describes the computational domain, which consists of a nine-cell heat exchanger core. Each cell is defined by a square cross sectional of 5.0 mm per side, bordered by a thin gap of 0.5 mm.

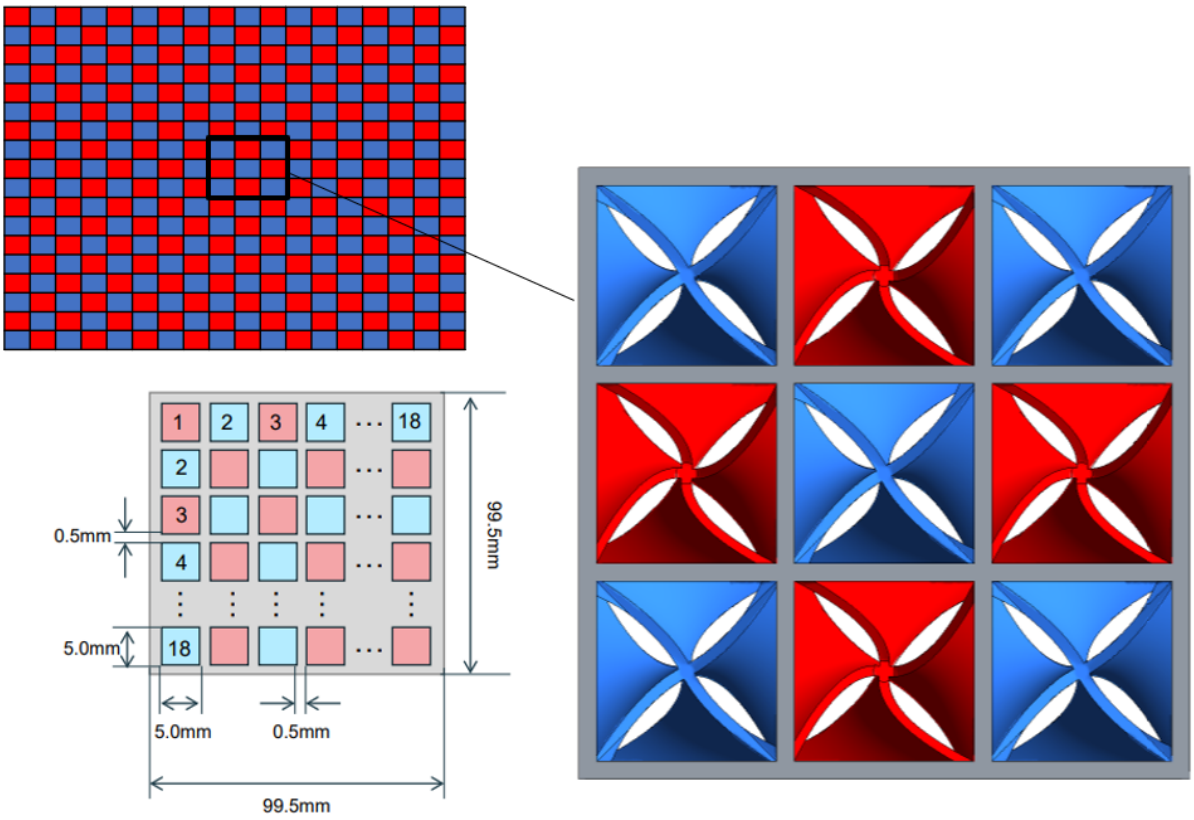

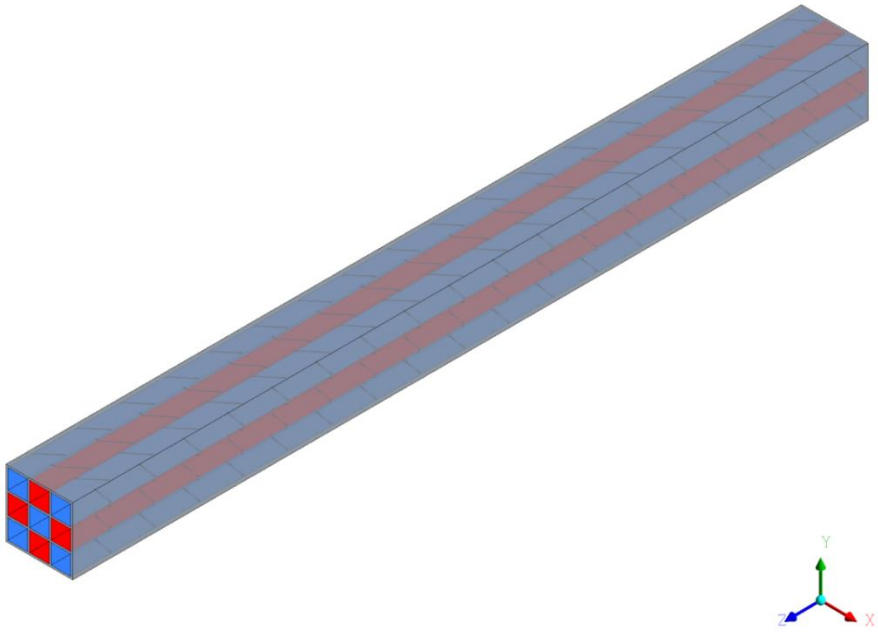

Figure 6-1: Computational domain of the nine HEX.

6.3 Mesh Generation and calculations

In this study, the computational domain's complexity necessitated a substantial number of mesh grids. To ensure accuracy and independence from the mesh size, a mesh independence study was conducted for both the smooth and novel heat exchanger designs. This study was performed under conditions where the mass flow rates for each cold and hot cell were set at 0.006 kg/s and 0.003 kg/s, respectively. The results indicated that a mesh count of approximately 35 million cells for the smooth design and 200 million cells for the new design was required to achieve mesh-independent solutions. These findings are detailed in Tables 6.1 and 6.2, respectively.

Table 6-1 Mesh sensitivity for smooth case

Mesh Sizes	Heat Transfer Rate, Q (W)	Pressure Drop, ΔP (Pa)
10 million	481.914	61.76
20 million	514.0416	65.88
35 million	535.46	68.63
50 million	537.06638	68.83

Table 6-2 Mesh sensitivity for novel design

Mesh Sizes	Heat Transfer Rate, Q (W)	Pressure Drop, ΔP (Pa)
90 million	1293.93	1186.80
150 million	1380.19	1265.92
200 million	1437.70	1318.67
250 million	1442.01	1322.62

6.4 Calculation

The heat transfer can be calculated from the following relations:

$$q = U\, A_s\, \Delta T_{LM} \tag{6.1}$$

$$q = \dot{m} C_p (T_{m,o} - T_{m,i)} \tag{6.2}$$

$$\Delta T_{LM} = \frac{\left(T_{h,o} - T_{c,i}\right) - \left(T_{h,i} - T_{c,o}\right)}{\ln \frac{\left(T_{h,o} - T_{c,i}\right)}{\left(T_{h,i} - T_{c,o}\right)}} \tag{6.3}$$

Where q is the heat transfer rate, U is the overall heat transfer coefficient.

Moreover, the effectiveness-NTU method were utilized to evaluate the effectiveness of the system using the following equations:

$$UA = \frac{q}{\Delta T_{LM}} \tag{6.4}$$

$$C_c = (\dot{m} C_p)_{cold} \quad and \quad C_h = (\dot{m} C_p)_{hot} \tag{6.5}$$

$$C_r = \frac{C_{min}}{C_{max}} \tag{6.6}$$

$$q_{max} = C_{min}(T_{h,i} - T_{c,i}) \tag{6.7}$$

$$NTU = \frac{UA}{C_{\ min}} \tag{6.8}$$

$$\varepsilon = \frac{q}{q_{max}} \tag{6.9}$$

$$Thermal - hydraulic\ Performance = \frac{\left(\frac{UA_{swirl}}{UA_{smooth}}\right)}{\left(\frac{\Delta P t_{swirl}}{\Delta P t_{smooth}}\right)^{\frac{1}{3}}} \tag{6.10}$$

6.5 Flow field and heat transfer results

High-performance computing facilities were utilized to manage the computational demands of the simulations, executed through journal files in ANSYS Fluent.

6.5.1 Smooth Base Case Analysis

The results of this chapter begin with a detailed examination of a smooth heat exchanger, which establishes the foundational baseline for the subsequent analysis of enhanced geometries. The exploration examines the fundamental flow dynamics and heat transfer characteristics of this configuration, to create a benchmark against the performance of modified designs that can be measured.

Figures 6.2 shows the temperature distributions along the streamwise direction for the smooth case. The trend was as expected, the hot cells losses heat along the streamwise direction while the cold cells gain that heat.

Figure 6.3 illustrates the performance of the smooth heat exchanger under various mass flow rates of the cold fluid. The graph reveals that, as the mass flow rate of the cold fluid increases, there is a corresponding gradual slight reduction in the outlet temperature of the hot fluid. The relatively small heat transfer, as evidenced by the small temperature differential between the inlet and outlet of the hot cell, suggests an area of potential optimization in the heat exchange process.

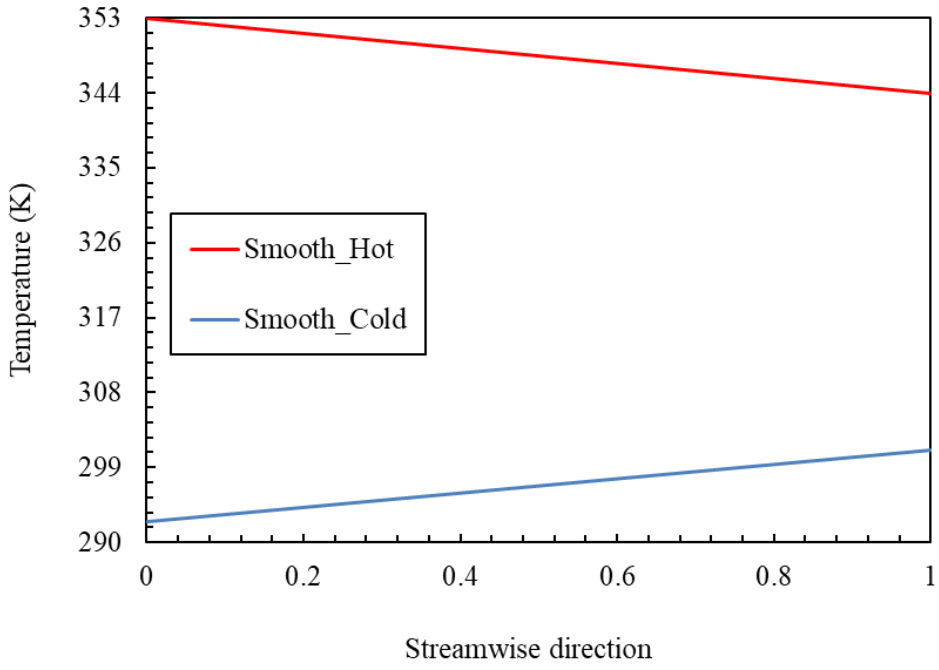

Figure 6-2 Temperature profile along the channel for the base case.

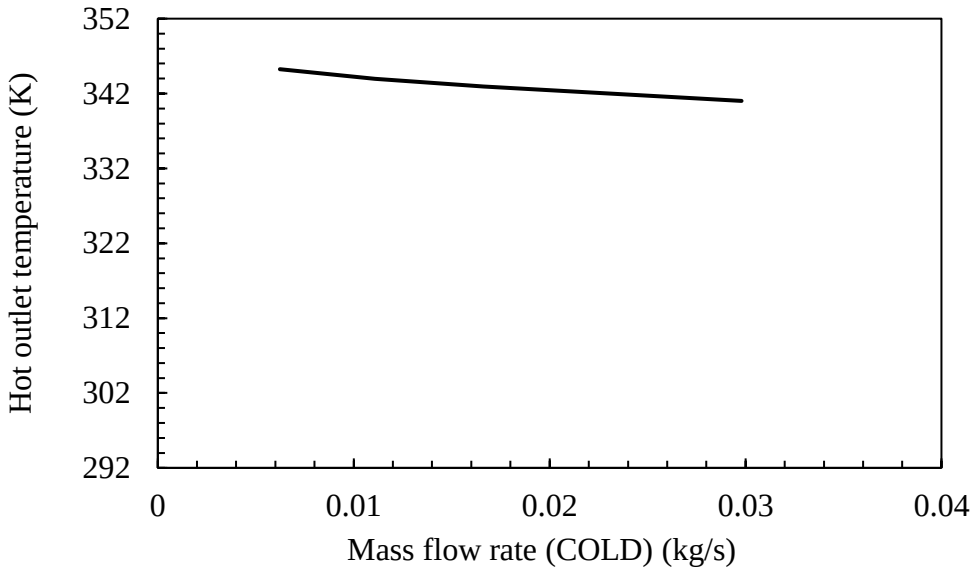

Figure 6-3 Hot outlet temperature at different cold flow rates

Figure 6.4 shows a plot of heat transfer rate (Q) in watts (W) as a function of the mass flow rate of the cold fluid in (kg/s) for the smooth heat exchanger. From the graph, it is evident that

as the mass flow rate of the cold fluid increases, the heat transfer rate (Q) also increases. This positive correlation suggests that the higher the mass flow rate of the cold fluid, the greater the amount of heat that is being transferred away from the hot fluid, which is consistent with the principles of convective heat transfer.

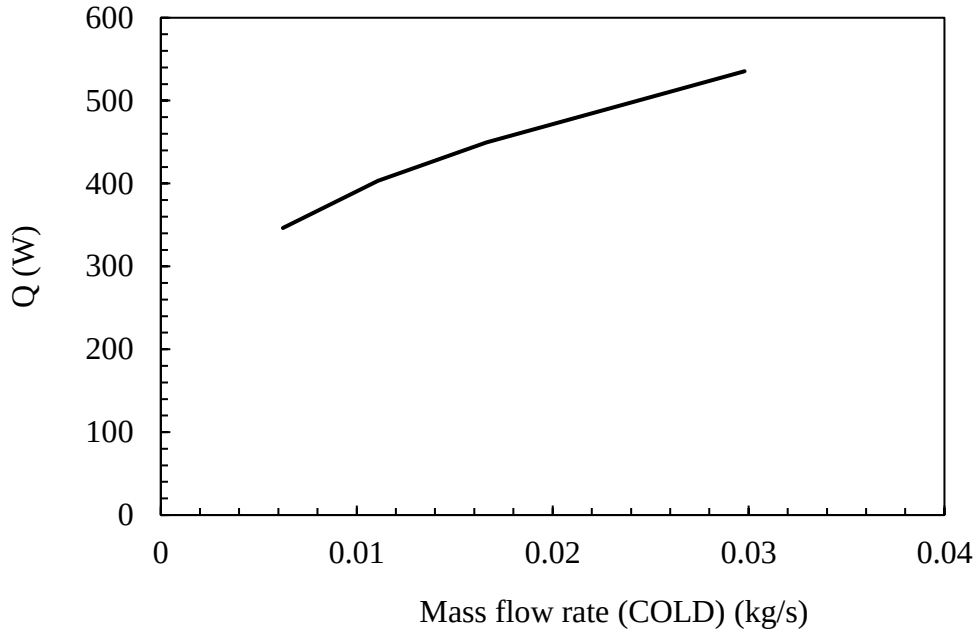

Figure 6-4 Heat transfer at different cold flow rates

Figure 6.5 is a plot of the overall heat transfer coefficient multiplied by the surface area (UA) against the mass flow rate of the cold fluid in a smooth heat exchanger. The UA value is a measure of the heat exchanger's ability to transfer heat and has units of (W/K).

From the graph, there is an upward trend, indicating that as the mass flow rate of the cold fluid increases, the UA value also increases. This implies that the heat transfer capability of the heat exchanger improves with higher mass flow rates of the cold fluid. A higher UA value suggests better performance of the heat exchanger, as it can transfer more heat per unit temperature difference between the hot and cold fluids.

The effectiveness versus NTU, with each point representing a different mass flow rate, shown in Figure 6.6, illustrates how the heat exchanger's performance varies with changes in the cold fluid's flow. As the NTU increases, which implies a larger surface area for heat transfer or a lower flow rate, the effectiveness of the heat exchanger increases, indicating a substantial proportion of the theoretical maximum heat transfer is being achieved.

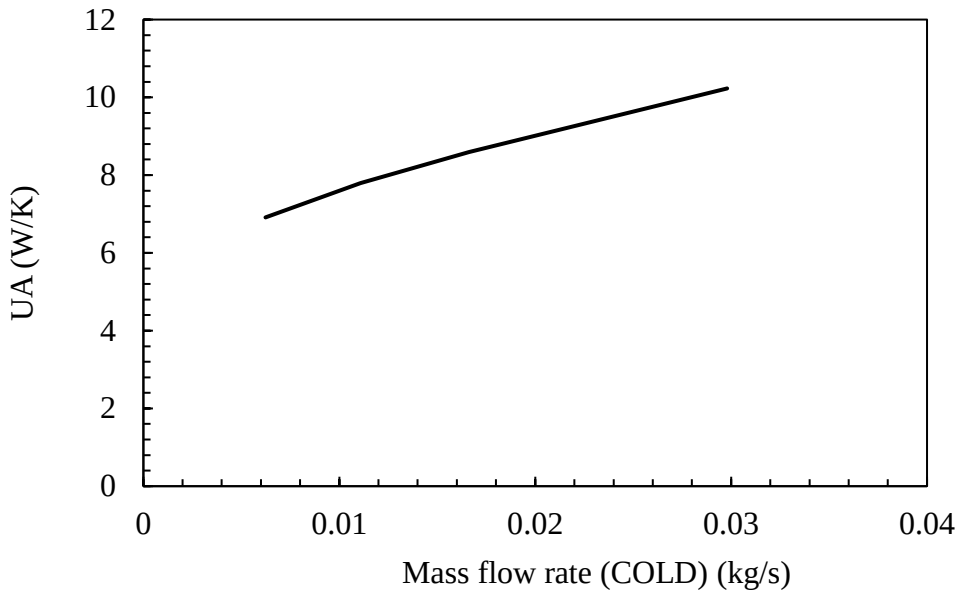

Figure 6-5 Variation of UA at different mass flow rates

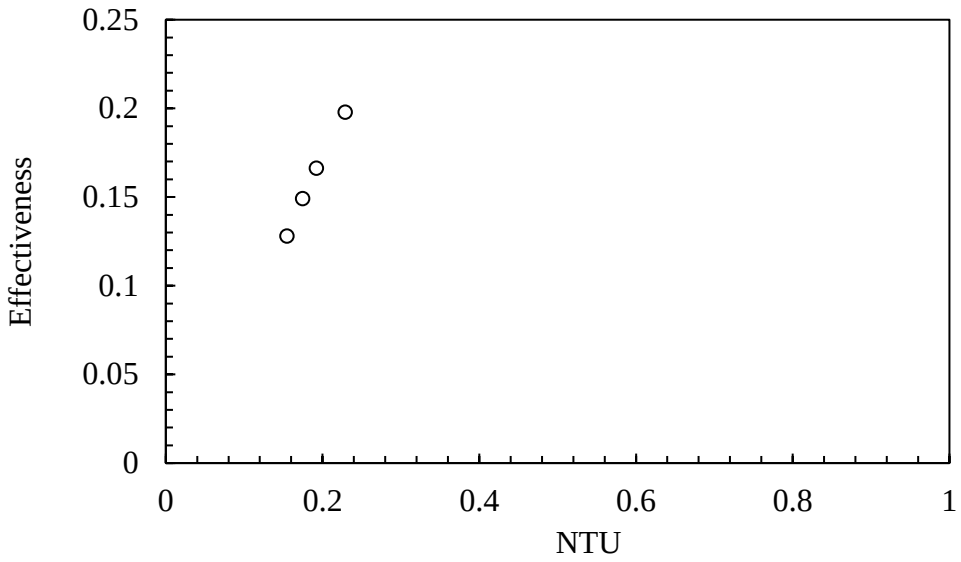

Figure 6-6 Effectiveness vs NTU for the smooth HEX

6.5.2 Novel design Heat Exchanger

The goal of this parallel/staggered arrangement study is to achieve the highest heat transfer rate while considering the pressure drop penalty. In this section, the author assesses the impact of novel design streamwise arrangements. Figure 6.7 shows the arrangements of staggered and parallel channels.

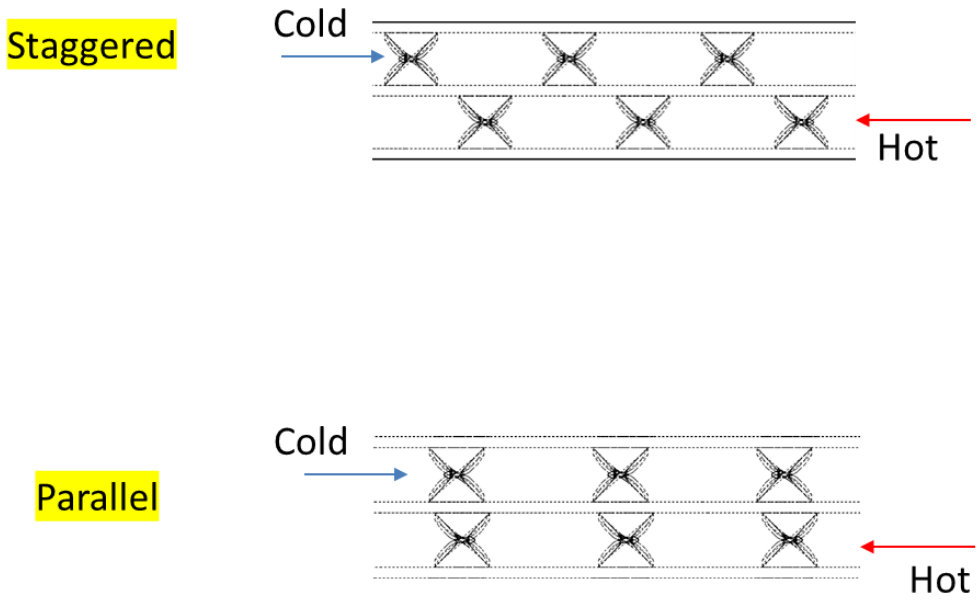

Figure 6-7 The staggered and parallel arrangements.

Figure 6.8 illustrates the specific location at which contours were taken. The figure provides two views: an isometric and side views of the three middle cells of the heat exchanger.

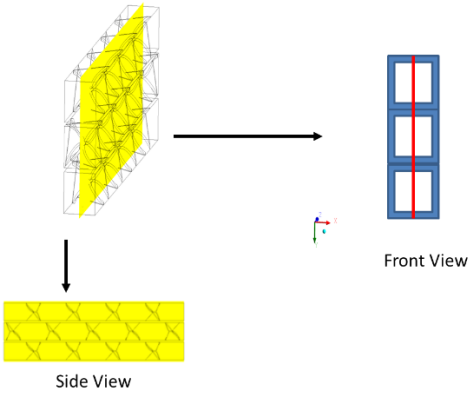

Figure 6-8: Location where contours are taken

Figure 6.9 and Figure 6.10 present the velocity contours and velocity vectors for the two different streamwise arrangements in the heat exchanger core, one being parallel and the other staggered. Interestingly, the parallel arrangement has resulted in a flow pattern that resembles a staggered structure. Conversely, the arrangement that was originally staggered now exhibits a flow structure that like a parallel configuration.

The circled areas in the figure highlight a significant trend: in the staggered arrangement, the flow impinges on the heat exchanger walls at each adjacent cells at focused spots. This consistent impingement can enhance heat transfer due to increased turbulence and localized high-velocity gradients which results in a reduced boundary layer thickness from both sides of the adjacent cells. In contrast, in the parallel arrangement, the flow impacts the walls at varying locations. This variation can result in a more uniform distribution of the thermal across the wall surfaces.

The implications of these flow behaviours on the heat exchanger's performance are profound. In the staggered arrangement, the targeted impingement could be utilized for areas requiring

intense heat transfer, whereas the parallel configuration's impact might be preferable for uniform temperature distribution.

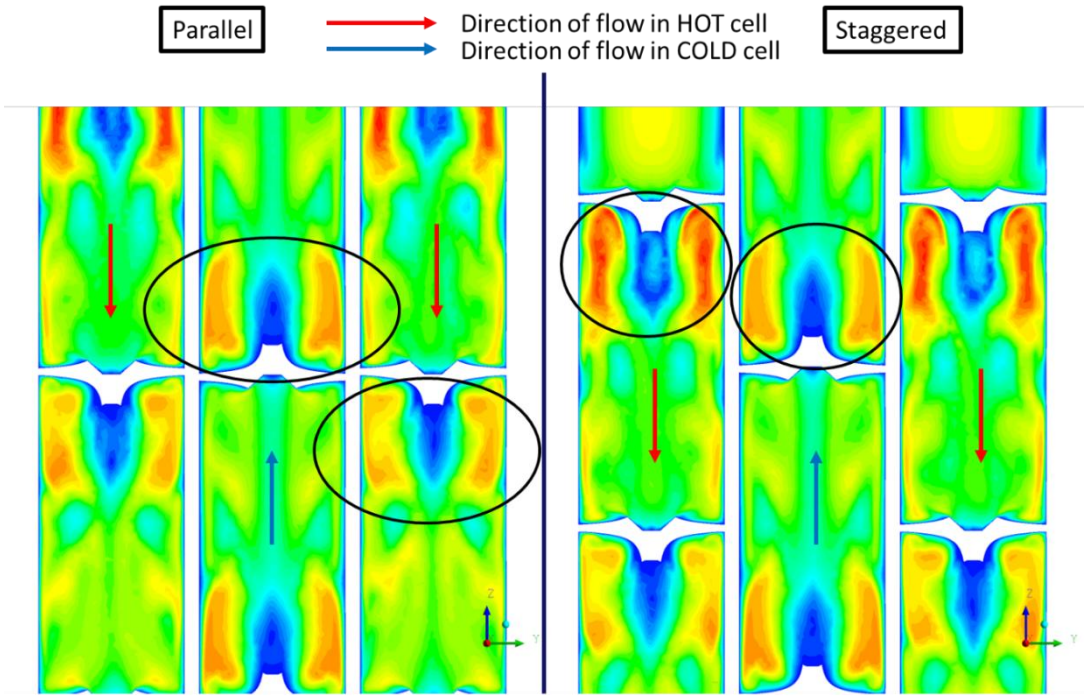

Figure 6-9 Velocity contours for hot and cold cells

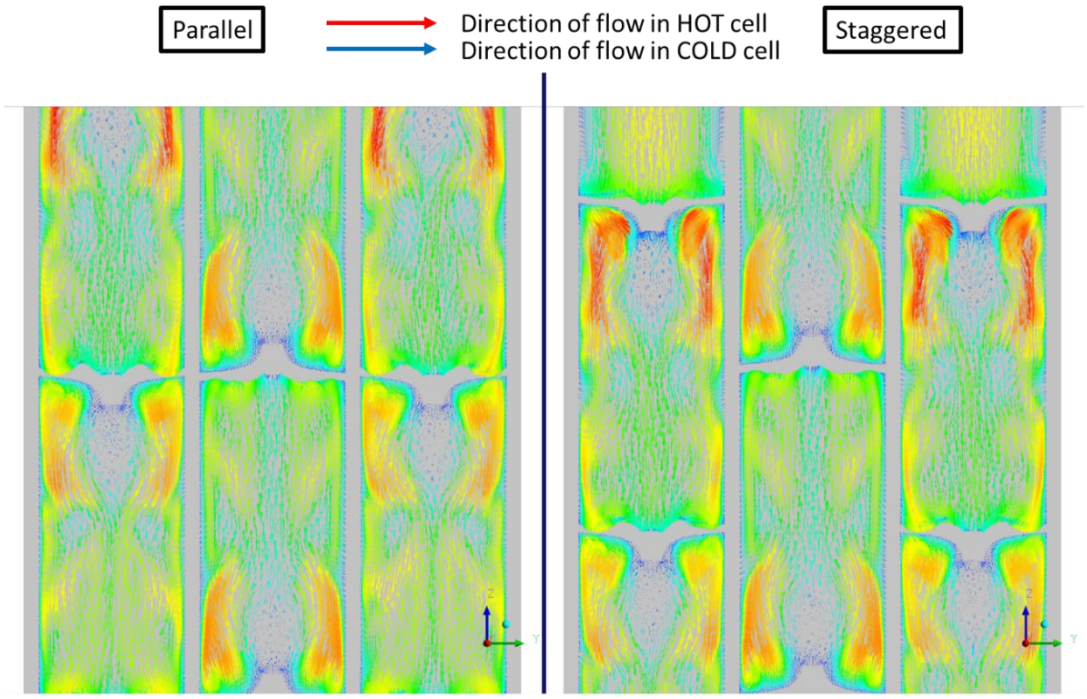

Figure 6-10 Velocity vectors in the hot and cold cells

Figure 6.11 provides a representation of the temperature distribution from the inlet to the outlet of the channel for the smooth, staggered, and parallel heat exchanger configurations

In the smooth configuration, the temperature gradient is linear and consistent, indicating a stable thermal boundary layer with minimal disturbance. This is characteristic of laminar flow, where the boundary layers are well-defined and relatively thick due to the orderly flow of fluid particles.

The parallel and staggered configurations introduce structural elements into the flow path, which disrupt the velocity profile and, consequently, the thermal boundary layer. The novel devices promote flow impingement, which significantly disrupts the boundary layer, leading to an even thinner thermal boundary layer and more effective heat transfer. Moreover, it creates a complex flow pattern that enhances mixing and transport of thermal energy away from the hot surfaces.

Comparatively, the smooth configuration exhibits a clear distinction between the core flow and the boundary layer, while the parallel and staggered configurations show increased mixing and reduced boundary layer thickness, indicative of higher heat transfer rates.

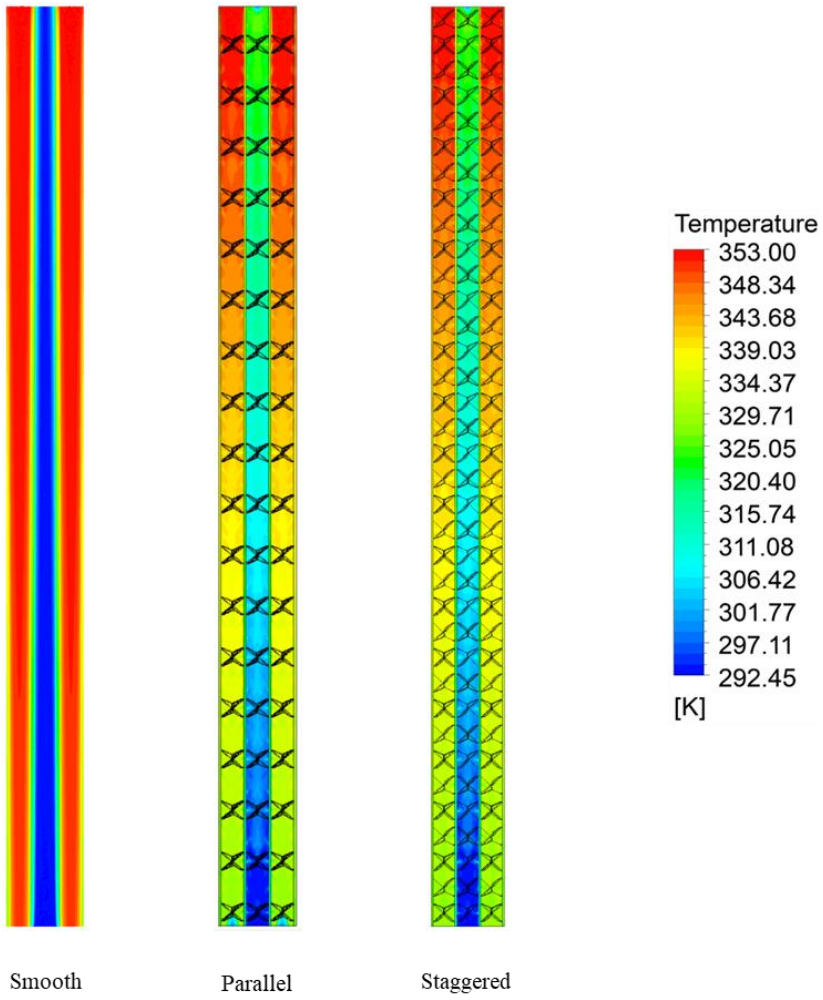

Figure 6-11 temperature distribution from the inlet to the outlet of the channel for the smooth, parallel, and staggered heat exchanger configurations

The sequence of Figures 6.12, 6.13, and 6.14 displays the progression of velocity and temperature profiles at increasing distances from the inlet in a heat exchanger channel for the three configurations: smooth, parallel, and staggered. These figures are helpful in illustrating the thermal-fluid dynamics as cold fluid enters and hot fluid exits the heat exchanger.

Figure 6.12 demonstrates the initial conditions at $Z/D_h = 5$, where Z is the streamwise distance from the inlet, and D_h is the hydraulic diameter of the channel. In the smooth configuration, the velocity profile is uniform, and the temperature distribution is symmetrical, indicating

laminar flow and steady thermal conditions. The boundary layer is clearly defined, and the thermal boundary layer is distinct, allowing for predictable heat transfer patterns.

As we move to Figure 6.13, at Z/D = 20, we see the evolution of the flow. In the parallel and staggered configurations, the increased interaction between the fluid and the channel's structural elements causes the velocity profiles to develop more complexity, disrupting the boundary layer. This is particularly noticeable in the staggered configuration, where flow impingement leads to a thinner boundary layer, enhancing the heat transfer due to increased turbulence. The temperature contours in these configurations start to show greater variation compared to the smooth setup, indicating an improved heat transfer from the disrupted flow.

Finally, Figure 6.14 at Z/D = 40 further down the channel, the developed flow in the parallel and staggered configurations exhibits even more pronounced disturbances. The staggered configuration, in particular, shows a significant impact on the temperature contours due to the intense mixing and vortex generation, which further disrupts the thermal boundary layer and enhances heat transfer.

Compared to smooth configuration, the staggered and parallel configurations demonstrate the significant influence of flow dynamics on thermal performance. The staggered configuration, with its pronounced flow impingement, results in the thinnest boundary layers and most efficient heat transfer.

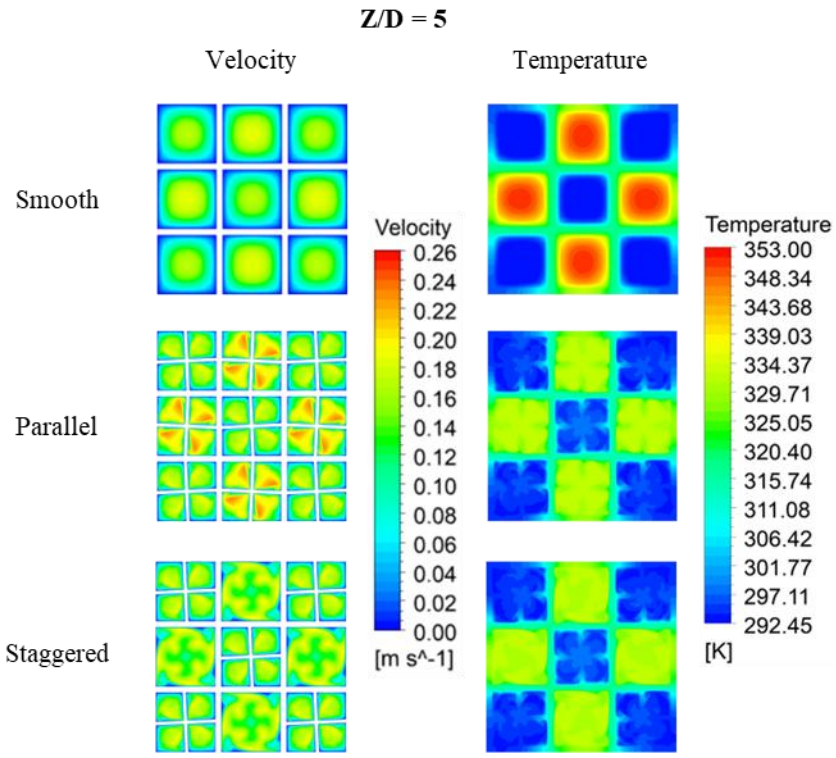

Figure 6-12 Velocity and temperature profiles of the hot and cold cells at Z/D = 5

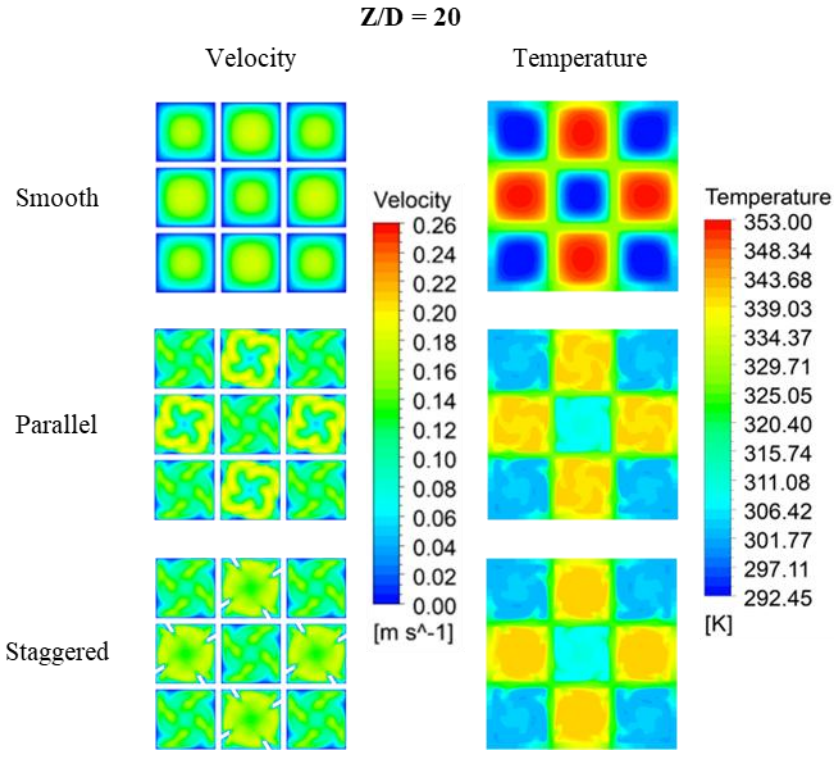

Figure 6-13 Velocity and temperature profiles of the hot and cold cells at Z/D = 20

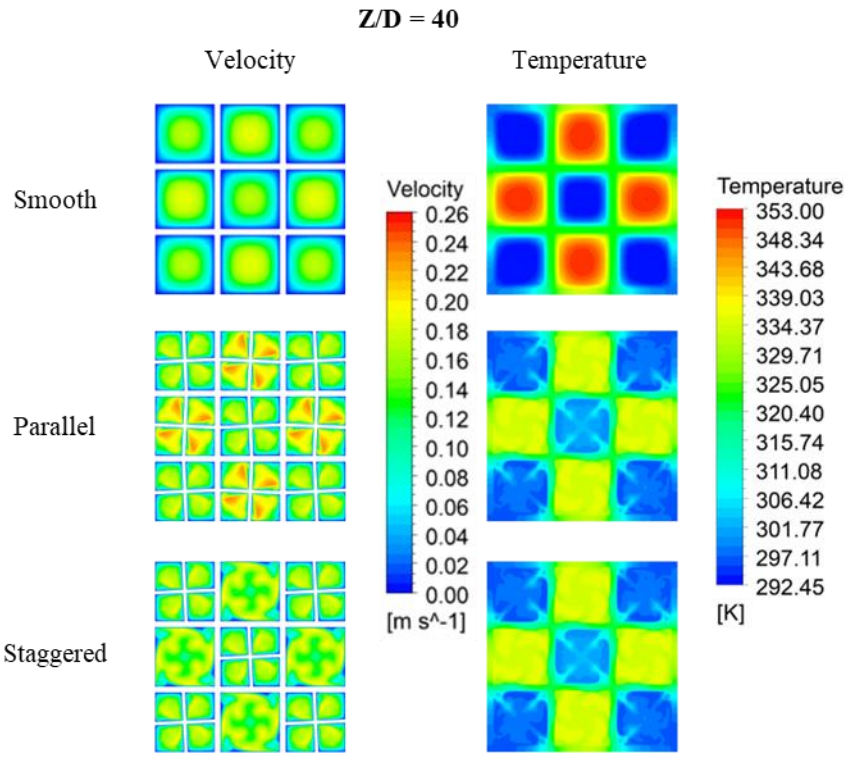

Figure 6-14 Velocity and temperature profiles of the hot and cold cells at Z/D = 40

Figure 6.15 presents the inlet and outlet temperatures for both hot and cold fluids in a heat exchanger (HEX) with the three design configurations: staggered, parallel, and smooth. The graph demonstrates how the design of the heat exchanger impacts the thermal gradient experienced by the fluids as they pass through the system. The staggered configuration shows a significant temperature drop for the hot fluid and a notable temperature rise for the cold fluid, indicating effective heat transfer. The parallel configuration exhibits a slightly less pronounced thermal gradient for both fluids, while the smooth configuration shows the least temperature change from inlet to outlet for both fluids.

This suggests that the staggered design is the most effective at transferring heat, likely due to the increased heat transfer rate generated from the flow impingement on the same spot from both sides of the adjacent cells. This confirms our early findings about the effectiveness of Novel design when compared against the smooth configuration.

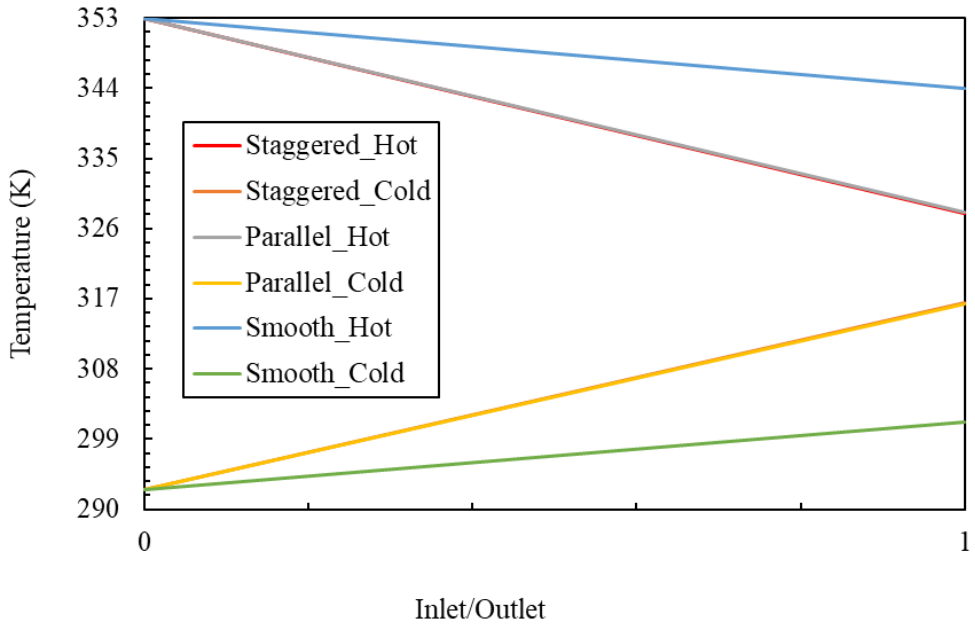

Figure 6-15 The inlet and outlet temperatures for both hot and cold fluids in a heat exchanger (HEX) with three different design configurations.

Figures 6.16 through 6.19 collectively examine the thermal performance of a nine-cell heat exchanger with the three designs—smooth, staggered, and parallel—focusing on the effects of altering the cold cell mass flow rate, while maintaining a constant mass flow rate for the hot cells. Each figure contributes a unique aspect to the holistic understanding of the heat exchanger's performance.

Figure 6.16 showcases the heat transfer rate (Q) across the different designs. As expected, the staggered and parallel configurations significantly outperform the smooth design, suggesting that these configurations enhance the heat exchanger's ability to transfer heat.

Figure 6.17 depicts the overall heat transfer coefficient multiplied by the surface area (UA). Again, the staggered and parallel configurations display superior performance over the smooth design, indicating more efficient heat exchange capabilities.

Figure 6.18 presents the outlet temperature of the hot fluid. The lower temperatures for the staggered and parallel designs, compared to the smooth configuration, indicate a more effective removal of heat from the hot fluid.

Figure 6.19 examines the thermal-hydraulic performance, a metric that combines thermal efficiency and pressure drop penalty of the heat exchanger. The staggered design shows a slight advantage over the parallel design, suggesting a balance of efficient heat transfer and fluid flow dynamics when compared to the smooth configuration.

In summary, these figures validate the heat transfer augmentation provided by the staggered and parallel designs when compared to the traditional smooth design.

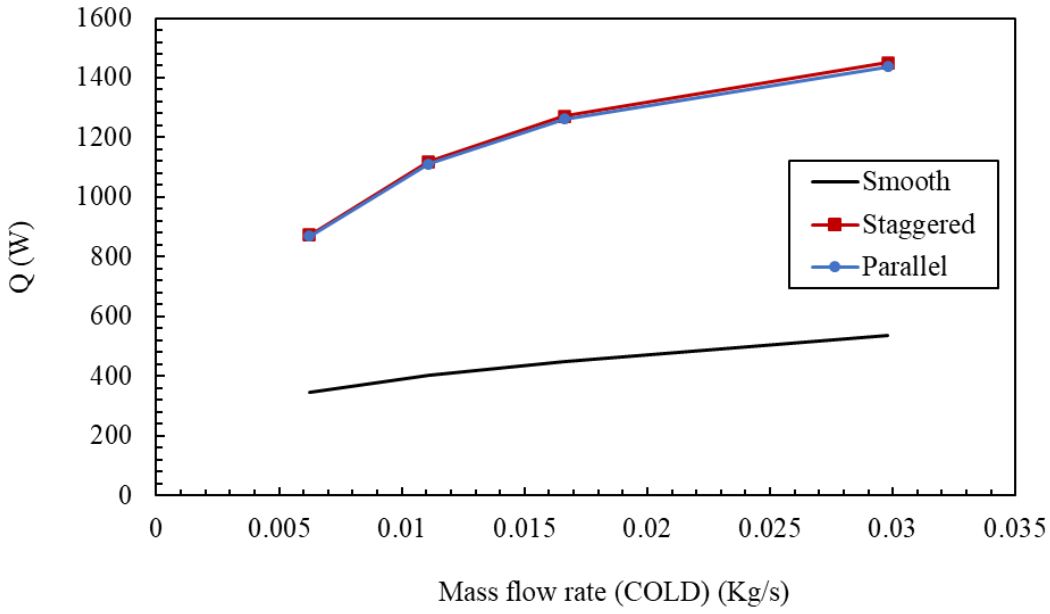

Figure 6-16: Effect of variation of mass flow rate of the cold cells while keeping the hot cells mass flow rate constant vs Q

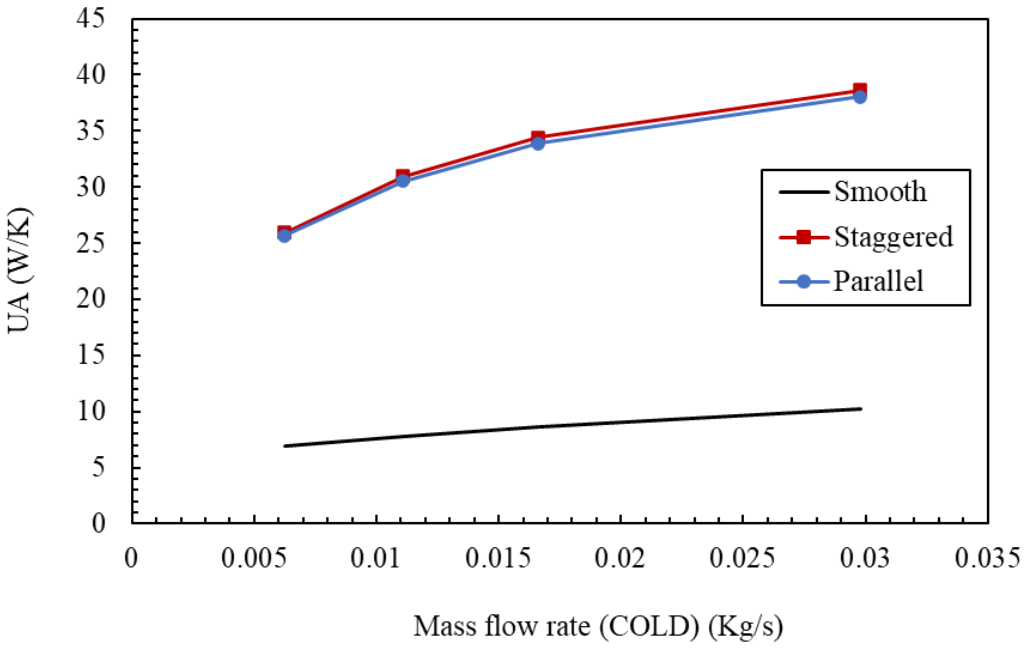

Figure 6-17: Effect of variation of mass flow rate of the cold cells while keeping the hot cells mass flow rate constant vs UA

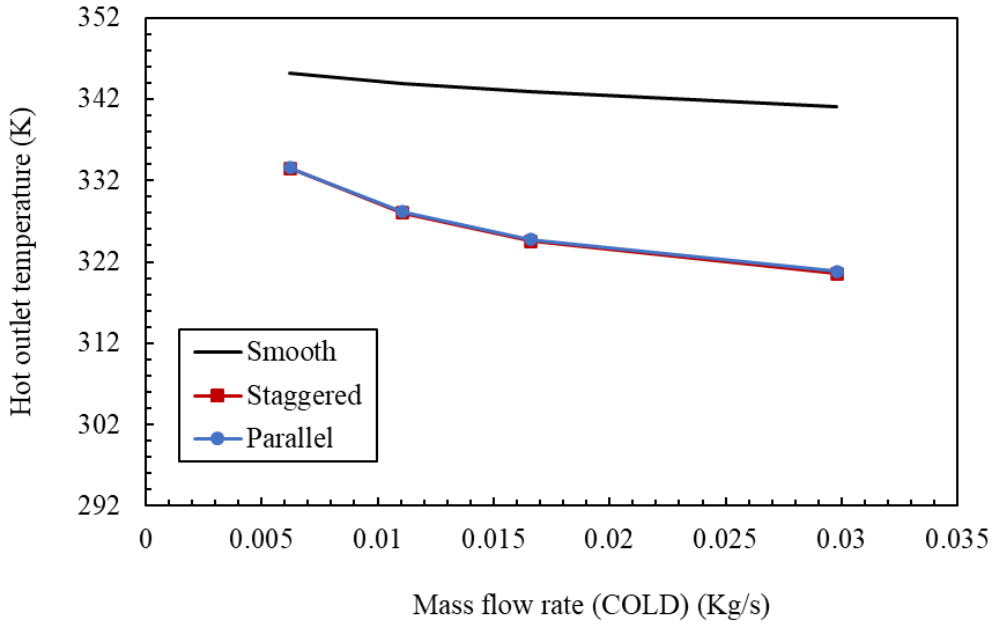

Figure 6-18: Effect of variation of mass flow rate of the cold cells while keeping the hot cells mass flow rate constant Vs hot outlet temperature.

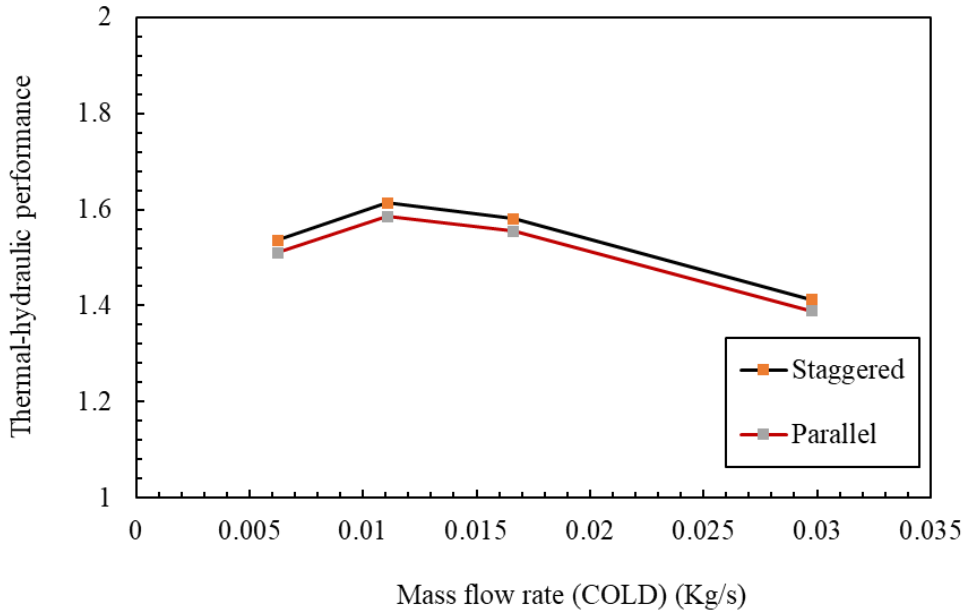

Figure 6-19: Effect of variation of mass flow rate of the cold cells while keeping the hot cells mass flow rate constant vs Thermal-hydraulic performance

Figure 6.20 presents a comparative analysis of heat exchanger effectiveness across three configurations: smooth, staggered, and parallel, plotted against the Number of Transfer Units (NTU). It is clear from the plot that as NTU increases, the effectiveness of the heat exchanger also generally increases for each design. Notably, the staggered configuration achieves an effectiveness of 55%, which is significantly higher than the 19.7% observed for the smooth configuration at the same mass flow rate. This marked disparity in performance demonstrates a percentage increase in effectiveness of approximately 179% when transitioning from a smooth to a staggered design. Such an increase underscores the substantial enhancement in heat transfer efficiency that can be achieved through design modifications.

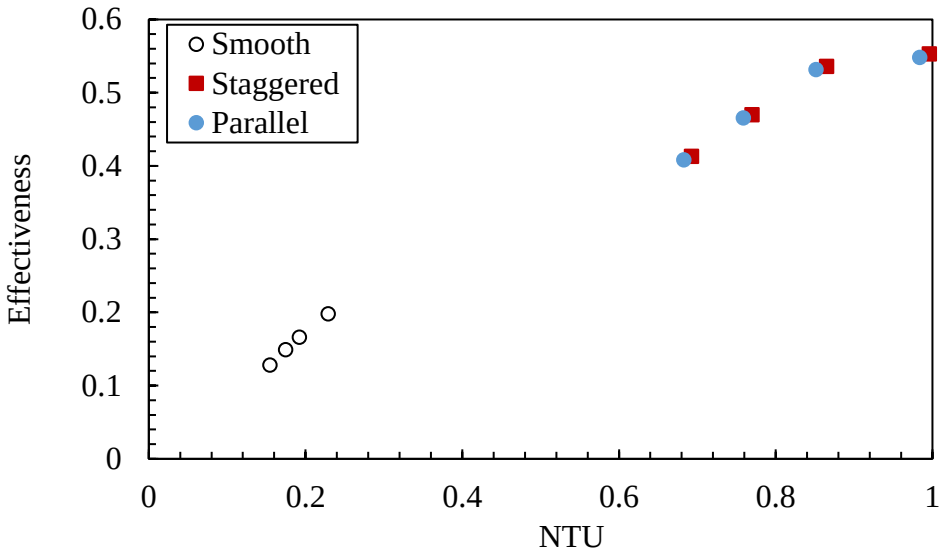

Figure 6-20: Number of transfer units vs Effectiveness.

CHAPTER 7 MANIFOLD DESIGN

7.1 Introduction

The objective of this chapter is to propose an innovative approach for addressing the problem of uneven flow distribution in the heat exchange core. While numerous designs and arrangements have been investigated, for the sake of conciseness, the author will only elaborate on the most promising design.

The design optimization of manifold in compact HEX needs to take in consideration the flow uniformity, thermal performance, cost, and space. This study did not focus on heat transfer analysis, but it acknowledges the crucial role of flow uniformity in compact heat exchanger design for optimal thermal performance. Uniform flow distribution minimizes maldistribution, which can cause inefficiencies, hotspots, or underutilized heat transfer surfaces. The manifold design aimed to achieve adequate flow uniformity, guided by computational fluid dynamics (CFD) simulations.

Although mass flow rate distribution was used as a performance metric, it is not the ultimate indicator of thermal performance. However, uniform mass flow is linked to improved thermal performance, ensuring even utilization of heat transfer surfaces [133–144]. Future work should consider the effect of the flow uniformity on overall thermal performance of the system.

7.2 Concept of flow mal-distribution inside manifold

A manifold, also known as a header, serves as an interface between the heat exchanger core and the external piping system. It consists of a distribution manifold, which distributes the incoming fluid across the heat exchanger core, and a collection manifold that collects the outgoing fluid from the core.

In most heat exchangers, the manifold consists of a series of interconnected tubes or passages that are designed to accommodate the required fluid flow rates, pressures, and temperatures. These tubes are often arranged in a parallel or series configuration, depending on the specific heat exchanger design and application. The parallel configuration allows for the simultaneous flow of multiple fluid streams, while the series configuration directs the fluid sequentially through the heat exchanger core.

The manifold's primary function is to distribute the incoming fluid uniformly across the heat exchanger core. This even distribution ensures that the entire surface area of the core is utilized effectively, maximizing the heat transfer potential. By avoiding preferential flow paths or hot spots, the manifold promotes balanced heat distribution, preventing thermal inefficiencies and potential damage to the heat exchanger.

To optimize the performance of the manifold, engineers consider factors such as dimensions, shape, and arrangement of the manifold passages.

7.3 Computational Domain and Grid Generation

7.3.1 Base Case: Z-shape and U-shape

To start investigating the optimal manifold design, base design of Z and U arrangements are considered. The first computational domain represents the Z manifold design, which consists of nine interconnected channels arranged in a sequential "Z" pattern. The dimensions of the manifold are as shown in Figure 7.1. It represents a three-dimensional fluid domain of one layer (cold/hot) of the heat exchanger stacks.

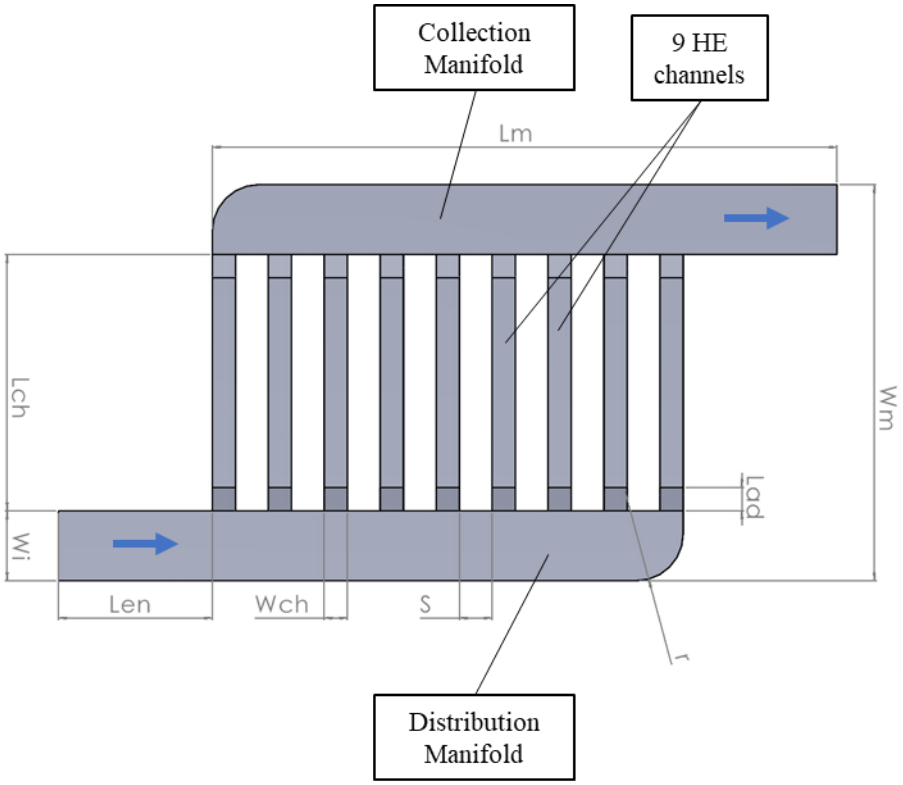

Figure 7-1 Drawing of the Z-shaped manifold

The dimension of the computational domain accurately captures the geometric features of the manifold, including the manifold inlet width (Wi), manifold length (Lm), manifold width (Wm), manifold entrance length (Len), manifold fillet radius (r), space between adjacent channels (S), channel length (Lch), channel width (Wch), adapter length (Lad).

The inlet of the manifold serves as the entry point for fluid into the distribution manifold. Meanwhile, the outlets, located at the ends of the interconnected channels, facilitate the exit of fluid through the collection manifold. The channels are arranged in a zigzag pattern, with each channel connecting to its adjacent channels in the other layer (hot/cold fluid) at regular intervals.

The second base case computational domain represents the U manifold design, which consists of exact number of channels and dimensions as that of the Z configuration. Figure 7.2 illustrates

the U arrangement computational domain used in this study. Table 7.1 provides all the dimensions values of the manifold base case.

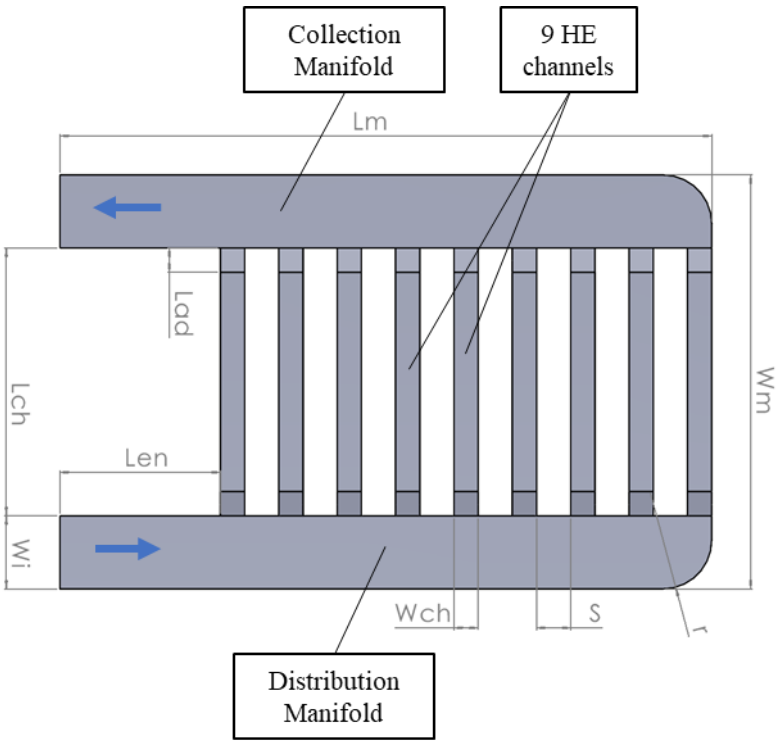

Figure 7-2 Drawing of the U-shaped manifold

Table 7-1 Dimensions values of the manifold base case

Parameter	Value
Wi	*65-90*
Lm	167
Wm	120
Len	33
r	10
S	7
Lch	55
Wch	5
Lad	5
All dimensions are in mm	

7.3.2 Manifold Design

The heat exchanger core arrangement discussed in this study is quite complex. It involves connecting four rectangular 'hot cells' to each side of a rectangular 'cold cell'. This design presents considerable challenges in designing the manifold. The complexity arises mainly from the necessity to accurately control how the fluid flows through the core, due to its unique layout.

To address these challenges, a specific design has been proposed. This design features an 18 x 18-layer arrangement of the fluid region, as depicted in Figure 7.3. The arrangement is carefully planned to ensure optimal heat exchange performance within the system. Essentially, this design provides a thorough solution to efficiently manage the flow uniformity, hence, heat transfer between the hot and cold regions, ensuring the system operates effectively.

In Figure 7.4 and Table 7.2, a comprehensive description of the design is presented, focusing on the incorporation of guide vanes at the manifold entrance. These guide

vanes play a crucial role in dividing the manifold into three sections, each of which contains an array of channels. These arrays vary in number, with options of 9, 12, 15, or 18 channels in total, thereby allowing for flexibility and customization in the system's configuration. This design element is instrumental in achieving an efficient distribution of fluid flow and optimizing heat transfer within the heat exchanger core.

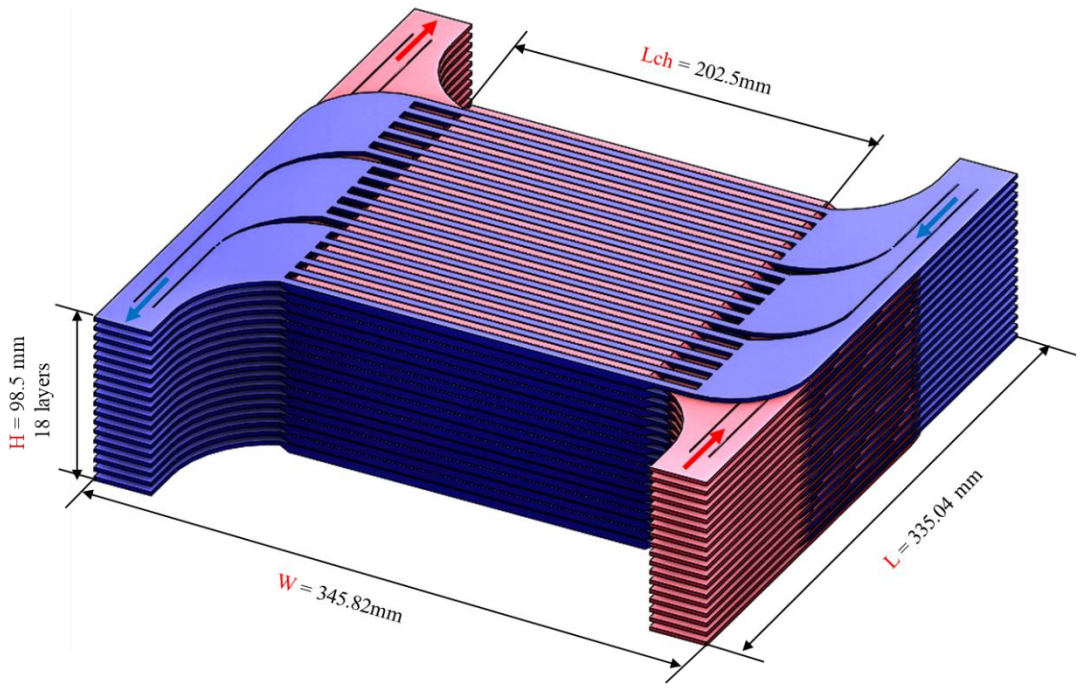

Figure 7-3: Manifold design.

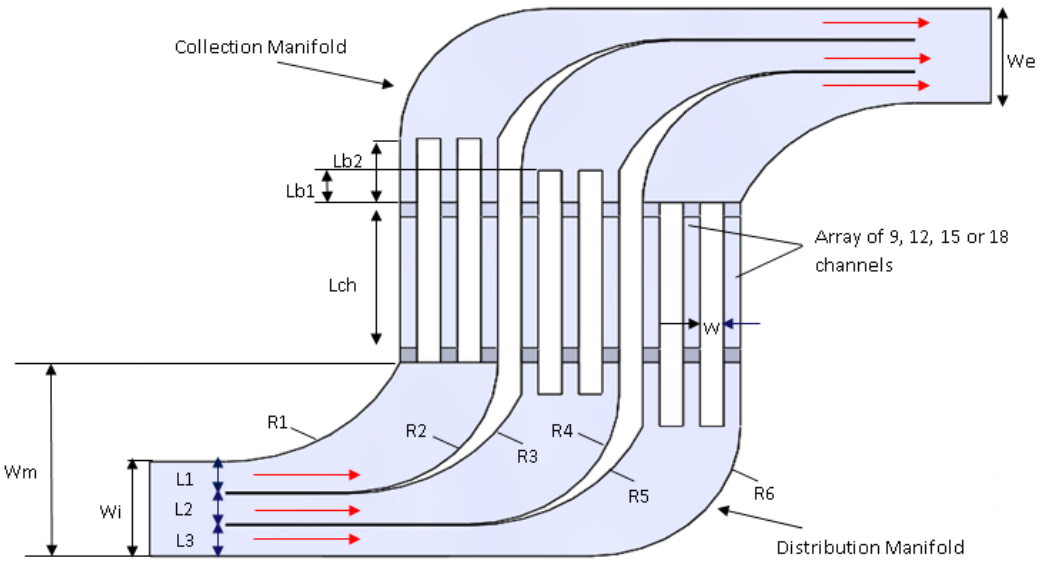

Figure 7-4 Manifold design with entrance guide vanes

Table 7-2 Dimensions values of the manifold with guide vanes at the inlet

Parameter	Value
R1 = R3 = R5	56.14mm
R2 = R4 = R6	44.66mm
L1 = L2 = L3	10.5mm
Wi = We	32.5mm
Wm	66.66mm
w	6mm
Lch	202.5mm
Lb1	11mm
Lb2	22mm

7.3.3 Grid Generation

To ensure the validity of the results, a mesh independent study was performed and the result of 10 million cells was used as an independent solution. Figure 7.5 represents the mesh independent study for the basic Z-shape. 20 Inflation layers were created to capture the physics near the wall as shown in Figure 7.6.

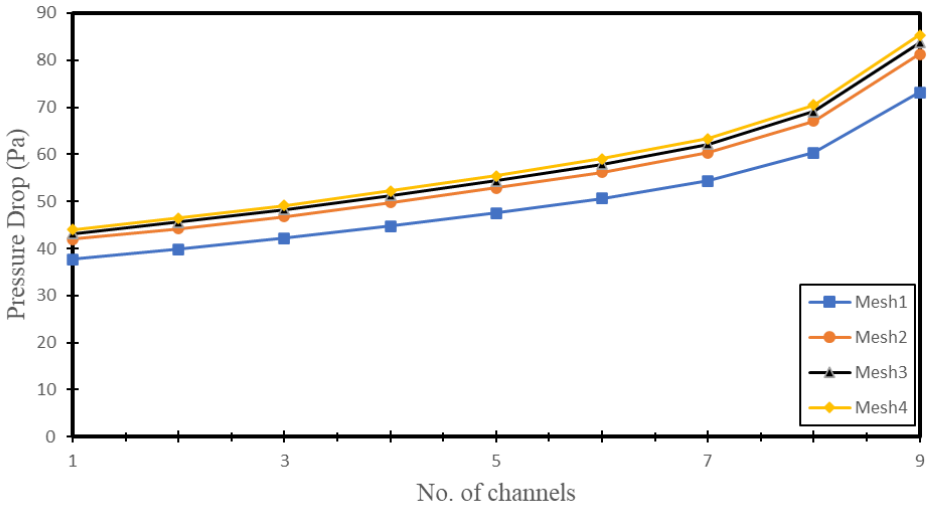

Figure 7-5 The pressure drop at different mesh sizes

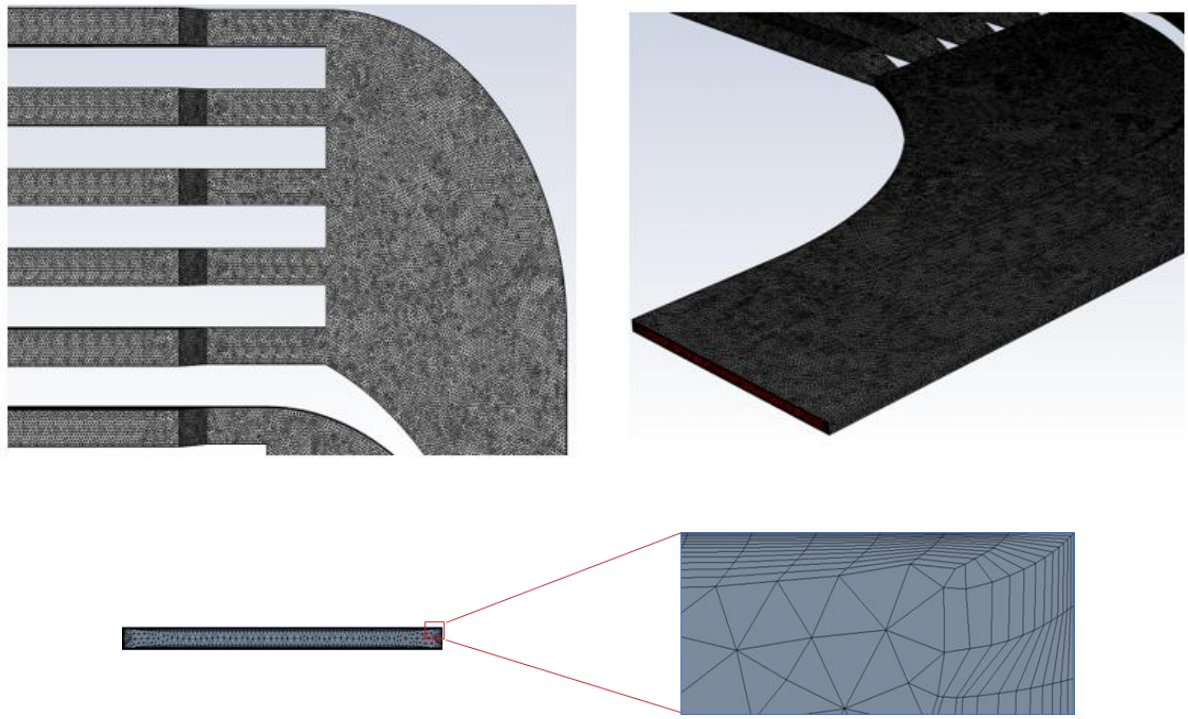

Figure 7-6 Mesh generation shows dense mesh at the walls

7.4 Boundary Conditions

Figure 7.7 showcases the boundary conditions applied in this study. The analysis operates within a Reynolds number range of 300 to 10,000, calculated based on the hydraulic diameter

of the manifold. At the inlet, a constant mass flow rate is applied, ensuring a steady supply of fluid into the manifold. The outlet is defined as a pressure outlet condition, where the pressure is set to atmospheric. All the faces are treated as walls, which implies that the fluid has no slip condition at these boundaries, meaning that the velocity of the fluid relative to the wall is zero.

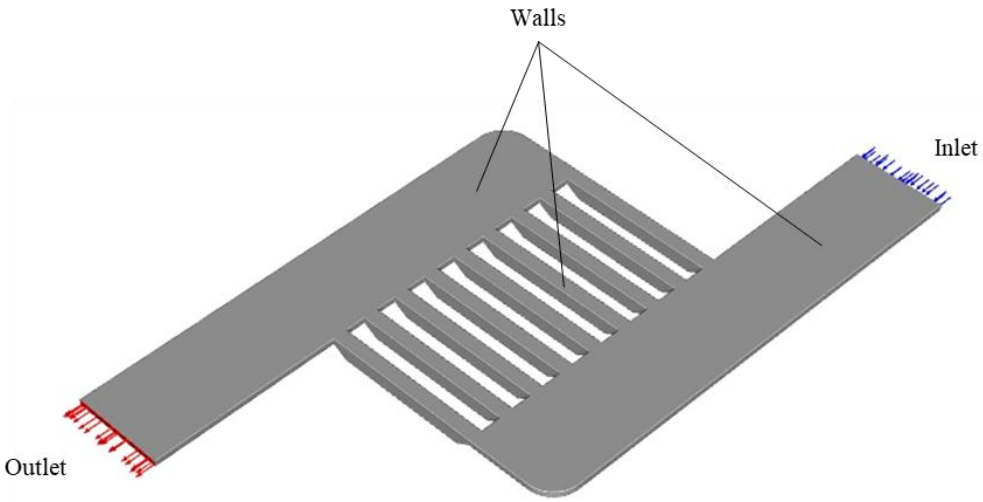

Figure 7-7 boundary conditions applied in this study

7.5 Calculation

The area-averaged mass flow rate is calculated for each channel, which is then compared to the averaged mass flow rate calculated at the inlet of the manifold. The Standard Deviation (SD) of the average channel mass flow rates for all channels is given by the formula:

$$SD = \sqrt{\frac{1}{N}\sum_{i=1}^{N}(\dot{m}_{ave,each\ channel} - \dot{m}_{in})^2} \tag{7.1}$$

Where $\dot{m}_{ave,each\ channel}$ represents the area-averaged mass flow rate of an individual channel, $\dot{m}_{in}$ is the area-averaged mass flow rate at the inlet, and N is the number of channels.

Another criterion used in this study is the ratio of the maximum mass flow rate to the minimum mass flow rate, which is used to assess the worst-case scenario of flow maldistribution:

$$W_{\dot{m}} = \frac{\dot{m}_{max}}{\dot{m}_{min}} \tag{7.2}$$

Here, $\dot{m}_{max}$ is the maximum mass flow rate observed among all the channels, and $\dot{m}_{min}$ is the minimum mass flow rate. This ratio is a key indicator of the extent of flow non-uniformity within the manifold.

7.6 Results and Discussions

7.6.1 Base design analysis

The base design of the Z and U configurations is fundamental to the investigation of fluid dynamics within manifold systems, with the objective of optimizing key performance indicators such as flow distribution and pressure drop. Conducting a comparative analysis of these designs is vital to grasp the details of fluid mechanics that govern the behaviour within the manifolds, thereby establishing a basis for future modifications aimed at enhancing specific operational efficiencies.

In the following sections, a comprehensive analysis of each configuration will be provided, exploring their individual performance attributes. The investigation will encompass the examination of flow velocity streamlines and pressure variations, as well as the assessment of flow uniformity within each design.

7.6.1.1 U and Z configurations

In the examination of the pressure contours of the Z and U arrangements presented in Figure 7.8, the overall pressure drops are similar. A closer inspection of both arrangements as shown in Figure 7.9 reveals that the U-configuration exhibits an initial steep decline in pressure drop

in the first three channels, which stabilizes as the number of channels increases from the inlet towards the outlets, suggestive of a steep reduction in the fluid flowing into these channels as the flow navigate from channel 1 to channel 9. Conversely, the Z-configuration demonstrates a more gradual increase in pressure drop as the number of the channel increases from 1 to 9.

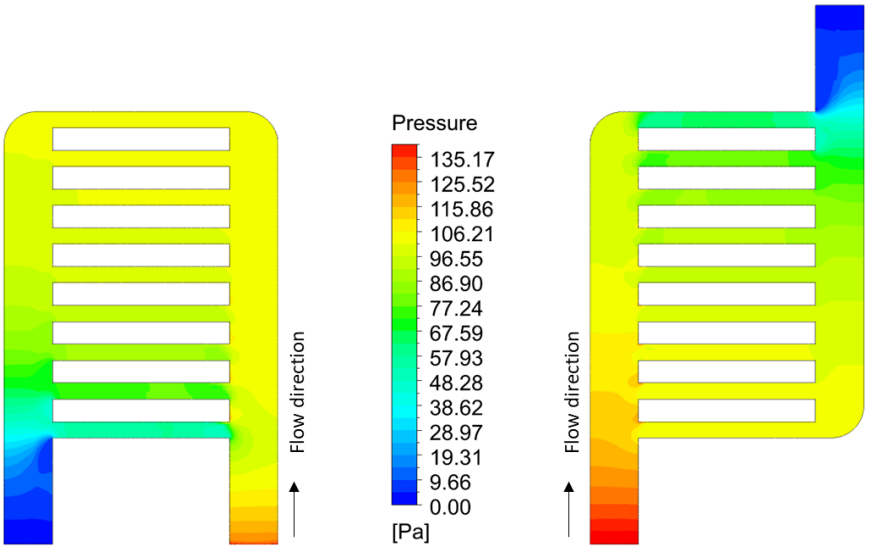

Figure 7-8 Pressure contours for Z and U-shaped manifolds

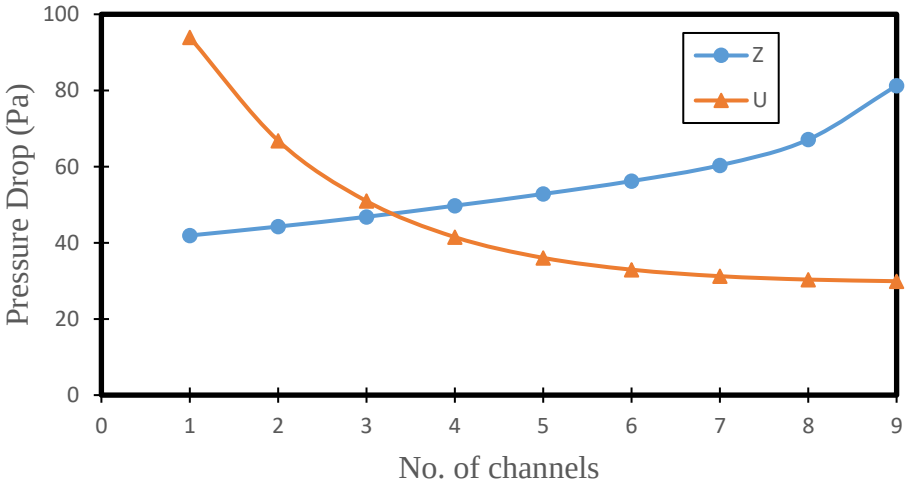

Figure 7-9 Pressure drops for Z and U-shaped manifolds

Figure 7.10 demonstrate the velocity streamlines and mass flow rate distribution along the channels which quantitatively complements the above findings. It indicates how pressure loss is affected by the fluid's path through the manifold. The recirculation created within the

manifold has a direct impact on these findings. As labelled in the figure, region 1 represents the largest recirculation zone in the U-distribution manifold. In the Z-configuration, most of the recirculation zones occur within the collection manifold.

Both configurations exhibit similar trends in the collection manifold where small recirculation zones are created after each channels exits as shown in region 2. As a result of these recirculation zones, the flow accelerates toward the exit of the collection manifold. Another similar trend can be seen at the inlet of each channel as shown in region 3 where secondary flows are created.

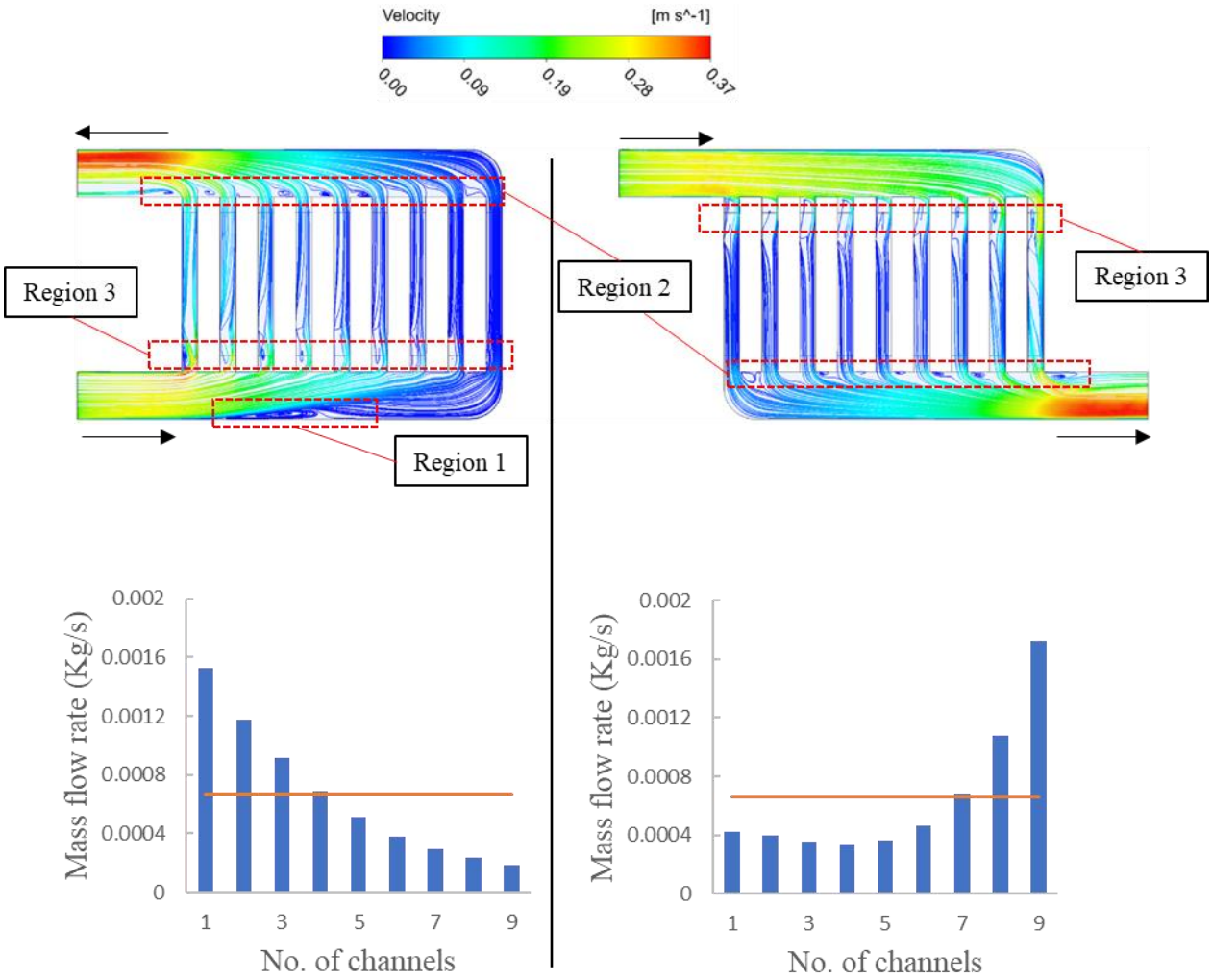

Figure 7-10 Velocity streamlines and mass flow rate distribution along the channels.

Wall shear stress is an important factor in the study of fluid dynamics as it reflects the flow behaviour near the walls. Figure 7.11 shows the distribution of wall shear stresses in both arrangements.

Both configurations exhibit high shear stress at the bends, which corresponds to the areas where the highest-pressure drops were likely observed. This suggests that these bends are critical points affecting both pressure and shear, impacting the overall performance of the manifold.

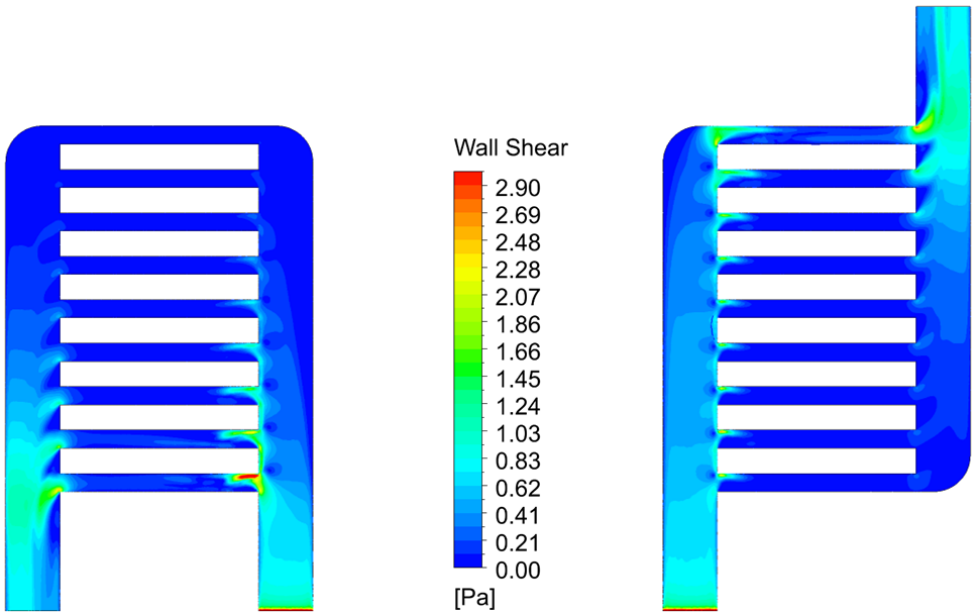

Figure 7-11 Wall shear stresses distribution in both arrangements.

To further measure the level of flow uniformity, Eq. 7.1 indicates that the standard of deviations is 0.000438095 and 0.00044169 for the U and Z configurations, respectively as shown in Figure 7.10. This confirms the earlier findings of the similarity flow uniformity level between the two configurations.

Despite the flow within the Z-configuration not being perfectly uniform, the observed wall shear stress trends suggest that the flow actively engages with the walls across all channels, from 1 to 9. This is a significant indicator that the flow, while not yet optimal, does indeed reach every channel, which is not clearly achieved in the U configuration when operating at

the same Reynolds number. Such a characteristic provides a solid foundation for potential improvements through further parametric studies. By adjusting design parameters such as manifold's inlet cross-sectional size and channel geometry, core channel number and Reynolds number, there is an opportunity to refine the Z-configuration to achieve a more uniform flow distribution. This foundational flow coverage gives the Z-configuration a distinct advantage as the starting point for optimization efforts to enhance overall fluid dynamics and heat exchange efficiency.

7.6.1.2 Effect of different manifold inlet cross-sectional size

The exploration of the manifold inlet cross-section sizes constitutes an integral part of the parametric study, specifically focusing on the Inlet Ratio (IR). The Inlet Ratio is a dimensionless parameter defined as the ratio of the cross-sectional area of the manifold inlet to the inlet cross-sectional area of a single core channel. This metric is crucial as it influences the initial velocity distribution within the manifold, which in turn can significantly affect the flow distribution to downstream channels.

For the purpose of this study, three Inlet Ratios (IR) have been chosen for investigation: IR values of 6, 13, and 18. These ratios represent a range from relatively small to large manifold inlets in relation to the size of an individual channel.

An IR of 6 indicates a more restricted inlet area, potentially leading to higher velocities at the entrance and possibly greater pressure drops. Moreover, an IR of 13 provides a moderate area ratio, which may balance between velocity distribution and pressure loss. Lastly, an IR of 18 signifies a more generous inlet cross-sectional area, which could allow for more gradual velocity changes and potentially lower pressure drops, though at the cost of a larger manifold size.

This segment of the study will assess how these different Inlet Ratios impact the flow characteristics within the Z arrangement manifold. By examining these variations, the study aims to identify an optimal Inlet Ratio that ensures efficient flow distribution and minimizes performance losses, contributing to the overall efficacy of the manifold design.

The red rectangular box in Figure 7.12 highlights the collection manifold area alongside half the length of the core channels, where detailed flow velocity streamlines and pressure contours will be analysed.

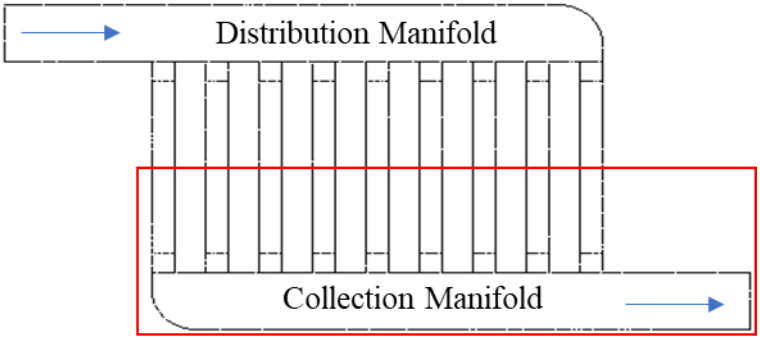

Figure 7-12: Location where the contours are taken

To understand the effect of the manifold's inlet size on the pressure and velocity distribution throughout the manifold, Figures 7.13 and 7.14 are provided.

For the IR = 6 configuration, the small inlet size presents a distinct pressure gradient that diminishes from the high-pressure inlet to the channels furthest from the entry, a design that could be beneficial for certain high-pressure applications. However, this configuration may induce uneven flow distribution due to the restrictive inlet size, which could be a drawback in systems requiring uniform flow.

Moving to the IR = 13 configuration, the medium-sized inlet provides an improved pressure profile. It mitigates the steep pressure gradient observed in the smaller inlet, allowing for a more uniform distribution of fluid and a more balanced flow across the manifold's channels.

This design's capacity to moderate the initial pressure while maintaining a compact form makes it particularly advantageous for applications where space efficiency is crucial.

The largest inlet, seen in the IR = 18 configuration, offers the most uniform pressure distribution across the manifold, significantly reducing pressure disparities and promoting even fluid distribution to the farthest channels. However, the trade-off is the potential requirement for more space, which may not be feasible in all applications.

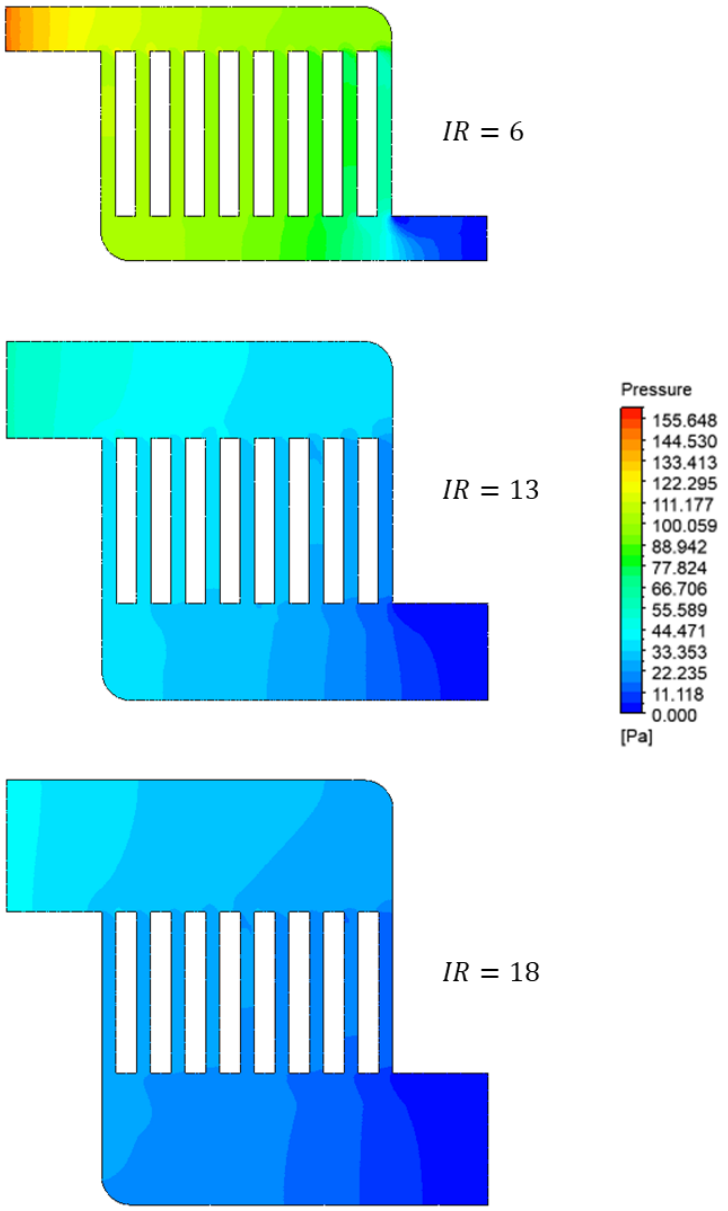

Figure 7-13 Pressure contours at different IR values

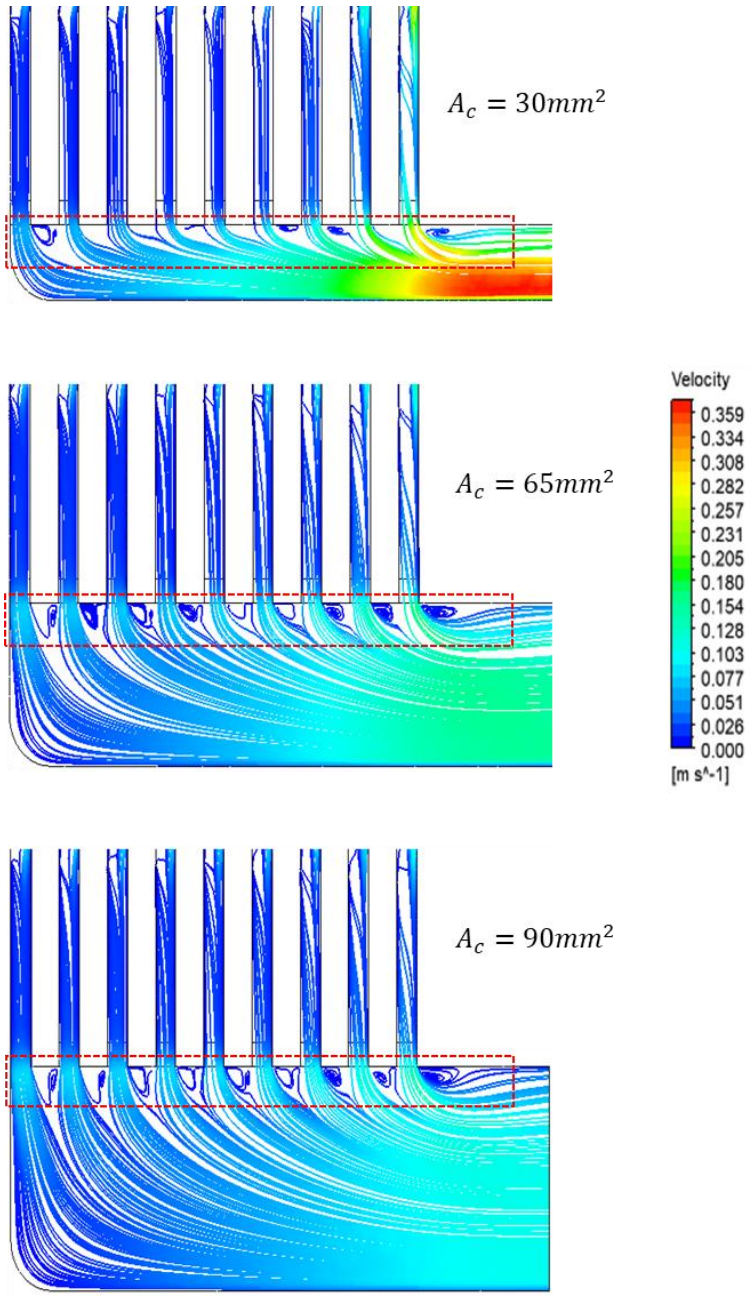

Figure 7-14 Velocity streamlines at different A_c values.

Figure 7.15 represents a bar graph depicting the mass flow rate through individual channels for the three different manifold configurations characterized by their inlet ratios (IR=6, IR=13, IR=18). The horizontal line represents the calculated average mass flow rate across all channels for comparison.

For IR=6, the mass flow rate per channel fluctuates, with some channels experiencing significantly lower flow rates compared to the average. This suggests a non-uniform distribution of flow, which could be due to the flow restrictions caused by the smaller inlet size as previously discussed. The IR=13 configuration shows a more uniform distribution of mass flow rates across the channels, closely aligning with the average mass flow rate. This indicates a more balanced flow distribution, likely due to the medium inlet size allowing a more even distribution of fluid without the extremes of restriction or excess. For IR=18, a more uniform flow can be seen. However, it is not favourable for this specific study due to space requirements.

Upon careful analysis, the IR=13 configuration stands out for further parametric studies and design optimization. This middle-ground approach not only meets the operational needs for a more consistent flow but also aligns with the industrial partner's specifications for a compact, efficient design. Consequently, the IR=13 configuration is selected as the most suitable for ongoing development, offering a reasonable blend of functionality and spatial economy.

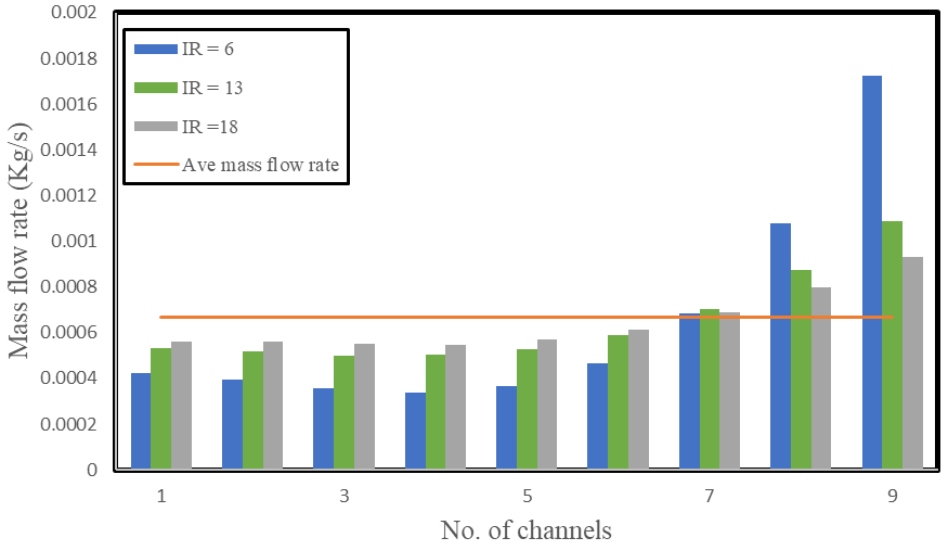

Figure 7-15 Mass flow rate vs. number of channels at different IR values

7.6.1.3 Novel design

Our manifold design aims to address the challenges of maldistribution in fluid dynamics systems. The new design, depicted in Figure 7.16, features complex design that guide fluid flow, with the goal of ensuring a more uniform mass flow rate distribution across the system.

Figure 7.16 shows velocity profiles at the inlet of each channel for the basic Z-configuration and the novel-configuration. A relatively uniform velocity across the channels with slight variation is present at the novel-configuration. This suggests that the design is effective in distributing flow across the channels. Comparatively, Z-configuration shows a more varied velocity profile across the channels. This could indicate that the flow is less evenly distributed.

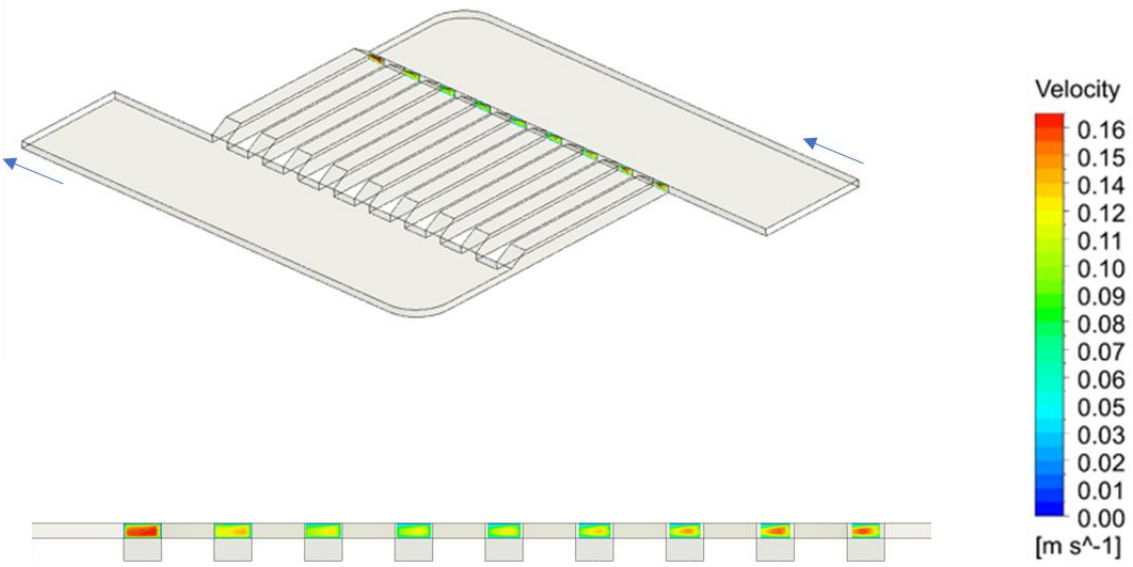

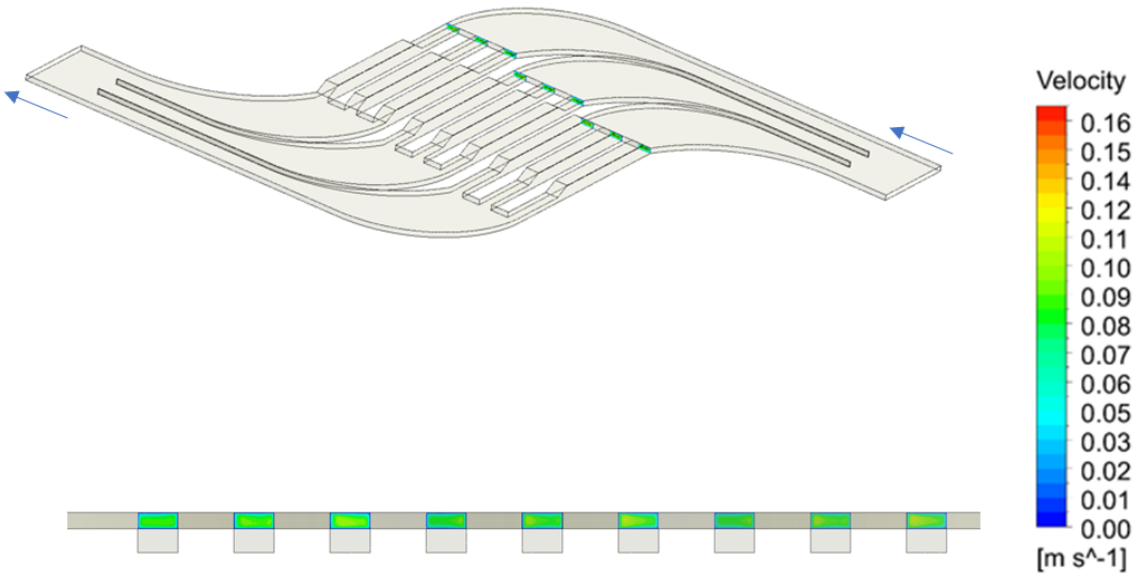

Figure 7-16 Velocity profiles at the inlet of each channel for the basic Z-configuration and the novel-configuration

The provided Figure 7.17 shows the velocity streamlines within the novel manifold system. As the fluid travels through the manifold's curved geometry, the streamlines remain well-ordered, indicating streamlined flow despite the complexity of the path.

Notably, there is no significant evidence of flow separation except at the outlet of the core channels, which would be characterized by a chaotic pattern of streamlines or recirculation zones, particularly around bends and junctions where flow detachment could occur. The design's smooth transitions and gradual curvature help maintain the flow's attachment to the walls, a crucial aspect in preventing efficiency losses due to turbulence or secondary flows.

As the flow divides into the individual channels, the streamlines spread out uniformly, suggesting an even distribution of flow among the outlets. This implies that each branch receives a similar flow rate, which is essential for systems requiring synchronized output, such as parallel cooling channels in a heat exchanger.

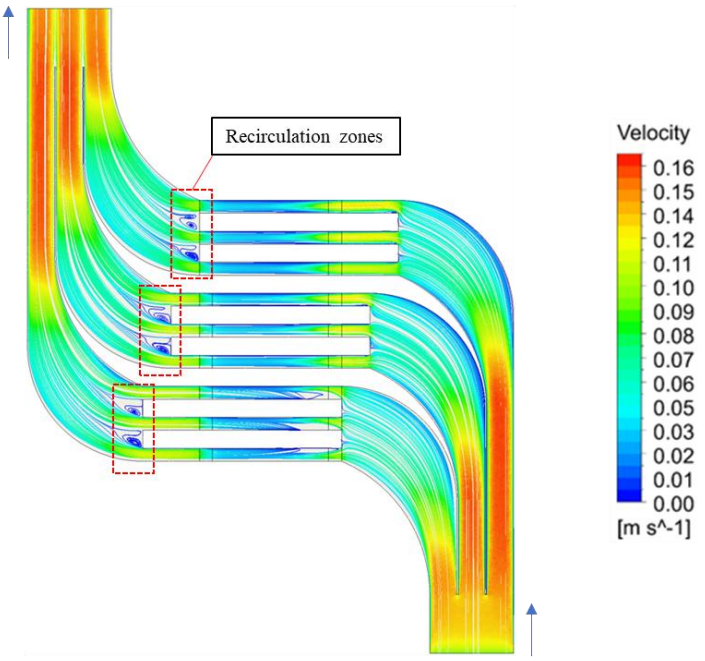

Figure 7-17 Velocity streamlines within the novel manifold system

The bar chart illustrated in Figure 7.18 demonstrates the mass flow rate through individual channels for two manifold designs in comparison to the average mass flow rate. The design shows mass flow rates across the channels that are closely clustered around the average, reflecting a uniform distribution of flow. This is quantitatively supported by a low standard deviation of 1.99321E-05, which signifies minimal variation in flow rate from one channel to the next. Such a low standard deviation is indicative of an effective manifold design, where each channel contributes almost equally to the total flow, a desirable feature for systems that rely on consistent flow characteristics.

In contrast, the "Z-design" displays a wider range of mass flow rates, with certain channels deviating more substantially from the average. The standard deviation for the "Z-design" is 0.000441697, an order of magnitude higher than that of the Novel-design, signifying greater variability in flow distribution. This higher standard deviation can result in performance

inconsistencies across the channels, potentially leading to localized inefficiencies in the system the manifold serves.

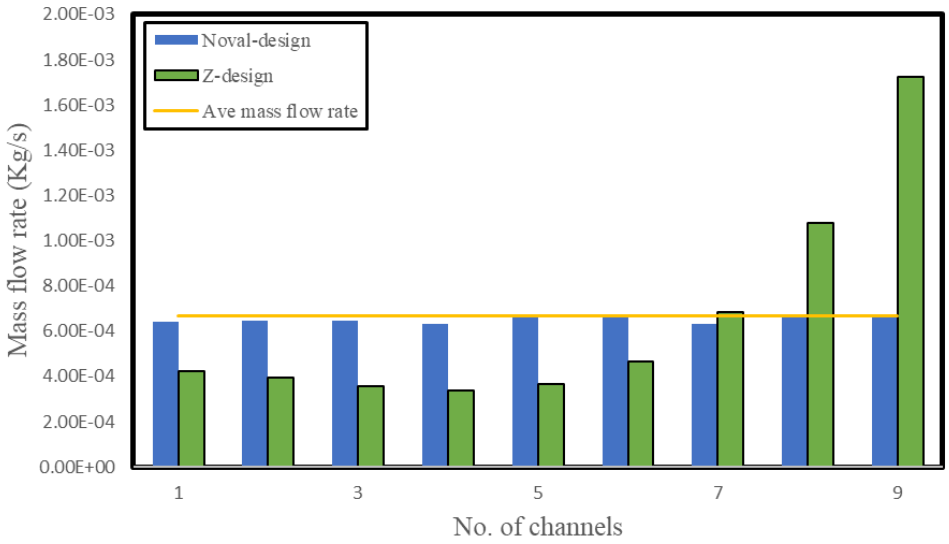

Figure 7-18 Mass flow rate through individual channels for two manifold designs in comparison to the average mass flow rate

7.6.1.4 Effect of Reynolds number

In the bar charts in Figure 7.19 depicting mass flow rates across various channels, the transition observed is from low laminar flow conditions at Re=346 to high laminar conditions at Re=2000. Throughout this range, the flow maintains a laminar characteristic, with flow rates relatively close to the average, indicative of stable and orderly fluid motion. However, as we approach the higher end of the laminar regime, slight increases in variability among the channels begin to emerge. The standard deviations corresponding to the progression from lower to higher laminar Reynolds numbers are 1.99321E-05, 5.85556E-05, 0.000152636, and 0.000305586, respectively. This gradual change reflects the increasing influence of inertial forces relative to viscous forces, which can lead to more significant differences in flow behaviour, particularly in complex geometries or near the critical transition to turbulence. The rising trend in standard deviation illustrates a move towards less uniformity in flow rates, which

could potentially become more pronounced as the Reynolds number increases beyond this laminar range.

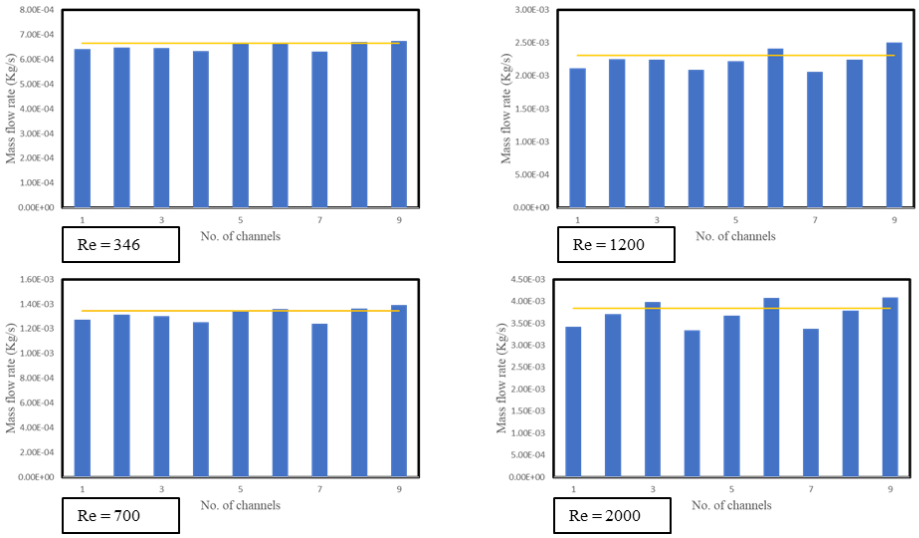

Figure 7-19 Mass flow rates across various channels for different Re numbers

7.6.1.5 Effect of number of core channels

The series of bar charts provided in Figure 7.20 illustrate the mass flow rates across manifold systems with varying numbers of channels (9, 12, 15 and 18 channels). The charts show that as the number of channels increases, the variation in flow rate between the channels remains low (as indicated by the consistency of the bar heights and their alignment with the average flow rate line), it would suggest that the manifold design effectively maintains uniform flow irrespective of the number of channels.

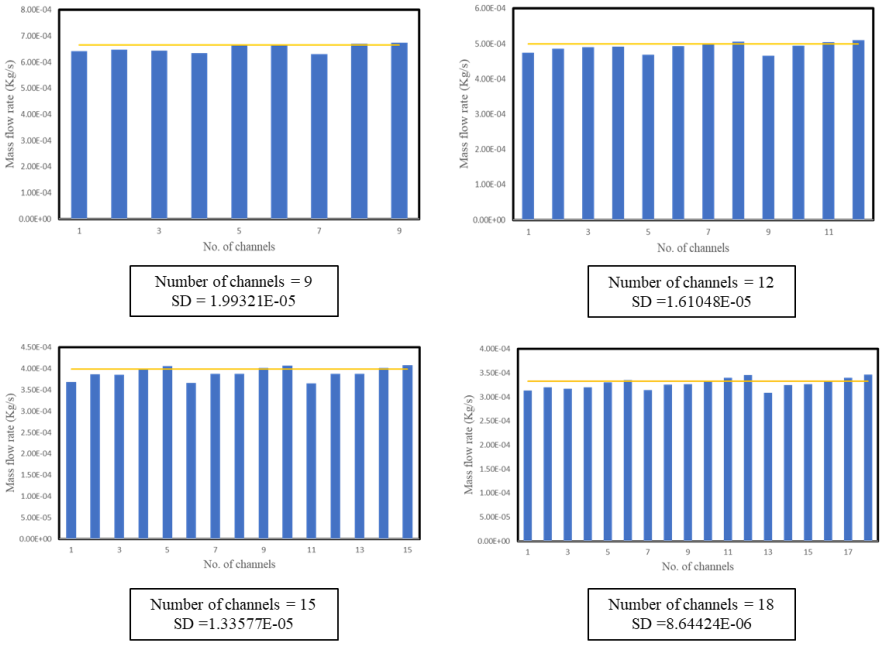

Figure 7-20 Mass flow rates across manifold systems with varying numbers of channels

7.6.2 Comparison of the novel design with U-shape instead of Z-shape.

Figure 7.21 showcases a comparative analysis of mass flow rates between the Z-novel and U-novel manifold configurations. The Z-novel design demonstrates a remarkably uniform flow distribution, evidenced by a low standard deviation of 1.99321E-5, indicating that the flow rates across the channels are well-aligned with the overall average. This suggests that the Z-novel design efficiently manages flow distribution, which is advantageous for systems where consistent channel performance is critical.

On the other hand, the U-novel configuration displays a higher standard deviation of 1.7424E-4, signaling a more variable flow across the channels. The increased standard deviation points to a flow that significantly diverges from the average in individual channels, a condition that may lead to operational challenges in applications requiring a balanced flow, as it could affect the uniformity of thermal transfer rates within the manifold.

The notable difference in standard deviation between the Z-novel and U-novel designs reinforces the earlier observation that the Z configuration outperforms the U arrangement in terms of achieving a more uniform flow. This conclusion underscores the importance of manifold design in influencing flow characteristics and system efficacy.

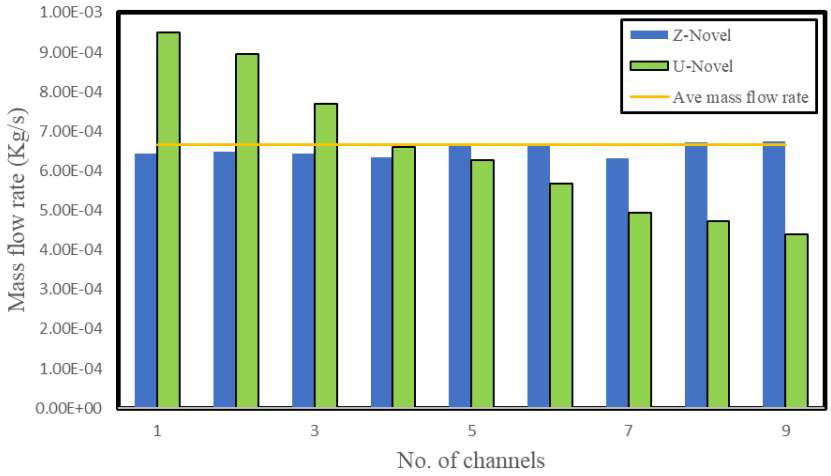

Figure 7-21 Mass flow rates of the Z-novel and U-novel manifold configurations

7.6.3 Conclusion

The manifold design optimizes space utilization by integrating approximately 44% of the collection and distribution manifold area into the heat exchange process. This design was achieved after evaluating multiple configurations. By mimicking natural flow patterns, the manifold minimizes flow separation, resulting in reduced pressure drops. The layered arrangement maximizes the heat exchange area within a compact volume, effectively using the available space.

CHAPTER 8 CONCLUSION AND FUTURE WORK

This thesis studied the potential AM to design a highly compact heat exchanger along with the manifold that supports the heat exchanger core. It started with examining the effect of heat transfer enhancement technology such as internal longitudinal fins (ILFC) and central inclined finned channel (CIFC). When considering the pressure drop penalty associated with the heat transfer enhancement, the performance factor drops below one for all the cases of ILFC. This means that the ILFC is only beneficial when considering augmenting the heat transfer rate. A parametric study was conducted in the case of CIFC, and the varied parameter were the angle of attack (α), Pitch Ratio (PR), and Height Ratio (HR). As a result, an enhancement on the overall system performance of about 115% was achieved when considering the pressure drop penalty associated with the heat transfer enhancement. The highest value obtained at $\alpha = 45^{o}$, PR = 3, HR = 0.2 at Re = 1500. The introduction of the swirl flow in the case of CIFC was the reason behind this augmentation. This mechanism highlighted the importance of such a technique to enhance thermal-hydraulic performance of similar systems. Therefore, the author investigated the performance a novel design consisting of swirl devices to enhance the heat transfer utilizing two mechanisms: extended surfaces area which will help in conducting the heat transfer and swirling the flow to impinge it in the four walls of the channels to enhance the flow mixing. After conducting the parametric study (number of blades (N), PR, and loft angle (θ)), the results showed that the highest thermal-hydraulic performance factor out of all the swirler cases found at the case with the following parameters (θ = 90 degree, PR = 2.25, N = 4). An increase of about 148% is achieved when compared against the smooth channel. Moreover, the effect of different material with high thermal conductivity was tested and an increase of about 9% to get the performance factor to 2.66 was achieved. The numerical simulations were validated experimentally and a decent agreement between the CFD and experimental results were achieved. The new low-speed rig was designed, manufactured, and

commissioned at the Oxford Thermofluids Institute (OTI). A modular design of the experimental facility is implemented to allow for the interchangeability of parts of the working section and testing of various heat transfer cooling techniques.

In the first two results chapters, the analysis of the heat transfer rate within the system was predicated on the assumption of constant thermal boundary conditions on the walls. The findings were further validated with a closer to reality boundary conditions. Heat exchanger of nine cells was designed and constant fluid temperatures to the inlet sections of each cell within the heat exchanger core were applied. This approach yields a temperature profile along the walls, diverging from the previously assumed constant temperature boundary conditions. The earlier findings trend was confirmed with this design. Finally, to ensure flow uniformity on the heat exchanger cells, a novel manifold was designed and tested against conventional designs and a flow uniformity level was achieved with a very low standard deviation.

Future research should prioritize the proper flow characterization at high Reynolds numbers and in transitional flows, considering the roughness characteristics of additive manufacturing (AM) surfaces, such as the directionality of the layers based on print orientation. This investigation will provide deeper insights into the flow and heat transfer mechanisms, particularly in turbulent flow regimes, and help build confidence in computational fluid dynamics (CFD) simulations.

The design optimization of complex surfaces in ultra-compact heat exchangers will require significant computational resources and advanced, accelerated flow solvers. Developing new velocity and thermal wall functions that account for the roughness of AM surfaces presents a promising approach to accelerating the design optimization process and improving the efficiency and performance of these systems. Furthermore, investigating the impact of surface roughness introduced by AM on heat transfer performance and friction factors will offer a

promising avenue for innovation, potentially leading to more efficient and cost-effective heat exchanger designs.

Additionally, future research should concentrate on validating the proposed manifold system, with an emphasis on experimentally testing its thermal performance to quantify the effect of flow uniformity on heat transfer enhancement. This investigation should involve experimental setups, computational analyses, flow visualization techniques, and high-resolution thermal imaging to identify areas of non-uniformity and optimize the manifold design. Understanding the relationship between flow uniformity and thermal performance will provide valuable insights into balancing optimization efforts, cost, and thermal efficiency.

REFERENCES

[1] A.H. Alami, A. Ghani Olabi, A. Alashkar, S. Alasad, H. Aljaghoub, H. Rezk, M.A. Abdelkareem, Additive manufacturing in the aerospace and automotive industries: Recent trends and role in achieving sustainable development goals, Ain Shams Eng. J. 14 (2023) 102516. https://doi.org/10.1016/J.ASEJ.2023.102516.

[2] Siemens achieves breakthrough with 3D printed gas turbine blades | Press | Company | Siemens, (n.d.). https://press.siemens.com/global/en/pressrelease/siemens-achieves-breakthrough-3d-printed-gas-turbine-blades (accessed April 14, 2024).

[3] M.E. Steinke, S.G. Kandlikar, Single-Phase Heat Transfer Enhancement Techniques in Microchannel and Minichannel Flows, (2008) 141–148. https://doi.org/10.1115/icmm2004-2328.

[4] K. Nilpueng, T. Keawkamrop, H.S. Ahn, S. Wongwises, Effect of chevron angle and surface roughness on thermal performance of single-phase water flow inside a plate heat exchanger, Int. Commun. Heat Mass Transf. 91 (2018) 201–209. https://doi.org/10.1016/J.ICHEATMASSTRANSFER.2017.12.009.

[5] D. Ho Nguyen, P. Quoc Nguyen, R. Ur Rehman, J.F. Kim, H. Seon Ahn, Optimizing the effect of micro-surface on the thermal hydraulic performance of plate heat exchanger, Appl. Therm. Eng. 239 (2024) 122172. https://doi.org/10.1016/J.APPLTHERMALENG.2023.122172.

[6] D.H. Nguyen, T.J. Kim, J.M. Kim, T. Kim, T. Arkadumnuay, O. Mahian, H.S. Ahn, S. Wongwises, Enhancing the vertical downward condensation heat transfer of a plate heat exchanger by electrochemical etching, Int. J. Heat Mass Transf. 225 (2024) 125277. https://doi.org/10.1016/J.IJHEATMASSTRANSFER.2024.125277.

[7] Y. Zhao, X. Lu, L. Liu, B. Zhang, M. Wang, H. Zhang, Heat transfer characteristics of external finned backfill coupled heat exchanger in mine, Geothermics. 119 (2024)

102953. https://doi.org/10.1016/J.GEOTHERMICS.2024.102953.

[8] S. Mohapatra, D.K. Das, A.K. Singh, Plate-fin heat exchanger optimal design for industry employing both single and multi-objective chaotic opposition based Kho-Kho algorithm, Chem. Eng. Sci. 293 (2024) 120024. https://doi.org/10.1016/J.CES.2024.120024.

[9] P. Blecich, J. Batista, M. Kirinčić, A. Trp, K. Lenić, Numerical study of heat transfer and fluid flow in the offset strip-fin heat exchanger: A fin-by-fin analysis, Int. Commun. Heat Mass Transf. 154 (2024) 107434. https://doi.org/10.1016/J.ICHEATMASSTRANSFER.2024.107434.

[10] Ranjith, K. Shaji, Numerical Analysis on a Double Pipe Heat Exchanger with Twisted Tape Induced Swirl Flow on Both Sides, Procedia Technol. 24 (2016) 436–443. https://doi.org/10.1016/J.PROTCY.2016.05.060.

[11] M. Bezaatpour, M. Goharkhah, Convective heat transfer enhancement in a double pipe mini heat exchanger by magnetic field induced swirling flow, Appl. Therm. Eng. 167 (2020) 114801. https://doi.org/10.1016/J.APPLTHERMALENG.2019.114801.

[12] M. Bezaatpour, H. Rostamzadeh, Energetic and exergetic performance enhancement of heat exchangers via simultaneous use of nanofluid and magnetic swirling flow: A two-phase approach, Therm. Sci. Eng. Prog. 20 (2020) 100706. https://doi.org/10.1016/J.TSEP.2020.100706.

[13] F. Yahiat, P. Bouvier, S. Russeil, C. André, D. Bougeard, Swirl influence on thermo-hydraulic performances within a heat exchanger/reactor with macro deformed walls in laminar flow regime, Chem. Eng. Process. - Process Intensif. 189 (2023) 109373. https://doi.org/10.1016/J.CEP.2023.109373.

[14] Y.Q. Kong, L.J. Yang, X.Z. Du, Y.P. Yang, Impacts of geometric structures on thermo-flow performances of plate fin-tube bundles, Int. J. Therm. Sci. 107 (2016) 161–178.

https://doi.org/10.1016/J.IJTHERMALSCI.2016.04.011.

[15] L. Sheik Ismail, R. Velraj, C. Ranganayakulu, Studies on pumping power in terms of pressure drop and heat transfer characteristics of compact plate-fin heat exchangers—A review, Renew. Sustain. Energy Rev. 14 (2010) 478–485. https://doi.org/10.1016/J.RSER.2009.06.033.

[16] S.K. Singh, M. Mishra, P.K. Jha, Nonuniformities in compact heat exchangers—scope for better energy utilization: A review, Renew. Sustain. Energy Rev. 40 (2014) 583–596. https://doi.org/10.1016/J.RSER.2014.07.207.

[17] M.A. Rahman, S.M.M. Hasnain, R. Zairov, Assessment of improving heat exchanger thermal performance through implementation of swirling flow technology, Int. J. Thermofluids. 22 (2024). https://doi.org/10.1016/j.ijft.2024.100689.

[18] Y.J. Baik, S. Jeon, B. Kim, D. Jeon, C. Byon, Heat transfer performance of wavy-channeled PCHEs and the effects of waviness factors, Int. J. Heat Mass Transf. 114 (2017) 809–815. https://doi.org/10.1016/j.ijheatmasstransfer.2017.06.119.

[19] J.G. Kwon, T.H. Kim, H.S. Park, J.E. Cha, M.H. Kim, Optimization of airfoil-type PCHE for the recuperator of small scale brayton cycle by cost-based objective function, Nucl. Eng. Des. 298 (2016) 192–200. https://doi.org/10.1016/j.nucengdes.2015.12.012.

[20] S.M. Shin, S.W. Lee, S. Chung, N. Kim, M.H. Kim, H.J. Jo, Mitigation of fouling with swirling flow induced in 3-D double-sided straight channel for printed circuit heat exchanger, Int. J. Heat Mass Transf. 233 (2024). https://doi.org/10.1016/j.ijheatmasstransfer.2024.125982.

[21] S. Liu, M. Sakr, A comprehensive review on passive heat transfer enhancements in pipe exchangers, Renew. Sustain. Energy Rev. 19 (2013) 64–81. https://doi.org/10.1016/J.RSER.2012.11.021.

[22] R. Tiruselvam, V.R. Raghavan, Double tube heat exchanger with novel enhancement:

Part I-flow development length and adiabatic friction factor, Heat Mass Transf. Und Stoffuebertragung. 48 (2012) 641–651. https://doi.org/10.1007/s00231-011-0915-4.

[23] F.P. Incropera, D.P. DeWitt, Fundamentals of Heat and Mass Transfer, Sixth Edit, J. Wiley, New York, 2002.

[24] S. Eiamsa-ard, C. Thianpong, P. Eiamsa-ard, P. Promvonge, Convective heat transfer in a circular tube with short-length twisted tape insert, Int. Commun. Heat Mass Transf. 36 (2009) 365–371. https://doi.org/10.1016/j.icheatmasstransfer.2009.01.006.

[25] S. Eiamsa-ard, P. Promvonge, Performance assessment in a heat exchanger tube with alternate clockwise and counter-clockwise twisted-tape inserts, Int. J. Heat Mass Transf. 53 (2010) 1364–1372. https://doi.org/10.1016/j.ijheatmasstransfer.2009.12.023.

[26] M. Rahimi, S.R. Shabanian, A.A. Alsairafi, Experimental and CFD studies on heat transfer and friction factor characteristics of a tube equipped with modified twisted tape inserts, Chem. Eng. Process. Process Intensif. 48 (2009) 762–770. https://doi.org/10.1016/j.cep.2008.09.007.

[27] S.R. Shabanian, M. Rahimi, M. Shahhosseini, A.A. Alsairafi, CFD and experimental studies on heat transfer enhancement in an air cooler equipped with different tube inserts, Int. Commun. Heat Mass Transf. 38 (2011) 383–390. https://doi.org/10.1016/j.icheatmasstransfer.2010.12.015.

[28] S. Eiamsa-Ard, N. Koolnapadol, P. Promvonge, Heat transfer behavior in a square duct with tandem wire coil element insert, Chinese J. Chem. Eng. 20 (2012) 863–869. https://doi.org/10.1016/S1004-9541(12)60411-X.

[29] S. Eiamsa-ard, K. Wongcharee, P. Eiamsa-ard, C. Thianpong, Heat transfer enhancement in a tube using delta-winglet twisted tape inserts, Appl. Therm. Eng. 30 (2010) 310–318. https://doi.org/10.1016/j.applthermaleng.2009.09.006.

[30] P. Promvonge, S. Suwannapan, M. Pimsarn, C. Thianpong, Experimental study on heat

transfer in square duct with combined twisted-tape and winglet vortex generators, Int. Commun. Heat Mass Transf. 59 (2014) 158–165. https://doi.org/10.1016/j.icheatmasstransfer.2014.10.005.

[31] K. Wongcharee, S. Eiamsa-ard, Heat transfer enhancement by twisted tapes with alternate-axes and triangular, rectangular and trapezoidal wings, Chem. Eng. Process. Process Intensif. 50 (2011) 211–219. https://doi.org/10.1016/j.cep.2010.11.012.

[32] T. Salameh, A.H. Alami, B. Sunden, Experimental investigation of the effect of variously-shaped ribs on local heat transfer on the outer wall of the turning portion of a U-channel inside solar air heater, Heat Mass Transf. Und Stoffuebertragung. 52 (2016) 539–546. https://doi.org/10.1007/s00231-015-1541-3.

[33] S. Caliskan, Experimental investigation of heat transfer in a channel with new winglet-type vortex generators, Int. J. Heat Mass Transf. 78 (2014) 604–614. https://doi.org/10.1016/j.ijheatmasstransfer.2014.07.043.

[34] P.W. Deshmukh, S. V. Prabhu, R.P. Vedula, Heat transfer enhancement for laminar flow in tubes using curved delta wing vortex generator inserts, Appl. Therm. Eng. 106 (2016) 1415–1426. https://doi.org/10.1016/j.applthermaleng.2016.06.120.

[35] P. Liu, N. Zheng, F. Shan, Z. Liu, W. Liu, An experimental and numerical study on the laminar heat transfer and flow characteristics of a circular tube fitted with multiple conical strips inserts, Int. J. Heat Mass Transf. 117 (2018) 691–709. https://doi.org/10.1016/j.ijheatmasstransfer.2017.10.035.

[36] R. Bhadouriya, A. Agrawal, S. V. Prabhu, Experimental and numerical study of fluid flow and heat transfer in an annulus of inner twisted square duct and outer circular pipe, Int. J. Therm. Sci. 94 (2015) 96–109. https://doi.org/10.1016/j.ijthermalsci.2015.02.019.

[37] C. Luo, K.W. Song, Thermal performance enhancement of a double-tube heat exchanger with novel twisted annulus formed by counter-twisted oval tubes, Int. J. Therm. Sci. 164

(2021). https://doi.org/10.1016/j.ijthermalsci.2021.106892.

[38] C. Luo, K. Song, T. Tagawa, Heat transfer enhancement of a double pipe heat exchanger by Co-Twisting oval pipes with unequal twist pitches, Case Stud. Therm. Eng. 28 (2021) 101411. https://doi.org/10.1016/j.csite.2021.101411.

[39] M.A. Arie, A.H. Shooshtari, R. Tiwari, S. V. Dessiatoun, M.M. Ohadi, J.M. Pearce, Experimental characterization of heat transfer in an additively manufactured polymer heat exchanger, Appl. Therm. Eng. 113 (2017) 575–584. https://doi.org/10.1016/j.applthermaleng.2016.11.030.

[40] Y. Rua, R. Muren, S. Reckinger, Limitations of additive manufacturing on microfluidic heat exchanger components, J. Manuf. Sci. Eng. Trans. ASME. 137 (2015). https://doi.org/10.1115/1.4030157.

[41] U. Scheithauer, E. Schwarzer, T. Moritz, A. Michaelis, Additive Manufacturing of Ceramic Heat Exchanger: Opportunities and Limits of the Lithography-Based Ceramic Manufacturing (LCM), J. Mater. Eng. Perform. 27 (2018) 14–20. https://doi.org/10.1007/s11665-017-2843-z.

[42] D.B. Tuckerman, R.F.W. Pease, High-Performance Heat Sinking for VLSI, IEEE Electron Device Lett. EDL-2 (1981) 126–129. https://doi.org/10.1109/EDL.1981.25367.

[43] P.-S. Lee, S. V. Garimella, Thermally developing flow and heat transfer in rectangular microchannels of different aspect ratios, Int. J. Heat Mass Transf. 49 (2006) 3060–3067. https://doi.org/10.1016/J.IJHEATMASSTRANSFER.2006.02.011.

[44] L. Chai, G.D. Xia, H.S. Wang, Numerical study of laminar flow and heat transfer in microchannel heat sink with offset ribs on sidewalls, Appl. Therm. Eng. 92 (2016) 32–41. https://doi.org/10.1016/j.applthermaleng.2015.09.071.

[45] I.A. Ghani, N.A.C. Sidik, R. Mamat, G. Najafi, T.L. Ken, Y. Asako, W.M.A.A. Japar,

Heat transfer enhancement in microchannel heat sink using hybrid technique of ribs and secondary channels, Int. J. Heat Mass Transf. 114 (2017) 640–655. https://doi.org/10.1016/j.ijheatmasstransfer.2017.06.103.

[46] Z.F. Dong, M.A. Ebadian, A numerical analysis of thermally developing flow in elliptic ducts with internal fins, Int. J. Heat Fluid Flow. 12 (1991) 166–172. https://doi.org/10.1016/0142-727X(91)90044-V.

[47] M. Huq, A.M. Aziz-ul Huq, M.M. Rahman, Experimental measurements of heat transfer in an internally finned tube, Int. Commun. Heat Mass Transf. 25 (1998) 619–630. https://doi.org/10.1016/S0735-1933(98)00049-9.

[48] A. Kumar, R.P. Saini, J.S. Saini, Experimental investigation on heat transfer and fluid flow characteristics of air flow in a rectangular duct with Multi v-shaped rib with gap roughness on the heated plate, Sol. Energy. 86 (2012) 1733–1749. https://doi.org/10.1016/J.SOLENER.2012.03.014.

[49] S. Singh, S. Chander, J.S. Saini, Heat transfer and friction factor of discrete V-down rib roughened solar air heater ducts, J. Renew. Sustain. Energy. 3 (2011) 013108. https://doi.org/10.1063/1.3558865.

[50] K.R. Aharwal, B.K. Gandhi, J.S. Saini, Experimental investigation on heat-transfer enhancement due to a gap in an inclined continuous rib arrangement in a rectangular duct of solar air heater, Renew. Energy. 33 (2008) 585–596. https://doi.org/10.1016/J.RENENE.2007.03.023.

[51] A. Srivastav, A.K. Patil, G. Nandan, Investigation of heat transfer and friction in rib rougned fin under forced convection, in: Int. J. Adv. Technol. Eng. Res., 2014: pp. 117–125.

[52] M.M. Sahua, J.L. Bhagoria, Augmentation of heat transfer coefficient by using 908 broken transverse ribs on absorber plate of solar air heater, Renew. Energy. 30 (2005)

2057–2073.

[53] J.-C. Han, Heat Transfer and Friction in Channels With Two Opposite Rib-Roughened Walls, J. Heat Transfer. 106 (1984) 8.

[54] J.C. Han, J.S. Park, C.K. Lei, Heat Transfer Enhancement in Channels With Turbulence Promoters, J. Eng. Gas Turbines Power. 107 (1985) 8.

[55] J.C. Han, J.S. Park, Developing heat transfer in rectangular channels with rib turbulators, Int. J. Heat Mass Transf. 31 (1988) 183–195. https://doi.org/10.1016/0017-9310(88)90235-9.

[56] S.C. Lau, R.D. McMillin, J.C. Han, Turbulent Heat Transfer and Friction in a Square Channel With Discrete Rib Turbulators, J. Turbomach. 113 (1990) 7.

[57] D.S. Park, Experimental and Numerical Study of Laminar Forced Convection Heat Transfer for a Dimpled Heat Sink, Texas A&M University, 2007.

[58] I.H. Patel, S.L. Borse, Experimental investigation of heat transfer enhancement over the dimpled surface, Int. J. Eng. Sci. Technol. 4 (2012).

[59] F. Careri, R.H.U. Khan, C. Todd, M.M. Attallah, Additive manufacturing of heat exchangers in aerospace applications: a review, Appl. Therm. Eng. 235 (2023). https://doi.org/10.1016/j.applthermaleng.2023.121387.

[60] I. Kaur, P. Singh, Critical evaluation of additively manufactured metal lattices for viability in advanced heat exchangers, Int. J. Heat Mass Transf. 168 (2021). https://doi.org/10.1016/j.ijheatmasstransfer.2020.120858.

[61] T. Maconachie, M. Leary, B. Lozanovski, X. Zhang, M. Qian, O. Faruque, M. Brandt, SLM lattice structures: Properties, performance, applications and challenges, Mater. Des. 183 (2019). https://doi.org/10.1016/j.matdes.2019.108137.

[62] H.N.G. Wadley, D.T. Queheillalt, Thermal applications of cellular lattice structures, Mater. Sci. Forum. 539–543 (2007) 242–247. https://doi.org/10.4028/0-87849-428-

6.242.

[63] K.J. Maloney, K.D. Fink, T.A. Schaedler, J.A. Kolodziejska, A.J. Jacobsen, C.S. Roper, Multifunctional heat exchangers derived from three-dimensional micro-lattice structures, Int. J. Heat Mass Transf. 55 (2012) 2486–2493. https://doi.org/10.1016/j.ijheatmasstransfer.2012.01.011.

[64] N. Lebaal, A. SettaR, S. Roth, S. Gomes, Conjugate heat transfer analysis within in lattice-filled heat exchanger for additive manufacturing, Mech. Adv. Mater. Struct. 29 (2022) 1361–1369. https://doi.org/10.1080/15376494.2020.1819489.

[65] L.Y. Chen, S.X. Liang, Y. Liu, L.C. Zhang, Additive manufacturing of metallic lattice structures: Unconstrained design, accurate fabrication, fascinated performances, and challenges, Mater. Sci. Eng. R Reports. 146 (2021). https://doi.org/10.1016/j.mser.2021.100648.

[66] D. Jafari, W.W. Wits, The utilization of selective laser melting technology on heat transfer devices for thermal energy conversion applications: A review, Renew. Sustain. Energy Rev. 91 (2018) 420–442. https://doi.org/10.1016/j.rser.2018.03.109.

[67] J.Y. Ho, K.C. Leong, T.N. Wong, Additively-manufactured metallic porous lattice heat exchangers for air-side heat transfer enhancement, Int. J. Heat Mass Transf. 150 (2020). https://doi.org/10.1016/j.ijheatmasstransfer.2019.119262.

[68] J. Noronha, M. Qian, M. Leary, E. Kyriakou, M. Brandt, Hollow-walled lattice materials by additive manufacturing: Design, manufacture, properties, applications and challenges, Curr. Opin. Solid State Mater. Sci. 25 (2021). https://doi.org/10.1016/j.cossms.2021.100940.

[69] M.C. Lu, C.C. Wang, Effect of the inlet location on the performance of parallel-channel cold-plate, IEEE Trans. Components Packag. Technol. 29 (2006) 30–38. https://doi.org/10.1109/TCAPT.2005.850539.

[70] S. Tang, Y. Zhao, Y. Diao, Z. Quan, Effects of various inlet/outlet positions and header forms on flow distribution and thermal performance in microchannel heat sink, Microsyst. Technol. 24 (2018) 2485–2497. https://doi.org/10.1007/s00542-017-3688-y.

[71] S.A. Memon, T.A. Cheema, G.M. Kim, C.W. Park, Hydrothermal investigation of a microchannel heat sink using secondary flows in trapezoidal and parallel orientations, Energies. 13 (2020). https://doi.org/10.3390/en13215616.

[72] X. Huang, W. Yang, T. Ming, W. Shen, X. Yu, Heat transfer enhancement on a microchannel heat sink with impinging jets and dimples, Int. J. Heat Mass Transf. 112 (2017) 113–124. https://doi.org/10.1016/j.ijheatmasstransfer.2017.04.078.

[73] T. Ming, C. Cai, W. Yang, W. Shen, W. Feng, N. Zhou, Optimization of Dimples in Microchannel Heat Sink with Impinging Jets—Part B: the Influences of Dimple Height and Arrangement, J. Therm. Sci. 27 (2018) 321–330. https://doi.org/10.1007/s11630-018-1019-y.

[74] T. Gan, T. Ming, W. Fang, Y. Liu, L. Miao, K. Ren, M.H. Ahmadi, Heat transfer enhancement of a microchannel heat sink with the combination of impinging jets, dimples, and side outlets, J. Therm. Anal. Calorim. 141 (2020) 45–56. https://doi.org/10.1007/s10973-019-08754-z.

[75] R. Loganathan, S. Gedupudi, Numerical study of single-phase heat transfer performance of a mini/micro-channel integrated with multiple bypass micro-nozzles, J. Therm. Sci. Eng. Appl. 13 (2021). https://doi.org/10.1115/1.4049430.

[76] M. Mohammadi, G.N. Jovanovic, K. V. Sharp, Numerical study of flow uniformity and pressure characteristics within a microchannel array with triangular manifolds, Comput. Chem. Eng. 52 (2013) 134–144. https://doi.org/10.1016/j.compchemeng.2012.12.010.

[77] S.K. Samal, M.K. Moharana, Effects of Inlet/Outlet Manifold Configuration on the Thermo-Hydrodynamic Performance of Recharging Microchannel Heat Sink, J. Therm.

Sci. Eng. Appl. 13 (2021). https://doi.org/10.1115/1.4047940.

[78] N. Tran, Y.J. Chang, J.T. Teng, T. Dang, R. Greif, Enhancement thermodynamic performance of microchannel heat sink by using a novel multi-nozzle structure, Int. J. Heat Mass Transf. 101 (2016) 656–666. https://doi.org/10.1016/j.ijheatmasstransfer.2016.04.111.

[79] N. Tran, Y.J. Chang, J.T. Teng, R. Greif, Enhancement heat transfer rate per unit volume of microchannel heat exchanger by using a novel multi-nozzle structure on cool side, Int. J. Heat Mass Transf. 109 (2017) 1031–1043. https://doi.org/10.1016/j.ijheatmasstransfer.2017.02.058.

[80] S.K. Samal, M.K. Moharana, Thermo-hydraulic performance evaluation of a novel design recharging microchannel, Int. J. Therm. Sci. 135 (2019) 459–470. https://doi.org/10.1016/j.ijthermalsci.2018.09.006.

[81] M. Peng, L. Chen, W. Ji, W. Tao, Numerical study on flow and heat transfer in a multi-jet microchannel heat sink, Int. J. Heat Mass Transf. 157 (2020). https://doi.org/10.1016/j.ijheatmasstransfer.2020.119982.

[82] S.K. Samal, M.K. Moharana, Thermohydrodynamic Performance Evaluation of Recharging, Interrupted and Simple Microchannels: A Comparative Study, J. Heat Transfer. 142 (2020). https://doi.org/10.1115/1.4045066.

[83] H. Shen, H. Liu, X. Shao, G. Xie, C.C. Wang, Thermofluids performances on innovative design with multi-circuit nested loop applicable for double-layer microchannel heat sinks, Appl. Therm. Eng. 219 (2023). https://doi.org/10.1016/j.applthermaleng.2022.119699.

[84] H. Shen, G. Xie, C.C. Wang, The numerical simulation with staggered alternation locations and multi-flow directions on the thermal performance of double-layer microchannel heat sinks, Appl. Therm. Eng. 163 (2019).

https://doi.org/10.1016/j.applthermaleng.2019.114332.

[85] H. Shen, G. Xie, C.C. Wang, Heat transfer and thermodynamic analysis by introducing multiple alternation structures into double-layer microchannel heat sinks, Int. J. Therm. Sci. 145 (2019). https://doi.org/10.1016/j.ijthermalsci.2019.105975.

[86] M. Wong, I. Owen, C.J. Sutcliffe, Pressure loss and heat transfer through heat sinks produced by selective laser melting, Heat Transf. Eng. 30 (2009) 1068–1076. https://doi.org/10.1080/01457630902922228.

[87] M.A. Arie, A.H. Shooshtari, V. V. Rao, S. V. Dessiatoun, M.M. Ohadi, Air-Side Heat Transfer Enhancement Utilizing Design Optimization and an Additive Manufacturing Technique, J. Heat Transfer. 139 (2017). https://doi.org/10.1115/1.4035068.

[88] Y. Huang, M.C. Leu, J. Mazumder, A. Donmez, Additive Manufacturing: Current State, Future Potential, Gaps and Needs, and Recommendations, J. Manuf. Sci. Eng. 137 (2015). https://doi.org/10.1115/1.4028725.

[89] T. CAFFREY, T., WOHLERS, R.I. CAMPBELL, Executive summary of the Wohlers Report 2016, (2016) 12.

[90] S. Tsopanos, M. Wong, I. Owen, C.J. Sutcliffe, Manufacturing Novel Heat Transfer Devices By Selective Laser Melting, (2006). https://doi.org/10.1615/ihtc13.p13.40.

[91] Mott Corporation, 3D Printed Heat Exchangers, 1 (n.d.). https://mottcorp.com/product/3d-printed-products/3d-printed-heat-exchangers/.

[92] Stratatys, Advancing Thermal Management with Additive Manufacturing, (n.d.). https://www.stratasysdirect.com/-/media/files/direct/white-papers/thermal-management-white-paper_web.pdf.

[93] Hyperganic, The Heat Exchanger, Algorithmic Engineering of heat exchangers, (n.d.). https://www.hyperganic.com/press-and-stories/2/.

[94] V. Bhavar, P. Kattire, V. Patil, S. Khot, K. Gujar, R. Singh, A review on powder bed

fusion technology of metal additive manufacturing, Addit. Manuf. Handb. Prod. Dev. Def. Ind. (2017) 251–261. https://doi.org/10.1201/9781315119106.

[95] M. Wong, S. Tsopanos, C.J. Sutcliffe, I. Owen, Selective laser melting of heat transfer devices, Rapid Prototyp. J. 13 (2007) 291–297. https://doi.org/10.1108/13552540710824797.

[96] M. Wong, I. Owen, C.J. Sutcliffe, A. Puri, Convective heat transfer and pressure losses across novel heat sinks fabricated by Selective Laser Melting, Int. J. Heat Mass Transf. 52 (2009) 281–288. https://doi.org/10.1016/j.ijheatmasstransfer.2008.06.002.

[97] J. Pakkanen, F. Calignano, F. Trevisan, M. Lorusso, E.P. Ambrosio, D. Manfredi, P. Fino, Study of Internal Channel Surface Roughnesses Manufactured by Selective Laser Melting in Aluminum and Titanium Alloys, Metall. Mater. Trans. A Phys. Metall. Mater. Sci. 47 (2016) 3837–3844. https://doi.org/10.1007/s11661-016-3478-7.

[98] C. Yan, L. Hao, A. Hussein, S.L. Bubb, P. Young, D. Raymont, Evaluation of light-weight AlSi10Mg periodic cellular lattice structures fabricated via direct metal laser sintering, J. Mater. Process. Technol. 214 (2014) 856–864. https://doi.org/10.1016/j.jmatprotec.2013.12.004.

[99] L. Ventola, F. Robotti, M. Dialameh, F. Calignano, D. Manfredi, E. Chiavazzo, P. Asinari, Rough surfaces with enhanced heat transfer for electronics cooling by direct metal laser sintering, Int. J. Heat Mass Transf. 75 (2014) 58–74. https://doi.org/10.1016/j.ijheatmasstransfer.2014.03.037.

[100] M.A. Arie, A.H. Shooshtari, S. V. Dessiatoun, M.M. Ohadi, Performance characterization of an additively manufactured titanium (Ti64) heat exchanger for an air-water cooling application, ASME 2016 Heat Transf. Summer Conf. HT 2016, Collocated with ASME 2016 Fluids Eng. Div. Summer Meet. ASME 2016 14th Int. Conf. Nanochannels, Microchannels, Minichannels. 2 (2016).

https://doi.org/10.1115/HT2016-1059.

[101] O.T. Ibrahim, J.G. Monroe, S.M. Thompson, N. Shamsaei, H. Bilheux, A. Elwany, L. Bian, An investigation of a multi-layered oscillating heat pipe additively manufactured from Ti-6Al-4V powder, Int. J. Heat Mass Transf. 108 (2017) 1036–1047. https://doi.org/10.1016/j.ijheatmasstransfer.2016.12.063.

[102] Y. Cormier, P. Dupuis, A. Farjam, A. Corbeil, B. Jodoin, Additive manufacturing of pyramidal pin fins: Height and fin density effects under forced convection, Int. J. Heat Mass Transf. 75 (2014) 235–244. https://doi.org/10.1016/j.ijheatmasstransfer.2014.03.053.

[103] N. Sahiti, F. Durst, A. Dewan, Heat transfer enhancement by pin elements, Int. J. Heat Mass Transf. 48 (2005) 4738–4747. https://doi.org/10.1016/j.ijheatmasstransfer.2005.07.001.

[104] H.R.S. Jazi, J. Mostaghimi, S. Chandra, L. Pershni, T. Coyle, Spray-formed, metal-foam heat exchangers for high temperature applications, J. Therm. Sci. Eng. Appl. 1 (2009) 1–7. https://doi.org/10.1115/1.4001049.

[105] Y. Cormier, P. Dupuis, B. Jodoin, A. Corbeil, Net shape fins for compact heat exchanger produced by cold spray, J. Therm. Spray Technol. 22 (2013) 1210–1221. https://doi.org/10.1007/s11666-013-9968-x.

[106] Y. Cormier, P. Dupuis, B. Jodoin, A. Corbeil, Pyramidal Fin Arrays Performance Using Streamwise Anisotropic Materials by Cold Spray Additive Manufacturing, J. Therm. Spray Technol. 25 (2016) 170–182. https://doi.org/10.1007/s11666-015-0267-6.

[107] A. Farjam, Y. Cormier, P. Dupuis, B. Jodoin, A. Corbeil, Influence of Alumina Addition to Aluminum Fins for Compact Heat Exchangers Produced by Cold Spray Additive Manufacturing, J. Therm. Spray Technol. 24 (2015) 1256–1268. https://doi.org/10.1007/s11666-015-0305-4.

[108] P. Dupuis, Y. Cormier, M. Fenech, A. Corbeil, B. Jodoin, Flow structure identification and analysis in fin arrays produced by cold spray additive manufacturing, Int. J. Heat Mass Transf. 93 (2016) 301–313. https://doi.org/10.1016/j.ijheatmasstransfer.2015.10.019.

[109] P. Dupuis, Y. Cormier, M. Fenech, B. Jodoin, Heat transfer and flow structure characterization for pin fins produced by cold spray additive manufacturing, Int. J. Heat Mass Transf. 98 (2016) 650–661. https://doi.org/10.1016/j.ijheatmasstransfer.2016.03.069.

[110] M. Mani, P. Witherell, Design Rules for Additive Manufacturing: Literature Review and Research Categorization | NIST, Int. J. Adv. Manuf. Technol. (2017).

[111] A. Muley, M. Stoia, D. Van Affelen, V. Reddy, V. Duggirala, S. Locke, Recent Advances in Thin-Wall Additively Manufactured Heat Exchangers, ASME Int. Mech. Eng. Congr. Expo. Proc. 2A-2021 (2021). https://doi.org/10.1115/IMECE2021-73212.

[112] B. Gutmann, M. Köckinger, G. Glotz, T. Ciaglia, E. Slama, M. Zadravec, S. Pfanner, M.C. Maier, H. Gruber-Wölfler, C. Oliver Kappe, Design and 3D printing of a stainless steel reactor for continuous difluoromethylations using fluoroform, React. Chem. Eng. 2 (2017) 919–927. https://doi.org/10.1039/c7re00176b.

[113] S.A. Niknam, M. Mortazavi, D. Li, Additively manufactured heat exchangers: a review on opportunities and challenges, Int. J. Adv. Manuf. Technol. 112 (2021) 601–618. https://doi.org/10.1007/s00170-020-06372-w.

[114] L.W. Hunter, D. Brackett, N. Brierley, J. Yang, M.M. Attallah, Assessment of trapped powder removal and inspection strategies for powder bed fusion techniques, Int. J. Adv. Manuf. Technol. 106 (2020) 4521–4532. https://doi.org/10.1007/s00170-020-04930-w.

[115] T. Vaneker, A. Bernard, G. Moroni, I. Gibson, Y. Zhang, Design for additive manufacturing: Framework and methodology, CIRP Ann. 69 (2020) 578–599.

https://doi.org/10.1016/j.cirp.2020.05.006.

[116] N. Hopkinson, P. Dickens, Analysis of rapid manufacturing - Using layer manufacturing processes for production, Proc. Inst. Mech. Eng. Part C J. Mech. Eng. Sci. 217 (2003) 31–40. https://doi.org/10.1243/095440603762554596.

[117] E. Atzeni, A. Salmi, Economics of additive manufacturing for end-usable metal parts, Int. J. Adv. Manuf. Technol. 62 (2012) 1147–1155. https://doi.org/10.1007/s00170-011-3878-1.

[118] R.E. Laureijs, J.B. Roca, S.P. Narra, C. Montgomery, J.L. Beuth, E.R.H. Fuchs, Metal additive manufacturing: Cost competitive beyond low volumes, J. Manuf. Sci. Eng. Trans. ASME. 139 (2017). https://doi.org/10.1115/1.4035420.

[119] D.S. Thomas, S.W. Gilbert, Costs and cost effectiveness of additive manufacturing: A literature review and discussion, Addit. Manuf. Costs, Cost Eff. Ind. Econ. (2015) 1–96.

[120] M. Fera, R. Macchiaroli, F. Fruggiero, A. Lambiase, A new perspective for production process analysis using additive manufacturing—complexity vs production volume, Int. J. Adv. Manuf. Technol. 95 (2018) 673–685. https://doi.org/10.1007/s00170-017-1221-1.

[121] A.M. Al-Mogbel, Analysis of human thermal comfort using a coupled model for prodicting human body-environment heat and mass exchange, (2000).

[122] Fluent User's Guide, (2013).

[123] R.L. Webb, Performance evaluation criteria for use of enhanced heat transfer surfaces in heat exchanger design, Int. J. Heat Mass Transf. 24 (1981) 715–726. https://doi.org/10.1016/0017-9310(81)90015-6.

[124] N. Zheng, F. Yan, K. Zhang, T. Zhou, Z. Sun, A review on single-phase convective heat transfer enhancement based on multi-longitudinal vortices in heat exchanger tubes, Appl. Therm. Eng. 164 (2020) 114475.

https://doi.org/10.1016/j.applthermaleng.2019.114475.

[125] P.T. Ireland, D.R.H. Gillespie, Z. Wang, Heating Element, US6181874B1, 2014. http://v3.espacenet.com/textdoc?DB=EPODOC&IDX=EP1782768&F=0.

[126] Miniature wire probe, boundary layer - Dantec Dynamics, (n.d.). https://www.dantecdynamics.com/product/miniature-wire-probe-boundary-layer/ (accessed April 1, 2024).

[127] FLIR Systems, FLIR Systems. FLIR X6900sc Datasheet, 2018., (n.d.).

[128] B. Kirollos, T. Povey, Laboratory infrared thermal assessment of laser-sintered high-pressure nozzle guide vanes to derisk engine design programs, J. Turbomach. 139 (2017). https://doi.org/10.1115/1.4035074.

[129] S. Luque, V. Kanjirakkad, I. Aslanidou, R. Lubbock, B. Rosic, S. Uchida, A new experimental facility to investigate combustor-turbine interactions in gas turbines with multiple can combustors, Proc. ASME Turbo Expo. 2C (2014). https://doi.org/10.1115/GT2014-26987.

[130] M.L.G. Oldfield, Impulse Response Processing of Transient Heat Transfer Gauge Signals, J. Turbomach. 130 (2008). https://doi.org/10.1115/1.2752188.

[131] M.H.I. LTD., Brief Overview of the Experiment for Heat Transfer Characteristic of Swirl Channel (Internal Report), 2020.

[132] Inconel 718: Properties, Applications and Production., (n.d.).

[133] S. Baek, C. Lee, S. Jeong, Effect of flow maldistribution and axial conduction on compact microchannel heat exchanger, Cryogenics (Guildf). 60 (2014) 49–61. https://doi.org/10.1016/j.cryogenics.2014.01.003.

[134] J. Jung, S. Jeong, Effect of flow mal-distribution on effective NTU in multi-channel counter-flow heat exchanger of single body, Cryogenics (Guildf). 47 (2007) 232–242. https://doi.org/10.1016/j.cryogenics.2007.01.004.

[135] L. Sheik Ismail, C. Ranganayakulu, R.K. Shah, Numerical study of flow patterns of compact plate-fin heat exchangers and generation of design data for offset and wavy fins, Int. J. Heat Mass Transf. 52 (2009) 3972–3983. https://doi.org/10.1016/j.ijheatmasstransfer.2009.03.026.

[136] A. Jiao, R. Zhang, S. Jeong, Experimental investigation of header configuration on flow maldistribution in plate-fin heat exchanger, Appl. Therm. Eng. 23 (2003) 1235–1246. https://doi.org/10.1016/S1359-4311(03)00057-7.

[137] J.B. Kitto, J.M. Robertson, Effects of maldistribution of flow on heat transfer equipment performance, Heat Transf. Eng. 10 (1989) 18–25. https://doi.org/10.1080/01457638908939688.

[138] B. PRABHAKARA RAO, SARIT K. DAS, Effect of Flow Distribution to the Channels on the Thermal Performance of the Multipass Plate Heat Exchangers, Heat Transf. Eng. (2004).

[139] R.B. Fleming, The Effect of Flow Distribution in Parallel Channels of Counterflow Heat Exchangers, Adv. Cryog. Eng. (1967) 352–362. https://doi.org/10.1007/978-1-4757-0489-1_37.

[140] M.M. Aslam Bhutta, N. Hayat, M.H. Bashir, A.R. Khan, K.N. Ahmad, S. Khan, CFD applications in various heat exchangers design: A review, Appl. Therm. Eng. 32 (2012) 1–12. https://doi.org/10.1016/j.applthermaleng.2011.09.001.

[141] U. Pasquier, W.X. Chu, M. Zeng, Y.T. Chen, Q.W. Wang, T. Ma, CFD simulation and optimization of fluid flow distribution inside printed circuit heat exchanger headers, Numer. Heat Transf. Part A Appl. 69 (2016) 710–726. https://doi.org/10.1080/10407782.2015.1090771.

[142] J. Wen, Y. Li, Study of flow distribution and its improvement on the header of plate-fin heat exchanger, Cryogenics (Guildf). 44 (2004) 823–831.

https://doi.org/10.1016/j.cryogenics.2004.04.009.

[143] Z. Zhang, Y.Z. Li, CFD simulation on inlet configuration of plate-fin heat exchangers, Cryogenics (Guildf). 43 (2003) 673–678. https://doi.org/10.1016/S0011-2275(03)00179-6.

[144] A. Raul, B.N. Bhasme, R.S. Maurya, A Numerical Investigation of Fluid Flow Maldistribution in Inlet Header Configuration of Plate Fin Heat Exchanger, Energy Procedia. 90 (2016) 267–275. https://doi.org/10.1016/j.egypro.2016.11.194.